TECHNISCHE
UNIVERSITÄT
WIEN
Vienna University of Technology

DISSERTATION

Study of Thermoelectric Properties of Multi-Material Composites and Thin Films versus the Single-Material Performances

ausgeführt zum Zwecke der Erlangung des akademischen Grades eines
Doktors der technischen Wissenschaften unter der Leitung von

Univ.Prof. Dipl.-Ing. Dr.techn. Ernst Bauer
E138
Institut für Festkörperphysik

eingereicht an der Technischen Universität Wien
Fakultät für Physik

von

Dipl.-Ing. Alexander Riss
Matrikelnummer 01325102

Wien, Februar 2024

[redacted]

Kurzfassung

Im Rahmen dieser Dissertation werden die thermoelektrischen Größen unter Annäherung der elektronischen Bandstruktur durch parabolische Bänder umfassend untersucht. In einer gemeinsamen Forschungsarbeit wurde ein Softwarepaket entwickelt, das detaillierte Informationen über die Bandstruktur aus Messdaten thermoelektrischer Größen extrahiert. Diese Anwendung ist öffentlich zugänglich und verfügt über eine übersichtliche Benutzeroberfläche. Zudem wird sie durch ein neuronales Netzwerk unterstützt, das es Forschern ermöglicht, die elektronische Struktur der untersuchten Materialien mit minimalem Aufwand zu analysieren.

Der anschließende Schwerpunkt der Arbeit konzentriert sich auf die Untersuchung der thermoelektrischen Eigenschaften von Systemen, die aus mehreren Materialien bestehen, insbesondere von Kompositen und Schicht-Substrat-Systemen. Durch mathematische Modelle, die elektrischen Schaltkreisen zugrunde liegen, werden die individuellen Beiträge der Komponenten zu den gemessenen Eigenschaften isoliert. Die Untersuchung ergab, dass das Substrat die Messung dünner Schichten beeinflussen kann, was das Risiko einer Fehleinschätzung der Leistung birgt. Um dieses oft vernachlässigte Problem zu lösen, wurden Modelle erstellt, die genauere Analysen gewährleisten.

Die Analyse von Kompositen, die ein thermoelektrisches Material und ein Metall enthalten, offenbarte die irreführende Bedeutung des elektrischen Widerstands und des Power-Faktors in diesen Systemen. Daher werden fehlerresistente Größen, wie die tatsächliche Leistung und der thermoelektrische Gütefaktor empfohlen, um potenzielle Fehlinterpretationen in zukünftigen Studien von Kompositen vorzubeugen.

Die Arbeit setzt sich des Weiteren mit Unterschieden zwischen den Target- und Schichteigenschaften beim Magnetronsputtern unter Verwendung von Schichten aus den Heusler-Verbindungen Fe_2VAl und $Fe_2V_{0,9}Ti_{0,1}Al$ als Fallstudien auseinander.

Ein neuer Ansatz zur Behandlung der Abweichungen in der Schichtzusammensetzung, der die Verwendung eines stöchiometrischen Targets durch einen iterativen Prozess einschließt, wird vorgestellt. Obwohl die thermoelektrischen Eigenschaften hinter den Erwartungen zurückblieben, ermöglicht diese Strategie die präzise Synthese von Schichten mit der gewünschten Stöchiometrie.

Zusätzlich wurden NiAu-Schichten erfolgreich aus einem Nickel-Target mit angebrachten Stücken aus Gold hergestellt, was zu einer erheblichen Kostenreduktion im Vergleich zum Bulk-Material führte. Bei einer Temperatur von 614 K wurde ein hoher Power-Faktor von $11,2\,\mathrm{mWm^{-1}K^{-2}}$ in $\mathrm{Ni_{0,27}Au_{0,73}}$ erreicht. Unter Vernachlässigung des Phononenbeitrags zur thermischen Leitfähigkeit ergab sich ein zT-Wert von $0,15$ bei 763 K.

Abstract

This thesis extensively studies thermoelectric properties within the parabolic-band regime. A collaborative effort resulted in the development of a tool that extracts detailed information about the band structure from thermoelectric measurement data. This tool, encapsulated in a publicly available application and supported by a neural network, features a user-friendly interface, enabling researchers to easily explore the electronic structure of materials under investigation.

The subsequent focus of the work extends to the study of thermoelectric properties in multi-material systems, encompassing both bulk composites and film-substrate configurations. Employing mathematical models based on electric circuits, the distinct contributions of individual constituents on the measured properties are elucidated. The investigation revealed that the substrate can distort measurements in film-substrate systems, potentially leading to a misinterpretation of the film's performance. To address this often-neglected issue, a set of robust formulas are derived, ensuring more accurate measurements.

Remarkably, the analysis of composites involving a thermoelectric material and a metal uncovered the misleading nature of electrical resistivity and power factor calculations. Consequently, error-resistant quantities, such as the power output and figure of merit, are proposed to mitigate potential misinterpretations in future composite studies.

Research then delved into exploring disparities between target and film properties concerning magnetron sputtering, utilizing full-Heusler Fe_2VAl and $Fe_2V_{0.9}Ti_{0.1}Al$ films as case studies. A novel approach to address film composition deviations is presented, involving the use of an off-stoichiometric target through an iterative process. Despite the thermoelectric properties falling below expectations due to imperfect film crystallization, the strategy successfully achieved the desired stoichiometry, enabling accurate film synthesis without the need of advanced sputter setups.

Additionally, NiAu films were successfully synthesized from a Ni target with affixed Au pieces, providing a material-efficient preparation compared to the respective bulk material. Ultimately, a remarkable power factor of 11.2 mWm^{-1}K^{-2} at 614 K was obtained in $Ni_{0.27}Au_{0.73}$. Neglecting the phonon contribution to thermal conduction yielded a figure of merit of $zT = 0.15$ at 763 K.

Contents

List of Acronyms

CVD	Chemical vapor deposition
DFT	Density functional theory
DOS	Density of states
EDX	Energy-dispersive X-ray
fcc	face-centered cubic
IoT	Internet of things
IPCC	Intergovernmental panel on climate change
MMRTG	Multi-mission radioisotope thermoelectric generator
NFE	Nearly free electrons
PLD	Pulsed laser deposition
PVD	Physical vapor deposition
RTG	Radioisotope thermoelectric generator
SEM	Secondary-electron microscope
SOC	Spin-orbit coupling
TEC	Thermoelectric cooling system
TEG	Thermoelectric generator
TB	Tight binding
XRD	X-ray diffraction
XRF	X-ray fluorescence
YSZ	Yttria-stabilized zirconia

1 Introduction

The climate crisis has caused dramatic and irreversible consequences that not only disrupt nature but also impact humanity in many ways [1–4]. Despite these alarming effects, it is only in recent years that this urgent issue has drawn the attention of politicians and citizens worldwide. Whether it is too late to reverse, even partially, the CO_2 pollution and the global warming resulting form the greenhouse effect, every possible effort must be made to halt further progression.

The latest report on climate change from the Intergovernmental Panel on Climate Change (IPCC) from 2023 states that the global temperature rise will reach 1.5 °C in the coming years with a likelihood of over 50 % [5].

One of the many problems concerns the conversion of various primary energy sources into electrical energy. The growing population (the world's population is expected to reach 8.5 billion people in 2030, 9.7 billion in 2050 and over ten billion in 2100 [6]) and surging demand for electricity to power electric vehicles, homes and devices related to the Internet of Things (IoT) intensifies the necessity for an ever-increasing energy supply. To make matters worse, a significant chunk of the world's electricity (36.8 % as of 2019) is generated in coal-fired power plants, although its share gradually decreases year by year [7]. On the contrary, the contribution of electricity produced via natural gas (23.6 %) is on the rise, and is only marginally surpassed by renewable energy sources (26.5 %). Furthermore, the vast majority ($\approx$ 72 %) of the global primary energy is lost at conversion, with thermal losses having by far the largest share [8].

The overall conversion efficiency can be improved by reusing the produced waste heat and partially convert it back into usable electrical energy. This can be achieved through two distinct approaches: indirect conversion and direct conversion. Indirect conversion involves the transformation of thermal energy into a different form of energy before generating electricity. For example, in a steam turbine, thermal energy from steam is converted into mechanical energy before transformed in an electric generator. Alternatively, direct conversion techniques utilize either thermionic emission or make use of the Seebeck effect. Thermionic emission relies on the emission of electrons from a heated surface, which are then absorbed by an opposed surface, resulting in the generation of an electric current [9]. However, research has waned in the past and thermionic applications are only rarely found nowadays [10].

The far more explored Seebeck effect describes the conversion of thermal energy into electrical energy through diffuse electron movement in a material, manifesting as a voltage when a temperature gradient is imposed across a thermoelectric material. Mathematically, this phenomenon can be described by

$$S = -\frac{\Delta V}{\Delta T} \ , \tag{1.1}$$

where S is the so-called Seebeck coefficient, ΔV the generated voltage and ΔT the temperature difference. Apart from the Seebeck coefficient, the electrical conductivity σ and thermal conductivity λ are further relevant quantities to describe a thermoelectric material. All of these can be combined into the dimensionless thermoelectric figure of merit

$$zT = \frac{S^2\sigma}{\lambda_\mathrm{e} + \lambda_\mathrm{ph}} T \ , \tag{1.2}$$

with the absolute temperature T. Here, the thermal conductivity is split into the contribution of electrons, λ_e, as well as phonons, λ_ph. The numerator is usually referred to as the power factor

$$PF = S^2\sigma \ , \tag{1.3}$$

as it is proportional to the generated power output. The figure of merit zT is strongly linked to the conversion efficiency η of a thermoelectric material:

$$\eta = \eta_\mathrm{carnot} \frac{\sqrt{1 + \overline{zT}} - 1}{\sqrt{1 + \overline{zT}} + T_c/T_h} \ . \tag{1.4}$$

Since thermoelectric materials function as heat engines coupled to two different temperature reservoirs, the Carnot efficiency $\eta_\mathrm{carnot} = \frac{T_h - T_c}{T_h}$, with T_h and T_c being the temperatures on the hot and cold side, respectively, marks the upper limit

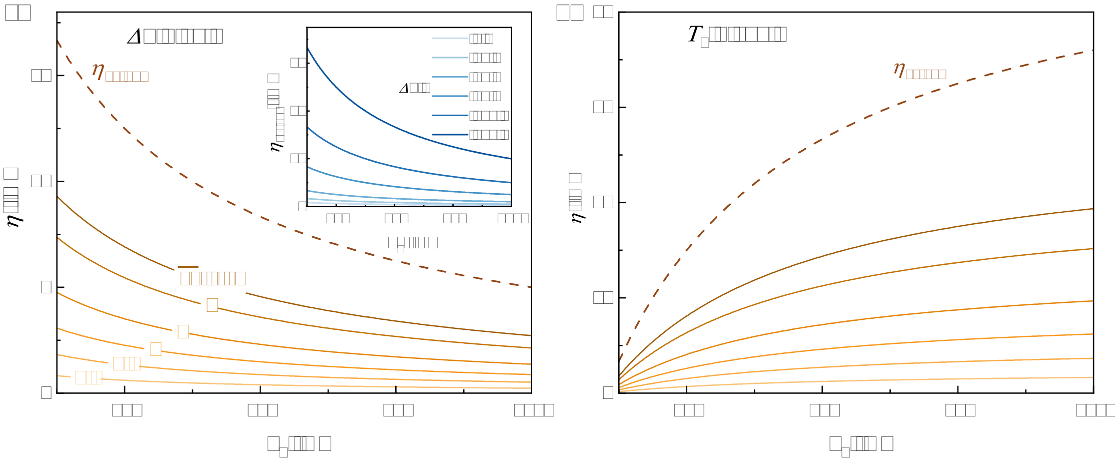

Figure 1.1: Conversion efficiency η versus the temperature on the hot side T_h of a thermoelectric material for various values of the average figure of merit $\overline{zT}$ for a) a fixed temperature difference $\Delta T = 50\,\mathrm{K}$ and b) a fixed temperature on the cold side T_c. The inset in a) shows the temperature-dependent Carnot efficiency for various ΔT.

of conversion. $\overline{zT}$ is the average figure of merit across the whole temperature interval. Figure 1.1 shows the efficiency for different values of $\overline{zT}$ and temperatures of the heat source and sink. Notably, even when $\overline{zT}$ adopts substantial values, the efficiency η consistently falls below the Carnot efficiency. For a fixed temperature difference, the Carnot efficiency is larger at lower temperatures, as shown in the inset of Figure 1.1a. More importantly, for a constant temperature at the cold side (e.g. room temperature or the temperature of cooling water), the Carnot efficiency increases with the temperature of the heat source T_h (see Figure 1.1b). Thus, in case of a constant heat sink, highest efficiency of a thermoelectric material is obtained for a large temperature on the hot side together with a substantial average figure of merit.

To increase zT, a large Seebeck coefficient and electrical conductivity together with a low thermal conductivity are necessities (see Equation 1.2). The former two ensure a large power output $P = U^2/R$ while the latter prevents the temperature gradient from leveling off. Unfortunately, these parameters are not independently tunable [11].

Since the discovery of the Seebeck effect by Thomas Johann Seebeck 200 years ago, numerous different materials have been invented, tested, improved and discarded. This research has lead to the state-of-the-art materials used nowadays. Regarding applications, systems composed of multiple materials or phases, e.g. composites and thin films, are particularly interesting, since the cost and weight can be effectively tuned by varying the amount or stoichiometry of the constituents. Furthermore, thin films can be a proper solution for micro applications, where space consumption of the thermoelectric module is more critical than power output.

This thesis is dedicated to study multi-phase systems both theoretically and experimentally. A large part is devoted to the contribution of the individual thermoelectric properties of the constituents to the measured properties and potential sources of error related to the measurement and interpretation of results. Furthermore, the disparity between the properties of thin films and their bulk counterparts are examined.

The manuscript is structured into two parts. In the first part, composed of chapter 2, chapter 3 and chapter 5, theoretical aspects of thermoelectric transport are discussed, including a description of state-of-the-art materials and current and potential applications. Then, the parabolic-band model, implemented in a publicly available software is presented. In the last chapter of the first part, the the thermoelectric properties of multi-material setups are calculated, encompassing both film-substrate systems and thermoelectric-metal composites.

The second part of this thesis, comprising chapter 6, chapter 7 and chapter 8, is devoted to experimental studies. First, the employed devices and their underlying physics are elucidated. Subsequently, the synthesis process, along with the structural and thermoelectric properties of Ni−Au films, is examined. lastly, the challenge of achieving nominal stoichiometry in films produced by magnetron sputtering is addressed through a promising approach that involves off-stoichiometric targets synthesized iteratively. This methodology is demonstrated for different Fe_2VAl-based films.

At the end of the work, one chapter is dedicated to an overall conclusion of the results.

Part I

Theoretical Descriptions and Models

2 Theoretical aspects of thermoelectricity

In this chapter, the theory of thermoelectricity is discussed, starting from the derivation of the fundamental quantities, while further elucidating the properties of a good thermoelectric material. Furthermore, review of current state-of-the-art thermoelectrics is provided. At the end of this chapter, current and potential applications of thermoelectric generators are highlighted.

2.1 Fundamentals of thermoelectricity

The description and computation of the thermoelectric quantities, such as the Seebeck coefficient S, the electrical conductivity σ or resistivity ρ and the thermal conductivity λ, typically rely on one of two fundamental theories: the Boltzmann transport equation (BTE) [12] or the Landauer formalism [13]. Although both theories adopt different approaches - the Landauer theory providing a microscopic, quantum mechanical description considering phenomena like point defect scattering, and the BTE comprising a statistical description investigating the response of a macroscopic system to external influences - they yield consistent results [14, 15].

Any electrical current density J within a system can generally be written as [14]

$$J(T) = -q \int_{-\infty}^{\infty} G(E) \nabla f(E, \mu, T) \, \mathrm{d}E \ , \tag{2.1}$$

where q represents the charge of the involved carriers, $G(E)$ is the energy-dependent transport function and $f(E, \mu, T)$ denotes the Fermi-Dirac distribution function

$$f(E, \mu, T) = \frac{1}{e^{\frac{E-\mu}{k_\mathrm{B} T}} + 1} \ . \tag{2.2}$$

Here, k_B is the Boltzmann constant and μ is the chemical potential. Frequently, μ is considered temperature-independent and denoted as the Fermi energy E_F. However, in semimetals or semiconductors, the chemical potential can exhibit substantial temperature dependence (see chapter 3).

The Fermi-Dirac distribution function depicts the energy distribution of electrons in a material. In a homogeneous material, this function remains independent of the position. In the presence of external influences, the distribution may vary, causing a spatial gradient ∇f. The characteristics and significance of the transport function $G(E)$ will be discussed later.

2.1.1 Voltage-driven charge transport

When a voltage V is applied across two ends of a material, the energy of the charge carriers varies across the potential, inducing a gradient in the chemical potential μ:

$$\nabla\mu = q\nabla V. \tag{2.3}$$

Moreover, expressing ∇f in terms of the chemical potential yields

$$\nabla f = \frac{\mathrm{d}f}{\mathrm{d}x} = \frac{\mathrm{d}f}{\mathrm{d}\mu}\frac{\mathrm{d}\mu}{\mathrm{d}x} = -\frac{\mathrm{d}f}{\mathrm{d}E}\nabla\mu\ . \tag{2.4}$$

Inserting Equation 2.3 and Equation 2.4 into Equation 2.1 results in the current induced by an applied voltage:

$$J_{\nabla V} = -q^2\nabla V\int_{-\infty}^{\infty} G(E)\left(-\frac{\mathrm{d}f}{\mathrm{d}E}\right)\mathrm{d}E\ . \tag{2.5}$$

Finally, the electrical conductivity σ is obtained by applying Ohm's law ($J_{\nabla V} = -\sigma\nabla V$):

$$\sigma = q^2\int_{-\infty}^{\infty} G(E)\left(-\frac{\mathrm{d}f}{\mathrm{d}E}\right)\mathrm{d}E\ . \tag{2.6}$$

The term $\left(-\frac{\mathrm{d}f}{\mathrm{d}E}\right)$ is commonly referred to as the selection function $\phi_\sigma(E)$, representing the energy distribution of particles contributing to electrical conduction. The shape of $\phi_\sigma(E)$ is depicted in Figure 2.1a.

Given the symmetry of the selection function with respect to the chemical potential μ, electrons and holes contribute similarly to the electrical conduction and combine additively. The width of the selection function is temperature-dependent; at low temperatures, only particles in proximity to the chemical potential contribute, whereas at higher temperatures, states further away also play a role.

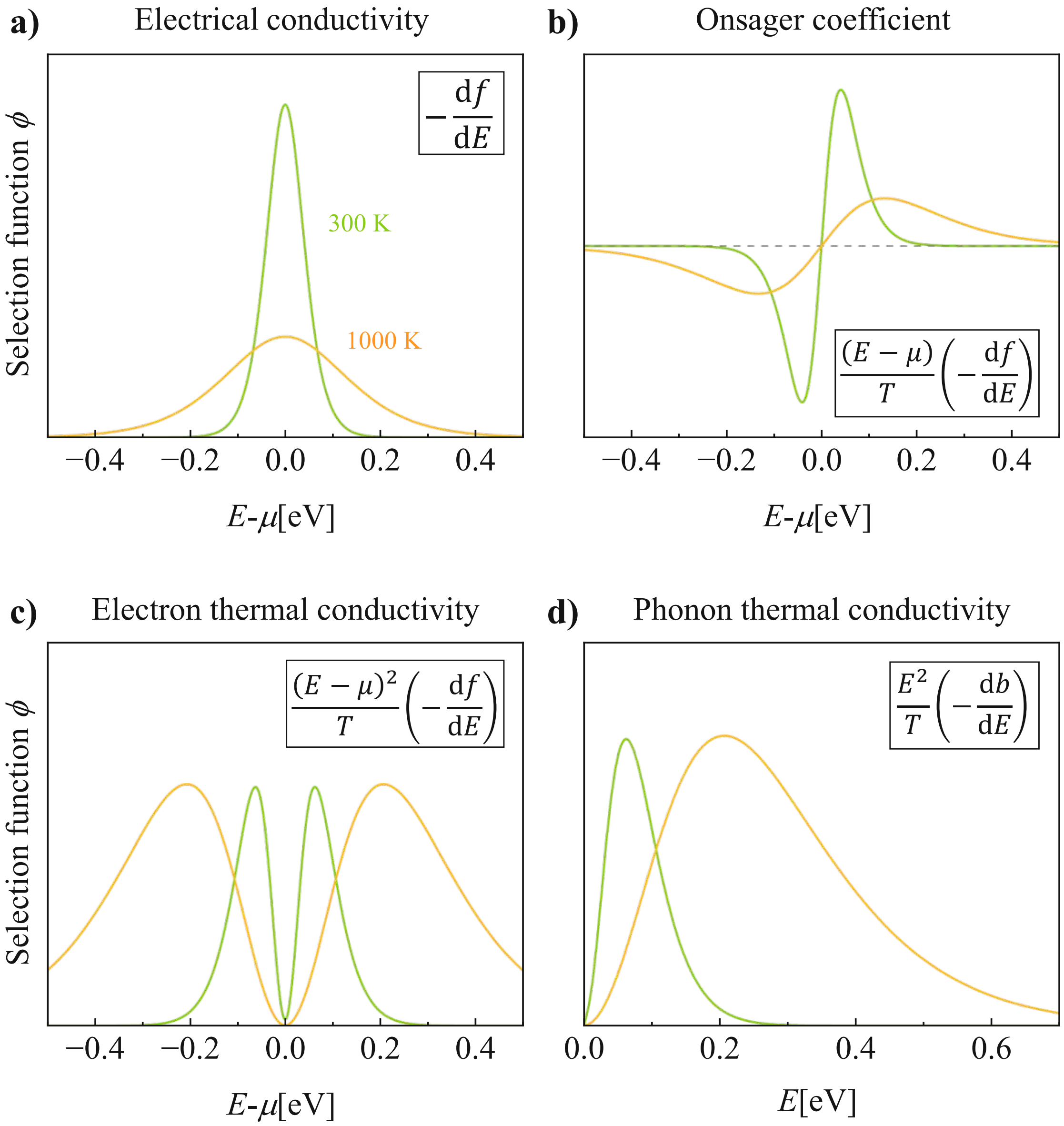

Figure 2.1: Selection function $\phi(E)$ for (a) the electrical conductivity, (b) Onsager coefficient as well as (c) electron and (d) phonon thermal conductivity. The green and orange line show the function at 300 K and 1000 K, respectively. The fermionic selection functions in a) - c) are either asymmetric or symmetric with respect to μ, while the bosonic selection function in d) only depends on the absolute energy E.

2.1.2 Temperature-driven charge transport

Another external factor that can introduces a variation in the Fermi-Dirac distribution function $f(E,\mu,T)$ is a temperature gradient ∇T. Analogous to Equation 2.4, ∇f can be expressed in terms of ∇T:

$$\nabla f = \frac{\mathrm{d}f}{\mathrm{d}T}\frac{\mathrm{d}T}{\mathrm{d}x} = -\frac{E-\mu}{T}\frac{\mathrm{d}f}{\mathrm{d}E}\nabla T\ . \tag{2.7}$$

Here, the relation

$$\frac{\mathrm{d}f}{\mathrm{d}T} = -\frac{E-\mu}{T}\frac{\mathrm{d}f}{\mathrm{d}E}\ , \tag{2.8}$$

is utilized. By incorporating Equation 2.8 into Equation 2.1, the temperature-driven current density is obtained:

$$J_{\nabla T} = -q\nabla T\int_{-\infty}^{\infty} G(E)\frac{E-\mu}{T}\left(-\frac{\mathrm{d}f}{\mathrm{d}E}\right)\,\mathrm{d}E\ . \tag{2.9}$$

Furthermore, introducing the quantity ν via $J_{\nabla T} = -\nu\nabla T$ yields [14]:

$$\nu = q\int_{-\infty}^{\infty} G(E)\frac{E-\mu}{T}\left(-\frac{\mathrm{d}f}{\mathrm{d}E}\right)\,\mathrm{d}E\ . \tag{2.10}$$

ν resembles an Onsager coefficient determining the current response to a temperature gradient. To obtain the Seebeck coefficient, both the current resulting from an applied temperature gradient and the opposing current due to the electric field that builds up need to be considered. The Seebeck measurement is defined under open-circuit conditions, hence the net current is zero:

$$J = J_{\nabla V} + J_{\nabla T} = 0\ , \tag{2.11}$$

$$-\sigma\nabla V - \nu\nabla T = 0\ . \tag{2.12}$$

The Seebeck coefficient S is defined as the voltage difference at a specific temperature difference ($S = -\Delta V/\Delta T$). This yields

$$S = -\frac{\Delta V}{\Delta T} = -\frac{\nabla V}{\nabla T} = \frac{\nu}{\sigma} \tag{2.13}$$

and thus

$$S = \frac{\int_{-\infty}^{\infty} G(E)\frac{E-\mu}{T}\left(-\frac{\mathrm{d}f}{\mathrm{d}E}\right)\,\mathrm{d}E}{q\int_{-\infty}^{\infty} G(E)\left(-\frac{\mathrm{d}f}{\mathrm{d}E}\right)\,\mathrm{d}E}\ . \tag{2.14}$$

$\phi_\nu(E) = \frac{E-\mu}{T}\left(-\frac{\mathrm{d}f}{\mathrm{d}E}\right)$ is the selection function of the Onsager coefficient and thus proportional to the Seebeck coefficient. Contrary to the selection function of the electrical conductivity, it is asymmetric with respect to the chemical potential μ (see Figure 2.1b). Consequently, charge carriers above and below the Fermi energy oppose each other, diminishing the net thermopower.

2.1.3 Voltage- and temperature-driven heat transport

In the preceding sections, charge transport induced by either a voltage or temperature gradient was discussed. In addition to that, each charge carrier inherently carries a specific amount of energy proportional to its own energy. Given that the change of a system's energy is linked to its entropy through the second law of thermodynamics, and the entropy is proportional to the number of possible arrangements of particles, the heat carried ($\partial Q/\partial c$) differs for fermions (f) and bosons (b) [14]:

$$\frac{\partial Q_f}{\partial c_f} = E - \mu \ , \tag{2.15}$$

$$\frac{\partial Q_b}{\partial c_b} = E \ , \tag{2.16}$$

where $c_f = D(E)f(E)$ and $c_b = D(E)b(E)$ represent the particles' occupation distribution for fermions and bosons, respectively. $b(E)$ is the Bose-Einstein distribution function, as elaborated later.

To determine the heat current stemming from a present voltage or temperature gradient, the charge q in Equation 2.1 can be substituted by the carried energy. For electrons, which are fermions, this yields

$$J_{Q,\nabla V} = -q\nabla V \int_{-\infty}^{\infty} G(E)\,(E-\mu)\left(-\frac{\mathrm{d}f}{\mathrm{d}E}\right)\mathrm{d}E \tag{2.17}$$

$$J_{Q,\nabla T} = -\nabla T \int_{-\infty}^{\infty} G(E)\frac{(E-\mu)^2}{T}\left(-\frac{\mathrm{d}f}{\mathrm{d}E}\right)\mathrm{d}E \ . \tag{2.18}$$

Note that one charge remains in $J_{Q,\nabla V}$ since it originates from Equation 2.3.

The electron thermal conductivity λ_e is defined as the ratio between the electron heat current density and the temperature gradient causing this current ($J_Q =$

$-\lambda_\mathrm{e}\nabla T$):

$$J_Q = J_{Q,\nabla T} + J_{Q,\nabla V} = -\lambda_\mathrm{e}\nabla T \ , \tag{2.19}$$

$$\lambda_\mathrm{e} = \frac{-J_{Q,\nabla T}}{\nabla T} + \frac{-J_{Q,\nabla V}}{\nabla T} \ , \tag{2.20}$$

$$\lambda_\mathrm{e} = \lambda_{\mathrm{e},\nabla T} + \lambda_{\mathrm{e},\nabla V} \ , \tag{2.21}$$

with

$$\lambda_{\mathrm{e},\nabla T} = \int_{-\infty}^{\infty} G(E)\frac{(E-\mu)^2}{T}\left(-\frac{\mathrm{d}f}{\mathrm{d}E}\right)\mathrm{d}E \ , \tag{2.22}$$

$$\lambda_{\mathrm{e},\nabla V} = q\frac{\nabla V}{\nabla T}\int_{-\infty}^{\infty} G(E)\,(E-\mu)\left(-\frac{\mathrm{d}f}{\mathrm{d}E}\right)\mathrm{d}E \ . \tag{2.23}$$

The electron thermal conductivity has two contributions: one from the temperature gradient itself ($\lambda_{\mathrm{e},\nabla T}$) and one from the voltage gradient induced by charge transport due to the temperature gradient ($\lambda_{\mathrm{e},\nabla V}$). The factor $\phi_{\mathrm{e},\lambda}(E) = \frac{(E-\mu)^2}{T}\left(-\frac{\mathrm{d}f}{\mathrm{d}E}\right)$ denotes the selection function of the electronic thermal transport. The energy dependence is depicted in Figure 2.1c. $\lambda_{\mathrm{e},\nabla V}$ can also be rewritten in accordance to Equation 2.10 and Equation 2.13 as

$$\lambda_{\mathrm{e},\nabla V} = -S^2\sigma T \ . \tag{2.24}$$

This term describes thermoelectric cooling. The negative sign, independent of the sign of the Seebeck coefficient, leads to a heat current in the direction of the temperature gradient, i.e. towards higher temperatures: $J_Q \propto +\nabla T$.

Since phonons are not associated with a charge, heat transport only occurs from a thermal gradient, not a voltage gradient. The Bose-Einstein occupation statistics for phonons

$$b(E,T) = \frac{1}{e^{\frac{E}{k_\mathrm{B}T}} - 1} \tag{2.25}$$

depends on the absolute energy, in clear contrast to the distribution of fermions, which depends on the energy relative to the chemical potential, as apparent in Equation 2.2. Otherwise, the derivation of the phonon heat transport is similar to Equation 2.18, yielding

$$J_{Q,\nabla T} = -\nabla T\int_0^{\infty} G(E)\frac{E^2}{T}\left(-\frac{\mathrm{d}b}{\mathrm{d}E}\right)\mathrm{d}E \tag{2.26}$$

and thus

$$\lambda_{\mathrm{ph},\nabla T} = \int_0^\infty G(E)\frac{E^2}{T}\left(-\frac{\mathrm{d}b}{\mathrm{d}E}\right)\mathrm{d}E\ . \tag{2.27}$$

Please note that the different energy scale modifies the integral range to 0 to ∞. The selection function $\phi_{\mathrm{ph},\lambda}(E) = \frac{E^2}{T}\left(-\frac{\mathrm{d}b}{\mathrm{d}E}\right)$ is shown in Figure 2.1d.

2.1.4 Transport function

From the results derived above, is is evident that all current densities can be expressed in the form

$$J(E) = A\int_\varepsilon^\infty G(E)\phi(E)\,\mathrm{d}E\ , \tag{2.28}$$

where A is a quantity-dependent pre-factor and ε adopts to 0 or $-\infty$ depending whether bosonic or fermionic transport is described. The transport function $G(E)$ denotes the capability of states within a temperature interval $\mathrm{d}E$ from the energy E to participate in the current. It can be expressed as [16]

$$G(E) = \sum_{\vec{k}} v_x^2(\vec{k})\tau(\vec{k})\delta(E - E(\vec{k}))\ , \tag{2.29}$$

where the summation covers the first Brillouin zone, $v_x(\vec{k})$ is the group velocity of carriers with the wave vector $\vec{k}$ and x denotes the direction of the applied temperature gradient and thus electric field. $E(\vec{k})$ is the dispersion relation. In systems where multiple bands contribute to the transport, the summation is extended over all bands. For parabolic bands, Equation 2.29 can be written more conveniently as [14]

$$G(E) = D(E)\langle v(E)^2\rangle\tau(E)\ . \tag{2.30}$$

Here, $D(E)$ is the electron density of states (DOS), denoting the number of states per volume at the energy E within the interval $\mathrm{d}E$. $\langle v(E)^2\rangle\tau(E)$ is the diffusivity of the particles at the energy E, composed of the average squared velocity $\langle v(E)^2\rangle$ and the scattering time $\tau(E)$. In many materials, the shape of the DOS dominates the thermoelectric behavior. This allows to neglect the velocity and scattering time in a rough approximation to obtain a qualitative picture of the thermoelectric properties. Figure 2.2 shows the integrand of Equation 2.28 without diffusivity, hence

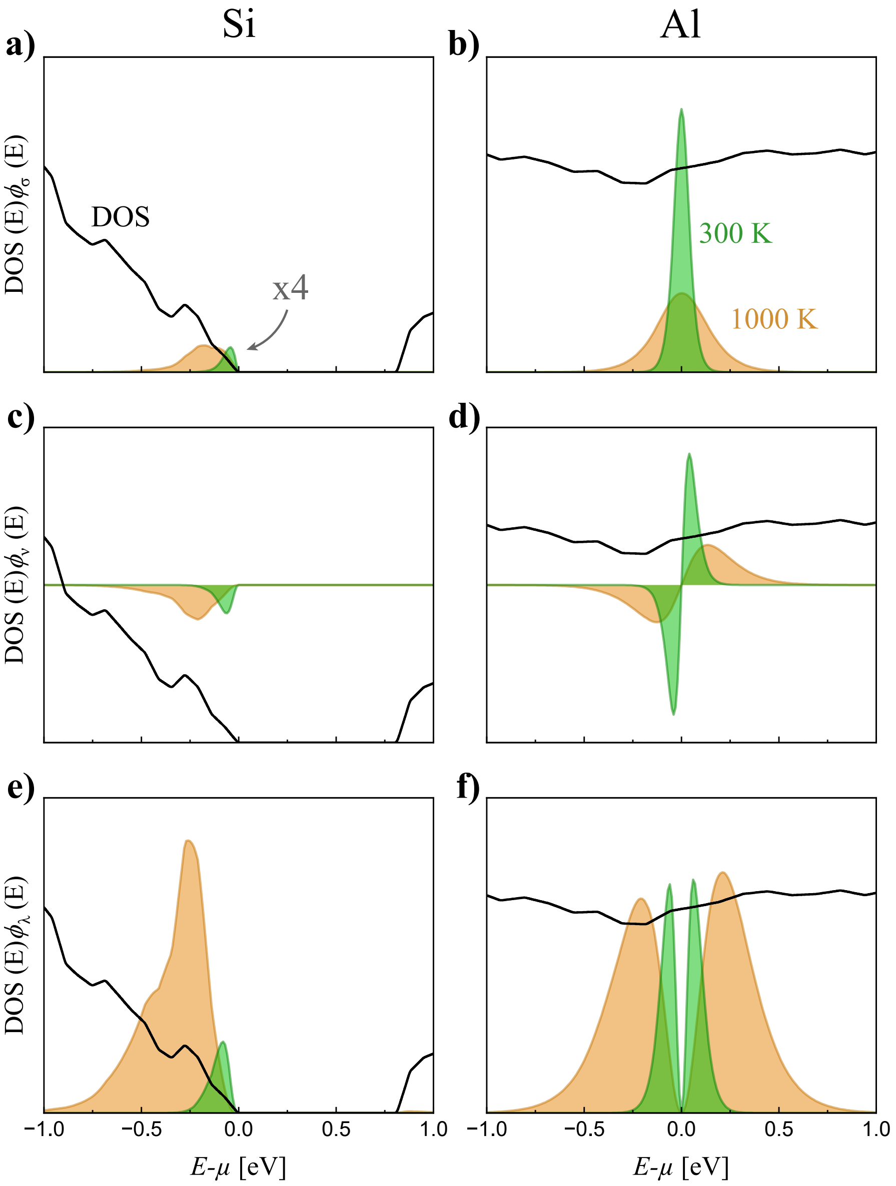

Figure 2.2: Density of states (DOS), weighted with the selection functions related to (a, b) the electrical conductivity $\phi_\sigma(E)$, (c, d) Seebeck coefficient $\phi_\nu(E)$ and (e, f) electron thermal conductivity $\phi_\lambda(E)$ of pristine Si (left column) and Al (right column), calculated at $300\,$K and $1000\,$K. For better visibility, the values for Si are multiplied by a factor of 4. The DOS of Si and Al, shown as black solid lines, are taken from Materials Project [17].

$D(E)\phi(E)$, for a metal (Al) and as well as a semiconductor (Si). The significantly higher DOS in Al results in larger electrical and thermal conductivity compared to Si (note that all values for Si are multiplied by a factor of 4 in Figure 2.2). Conversely, the relatively uniform nature of the DOS of Al, causing a partial erasure of the integral, leads to similar Onsager coefficients of Al and Si. Considering the inverse dependence of the Seebeck coefficient on the electrical conductivity (see Equation 2.13), a significantly larger Seebeck coefficient is obtained in Si.

Given that the Seebeck coefficient contributes with a square dependence to the figure of merit zT (see chapter 1), semiconductor are generally considered superior compared to metals. Additionally, as illustrated in Figure 2.2, it is evident that numerous parameters, including the position of the Fermi energy, the width of the band gap and the height and mass of the individual bands, play pivotal roles in determining the electronic properties. Various strategies to tune these values to enhance the performance are discussed in the next section.

The group velocity in Equation 3.7 is strongly linked to the electronic band structure and is calculated using

$$\vec{v}(E) = \frac{1}{\hbar}\frac{\partial E}{\partial \vec{k}} \,. \tag{2.31}$$

In flat and heavy bands (band mass $m^{\star} \gg m_{\mathrm{e}}$), the group velocity is substantially reduced compared to more dispersive bands with lighter band mass.

The scattering time $\tau(E,T)$, on the other hand, is much harder to evaluate due to the large number of possible scattering mechanisms. In general, the total scattering time is determined by the summation of the individual scattering rates of different processes:

$$\frac{1}{\tau_{\mathrm{tot}}} = \sum_i \frac{1}{\tau_i} \,, \tag{2.32}$$

with i denoting the scattering mechanism. Equation 2.32 is commonly referred to as Matthiessen's rule. In an ideal, periodic lattice, electrons are not scattered at all and behave as non-local, infinitely extended Bloch waves. However, deviations from the ideal periodicity lead to an interference of the Bloch wave with the surrounding lattice. This interference can be caused by several factors such as impurities, crystal defects and thermal vibrations. In all cases, the scattering probability depends on the phase space of the state which the electron is scattered into, which is represented by the density of states $D(E)$. The most important scattering mechanisms include acoustic-phonon scattering, alloy-disorder scattering and impurity scattering. In addition to that, electrons can scatter with other nearby electrons through Coulomb interaction.

Generally, the dependencies of the scattering time can be summarized as [18–21]

$$\tau = \widetilde{\tau} E^{\lambda - 1/2} T^{\gamma} (m^{\star})^{-3/2} \,, \tag{2.33}$$

where λ and γ describe the dependence of the scattering time on the energy and temperature, respectively, and $\widetilde{\tau}$ contains all energy- and temperature-independent parameters[1]. The exponent $-1/2$ represents the dependence on the DOS. For acoustic-phonon (ph), alloy-disorder (dis), ionized-impurity (ion) and electron-electron (el-el) scattering, the exponents are [18, 19, 22, 23]

$$\tau_{\mathrm{ph}} \propto E^{-1/2} T^{-1} \qquad (\lambda = 0 \,, \quad \gamma = -1) \,, \tag{2.34}$$

$$\tau_{\mathrm{dis}} \propto E^{-1/2} \qquad (\lambda = 0 \,, \quad \gamma = 0) \,, \tag{2.35}$$

$$\tau_{\mathrm{ion}} \propto E^{3/2} \qquad (\lambda = 2 \,, \quad \gamma = 0) \,, \tag{2.36}$$

$$\tau_{\text{el-el}} \propto T^{-2} \qquad (\lambda = 1/2 \,, \quad \gamma = -2) \,. \tag{2.37}$$

The temperature dependence of acoustic-phonon scattering arises from the increasing vibration amplitude of excited phonons with increasing temperature. In contrast, both alloy-disorder and ionized-impurity scattering, which describe the scattering on local structures, exhibit no temperature dependence in the scattering time. Instead, the additional energy dependence of τ_{ion} accounts for the smaller scattering cross section as the velocity of the incident charge carrier increases. For electron-electron interaction, the density of states is approximated as constant in the vicinity of the Fermi energy, removing any energy dependence. Instead of the DOS representing the scattering phase space, the temperature interval $-k_{\mathrm{B}}T$ to $k_{\mathrm{B}}T$ around the Fermi energy is proportional to the number of states from and into which both electrons can scatter, resulting in a T^2 dependence of the scattering probability τ^{-1}.

---

[1] Note that $\widetilde{\tau}$ does not have the unit of time but can rather be treated as a pre-factor. This fact is represented by the tilde.

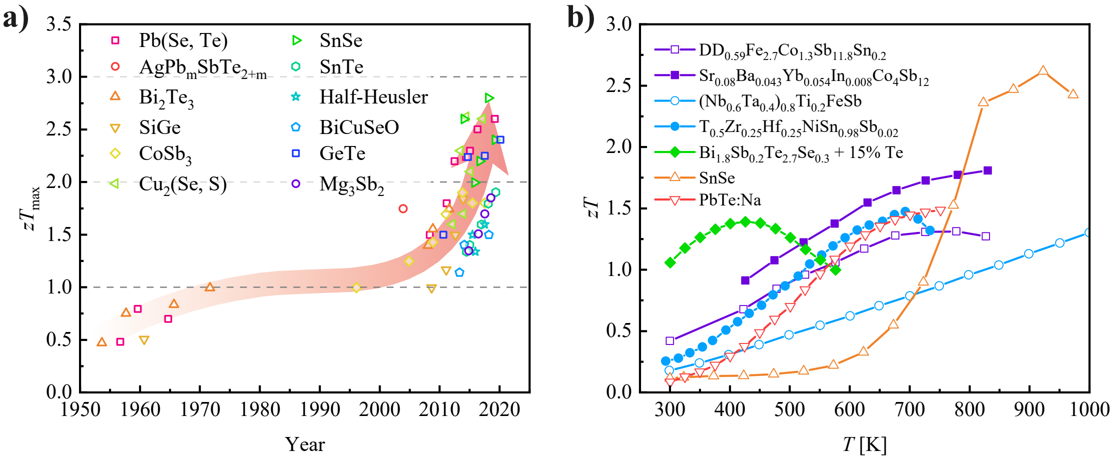

Figure 2.3: a) Maximum figure of merit zT_{max} achieved for different materials over the years (data taken from Ref. [60]). b) Temperature-dependent zT for different materials. Open symbols represent p-type materials, where closed symbols depict n-type materials. The values were taken from Ref. [34, 35, 61–65].

2.2 State-of-the-art thermoelectric materials

Since the discovery of the Seebeck effect by Thomas Johann Seebeck over 200 years ago [24], many different materials were investigated and tested with respect to their thermoelectric performance. Ultimately, semiconductors emerged as the class of materials with superior properties, thanks to special features in their band structure [25–29]. Nonetheless, also insulating materials and even metals with decent properties have been identified [30–33].

Today, a vast number of different types of materials with notable thermoelectric properties are known. These include skutterudites [34–37] , chalcogenides [38–40] , clathrates [41–44], half-Heusler [45–48] , full-Heusler [49–51], Si-Ge [52–56] and organic thermoelectrics [57–59], among others. Each material type has its strength and weaknesses, performing optimally within specific temperature ranges. Figure 2.3 illustrates the evolution of thermoelectric research over the years, along with the temperature dependence of some of the best-performing materials. In the last two decades, the discovery of several new materials has led to substantial progress in this field.

In the following sections, three representative classes of materials - Si$-$Ge, Bi$_2$Te$_3$ and Fe$_2$VAl - will be discussed.

2.2.1 Si-Ge

Si-Ge alloys are today mostly known for their application in space missions such as in the Soviet Union's BUK or NASA's SNAP power systems [66]. The origin of Si-Ge lies in the remarkable properties of silicon, the second most abundant element in earth's crust [67].

Si not only exhibits excellent thermoelectric properties in terms of the Seebeck coefficient and power factor [68], but it also shows great mechanical and chemical stability, is non-toxic and highly compatible with industrial processes [54].

However, the thermal conductivity of pure Si showcases extreme values, reaching $140\,\mathrm{Wm^{-1}K^{-1}}$ at 300 K and $30\,\mathrm{Wm^{-1}K^{-1}}$ at 1000 K [69]. This results in very low values of zT. To address this problem, partial substitution with isovalent germanium significantly diminishes the thermal conductivity, allowing for substantial enhancement of the thermoelectric properties.

Silicon and germanium form a complete solid solution, $\mathrm{Si}_{1-x}\mathrm{Ge}_x$, where x can range from 0 to 1 [54]. Consequently, similar to both elements, Si–Ge crystallizes into the diamond-like space group $Fd3m$ (no. 227), comprising two interpenetrating face-centered cubic (fcc) sublattices. The lattice parameter typically follows the linear dependence of Vegard's law with minor variations [70]. A visual representation of the crystal structure is illustrated in Figure 2.4a. Given the fact that the elements are perfectly miscible, Si–Ge is a typical disordered material. In Figure 2.4b, the band gap E_g is depicted as a function of the Ge fraction x [71]. Below $x \approx 0.85$, the behavior of the band gap is influenced by the shift of the Δ pocket, while above this value, the L pocket determines the band gap. Moreover, around $x \approx 0.3$, the pockets overlap, forming a highly degenerate conduction band. SiGe can further be synthesized in a hexagonal structure, relocating the L point back to the Γ point [54]. Although this doesn't alter the indirect band gap of Si, it transforms the band gap of Ge into a direct one with a magnitude close to 0.3 eV [72].

The band convergence of Si and Ge increases the degeneracy, significantly impacting the thermoelectric performance, especially the Seebeck coefficient (refer to chapter 3 for details). Conversely, nanostructuring can substantially lower thermal conductivity [73]. Figure 2.5 shows the thermoelectric power factor and zT value of nanostructured Si [74] alongside p-type $\mathrm{Si}_{0.8}\mathrm{Ge}_{0.2}\mathrm{B}_5$ [52] and n-type $\mathrm{Si}_{0.8}\mathrm{Ge}_{0.2}\mathrm{P}_5$

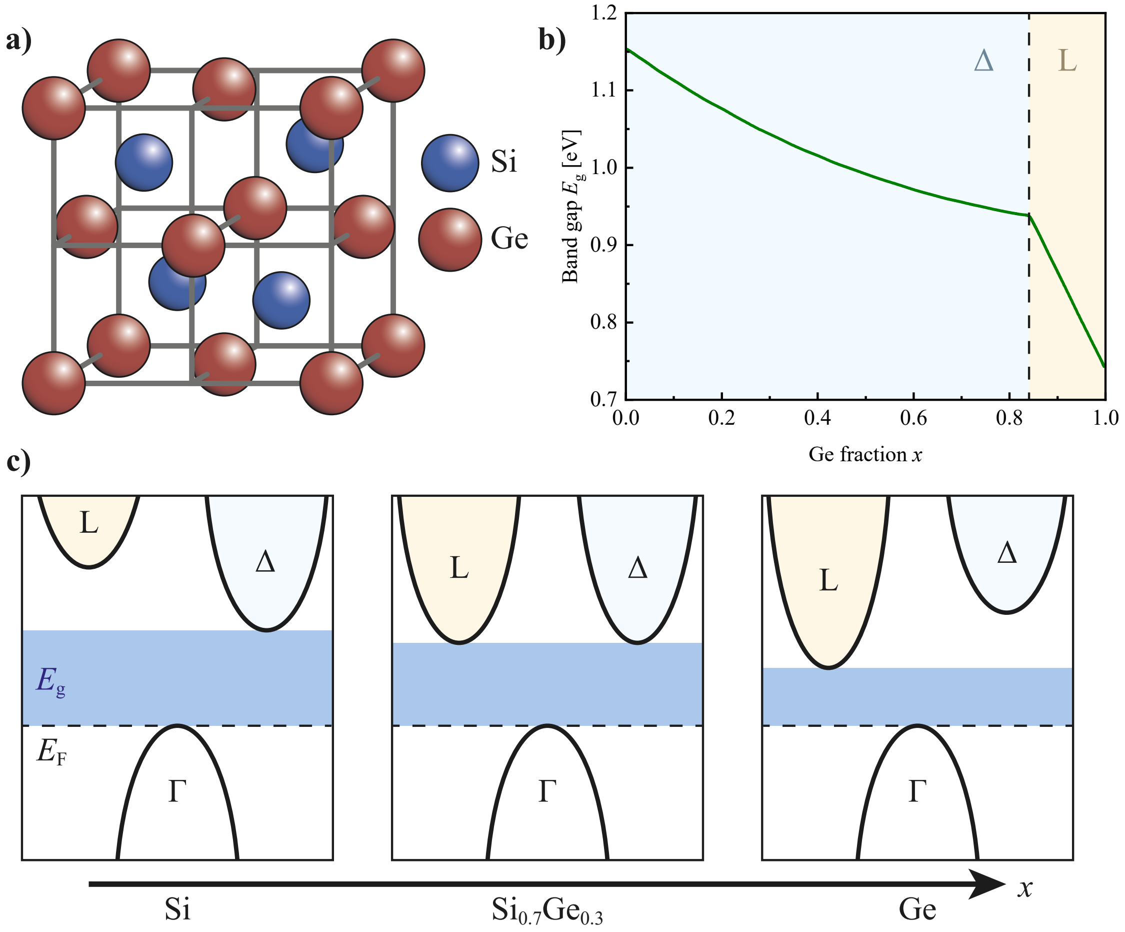

Figure 2.4: a) Visualization of the diamond-like $Fd3m$ crystal structure (no. 227) of Si–Ge, composed of two interpenetrating fcc sublattices. For better clarity, the Si atoms are depicted on the (1/4, 1/4, 1/4) site, although the disordered arrangement of Si and Ge allows for any distributions. b) Band gap E_g of $\mathrm{Si}_{1-x}\mathrm{Ge}_x$ as a function of the Ge amount x [71]. The blue shaded area represents the region where the band gap is dominated by the shift of the conduction band Δ pocket, whereas the yellow area marks the influence region of the L pocket. c) Sketch of the band structure in the vicinity of the Fermi energy E_F for Si, $\mathrm{Si}_{0.7}\mathrm{Ge}_{0.3}$ and Ge. The blue shaded area shows the band gap. For $x = 0.3$, the conduction bands overlap.

[53]. Despite pure silicon exhibiting a larger power factor than Si–Ge, its significantly higher thermal conductivity diminishes the overall performance. With the introduction of disorder scattering through Ge substitution, the thermal con-

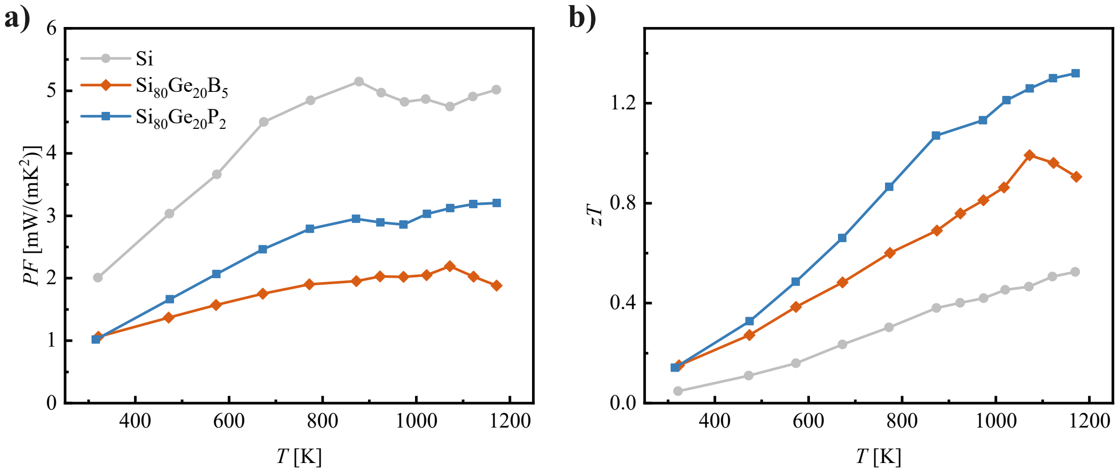

Figure 2.5: Temperature-dependent a) thermoelectric power factor PF and b) figure of merit zT of nanostructured Si as well as p- and n-type nanostructured $Si_{0.8}Ge_{0.2}$. The data were taken from Ref. [52, 53, 74].

ductivity drops from $\approx 10\,\mathrm{Wm^{-1}K^{-1}}$ in nanostructured Si to $\approx 2.5\,\mathrm{Wm^{-1}K^{-1}}$ in nanostructured p- and n-type $Si_{0.8}Ge_{0.2}$. The resulting larger zT value above 1000 K makes Si−Ge a great candidate for high-temperature applications. It should, however, be noted that Ge is a rather expensive element.

2.2.2 Bi_2Te_3

Bismuth telluride stands out as one of the most promising thermoelectric materials, particularly near room temperature [75]. Despite being discovered nearly 70 years ago [26], the majority of commercially available thermoelectric modules still consist of Bi_2Te_3-based alloys [76].

Bi_2Te_3 crystallizes into a rhombohedral tetradymite-type structure with a space group $R\bar{3}m$ (no. 166), which can be described as a hexagonal unit cell [75, 77]. The unit cell comprises five covalently bonded monoatomic sheets along the c axis in the order -Te_1-Bi-Te_2-Bi-Te_1-Te_1-Bi-Te_2-Bi-Te_1-, where Te_1 and Te_2 denote different chemical states of the anions [77]. A visualization of the crystal structure is shown in Figure 2.6a. The two consecutive Te_1 layers are bonded via a weak van der Waals attraction, while a predominant covalent bonding exists between Bi and Te. The anisotropy in the crystal structure of Bi_2Te_3 is reflected in the anisotropy of its

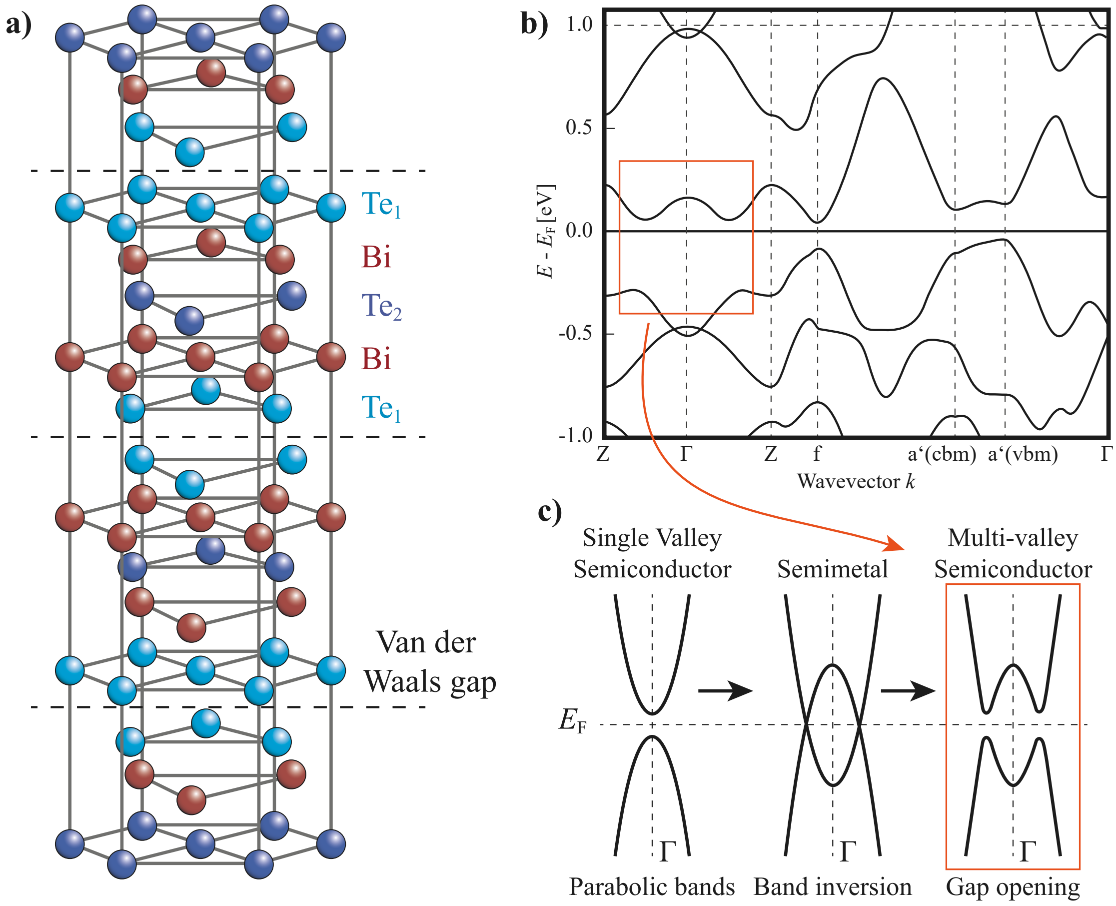

Figure 2.6: a) Crystal structure of Bi_2Te_3, showing the monoatomic layers perpendicular to the c axis. The position of the weak van der Waals coupling is highlighted as dashed line. b) Band structure of Bi_2Te_3. c) Origin of the band gap in the vicinity of the Γ point, leading to two band maxima and minima of the valence and conduction band, respectively. The data of b) and c) were taken from Ref. [75].

thermoelectric properties. While the Seebeck coefficient is isotropic, the electrical and thermal conductivities perpendicular and parallel to the c axis exhibit different values, following the ratios $\sigma_\perp = 3\sigma_\parallel$ and $\lambda_\perp = 3\lambda_\parallel$ [78]. The large size of the atoms, together with relatively weak interatomic coupling, results in an inherently low thermal conductivity in this material [79, 80]. Furthermore, Bi_2Te_3 displays different mechanical properties at different crystallographic directions [81].

Bismuth telluride features a narrow indirect band gap of 0.14 eV [82] (see Fig-

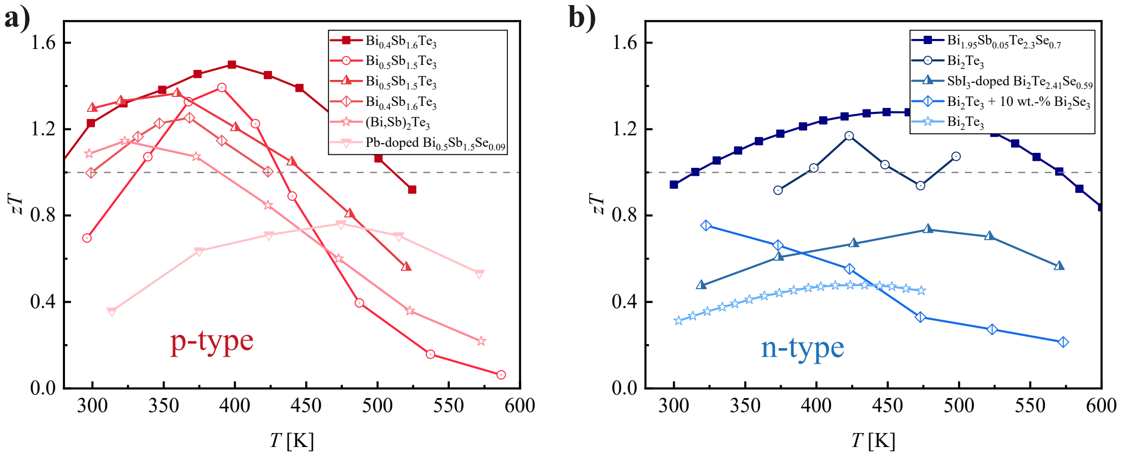

Figure 2.7: Temperature-dependent figure of merit zT for a) p-type and b) n-type Bi_2Te_3-based materials. The dashed lines labels $zT = 1$. The values were taken from Ref. [86–95].

ure 2.6b). Spin-orbit coupling (SOC) plays a pivotal role in shaping the band structure near the Fermi energy[75]. As illustrated in Figure 2.6c, in the absence of SOC, the structure consists of two parabolic bands centered at the Γ point with a small positive gap. SOC lowers the Bi p states, causing a crossing of the bands and a subsequent band inversion. The strong interaction results in an avoided crossing, opening the band gap and creating degenerate valleys with a small distance to the Γ point. Additionally, Bi_2Te_3, along with related materials such as Sb_2Te_3 and Bi_2Se_3, has been identified as a topological insulator with a single Dirac cone at the Γ point [83, 84].

Enhancing the thermoelectric performance of bismuth telluride involves nanostructuring, texture alignment and band gap enlargement [85]. Commonly employed synthesis approaches include ball milling and melt spinning. Figure 2.7 presents the temperature-dependent zT value of selected of p- and n-type materials. As can be observed, p-type materials generally exhibit higher zT values, while n-type materials reach maximum zT at higher temperatures. The superior performance of p-type Bi_2Te_3 is attributed to higher band convergence and a smaller effective band mass in the valence band [96].

2.2.3 Full-Heusler Fe_2VAl

An interesting class of material with significant potential, although not yet surpassing the current top-performing materials, is that of full-Heusler compounds, named after their discoverer Friedrich Heusler [97]. Heusler observed that the intermetallic compound Cu_2MnAl exhibits ferromagnetic properties despite each constituent being para- or diamagnetic. To date, the Heusler family comprises over 1000 members, including half-Heusler and quaternary Heusler materials [98–102].

Full-Heusler compounds crystallize in the cubic space group $Fm\bar{3}m$ (no. 225), composed of four interpenetrating fcc sublattices. These materials exhibit a X_2YZ stoichiometry, with the X atom located at the Wyckoff position 8c (1/4, 1/4, 1/4), while the Y and Z atoms occupy the 4a (0, 0, 0) and 4b (1/2, 1/2, 1/2) position, respectively [99]. The crystal structure is depicted in Figure 2.8a. Typically, X and Y are transition metals, while Z is a main-group element [103].

Full-Heusler materials have recently garnered significant interest in both bulk and film form for thermoelectric applications [49, 104–107]. This is due to their composition of abundant and low-cost elements, coupled with their chemical and mechanical long-term stability [99, 108].

Fe_2VAl is among the most studied full-Heusler materials. Despite Fe accounting for half of the atoms, the compound does not exhibit long-range magnetic order in the absence of disorder [109]. This absence of magnetism follows the Slater-Pauling rule, stating that the magnetic moment per unit cell M_t depends on the deviation of the number of valence electrons Z_t from 24 [110]:

$$M_t = Z_t - 24\ . \tag{2.38}$$

However, there are cases where Fe_2VAl-based materials deviate from this rule [51].

Materials based on Fe_2VAl inherently possess a substantial power factor due to their peculiar DOS (see Figure 2.8b) [111–116]. However, the highly symmetrical crystal structure allows for easy phonon propagation, resulting in a remarkably high thermal conductivity of approximately $\approx 25\,\mathrm{Wm^{-1}K^{-1}}$ at 300 K [117]. Nevertheless, substantial progress has been made in mitigating the phonon contribution through heavy-element substitution [103, 114, 118, 119], thin-film deposition [49, 120–122] or microstructural tailoring [107]. The power factor PF and room

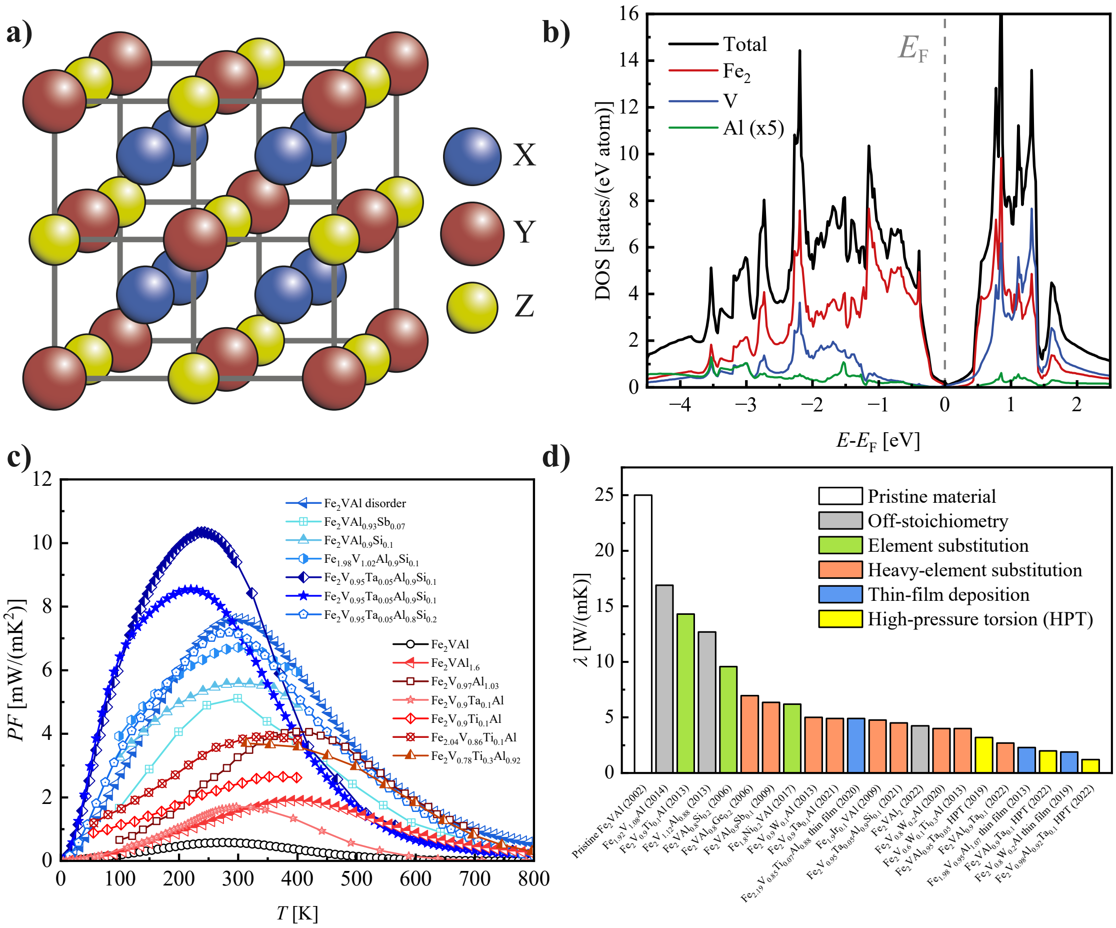

Figure 2.8: a) Visualization of the $Fm\bar{3}m$ crystal structure (no. 225), composed of four interpenetrating fcc sublattices. b) Partial (red, blue and green lines) and total (black line) density of states (DOS) of Fe_2VAl with respect to the Fermi energy E_F, taken from Ref [50]. c) Temperature-dependent power factor PF of a selection of Fe_2VAl-based compounds, divided into p-type (red symbols) and n-type (blue symbols) materials. d) Room-temperature thermal conductivity λ for different Fe_2VAl-based materials, arranged in descending order. The color indicates the origin of the reduction of thermal conductivity. The year of the published results is shown in the brackets. The data of c) and d) were taken from Ref. [73].

temperature thermal conductivity λ of a selection of the most promising p- and n-type materials are presented in Figure 2.8c and Figure 2.8d, respectively.

In 2019, a substantial enhancement in the performance of $Fe_2V_{0.8}W_{0.2}Al$ films

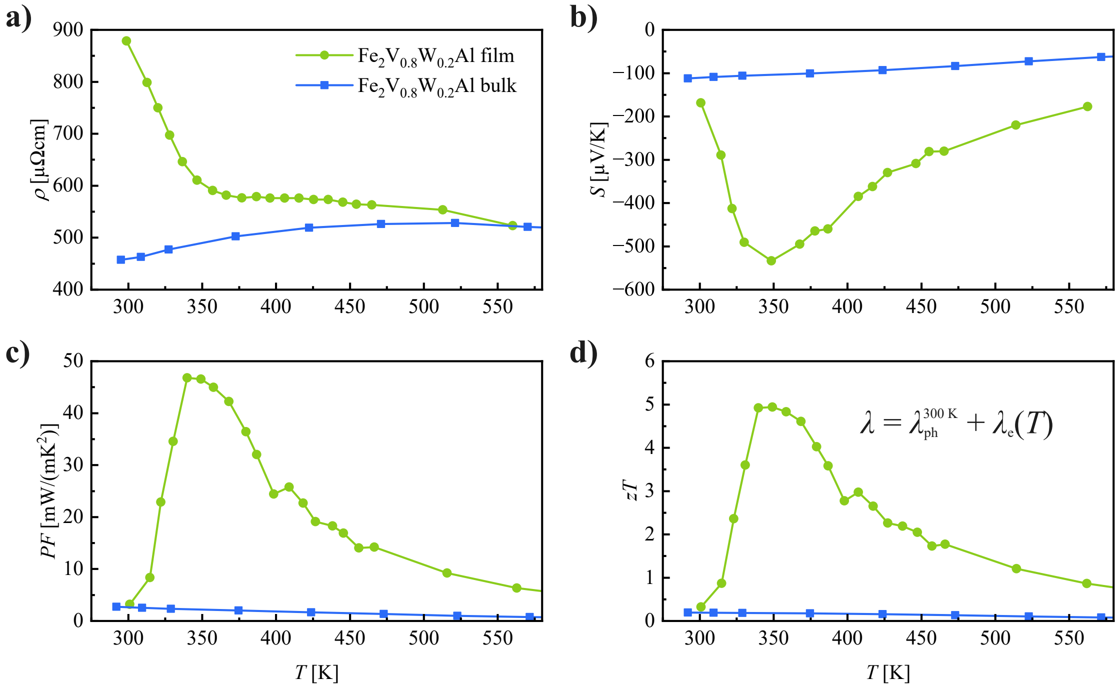

Figure 2.9: a) Electrical resistivity ρ, b) Seebeck coefficient S, c) power factor PF and d) figure of merit zT of bulk (blue line) and thin film (green line) $Fe_2V_{0.8}W_{0.2}Al$. zT was estimated by approximating the thermal conductivity from the value measured at room temperature and the temperature dependence of the electrical resistivity. The values of the bulk and the film sample were taken from Ref. [103] and [49], respectively.

on Si was achieved [49]. These films exhibited an exceptionally large power factor of approximately 48 $\mathrm{mWm^{-1}K^{-2}}$ and zT value of around 5 at 350 K. The thermoelectric properties are illustrated in Figure 2.9, along with the respective bulk properties [103]. In both systems, zT is estimated based on the measured thermal conductivity at room temperature and the temperature-dependent electrical resistivity, using the Wiedemann-Franz law.

The atypical behavior of all quantities of the film sample was attributed to the distinctive crystal structure. X-ray diffraction measurements revealed a low degree of order within the crystal, transitioning the crystal structure from the fully ordered $L2_1$ phase into the completely disordered A_2 structure [49]. Although the A_2 structure is known to yield metallic behavior and consequently a low Seebeck coefficient [123], the finite dimensionality in film systems might alter the density of states in a favorable manner, as indicated by theoretical calculations [49]. Subsequently, an additional explanation for the extraordinary Seebeck coefficient was proposed, considering a potential magnon drag within the material [124].

2.3 Current and potential applications

Thermoelectric materials serve two different functions: they can be employed for power generation as a thermoelectric generator (TEG) or utilized for cooling purposes through the Peltier effect, commonly known as a thermoelectric cooling system (TEC) or Peltier module. Both applications share a similar configuration of the thermoelectrics, as illustrated in Figure 2.10. I a TEG, the arrangement consists of a p-type and a n-type material, electrically connected on one side and insulated on the other, while thermally, they are connected in parallel. To enhance the generated voltage or the cooling power, additional alternating p- and n-type materials can be serially incorporated. Each leg generates voltage proportional to its Seebeck coefficient, independent of dimensions, while the resistance depends on the material size. Tuning the overall power output or cooling power of a TEG or TEC can be achieved by optimizing the size and shape of the materials [125].

Thermoelectric generators can be utilized in two main areas: i) waste-heat recovery by connecting a TEG to a heat source and ii) for power generation, particularly in challenging or remote locations. Figure 2.11 provides a graphical visualization of current and potential implementations of thermoelectric modules.

Despite the advancements in thermoelectric materials, their low efficiency, as evident from the zT values in the previous section, has limited their commercial applications [126]. Practical power generation is viable in areas that necessitate enduring and low-maintenance solutions, such as space missions, off-shore constructions or hazardous environments. Additionally, thermoelectric generators are valuable where a heat source is already present and a modest power output is sufficient, such as in monitoring, IoT devices or skin-based applications [127–129]. In the context of waste-heat recovery, thermoelectric modules prove beneficial in various fields, including transportation, where engines produce significant unwanted heat, and in heat-producing industrial facilities, where a considerable amount of energy is lost e.g. in high-temperature furnaces, power plants or waste incinerators

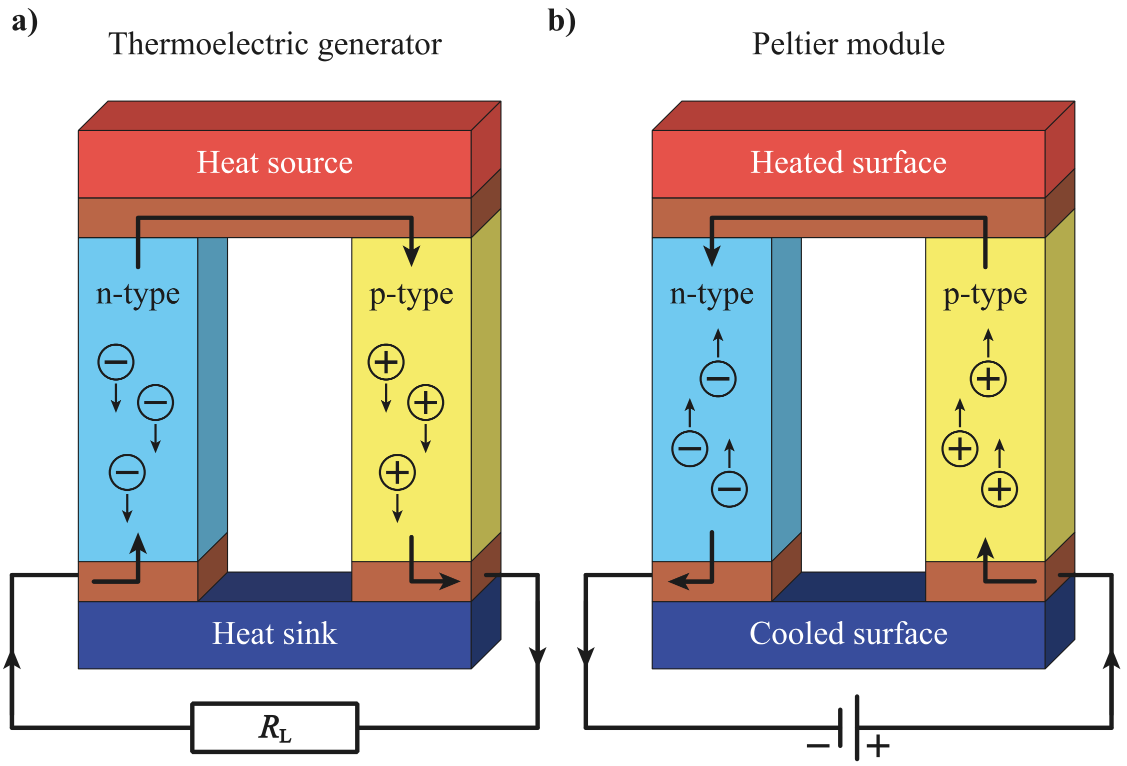

Figure 2.10: Setup of a thermoelectric module composed of a n-type (blue) and a p-type (yellow) material in two different configurations. a) Thermoelectric generator, utilizing the temperature difference due to a heat source and heat sink to generate a circular current when a load resistance R_L is connected to the end of both legs. b) Peltier module, heating one and cooling the opposing surface after a voltage is applied to the end of the legs.

[130–132].

2.3.1 Power generation

One of the earliest applications of thermoelectric materials was in interstellar missions, where a radioactive material serves as heat source for the TEG during decay, enabling enabling electricity generation in outer space. Devices designed for this purpose, consisting mainly of a radioactive material and a thermoelectric module, are known as radioisotope thermoelectric generators (RTGs). The choice of the radioisotope involves meeting specific criteria, such as the ability to generate suffi-

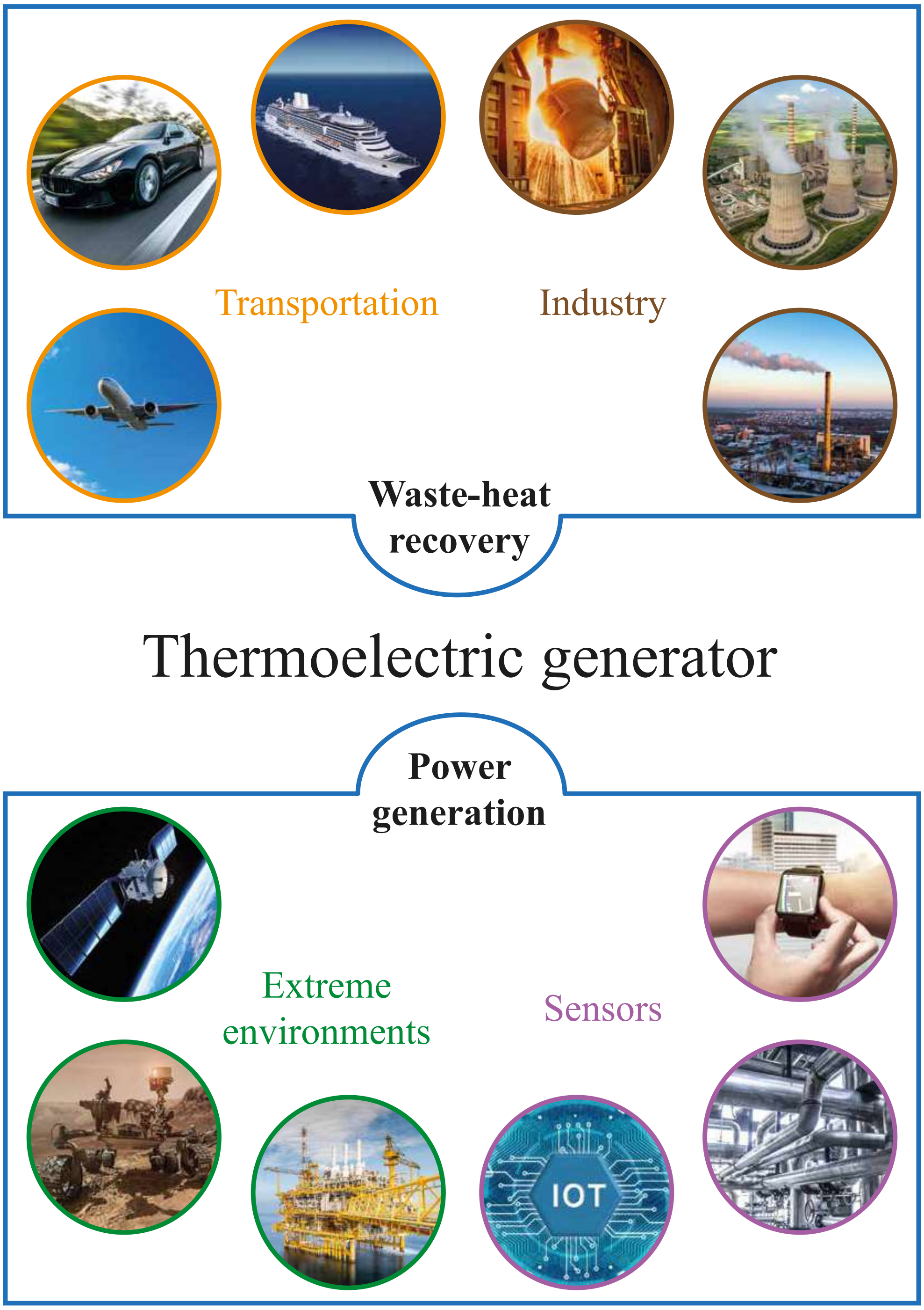

Figure 2.11: Overview of a selection of current and potential applications of a thermoelectric generator, divided into power-generating and waste-heat harvesting purposes.

cient energy through radioactive decay, possessing a long decay time having a high energy density [133].

While the first criterion is relatively straightforward, elements emitting gamma rays are impractical due to the large absorption length of gamma waves, making an efficient absorption within the surrounding container impossible. In contrast, alpha emitters have proven well-suited to overcome this issue. The second criterion emphasizes the need for a long-lasting energy source, though a long decay time reduces the emitted power, requiring a balance. Finally, a large energy density minimizes the weight of the RTG, a crucial parameter for interstellar missions. In a study by Blanke *et al.* , around 1300 different radioactive isotopes were investigated, with only 47 exhibiting promising properties for RTG applications [134]. Initially, cerium-144 was considered as the most promising energy source and employed in the SNAP nanosatellite [135]. However, plutonium-238 is now commonly used in state-of-the-art multi-mission RTGs (MMRTGs) [135, 136]. MMRTGs utilize $(GeTe)_{85}(AgSbTe_2)_{15}$ (TAGS) and PbTe as p-type and n-type thermoelectric materials [137]. Future NASA missions will, however, use RTGs based on more efficient skutterudites [138, 139].

The power generated by a typical module is sufficient to supply energy to small sensors. Modern sensors only require few hundred microwatts or few milliwatts to operate [140]. This sensors can transmit data from challenging-to-access locations, such as deep-sea pipes, or from areas where avoiding unnecessary wiring is beneficial, like a car engine. Several companies nowadays produce and sell small-scale thermoelectric modules designed to power such sensors. In recent years, there has been increased interest in wearable thermoelectrics, which utilize the body's heat to generate power [129, 141]. These applications include pressure sensors, electrocardiographic sensors, temperature sensors and motion sensors [142]. Typically, the materials are composed of a flexible substrate to match the skin's shape [143–146].

2.3.2 Waste-heat recovery

The automotive industry represents one of the most-studied fields for waste-heat-recovery applications. Only 25 % of the chemical energy consumed by a typical gasoline combustion engine is converted into mechanical energy [140]. Conversely, a substantial 40 % is lost through exhaust gases, which reach temperatures in the range of several hundred degrees. This significant amount of wasted energy has inspired extensive research by automotive manufacturers. The incorporation of a TEG into a vehicle necessitates meeting three key requirements: i) it must not alter the engine's operating point, ii) the TEG must withstand the present temperature difference and iii) the temperature difference across the module should be maximized for optimal performance [140]. Numerous countries, including the United States, Japan, China, Germany and Austria, have engaged in in research on recovering energy from exhaust gases, achieving notable success, such as a power output exceeding 1 kW from a thermoelectric module composed of half-Heusler materials [147]. Despite these achievements, no commercially produced car currently integrates a TEG, primarily due to the high production costs of over 8€/W [148]. For feasibility, costs must be reduced to around 1€/W. Additionally, with the rapid increase in produced electric cars [149], the need for thermoelectric modules in cars is diminishing.

A significant amount of heat is also produced in airplane and helicopter engines [140]. Nevertheless, a numerical study investigating the power generated by a TEG mounted on the nozzle of a helicopter indicated that while the produced power is substantial, the weight-to-power ratio is currently too low for feasibility [150].

High-temperature industrial factories, such as steel-making or cement production, provide another opportunity for harvesting substantial waste heat. In an experimental study, a TEG mounted on a combustion chamber yielded 21 W with a power density of approximately $100\,\mathrm{W/m^2}$ [151]. Another investigation focused on the potential of recovering heat from the steel-making process using 16 Bi-Te modules, ultimately generating 250 W at a temperature difference of 300 K [152].

3 Thermoelectric properties within the parabolic-band model

This section discusses the transport properties within the approximation of parabolic bands. Simple and convenient formulas will be obtained that will serve as the groundwork for the fitting algorithm presented in chapter 4.

The temperature-dependent Seebeck coefficient reflects important features of the band structure, such as the size of the band gap E_{g} and position of the Fermi energy E_{F}. Although the shape of the band structure can exhibit a complex behavior, bands can often be effectively approximated as parabolas near their upper and lower edges [50, 117, 153–157]. This approximation is particularly reasonable in the context of both the nearly free electrons (NFE) model and the tight-binding (TB) model.

In the NFE model, electrons are treated as freely moving particles and described by a parabolic dispersion relation near the center of the Brillouin zone, $\vec{k} = 0$, also referred to as the Γ point:

$$E(\vec{k}) = E(\vec{k} + \vec{G}) = \frac{\hbar^2}{2m_{\mathrm{e}}} \left| \vec{k} + \vec{G} \right|^2 \ . \tag{3.1}$$

Here, $\vec{G}$ is the reciprocal lattice vector and m_{e} the electron mass. At the edge of the Brillouin zone, the group velocity becomes zero ($\partial E / \partial \vec{k} = 0$) due to the emergence of standing waves. This again allows for a quadratic description of the dispersion relation similar to Equation 3.1.

Within the TB regime, the dispersion relation of electrons in a spherically symmetric potential is expressed as follows:

$$E(\vec{k}) = E_0 - A - T \sum_{nn} e^{i\vec{k}\vec{R}} \ . \tag{3.2}$$

here, E_0 represents an energy level of the unperturbed atomic potential, $\vec{R}$ is the lattice vector and A and T denote contributions from crystal field effects and hopping, respectively. The sum extends over all next neighbors nn. In many cases, the exponential function can be rewritten in terms of cosine functions. For example, in a cubic lattice with lattice parameter a, the dispersion relation becomes

$$E(\vec{k}) = E_0 - A - 2T\left[\cos\left(ak_x\right) + \cos\left(ak_y\right) + \cos\left(ak_z\right)\right] \ . \tag{3.3}$$

Furthermore, the cosine function can be approximated with a polynomial of second order in the vicinity of $k_i = 0$ and $k_i = \pi/a$, further justifying the parabolic-band model.

While the parabolic description may not accurately capture entire bands - for example, the parabola is infinitely extended in one direction - it remains valid up to several hundreds or thousands of Kelvin if E_F is situated in the vicinity of the band edge. Therefore, employing a parabolic-band model enables the description of electronic behavior from temperature-dependent measurement data of the electrical resistivity, Seebeck coefficient and Hall coefficient.

For improved readability and simplicity, the vector notation is omitted in the remaining chapter. Consequently, the description of the parabolic bands below is only valid in one reciprocal direction. To describe the full crystal, multiple bands or a degeneracy of the band might be necessary.

3.1 Electrical conductivity of parabolic bands

The dispersion relation of a parabolic band is described by the equation

$$E\left(k\right) = \frac{\hbar^2 k^2}{2m^\star} \ , \tag{3.4}$$

with E and k representing the energy and wavevector of the electron's state, respectively, and $m^\star$ being the effective mass of the band. In the context of quasi-free electrons, $m^\star$ equals the electron mass m_e. However, in real materials, $m^\star$ can significantly deviate from m_e due to various electromagnetic interactions. Notably, within a parabolic band, the effective mass remains constant.

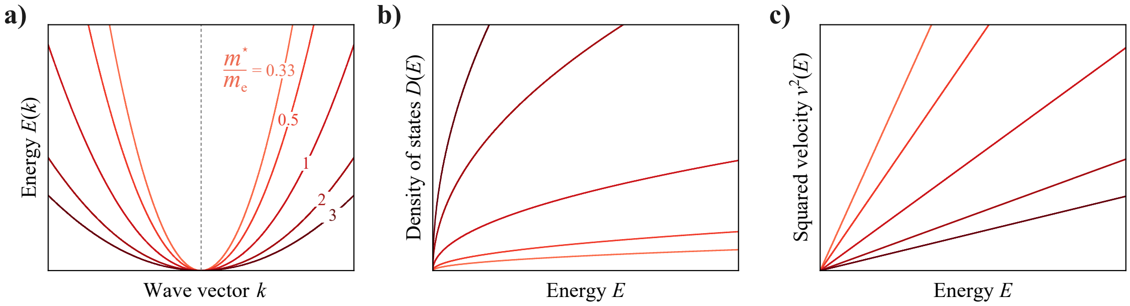

Figure 3.1: a) k-dependent band energy and energy-dependent b) density of states and c) squared velocity for a parabolic conduction band for different effective band masses $m^\star$.

The density of sates (DOS) of a parabolic band is expressed as

$$D\left(E\right) = \frac{\left(2m^\star\right)^{3/2}}{2\pi^2\hbar^3}\sqrt{E}\ . \tag{3.5}$$

Accordingly, the velocity within the band can be written as

$$v\left(E\right) = \frac{1}{\hbar}\frac{\partial E(k)}{\partial k} = \sqrt{\frac{2}{m^\star}}\sqrt{E}\ . \tag{3.6}$$

As previously mentioned in chapter 2, the transport function G of parabolic band can be expressed as

$$G(E) = D(E)v^2(E)\tau(E)\ . \tag{3.7}$$

Consequently, the scattering time τ is the only parameter that can not be obtained solely from the shape of the band structure. Figure 3.1 presents a visualization of the dispersion relation as well as $D(E)$ and $v^2(E)$ for a parabolic conduction band. The band becomes less dispersive as the effective band mass increases. Consequently, the density of states is higher and compressed, while the band velocity is reduced.

By inserting the transport function of parabolic bands, as given by Equation 3.7, into the electrical conductivity expression in Equation 2.6, the electrical conductivity is obtained as follows:

$$\begin{aligned}\sigma &= e^2\int_0^\infty D(E)v^2(E)\tau(E)\left(-\frac{\mathrm{d}f}{\mathrm{d}E}\right)\,\mathrm{d}E\\ &= \frac{\left(8m^\star\right)^{1/2}e^2}{\pi^2\hbar^3}\int_0^\infty E^{3/2}\tau(E)\left(-\frac{\mathrm{d}f}{\mathrm{d}E}\right)\,\mathrm{d}E\ .\end{aligned} \tag{3.8}$$

Note that this expression specifically describes conduction bands, as the DOS is defined as

$$D(E) \propto \begin{cases} 0 & E < 0 \\ \sqrt{E} & E \geqslant 0 \end{cases} \tag{3.9}$$

However, considering the positive definiteness of both the transport and the selection function yields the same result for valence bands if the position of the chemical potential with respect to the band edge is treated accordingly. From the general dependencies of the scattering time, as outlined in Equation 2.33, it follows that

$$\sigma = \frac{2\sqrt{2}e^2}{\pi^2\hbar^3 m^\star}\widetilde{\tau}T^\gamma \int_0^\infty E^{\lambda+1}\left(-\frac{\mathrm{d}f}{\mathrm{d}E}\right)\mathrm{d}E\ . \tag{3.10}$$

Following partial integration and the substitutions $\xi = E/k_\mathrm{B}T$ and $\eta = \mu/k_\mathrm{B}T$, denoting the reduced energy and chemical potential, respectively, the expression can be written as

$$\sigma = \frac{2\sqrt{2}e^2}{\pi^2\hbar^3 m^\star}\widetilde{\tau}(\lambda+1)(k_\mathrm{B}T)^{\lambda+1}T^\gamma F_\lambda\left(\eta(T)\right)\ , \tag{3.11}$$

with

$$F_j\left(\eta(T)\right) = \int_0^\infty \frac{\xi^j}{e^{\xi-\eta}+1}\mathrm{d}\xi \tag{3.12}$$

being the Fermi-Dirac integral of j^th order.

3.1.1 Acoustic-phonon scattering

In case of dominant acoustic-phonon scattering ($\lambda = 0$, $\gamma = -1$), the scattering time is defined as [18]:

$$\begin{aligned} \tau_\mathrm{ph}(E,T) &= \frac{\pi\hbar^4 v_\mathrm{s}^2\rho_\mathrm{m}}{\sqrt{2}\,\Xi_\mathrm{ph}^2\left(m^\star\right)^{3/2}k_\mathrm{B}T}E^{-1/2} \\ &= \widetilde{\tau}_\mathrm{ph}T^{-1}E^{-1/2}(m^\star)^{-3/2} \end{aligned}\ , \tag{3.13}$$

where v_s is the sound velocity, ρ_m is the density and Ξ_ph is the deformation potential of acoustic-phonon scattering.

Inserting $\widetilde{\tau}_{\mathrm{ph}}$ into Equation 3.11 results in the electrical conductivity of acoustic-phonon scattering:

$$\sigma_{\mathrm{ph}} = \frac{2e^2\hbar v_{\mathrm{s}}^2 \rho_{\mathrm{m}}}{\pi m^\star \Xi_{\mathrm{ph}}^2} F_0\left(\eta(T)\right) \ . \tag{3.14}$$

The Fermi-Dirac integral of 0^{th} order can be explicitly written and yields

$$\sigma_{\mathrm{ph}} = \frac{2e^2\hbar v_{\mathrm{s}}^2 \rho_{\mathrm{m}}}{\pi m^\star \Xi_{\mathrm{ph}}^2} \ln\left(1 + e^{\frac{\mu}{k_{\mathrm{B}}T}}\right) \ , \tag{3.15}$$

For $\mu \gg k_{\mathrm{B}}T$, i.e. when the chemical potential is deep inside the band, the equation simplifies to

$$\sigma_{\mathrm{ph}} \approx \frac{2e^2\hbar v_{\mathrm{s}}^2 \rho_{\mathrm{m}}}{\pi m^\star \Xi_{\mathrm{ph}}^2} \frac{\mu}{k_{\mathrm{B}}T} \ . \tag{3.16}$$

Consequently, the resistivity increases linearly with temperature. At lower temperatures below the Debye temperature, the resistivity adopts a non-linear T^5 behavior, which can not be obtained from a $1/T$ dependence of the scattering time. Instead, the increasing number of excited phonon modes needs to be considered.

A more general description of the temperature-dependent resistivity of metals is provided by the Bloch-Grüneisen law:

$$\rho_{\mathrm{ph}}(T) \propto \left(\frac{T}{\Theta_{\mathrm{D}}}\right)^5 \int_0^{\frac{\Theta_{\mathrm{D}}}{T}} \frac{4x^5}{\left(e^x - 1\right)\left(1 - e^{-x}\right)} \mathrm{d}x \ , \tag{3.17}$$

which yields a resistivity behavior given by

$$\rho_{\mathrm{ph}}(T) \propto \begin{cases} T^5 & \text{for} \quad T < \Theta_{\mathrm{D}} \\ T & \text{for} \quad T > \Theta_{\mathrm{D}} \end{cases} \ , \tag{3.18}$$

where Θ_{D} represents the Debye temperature of the material. Equation 3.17 is based on the Debye model, assuming a constant sound velocity v_{s} up to a specific frequency $\omega_{\mathrm{D}} = k_{\mathrm{B}}T/\hbar$. Given that acoustic modes usually exhibit a substantially larger group velocity than optical modes and are thus more relevant for transport, the model usually aligns very well with experimental values. However, optical phonons can be considered with a constant frequency ω_{E}, similar to the Einstein model.

Apart from the sound velocity, the Debye temperature is proportional to the particle density n of the material [158]:

$$\Theta_\mathrm{D} = \frac{\hbar v_\mathrm{s}}{k_\mathrm{B}} \sqrt[3]{6\pi^2 n} \,. \tag{3.19}$$

The sound velocity is obtained by averaging the group velocity of the two transversal (t) branches and the longitudinal (l) branch. In case of isotropy, it can be expressed as [159]

$$v_\mathrm{s} = \left[\frac{1}{3}\left(\frac{2}{v_\mathrm{t}^3} + \frac{1}{v_\mathrm{l}^3}\right)\right]^{-1/3} \,. \tag{3.20}$$

The values of v_t and v_l depend on the material's shear and bulk modulus, i.e. the stiffness of the material, as well as on the inverse density. For example, the low mass density of diamond ($3.5\,\mathrm{gcm^{-3}}$) combined with extreme hardness yields superior velocities of $v_\mathrm{l} \approx 18000\,\mathrm{ms^{-1}}$ and $v_\mathrm{t} \approx 12800\,\mathrm{ms^{-1}}$ [160]. In contrast, gold, with a high density ($19.3\,\mathrm{gcm^{-3}}$) and relatively soft characteristics, exhibits much lower group velocities of $v_\mathrm{l} \approx 3200\,\mathrm{ms^{-1}}$ and $v_\mathrm{t} \approx 1200\,\mathrm{ms^{-1}}$. This drastic difference in group velocities contributes to the distinct Debye temperatures of diamond ($\Theta_\mathrm{D} = 2240\,\mathrm{K}$) and gold ($\Theta_\mathrm{D} = 165\,\mathrm{K}$) [161].

3.1.2 Alloy-disorder scattering

Another important type of scattering involves temperature-independent defects and disorders, contributing to a non-zero resistivity at 0 K, as depicted below. For a binary alloy, the scattering time of alloy-disorder scattering can be written as [19]

$$\begin{aligned} \tau_\mathrm{dis} &= \frac{\mathcal{R}}{x(1-x)\Delta U^2 (m^\star)^{3/2}} E^{-1/2} \\ &= \widetilde{\tau}_\mathrm{dis} E^{-1/2} (m^\star)^{-3/2} \,, \end{aligned} \tag{3.21}$$

with x being the atomic fraction of one of the constituents, $\mathcal{R}$ being a pre-factor that depends on the material and ΔU representing the scattering potential. In contrast to the scattering time of acoustic-phonon scattering, the scattering time is temperature-independent, as the scattering centers do not exhibit the motion characteristics of phonons, which change with temperature.

The electrical conductivity in Equation 3.11 now becomes (with $\lambda = 0$ and $\gamma = 0$)

$$\begin{aligned}\sigma_{\mathrm{dis}} &= \frac{2\sqrt{2}e^2\mathcal{R}}{x(1-x)\pi^2\hbar^3 m^\star \Delta U^2} k_{\mathrm{B}} T F_0\left(\eta(T)\right) \\ &= \frac{2\sqrt{2}e^2\mathcal{R}}{x(1-x)\pi^2\hbar^3 m^\star \Delta U^2} k_{\mathrm{B}} T \ln\left(1 + e^{\frac{\mu}{k_{\mathrm{B}}T}}\right)\end{aligned} . \tag{3.22}$$

Similar to acoustic-phonon scattering, this simplifies for $\mu \gg k_{\mathrm{B}}T$ to

$$\sigma_{\mathrm{dis}} = \frac{2\sqrt{2}e^2\mathcal{R}}{x(1-x)\pi^2\hbar^3 m^\star \Delta U^2} \mu \, , \tag{3.23}$$

which is independent of the temperature.

In metals, where acoustic-phonon and alloy-disorder scattering are usually dominant, the total resistivity can be expressed as

$$\rho = \rho_{\mathrm{dis}} + \rho_{\mathrm{ph}}(T) \, . \tag{3.24}$$

In semimetals or semiconductors, the resistivity is further modified by the increase of charge carriers - holes or electrons - through excitations of electrons into the conduction band. This is accounted for within the Fermi integral in Equation 3.11 and can overshadow the metallic behavior in Equation 3.24.

The temperature dependence of acoustic-phonon and alloy-disorder scattering is depicted in Figure 3.2 for various Fermi energies. When neglecting the temperature dependence of the chemical potential ($\mu(T) = E_{\mathrm{F}}$), the electrical resistivity of acoustic-phonon scattering exhibits a linear increase at lower temperatures when the Fermi energy is located inside the band ($\mu > 0$). Above $3k_{\mathrm{B}}T \approx \mu$, the Fermi-Dirac distribution in Equation 3.11 softens to the extend that it reaches the edge of the band. Consequently, the integral increases, reducing the temperature dependence of the conductivity and resistivity. A similar behavior is observed for alloy-disorder scattering, where a deviation from the value at 0 K occurs at higher temperatures.

In this scenario, the chemical potential of a ideal metal with a constant DOS can be treated as infinite, as $E_{\mathrm{F}} \pm k_{\mathrm{B}}T$ never reaches the band's edge. Thus, in metals the resistivity shows a linear behavior for acoustic-phonon and a constant behavior for alloy-disorder scattering up to very high temperatures. On the other hand, this tendencies are overshadowed in semiconductors, where the charge carrier concentration significantly increases with temperature (see the gray lines in Figure 3.2, where $E_{\mathrm{F}} = -500\,\mathrm{K}$), resulting in a negative slop of the resistivity.

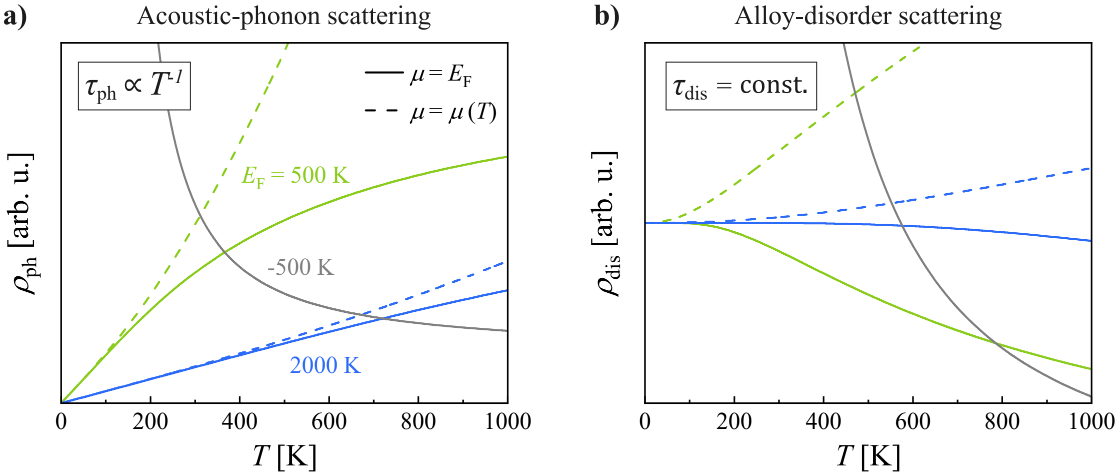

Figure 3.2: Electrical resistivity within the single-parabolic-band model, stemming from a) acoustic-phonon scattering (ρ_{ph}) and b) alloy-disorder scattering (ρ_{dis}), as a function of the temperature. The dashed and solid lines show the resistivity calculated with and without consideration of the temperature dependence of the chemical potential μ, respectively. The colors represent different positions of the Fermi energy E_F with respect to the zero of the band.

In reality, the temperature dependence of the chemical potential needs to be considered as well, ensuring a constant charge carrier concentration. This has a strong influence on the temperature dependence of the resistivity, especially when the Fermi energy is located in the vicinity of the band edge. Conversely, it has little effect in metals, where the chemical potential is approximately constant (see section 3.4 for details).

The temperature dependence of ρ_{dis}, illustrated in Figure 3.2, reveals a notable phenomenon. At very low temperatures, the resistivity demonstrates a non-linear increase, while at elevated temperatures, it exhibits a linear behavior. Typically, a linear rise in resistivity is attributed to acoustic-phonon scattering rather than alloy-disorder scattering. This unexpected trend, influenced by a shift of the chemical potential necessitates a reinterpretation of measured resistivity data, as shown in chapter 4.

3.1.3 Electrical conductivity of multiple bands

For a density of states comprising n bands with degeneracies N_i, i.e.

$$D(E) = \sum_{i=1}^{n} N_i D_i(E) \; , \tag{3.25}$$

the electrical conductivity is given by

$$\begin{aligned} \sigma &= e^2 \sum_{i=1}^{n} \int_{-\infty}^{\infty} G_i(E) \left(-\frac{\mathrm{d}f}{\mathrm{d}E}\right) \mathrm{d}E \\ &= \frac{2\sqrt{2}e^2}{\pi^2\hbar^3} T^\gamma \sum_{i=1}^{n} \frac{N_i}{m_i^\star} \widetilde{\tau}_i \int_{E_{0,i}}^{\infty} (E - E_{0,i})^{\lambda+1} \left(-\frac{\mathrm{d}f}{\mathrm{d}E}\right) \mathrm{d}E \; , \end{aligned} \tag{3.26}$$

where $E_{0,i}$ is the origin of the i^{th} parabola. The lower limit of integration can be shifted to zero if the integrands are shifted accordingly. This yields

$$\sigma = \frac{2\sqrt{2}e^2}{\pi^2\hbar^3} T^\gamma \sum_{i=1}^{n} \frac{N_i}{m_i^\star} \widetilde{\tau}_i \int_{0}^{\infty} E^{\lambda+1} \left(-\frac{\mathrm{d}f_i}{\mathrm{d}E}\right) \mathrm{d}E \; , \tag{3.27}$$

with

$$f_i(E, \mu, T) = \frac{1}{e^{\frac{E+E_{0,i}-\mu}{k_\mathrm{B}T}} + 1} \; . \tag{3.28}$$

Finally, in accordance with Equation 3.11, a general expression for the electrical resistivity of n bands with one dominant type of scattering is obtained:

$$\sigma = \frac{2\sqrt{2}e^2}{\pi^2\hbar^3} (\lambda+1)(k_\mathrm{B}T)^{\lambda+1} T^\gamma \sum_{i=1}^{n} \frac{N_i}{m_i^\star} \widetilde{\tau}_i F_\lambda\left(\eta_i(T)\right) \; . \tag{3.29}$$

Here, $\eta_i = (\mu - E_{0,i})/k_\mathrm{B}T$ is the reduced chemical potential with respect to the origin of the parabola.

3.2 Seebeck coefficient of parabolic bands

Similar to the derivation for electrical conductivity, the Seebeck coefficient for a parabolic band can be explicitly obtained. From Equation 2.14 follows for electrons $(q = -e)$

$$S\left(T\right) = -\frac{1}{eT} \frac{\int_{-\infty}^{\infty} D\left(E\right) \tau\left(E\right) v^2\left(E\right) \left(E-\mu\right) \left(-\frac{\partial f}{\partial E}\right) \mathrm{d}E}{\int_{-\infty}^{\infty} D\left(E\right) \tau\left(E\right) v^2\left(E\right) \left(-\frac{\partial f}{\partial E}\right) \mathrm{d}E} \; . \tag{3.30}$$

In contrast to the conductivity, any terms in the integral that are energy-independent, such as those related of the density of states ($D(E)$), velocity ($v(E)$) and scattering time ($\tau(E)$) can be factored out of the integral and ultimately cancel out as long as all scattering processes share the same energy dependency (e.g. acoustic-phonon and alloy-disorder scattering). This consideration extends to any temperature-dependent term as well.

By incorporating the energy dependencies (as defined in Equation 3.5, Equation 3.6 and Equation 2.33), the expression for the Seebeck coefficient (Equation 3.30) can be rewritten as[2]

$$S\left(T\right) = -\frac{1}{eT}\left(\frac{\int_0^\infty E^{\lambda+2}\left(-\frac{\partial f}{\partial E}\right)\mathrm{d}E}{\int_0^\infty E^{\lambda+1}\left(-\frac{\partial f}{\partial E}\right)\mathrm{d}E} - \mu\right) . \tag{3.31}$$

Substituting $\xi = E/k_\mathrm{B}T$ and $\eta = \mu/k_\mathrm{B}T$ leads to the final expression:

$$S\left(T\right) = \frac{k_\mathrm{B}}{e}\left[\eta - \frac{\lambda+2}{\lambda+1}\frac{F_{\lambda+1}\left(\eta(T)\right)}{F_\lambda\left(\eta(T)\right)}\right] . \tag{3.32}$$

As previously discussed, the value of λ depends on the predominant scattering mechanisms for electrons. Specifically, for acoustic-phonon and alloy-disorder scattering, $\lambda = 0$, whereas ionized-impurity and electron-electron scattering yield $\lambda = 2$ and $\lambda = 1/2$, respectively. Figure 3.3 illustrates the behavior of the Seebeck coefficient for $\lambda = 0$. Regardless of the position of the Fermi energy, the Seebeck coefficient converges at elevated temperatures (refer to Appendix A for details):

$$\lim_{T\to\infty} S(T) = -\frac{2k_\mathrm{B}}{e}\frac{\pi^2}{12\ln(2)} \approx -204.5\,\mathrm{\mu VK^{-1}} . \tag{3.33}$$

For a single parabolic band, the Seebeck coefficient can not surpass this limit when the temperature dependence of the chemical potential disregarded (see Figure 3.3a). As the temperature rises, the chemical potential shifts outside the band, diminishing bipolar conduction and amplifying the Seebeck coefficient. The temperature dependence of the chemical potential will be thoroughly discussed in section 3.4.

In Figure 3.3b, the low-temperature Seebeck coefficient is presented for various Fermi energies E_F. The slope of the linear increase is determined solely by the

---

[2] Similar to the electrical conductivity, the derivation assumes a conduction band with $D(E) = 0$ for $E < 0$. For valence bands, the asymmetric selection function yields opposite signs.

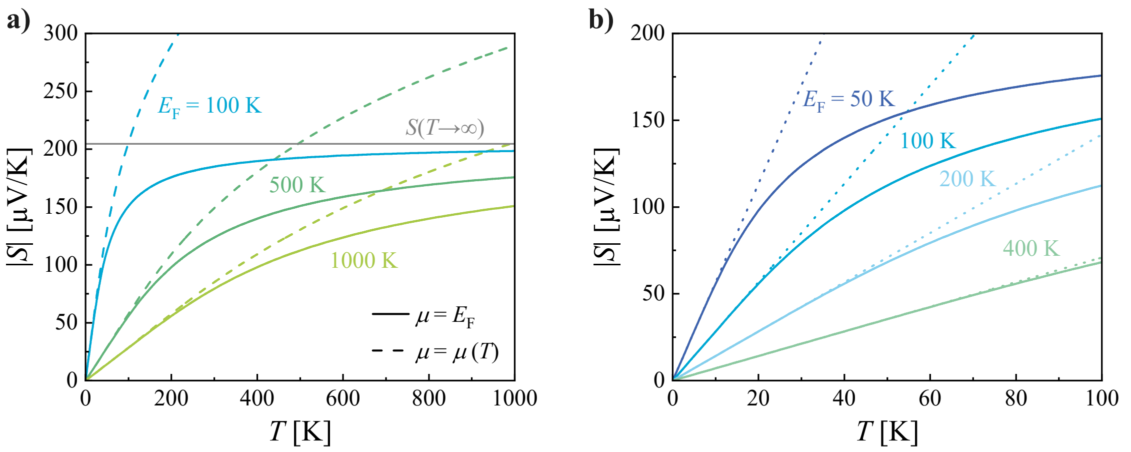

Figure 3.3: Seebeck coefficient within the single-parabolic-band model, calculated for $\lambda = 0$, as a function of the temperature. The dashed and solid lines show the Seebeck coefficient calculated with and without consideration of the temperature dependence of the chemical potential μ, respectively. Different colors indicate various positions of the Fermi energy E_F relative to the band edge. The gray line represents the threshold value for $T \to \infty$. Dotted lines illustrate the linear slope at low temperatures, as derived in the text.

Fermi energy (see Appendix A for details):

$$|S(T)| = \frac{\pi^2 k_\mathrm{B}}{3e} \frac{k_\mathrm{B} T}{E_\mathrm{F}} \,. \tag{3.34}$$

3.2.1 Seebeck coefficient of multiple bands

The overall Seebeck coefficient comprising contributions of n bands, depends on the individual Seebeck coefficients weighted with the respective conductivities [117]:

$$S\,(T) = \frac{\sum_{i=1}^{n} N_i \sigma_i(T) S_i(T)}{\sum_{i=1}^{n} N_i \sigma_i(T)} \tag{3.35}$$

$$= \frac{\sum_{i=1}^{n} \frac{N_i}{m_i^\star} \widetilde{\tau}_i F_\lambda\left(\eta_i(T)\right) S_i\left(T\right)}{\sum_{i=1}^{n} \frac{N_i}{m_i^\star} \widetilde{\tau}_i F_\lambda\left(\eta_i(T)\right)} \,. \tag{3.36}$$

Here, N_i is the degeneracy of the i^{th} band. Equation 3.36 can be conveniently expressed by introducing the substitutions $\delta\widetilde{\tau}_{i1} = \widetilde{\tau}_i / \widetilde{\tau}_1$ and $\varepsilon_{i1} = N_1 m_i^\star / \left(N_i m_1^\star\right)$, signifying the mass of the i^{th} band with respect to the first one:

$$S\left(T\right)=\frac{\sum_{i=1}^{n}\frac{1}{\varepsilon_{i1}}\delta\widetilde{\tau}_{i1}F_{\lambda}\left(\eta_{i}(T)\right)S_{i}\left(T\right)}{\sum_{i=1}^{n}\frac{1}{\varepsilon_{i1}}\delta\widetilde{\tau}_{i1}F_{\lambda}\left(\eta_{i}(T)\right)}\ . \tag{3.37}$$

Notably, $\delta\widetilde{\tau}_{11}=\varepsilon_{11}=1$. $S_i(T)$ can be calculated, in accordance with Equation 3.32, as

$$S_{i}\left(T\right)=\frac{k_{\mathrm{B}}}{e}\left[\eta_{i}-\operatorname{sgn}\left(m_{i}^{\star}\right)\frac{\lambda+2}{\lambda+1}\frac{F_{\lambda+1}\left(\eta_{i}(T)\right)}{F_{\lambda}\left(\eta_{i}(T)\right)}\right]\ , \tag{3.38}$$

with $\eta_i=(\mu-E_{0,i})/k_{\mathrm{B}}T$ representing the reduced chemical potential of the i^{th} band with respect to its band origin $E_{0,i}$. Here, the sign function was introduced to account for opposing signs of valence ($m^{\star}<0$) and conduction ($m^{\star}>0$) bands.

3.3 Hall coefficient of parabolic bands

The Hall coefficient R_{H} and Hall mobility μ_{H} are additional quantities that are easily calculated within the parabolic-band approximation. For a single parabolic band, the Hall mobility is given by [18]

$$\mu_{\mathrm{H}}=\frac{e}{m^{\star}}\frac{\int_{0}^{\infty}E^{3/2}\tau^{2}\left(-\frac{\partial f}{\partial E}\right)\mathrm{d}E}{\int_{0}^{\infty}E^{3/2}\tau\left(-\frac{\partial f}{\partial E}\right)\mathrm{d}E}\ . \tag{3.39}$$

This expression closely resembles the Hall mobility derived from the Drude model [162], $\mu_{\mathrm{H}}=e\tau/m$, with an energy-averaged scattering time τ. Inserting the dependencies of the scattering time from Equation 2.33 yields

$$\mu_{\mathrm{H}}=\frac{e}{(m^{\star})^{5/2}}\widetilde{\tau}T^{\gamma}\frac{\int_{0}^{\infty}E^{3/2}E^{2\lambda-1}\left(-\frac{\partial f}{\partial E}\right)\mathrm{d}E}{\int_{0}^{\infty}E^{3/2}E^{\lambda-1/2}\left(-\frac{\partial f}{\partial E}\right)\mathrm{d}E}\ . \tag{3.40}$$

After partial integration, this expression simplifies to

$$\begin{aligned}\mu_{\mathrm{H}}&=\frac{e}{(m^{\star})^{5/2}}\widetilde{\tau}(k_{\mathrm{B}}T)^{\lambda-1/2}T^{\gamma}\frac{2\lambda+1/2}{\lambda+1}\frac{F_{2\lambda-1/2}\left(\eta(T)\right)}{F_{\lambda}\left(\eta(T)\right)} &(3.41)\\&=\mu_{\mathrm{H},0}\frac{2\lambda+1/2}{\lambda+1}\frac{F_{2\lambda-1/2}\left(\eta(T)\right)}{F_{\lambda}\left(\eta(T)\right)}\ , &(3.42)\end{aligned}$$

with $\mu_{\mathrm{H},0}=\frac{e}{(m^{\star})^{5/2}}\widetilde{\tau}(k_{\mathrm{B}}T)^{\lambda-1/2}T^{\gamma}$.

Furthermore, the Hall coefficient can be written as

$$R_\mathrm{H} = \frac{\mu_\mathrm{H}}{\sigma} \tag{3.43}$$

$$= \frac{\pi^2\hbar^3}{e(2m^\star k_\mathrm{B}T)^{3/2}} \frac{2\lambda + 1/2}{(\lambda+1)^2} \frac{F_{2\lambda-1/2}\left(\eta(T)\right)}{F_\lambda^2\left(\eta(T)\right)} \propto \frac{1}{(m^\star T)^{3/2}} \frac{F_{2\lambda-1/2}\left(\eta(T)\right)}{F_\lambda^2\left(\eta(T)\right)} \; . \tag{3.44}$$

Here, die general notation of the electrical conductivity Equation 3.11 was used. Unlike the Hall mobility, the Hall coefficient does not explicitly depend on the dominant scattering mechanism but rather on its energy dependence E^λ.

In the following sections, the Hall mobility will be calculated for the two arguably most common scattering processes: acoustic-phonon and alloy-disorder scattering.

3.3.1 Acoustic-phonon scattering

The exponents of the scattering time for acoustic-phonon scattering are $\lambda = 0$ and $\gamma = -1$. Consequently, $\mu_{\mathrm{H},0}^{\mathrm{ph}} = \frac{e}{(m^\star)^{5/2}}\widetilde{\tau}_\mathrm{ph}(k_\mathrm{B}T)^{-1/2}T^{-1}$, leading to the expression for the Hall mobility:

$$\mu_\mathrm{H}^\mathrm{ph} = \mu_{\mathrm{H},0}^{\mathrm{ph}} \frac{1}{2} \frac{F_{-1/2}\left(\eta(T)\right)}{F_0\left(\eta(T)\right)} \propto \frac{1}{(m^\star)^{5/2}T^{3/2}} \frac{F_{-1/2}\left(\eta(T)\right)}{F_0\left(\eta(T)\right)} \; . \tag{3.45}$$

The ratio of the Fermi integrals exhibits different behavior based on the reduced chemical potential $\eta = \mu/k_\mathrm{B}T$ [18]

$$\frac{F_{-1/2}\left(\eta(T)\right)}{F_0\left(\eta(T)\right)} \propto \begin{cases} T^{1/2} & 1/\eta = k_\mathrm{B}T/\mu \ll 1 \\ 1 & 1/\eta \gg 1 \end{cases} \; . \tag{3.46}$$

Accordingly, the Hall mobility has the following limits:

$$\mu_\mathrm{H}^\mathrm{ph}(T) \propto \begin{cases} T^{-1} & 1/\eta \ll 1 \\ T^{-3/2} & 1/\eta \gg 1 \end{cases} \; . \tag{3.47}$$

3.3.2 Alloy-disorder scattering

In case of alloy-disorder scattering being the dominant scattering mechanism, where $\lambda = \gamma = 0$, the pre-factor of the Hall mobility becomes $\mu_{\mathrm{H},0}^{\mathrm{dis}} = \frac{e}{(m^\star)^{5/2}}\widetilde{\tau}(k_\mathrm{B}T)^{-1/2}$, leading to the Hall mobility

$$\mu_\mathrm{H}^\mathrm{dis} = \mu_{\mathrm{H},0}^{\mathrm{dis}} \frac{1}{2} \frac{F_{-1/2}\left(\eta(T)\right)}{F_0\left(\eta(T)\right)} \propto \frac{1}{(m^\star)^{5/2}T^{1/2}} \frac{F_{-1/2}\left(\eta(T)\right)}{F_0\left(\eta(T)\right)} \; . \tag{3.48}$$

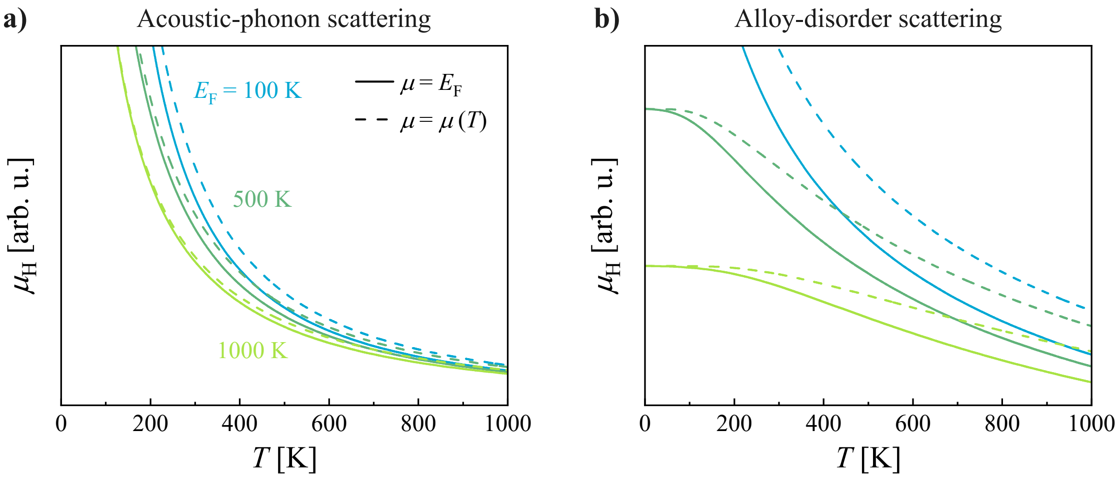

Figure 3.4: Hall mobility within the single-parabolic-band model, calculated for a) acoustic-phonon and b) alloy-disorder scattering as a function of the temperature. The dashed and solid lines show the Hall mobility with and without consideration of the temperature dependence of the chemical potential μ, respectively. The colors represent different positions of the Fermi energy E_F with respect to the zero of the band.

Applying the limits for the ratio of the Fermi integrals from Equation 3.46 yields

$$\mu_H^{\mathrm{dis}}(T) \propto \begin{cases} 1 & 1/\eta \ll 1 \\ T^{-1/2} & 1/\eta \gg 1 \end{cases} . \tag{3.49}$$

Figure 3.4 illustrates the temperature dependence of the Hall mobility for both acoustic-phonon and alloy-disorder scattering. When acoustic-phonon scattering is dominant (Equation 3.42a), the Hall mobility sharply decreases with increasing temperature, reflecting the increase in phonon scattering and decrease in the scattering time. Additionally, when the Fermi energy is shifted inside the band, the Hall mobility is further reduced due to the scattering rate τ^{-1} being proportional to the nearby density of states. Similarly, for alloy-disorder scattering (see Equation 3.42b), the mobility remains constant at very low temperatures ($\eta \ll 1$), as expected, and only starts decreasing at higher temperatures. A comparison with the temperature dependence of the electrical conductivity (Equation 3.21 and Figure 3.2) reveals that the decrease of the Hall mobility $\mu(T) \propto \sigma(T)/n(T)$ is less due to a change in the conductivity than due to an increase of the charge carrier participating in the transport, as indicated by the charge carrier concentration n.

3.3.3 Hall coefficient of multiple bands

In case of multiple parabolic bands, the Hall coefficient can be derived by considering the Hall coefficients of the individual bands, weighted by the squared conductivity:

$$R_{\mathrm{H}}(T) = \frac{\sum_{i=1}^{n} N_i R_{\mathrm{H},i}(T)\sigma_i^2(T)}{[\sum_{i=1}^{n} N_i \sigma_i(T)]^2} \, . \tag{3.50}$$

Here, N_i represents the degeneracy of the i^{th} band, and

$$R_{\mathrm{H},i}(T) = \frac{\pi^2\hbar^3}{e(2m_i^\star k_{\mathrm{B}}T)^{3/2}} \frac{2\lambda + 1/2}{(\lambda+1)^2} \frac{F_{2\lambda-1/2}\left(\eta_i(T)\right)}{F_\lambda^2\left(\eta_i(T)\right)} \, . \tag{3.51}$$

This leads to the overall expression for the Hall coefficient:

$$R_{\mathrm{H}}(T) = \frac{\pi^2\hbar^3}{e(2k_{\mathrm{B}}T)^{3/2}} \frac{2\lambda + 1/2}{(\lambda+1)^2} \frac{\sum_{i=1}^{n} \frac{1}{\varepsilon_{i1}(m_i^\star)^{5/2}} \delta\widetilde{\tau}_{i1}^2 F_{2\lambda-1/2}\left(\eta_i(T)\right)}{[\sum_{i=1}^{n} \frac{1}{\varepsilon_{i1}} \delta\widetilde{\tau}_{i1} F_\lambda\left(\eta_i(T)\right)]^2} \, . \tag{3.52}$$

Similar to the electrical conductivity in Equation 3.29, the Hall coefficient depends not only on the relative masses ε_{i1} as in the Seebeck coefficient, but also on their absolute values. This characteristic allows for the determination of individual band masses from the measured Hall coefficient data, as will be shown in the following chapter.

3.4 Consideration of the temperature dependence of the chemical potential

The number of charge carriers per volume in a material n can be determined by integrating the DOS $D(E)$, multiplied with the Fermi-Dirac distribution function $f\left(E,\mu,T\right) = \left[\exp\left(\frac{E-\mu}{k_{\mathrm{B}}T}\right)+1\right]^{-1}$ l across all energy levels:

$$n = \int_{-\infty}^{\infty} D\left(E\right) f\left(E,\mu,T\right) \mathrm{d}E \, . \tag{3.53}$$

Here, μ is the chemical potential, typically set to the value at 0 K, which is the Fermi energy E_{F}. In accordance with the conservation of charge, the charge carrier concentration should, by definition, remain temperature-independent for any material, hence

$$\frac{\mathrm{d}n}{\mathrm{d}T} \equiv 0 \; . \tag{3.54}$$

However, it is evident from Equation 3.53 that n does vary with T due to the temperature dependence of the Fermi-Dirac distribution. This dependence must be compensated by a shift of the chemical potential. Equation 3.54 can also be expressed as

$$\frac{\mathrm{d}n\left(\mu\left(T\right),T\right)}{\mathrm{d}T} = \frac{\partial n}{\partial T} + \frac{\partial n}{\partial \mu}\frac{\mathrm{d}\mu}{\mathrm{d}T} = 0 \; , \tag{3.55}$$

which yields

$$\frac{\mathrm{d}\mu}{\mathrm{d}T} = -\frac{\partial n}{\partial T}\left(\frac{\partial n}{\partial \mu}\right)^{-1} \; . \tag{3.56}$$

To determine the temperature dependence of μ, the partial derivations $\partial n/\partial T$ and $\partial n/\partial \mu$ need to be calculated. From Equation 3.53, it is clear that these derivations only effect the Fermi-Dirac distribution:

$$\frac{\partial n}{\partial T} = \int_{-\infty}^{\infty} D\left(E\right)\frac{\partial f\left(E,\mu,T\right)}{\partial T}\mathrm{d}E \; , \tag{3.57}$$

$$\frac{\partial n}{\partial \mu} = \int_{-\infty}^{\infty} D\left(E\right)\frac{\partial f\left(E,\mu,T\right)}{\partial \mu}\mathrm{d}E \; . \tag{3.58}$$

In metals with s- and p-electron character, $D(E)$ can be approximated as nearly constant over temperature, resulting in negligible derivatives of n due to

$$n \approx D\int_{-\infty}^{\infty} f\left(E,\mu,T\right)\mathrm{d}E = \mathrm{const} \; . \tag{3.59}$$

This assumption is the origin of the notion of a constant chemical potential. However, in d or f metals, semiconductors or insulators, which may exhibit a DOS with significant energy dependence, the derivatives can become substantial. Neglecting the temperature dependence of μ in such cases can lead to significant errors. Thus, the calculation of the temperature behavior of μ is crucial for accurately describing a wide range of materials.

3.4.1 Calculation of $\mu(T)$

The partial derivatives of the Fermi-Dirac distribution in Equation 3.57 and Equation 3.58 can easily be calculated as

$$\frac{\partial f}{\partial T} = \frac{E-\mu}{k_\mathrm{B}T^2} \frac{\exp\left(\frac{E-\mu}{k_\mathrm{B}T}\right)}{\left[\exp\left(\frac{E-\mu}{k_\mathrm{B}T}\right)+1\right]^2} \tag{3.60}$$

and

$$\frac{\partial f}{\partial \mu} = \frac{1}{k_\mathrm{B}T} \frac{\exp\left(\frac{E-\mu}{k_\mathrm{B}T}\right)}{\left[\exp\left(\frac{E-\mu}{k_\mathrm{B}T}\right)+1\right]^2} \ . \tag{3.61}$$

Comparing these equations with the partial derivative $\partial f/\partial E$,

$$\frac{\partial f}{\partial E} = -\frac{1}{k_\mathrm{B}T} \frac{\exp\left(\frac{E-\mu}{k_\mathrm{B}T}\right)}{\left[\exp\left(\frac{E-\mu}{k_\mathrm{B}T}\right)+1\right]^2} \ , \tag{3.62}$$

reveals that

$$\frac{\partial f}{\partial \mu} = -\frac{\partial f}{\partial E} \tag{3.63}$$

and

$$\frac{\partial f}{\partial T} = -\frac{E-\mu}{T}\frac{\partial f}{\partial E} \ . \tag{3.64}$$

These results can be inserted into Equation 3.57 and Equation 3.58. Similar to Equation 3.32, the equations can be written in terms of Fermi-Dirac integrals $F_j\left(\eta(T)\right)$:

$$\frac{\partial n}{\partial T} = \frac{\left(2m^\star k_\mathrm{B}\,T\right)^{3/2}}{4\pi^2\hbar^3 T}\left[3F_{1/2}\left(\eta(T)\right) - \eta\, F_{-1/2}\left(\eta(T)\right)\right] \ , \tag{3.65}$$

$$\frac{\partial n}{\partial \mu} = \frac{\left(2m^\star\right)^{3/2}\left(k_\mathrm{B}T\right)^{1/2}}{4\pi^2\hbar^3} F_{-1/2}\left(\eta(T)\right) \ . \tag{3.66}$$

Again, $\eta = \mu/k_\mathrm{B}T$ is the reduced chemical potential. In general, these integrals can be solved for any DOS landscape. However, when dealing with n parabolic bands with DOS D_i, (were $i = \{1, ...n\}$), the integrals can be split into individual integrals over each band:

$$\begin{aligned}\frac{\partial n}{\partial \varphi} &= \int_{-\infty}^{\infty} \sum_{i=1}^{n} N_i D_i(E) \frac{\partial f(E,\mu,T)}{\partial \varphi} \mathrm{d}E \\ &= \sum_{i=1}^{n} N_i \int_{-\infty}^{\infty} D_i(E) \frac{\partial f(E,\mu,T)}{\partial \varphi} \mathrm{d}E \ ,\end{aligned} \tag{3.67}$$

with $\varphi = \{T, \mu\}$. By plugging these partial derivatives into Equation 3.56, the total derivative $\mathrm{d}\mu/\mathrm{d}T$ can be calculated:

$$\frac{\mathrm{d}\mu}{\mathrm{d}T} = -k_\mathrm{B} \frac{\sum_{i=1}^{n} N_i \left(m_i^\star\right)^{3/2} \left[3F_{1/2}\left(\eta_i(T)\right) - \eta_i\, F_{-1/2}\left(\eta_i(T)\right)\right]}{\sum_{i=1}^{n} N_i \left(m_i^\star\right)^{3/2} F_{-1/2}\left(\eta_i(T)\right)} \ . \tag{3.68}$$

Notably, unlike the total Seebeck coefficient for multiple bands (see Equation 3.37), the different exponents of $m^\star$ and N prevent the summation of these parameters into ε. Hence, another quantity, $\delta N_{i1} = N_i/N_1$, denoting the degeneracy ratio, is required:

$$\frac{\mathrm{d}\mu}{\mathrm{d}T} = -k_\mathrm{B} \frac{\sum_{i=1}^{n} \left(\delta N_{i1}\right)^{5/2} \varepsilon_{i1}^{3/2} \left[3F_{1/2}\left(\eta_i(T)\right) - \eta_i\, F_{-1/2}\left(\eta_i(T)\right)\right]}{\sum_{i=1}^{n} \left(\delta N_{i1}\right)^{5/2} \varepsilon_{i1}^{3/2} F_{-1/2}\left(\eta_i(T)\right)} \ . \tag{3.69}$$

Ultimately, $\mu(T)$ can be obtained from Equation 3.69 as

$$\mu(T) = \int \frac{\mathrm{d}\mu}{\mathrm{d}T} \mathrm{d}T + C \ , \tag{3.70}$$

where the constant C is determined such that $\mu(0) = E_\mathrm{F}$.

3.4.2 Illustration of $\mu(T)$

As previously discussed, the chemical potential is often approximated as the temperature-independent Fermi energy E_F. However, in many materials utilized in the field of thermoelectricity, especially when E_F is close to or inside a band gap, $\mu(T)$ can exhibit a significant temperature dependence. Figure 3.5 illustrates the behavior for typical scenarios. In Figure 3.5a, μ is plotted against temperature for a single valence band with varying Fermi energies. In each case, μ is shifted outside the band. This can be understand by looking at the number of electrons per volume n (see Equation 3.53), which governs the position of the Fermi energy.

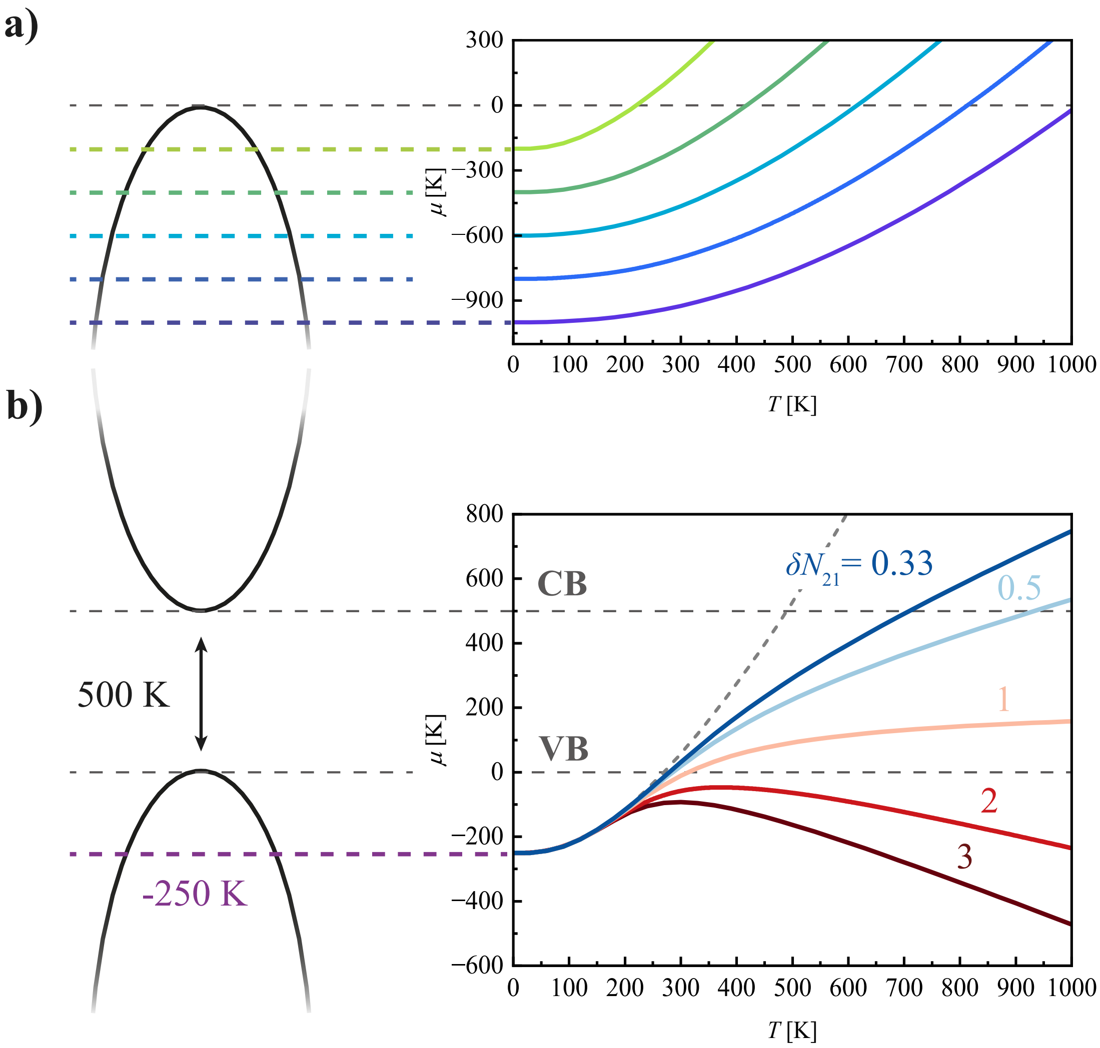

Figure 3.5: Chemical potential μ versus temperature T for (a) a single valence band for different Fermi energies and (b) a two-band system comprising a valence band and a conduction band with a band gap of $500\,$K for different ratios of degeneracies δN_{21}. The masses of the bands are set to equal values. The dashed gray line in b) shows the single-band behavior of μ for comparison.

As the temperature increases, the step-function-like distribution function becomes less sharp. The asymmetry of the DOS with respect to E_F leads to a decrease of n. To compensate, μ increases to enhance the overlap of the selection function with the DOS. This increase in the chemical potential follows a quadratic trend within

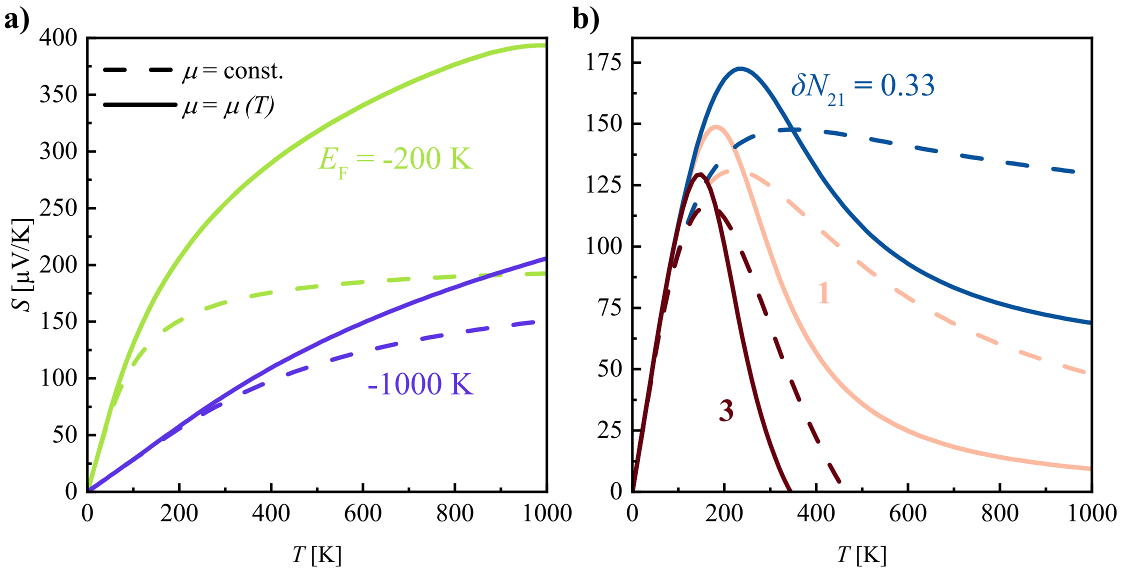

Figure 3.6: Seebeck coefficient S as a function of the temperature T for (a) a single valence band for different Fermi energies E_{F} and (b) a two-band system consisting of a valence band and a conduction band with varying ratios of degeneracies δN_{21}. The dashed and solid lines refer to Seebeck coefficients calculated with a constant and temperature-dependent chemical potential μ, respectively.

the band but becomes linear outside. Deep inside the band (as seen with the purple line in Figure 3.5a, where $E_{\mathrm{F}} = -1000\,\mathrm{K}$), the temperature dependence of μ becomes substantially smaller, justifying the approximation of a constant chemical potential in metals. In Figure 3.5b, the temperature dependence of μ is depicted for a two-band system, which includes a valence band and a conduction band with a 500 K band gap. The extent of influence of the conduction band varies with the degeneracy ratio δN_{21}. When the bands have equal degeneracies and masses, μ tends to settle in the middle of the band gap. In cases where the masses of the bands differ instead of degeneracies, the behavior of the chemical potential follows a similar trend (see Equation 3.69).

Finally, the consequence of a temperature-dependent μ on the thermoelectric properties is discussed. Figure 3.6 presents the Seebeck coefficient versus temperature, both with and without a constant chemical potential, for the two scenarios depicted in Figure 3.5. In the case of a single valence band, shown in Figure 3.6a, the Seebeck coefficient exhibits larger values when considering the temperature dependence of μ. This increase is a result of the shift of the chemical potential towards the band edge and the consequent decline in bipolar conduction. This difference is even more pronounced when the Fermi energy E_F is situated close to the band gap. Figure 3.6b illustrates the Seebeck coefficient for a two-band system with varying degeneracy ratios δN_{21}. By incorporating the temperature dependence of μ, the Seebeck coefficient shows a much sharper peak. This phenomenon is explained by the dynamic movement of μ. Initially, it shifts towards the band edge at lower temperatures, followed by a shift away from the edge in either direction (see Figure 3.5b). Depending on the degeneracies, both the temperature dependence of μ as well as the contribution of the conduction band to the Seebeck coefficient can differ substantially, yielding distinct features of $S(T)$. Ultimately, the shift of μ results in a significant deviation of the Seebeck coefficient from simple parabolic-band expectations, particularly at higher temperatures.

In conclusion, it is evident that neglecting the temperature dependence of the chemical potential, hence approximating $\mu(T) = E_\mathrm{F}$, can yield substantially incorrect parameters for the band structure when the fitting Seebeck data. This effect is particularly prominent in materials where the Fermi energy is located in the vicinity of the band gap, a common scenario in the field of thermoelectricity.

4 Algorithm for fitting transport properties within the parabolic-band regime

This chapter introduces and discusses a comprehensive tool, specifically designed for fitting distinct thermoelectric properties, which will be integrated into an openly accessible software. The fitting algorithm is based on approximating the band structure with parabolic bands, utilizing equations derived in chapter 3. The tool excels in fitting the Seebeck coefficient, electrical conductivity and Hall coefficient, with the flexibility that not all measurement data are mandatory to derive band-structure information.

As demonstrated in the sections below, the developed tool provides insights into the underlying band structure and associated scattering processes. Consequently, it serves as a valuable resource for thermoelectric researchers in need of a convenient and robust methodology to characterize materials within the parabolic-band regime.

4.1 Mathematical foundation

The experimental data are fitted using the functions derived in the preceding chapter 3. In summary, these are

$$S\left(T\right) = \frac{\sum_{i=1}^{n} \frac{1}{\varepsilon_{i1}} \delta\widetilde{\tau}_{i1} F_{\lambda}\left(\eta_i(T)\right) S_i\left(T\right)}{\sum_{i=1}^{n} \frac{1}{\varepsilon_{i1}} \delta\widetilde{\tau}_{i1} F_{\lambda}\left(\eta_i(T)\right)} \;, \tag{4.1}$$

$$\sigma(T) = \frac{2\sqrt{2}e^2}{\pi^2\hbar^3}(\lambda+1)\left(k_{\mathrm{B}}T\right)^{\lambda+1} T^{\gamma} \sum_{i=1}^{n} \frac{N_i}{m_i^{\star}} \widetilde{\tau}_i F_{\lambda}\left(\eta_i(T)\right) \tag{4.2}$$

and

$$R_{\mathrm{H}}(T) = \frac{\pi^2\hbar^3}{e(2k_{\mathrm{B}}T)^{3/2}}\frac{2\lambda+1}{(\lambda+1)^2}\frac{\sum_{i=1}^{n}\frac{1}{\varepsilon_{i1}(m_i^\star)^{5/2}}\delta\widetilde{\tau}_{i1}^{2}F_{2\lambda-1/2}\left(\eta_i(T)\right)}{[\sum_{i=1}^{n}\frac{1}{\varepsilon_{i1}}\delta\widetilde{\tau}_{i1}F_{\lambda}\left(\eta_i(T)\right)]^2}\ , \tag{4.3}$$

with

$$S_i\left(T\right) = \frac{k_{\mathrm{B}}}{e}\left[\eta_i - \operatorname{sgn}\left(m_i^\star\right)\frac{\lambda+2}{\lambda+1}\frac{F_{\lambda+1}\left(\eta_i(T)\right)}{F_{\lambda}\left(\eta_i(T)\right)}\right]\ . \tag{4.4}$$

While the Seebeck coefficient S, electrical conductivity σ and Hall coefficient R_{H} are all influenced by the shape of the band structure, they also depend on distinct features, making this set of formulas a robust foundation for gaining significant insight into the electronic behavior of a material. It is crucial to note that the formulas mentioned above required the same energy dependence, or λ, of the scattering mechanism. Without this uniformity, the total scattering type, following Matthiessen's rule, can not be expressed as $\tau \propto E^{\lambda}$, thereby hindering the use of Fermi-Dirac integrals.

The reduced chemical potential $\eta_i = \operatorname{sgn}(m^\star)(\mu - E_{0,i})/k_{\mathrm{B}}T$ denotes be position of the chemical potential μ relative to the band edge $E_{0,i}$ [3]. Furthermore, without limiting the generality, the position of the first band, fixed as a valence band, is set to $E = 0$, resulting in $E_{0,i} = E_{\mathrm{g},i}$ describing the gap of the i^{th} band with respect to the first band. Hence, $E_{\mathrm{g},1} = 0$. A visualization of these parameters is presented in Figure 4.1 for three bands.

In case of n bands and a single dominant scattering mechanism, the Seebeck coefficient depends on $3n-2$ parameters, the electrical conductivity on $3n$ parameters and the Hall coefficient on $3n-1$ parameters. If two scattering mechanisms share the same energy dependence but exhibit different temperature dependencies - e.g. acoustic-phonon and alloy-disorder scattering, which are both considered in the algorithm (see below) - the scattering time involves two parameters, resulting in an increased total parameter count of $4n-2$, $4n$ and $4n-1$, respectively. Table 4.1 provides a detailed list of the quantities' dependence on the parameters. Understanding that fitting each quantity with the full set of parameters is impractical and will likely lead to overfitting, the approach discussed in the next section involves using the quantities to derive different parameters while keeping others fixed.

---

[3] The sign function, determining the sign of the chemical potential within the Fermi integrals, accounts for the different shape of the density of states for valence and conduction bands.

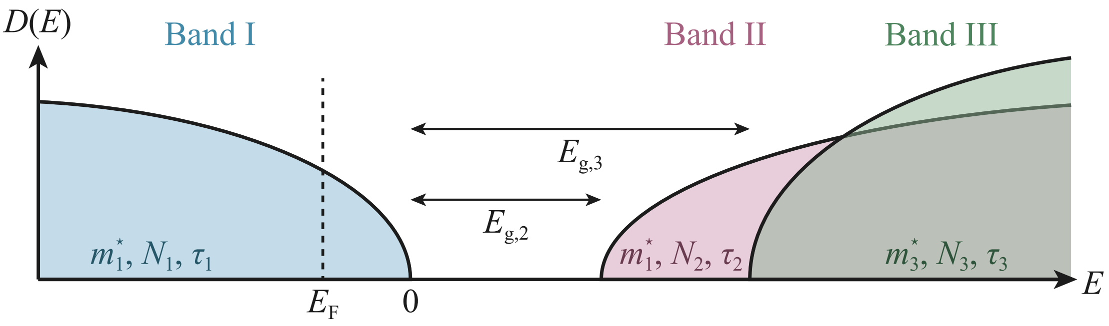

Figure 4.1: Visualization of the fit parameters for three bands. The first band is consistently configured as a valence band with the edge positioned at $E = 0$. Each additional band introduces three parameters for a single dominant scattering mechanism and four parameters for two scattering mechanisms, namely the gap to the first band $E_{\mathrm{g},i}$, the band mass $m_i^\star$ and the scattering time τ_i, the latter depending on the pre-factor of all concurrent scattering mechanisms, such as acoustic-phonon and alloy-disorder scattering. Although the degeneracy N_i of the band is another important quantity, its value is set by the user.

Quantity	Parameter					Sum	
	E_F	E_g	$m^\star$	$\widetilde{\tau}_\mathrm{single}$	$\widetilde{\tau}_\mathrm{double}$	Σ_single	Σ_double
S	1	$n-1$	$n-1$	$n-1$	$2n-1$	$3n-2$	$4n-2$
σ	1	$n-1$	n	n	$2n$	$3n$	$4n$
R_H	1	$n-1$	n	$n-1$	$2n-1$	$3n-1$	$4n-1$

Table 4.1: Number of parameters on which the quantities S, σ, and R_H depend on in case of n bands, provided for the Fermi energy E_F, band gaps E_g, effective masses $m^\star$, and scattering time $\widetilde{\tau}$, considering either a single or two dominant scattering mechanisms with equal energy dependence.

A final noteworthy point is that the Fermi-Dirac integrals F_j can be expressed using polylogarithms Li_{j+1}:

$$F_j\left(x\right) = -\mathrm{Li}_{j+1}\left(-e^{-x}\right)\Gamma(j+1)\ , \tag{4.5}$$

where Li_j is defined as

$$\mathrm{Li}_j\left(x\right) = \sum_{k=1}^{\infty}\frac{x^k}{k^j}\ , \tag{4.6}$$

and

$$\Gamma(j) = \frac{1}{(j-1)!} \ . \tag{4.7}$$

This formulation allows for the avoidance of numerical integration, significantly facilitating the computation of these quantities.

4.2 Chemical potential

Within the software used for fitting the Seebeck data, the implementation of $\mu\,(T)$ is performed numerically for each temperature T_i on an evenly spaced grid with indices $i = \{0, ..., m\}$. Instead of using the exact but unsolvable Equation 3.70, it is more feasible to calculate the chemical potential at the temperature T_i from the value at the previous temperature T_{i-1}, employing a linear approximation:

$$\mu\,(T_i) \approx \mu\,(T_{i-1}) + \frac{\mathrm{d}\mu}{\mathrm{d}T}\,(T_{i-1})\,\Delta T_i \ , \tag{4.8}$$

with $\Delta T_i = T_i - T_{i-1}$ and $\mu\,(T_0) = E_\mathrm{F}$. The derivative can be calculated from

$$\frac{\mathrm{d}\mu}{\mathrm{d}T} = -k_\mathrm{B} \frac{\sum_{i=1}^{n} (\delta N_{i1})^{5/2}\, \varepsilon_{i1}^{3/2} \left[3F_{1/2}\,(\eta_i(T)) - \eta_i\, F_{-1/2}\,(\eta_i(T))\right]}{\sum_{i=1}^{n} (\delta N_{i1})^{5/2}\, \varepsilon_{i1}^{3/2} F_{-1/2}\,(\eta_i(T))} \ , \tag{4.9}$$

as was derived in the previous chapter. $\delta N_{i1} = N_i/N_1$ is the ratio of the degeneracy of the i^{th} to the first band. A visualization of Equation 4.8 is shown in Figure 4.2.

4.2.1 Adding the second derivative of $\mu\,(T)$

In cases where the chemical potential exhibits significant temperature dependence, a linear extrapolation may lead to inaccuracies, particularly when the temperature steps ΔT are substantial (see Figure 4.2). In such situations, accounting for the second derivative can help to reduce deviations from the actual temperature dependence $\mu(T)$. The recursive formula of the chemical potential, considering the second derivative, can be written as

$$\mu\,(T_i) \approx \mu\,(T_{i-1}) + \frac{\mathrm{d}\mu}{\mathrm{d}T}\,(T_{i-1})\,\Delta T_i + \frac{1}{2}\frac{\mathrm{d}^2\mu}{\mathrm{d}T^2}\,(T_{i-1})\,\Delta T_i^2 \ . \tag{4.10}$$

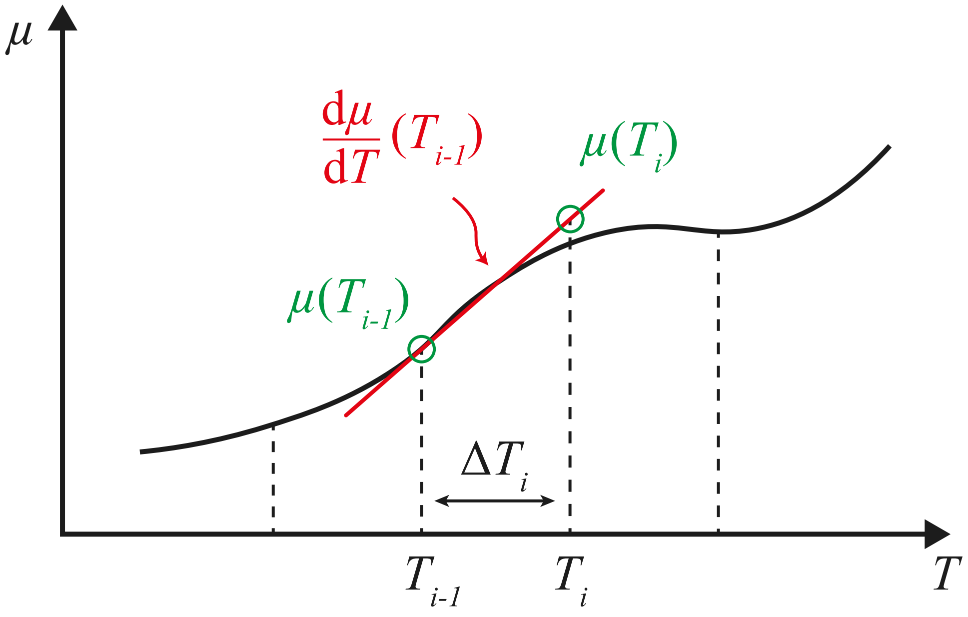

Figure 4.2: Illustration of the recursive calculation of $\mu(T)$. The value at T_i is determined from the value at T_{i-1} along with the corresponding slope at that temperature.

This expression takes into account the curvature of $\mu(T)$. Similar to the derivation of $\mathrm{d}\mu/\mathrm{d}T$, the identity $\mathrm{d}^2 n/\mathrm{d}T^2 \equiv 0$ can be used to derive an equation for $\mathrm{d}^2\mu/\mathrm{d}T^2$:

$$\frac{\mathrm{d}^2 n(\mu(T), T)}{\mathrm{d}T^2} = \frac{\partial^2 n}{\partial T^2} + \frac{\partial^2 n}{\partial \mu^2}\frac{\mathrm{d}^2\mu}{\mathrm{d}T^2} + 2\frac{\partial^2 n}{\partial\mu\,\partial T}\frac{\mathrm{d}\mu}{\mathrm{d}T} = 0\,, \tag{4.11}$$

$$\frac{\mathrm{d}^2\mu}{\mathrm{d}T^2} = -\left(\frac{\partial^2 n}{\partial T^2} + 2\frac{\partial^2 n}{\partial\mu\,\partial T}\frac{\mathrm{d}\mu}{\mathrm{d}T}\right)\left(\frac{\partial^2 n}{\partial\mu^2}\right)^{-1}. \tag{4.12}$$

Here, $\mathrm{d}\mu/\mathrm{d}T$ is obtained from the previously defined Equation 3.69. The other terms are calculated from integrals, which can be written as

$$\frac{\partial^2 n}{\partial T^2} = \int_{-\infty}^{\infty} D(E)\,\frac{\partial^2 f(E,\mu,T)}{\partial T^2}\mathrm{d}E\,, \tag{4.13}$$

$$\frac{\partial^2 n}{\partial\mu^2} = \int_{-\infty}^{\infty} D(E)\,\frac{\partial^2 f(E,\mu,T)}{\partial\mu^2}\mathrm{d}E\,, \tag{4.14}$$

and

$$\frac{\partial^2 n}{\partial\mu\,\partial T} = \int_{-\infty}^{\infty} D(E)\,\frac{\partial f(E,\mu,T)}{\partial\mu\,\partial T}\mathrm{d}E\,. \tag{4.15}$$

The partial derivatives within these integrals can be calculated similar to Equation 3.60 and Equation 3.61.

4.2.2 Alternative computation method of μ

Instead of determining the temperature dependence of the chemical potential from its derivative $\mathrm{d}\mu/\mathrm{d}T$ (see Equation 4.9), it can alternatively evaluated using a root-finding algorithm. Starting with

$$\frac{\mathrm{d}n}{\mathrm{d}T} = 0 \tag{4.16}$$

it follows for all temperatures:

$$n(T) = n(0)\ . \tag{4.17}$$

By inserting the expression for the charge carrier density Equation 3.53, the equation can be expressed as

$$\int_{-\infty}^{\infty} D(E)\frac{1}{e^{\frac{E-\mu}{k_\mathrm{B}T}}+1}\mathrm{d}E = \int_{-\infty}^{E_\mathrm{F}} D(E)\mathrm{d}E\ . \tag{4.18}$$

This equation can not be modified to yield the chemical potential. However, it can be obtained by finding the minimum of the function

$$\begin{aligned} f(\mu) &= \left| \int_{-\infty}^{\infty} D(E)\frac{1}{e^{\frac{E-\mu}{k_\mathrm{B}T}}+1}\mathrm{d}E - \int_{-\infty}^{E_\mathrm{F}} D(E)\mathrm{d}E \right| \qquad (4.19) \\ &= \left| \int_{-\infty}^{\infty} D(E)\frac{1}{e^{\frac{E-\mu}{k_\mathrm{B}T}}+1}\mathrm{d}E - \frac{(2m^\star)^{3/2}}{3\pi^2\hbar^3}E_\mathrm{F}^{3/2} \right|\ . \qquad (4.20) \end{aligned}$$

Depending on the number of bands and temperature steps, either of the two presented approaches can require less computation time.

4.3 Fitting process

The fitting procedure involves an iterative fitting of all provided measurement quantities. While the chemical potential theoretically depends on the ratio of degeneracies δN, attempting to derive its value from fitting either quantity proved challenging. The dependence on the degeneracy ratio was found to be insufficiently

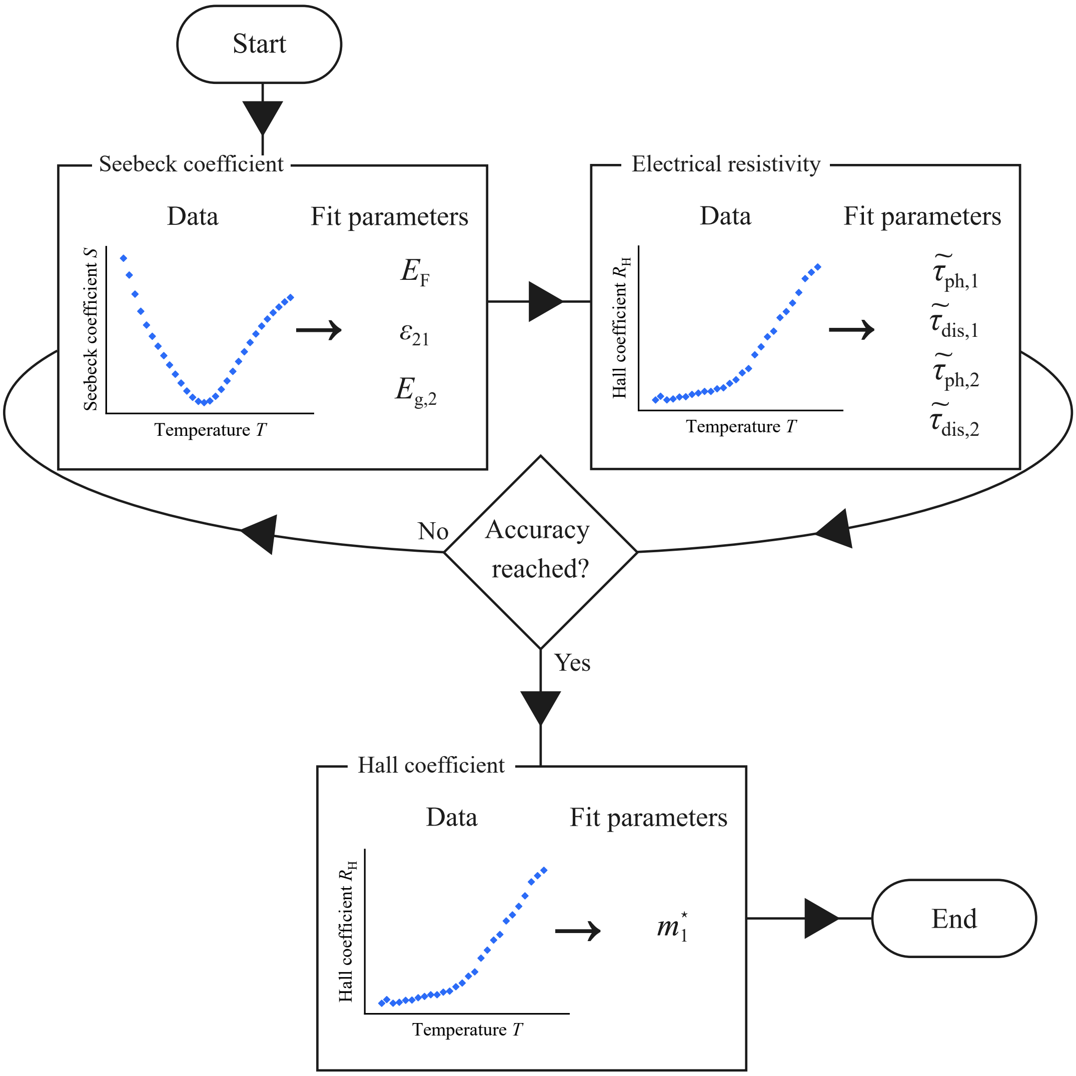

Figure 4.3: Flow chart of the fitting procedure, depicted for the case of two parabolic bands with consideration of both acoustic-phonon and alloy-disorder scattering. The algorithm alternately fits the Seebeck coefficient and electrical resistivity, obtaining band structure (E_F, ε_{21} and $E_{\mathsf{g},2}$) and scattering parameters ($\widetilde{\tau}_{\mathsf{ph},1}$, $\widetilde{\tau}_{\mathsf{dis},1}$, $\widetilde{\tau}_{\mathsf{ph},2}$ and $\widetilde{\tau}_{\mathsf{dis},2}$), until the demanded convergence is reached. Then, the Hall coefficient is fitted in a single step which yields the band masses $m_1^\star$ and $m_2^\star$.

determined, resulting in degenerate results. Therefore, it is necessary to manually input the degeneracies of the bands before the fitting procedure.

The fitting process is illustrated in Figure 4.3 for the scenario of two bands. Initiated by fitting the Seebeck coefficient, the band structure parameters - namely the Fermi energy E_F, the band gap $E_{\mathrm{g},2}$ and the relative mass ε_{21} are obtained. This yields comprehensive information about the band structure, excluding degeneracies and actual band masses. Throughout the Seebeck coefficient fitting, the temperature-dependent ratio of scattering times $\delta\widetilde{\tau}_{21}$ is kept fixed, starting with $\delta\widetilde{\tau}_{21} = 1$ in the initial iteration. Notably, in cases where only one type of scattering dominates the system, all temperature dependencies of that specific scattering type cancel out of the total Seebeck coefficient. Only the factor $\delta\widetilde{\tau}_{i1}/\varepsilon_{i1}$ remains as a fitting parameter (see Equation 4.1). However, in scenarios involving two distinct scattering mechanisms, the varying temperature dependencies prevent such simplifications. For instance, the scattering time resulting from acoustic-phonon (ph) and alloy-disorder (dis) scattering is given by:

$$\tau = \frac{1}{\frac{1}{\tau_\mathrm{ph}} + \frac{1}{\tau_\mathrm{dis}}} = \frac{\widetilde{\tau}_\mathrm{ph}\widetilde{\tau}_\mathrm{dis}}{\widetilde{\tau}_\mathrm{ph} + \widetilde{\tau}_\mathrm{dis} T}(m^\star)^{-3/2} E^{-1/2} \tag{4.21}$$

Once the characteristic features of the band structure are extracted from the Seebeck coefficient, the electrical resistivity is fitted to reveal insights into the dominant scattering mechanisms. While electron-electron and ionized-impurity scattering can be significant in materials, particularly at lower temperatures, their distinct energy dependence complicates their simultaneous implementation with acoustic-phonon scattering, which is commonly dominant at higher temperatures. Consequently, the fit is limited to acoustic-phonon and alloy-disorder scattering, aiming to describe the behavior of the majority of systems. It is worth noting that the algorithm inherently provides the flexibility to neglect one type of scattering by adjusting its strength relative to the other, ensuring a description of the electrical resistivity with a single dominant scattering mechanism.

Following the resistivity fit, both steps are reiterated until convergence is achieved. Convergence is reached when all fit parameters of the Seebeck coefficient and electrical resistivity exhibit changes of no more than 0.1 % compared to the previous iteration. This preset value can, however, be adjusted by the user.

Ultimately, the Hall coefficient data are fitted to deduce the band masses of each band. Given that the ratio of masses is already obtained from the Seebeck coefficient, only one fit parameter remains.

Quantity	Parameter					Sum	
	E_F	E_g	$m^\star$	$\widetilde{\tau}_\mathrm{single}$	$\widetilde{\tau}_\mathrm{double}$	Σ_single	Σ_double
S	1	$n-1$	$n-1$	0	0	$2n-1$	$2n-1$
σ	0	0	0	n	$2n$	n	$2n$
R_H	0	0	1	0	0	1	1

Table 4.2: Number of fit parameters for the quantities S, σ and R_H in case of n bands, provided for the Fermi energy E_F, the band gaps E_g, the effective masses $m^\star$ and the scattering time $\widetilde{\tau}$, considering either a single or two dominant scattering mechanisms with equal energy dependence.

The distribution of fit parameters among the three thermoelectric quantities is not unique. For instance, the relative effective mass ε_{i1} can be derived from the Hall coefficient together with the band masses, while the mass ratio is held constant in the Seebeck fit. Despite this flexibility, the presented approach offers several advantages:

1. The Hall coefficient proved to be the most challenging quantity to describe accurately. Therefore, it is excluded from the fitting iteration and employed only afterwards to obtain the band masses and assess the quality of the fit.
2. While all quantities depend on more or less the same parameters (see Table 4.1), the Seebeck coefficient exhibits the strongest dependence on the band structure, whereas the electrical resistivity is more influenced by the scattering parameters.
3. For broad applicability, the fit prioritizes the Seebeck coefficient and electrical conductivity. Given that common thermoelectric measurements typically involve these two quantities rather than the Hall coefficient, this approach ensures the extraction of all crucial parameters except the explicit band masses.

The number of parameters obtained from each thermoelectric quantity is presented in Table 4.2.

For the fit to converge successfully and find the set of parameters minimizing the error between experimental and predicted values, an effective initial guess is crucial. This necessitates setting the relative band masses ε, band gaps E_g and

Fermi energy E_F to values closely approximating the true parameters. The specific error range varies across variables and different systems, making it challenging to provide exact numbers.

Although the software permits users to manually adjust values and fine-tune theoretical curves (as discussed later), understanding the behavior of all parameters, particularly for less experienced users, can be time-consuming. To expedite the process of finding close initial values, a neural network has been trained using an artificially generated dataset comprising Seebeck coefficients and corresponding band structures. Further details regarding the training and architecture of the network can be found in Appendix D.

4.4 Example

To elucidate the procedure further, the Seebeck coefficient, electrical resistivity and Hall coefficient of of $Fe_2VAl_{1-x}Si_x$, with $x = 0.025, 0.05$ and 0.1, were both measured and subjected to fitting. The outcomes are depicted in Figure 4.4. The obtained experimental data align with previously reported results [111, 163]. The substitution of Al with Si induces a rigid-band shift of the Fermi energy into the conduction band, resulting in a sign reversal of the Seebeck coefficient, coupled with a decrease in electrical resistivity. Various theoretical calculations have suggested a small negative or positive indirect band gap between the Γ and the X point, with both bands having an equal degeneracy of 3 [164–167]. Consequently, the ratio of degeneracy, δN_{21}, is set to 1.

In Figure 4.4, the light and dark lines depict the modeled properties after the first and final iteration, respectively. The fitted curves of the Seebeck coefficient and electrical resistivity closely align with the experimental data. However, the Hall coefficient fit is relatively inaccurate, especially for the $x = 0.025$ sample. This discrepancy arises from only one parameter being available for fitting R_H. It was observed that the Hall coefficient often requires a different set of band structure parameters when fitted alongside additional parameters. While this issue remains unresolved at the time of writing, a more robust treatment of the Hall coefficient is planned until publication of the software.

Although the lines align closely with each other, the parameters exhibit substan-

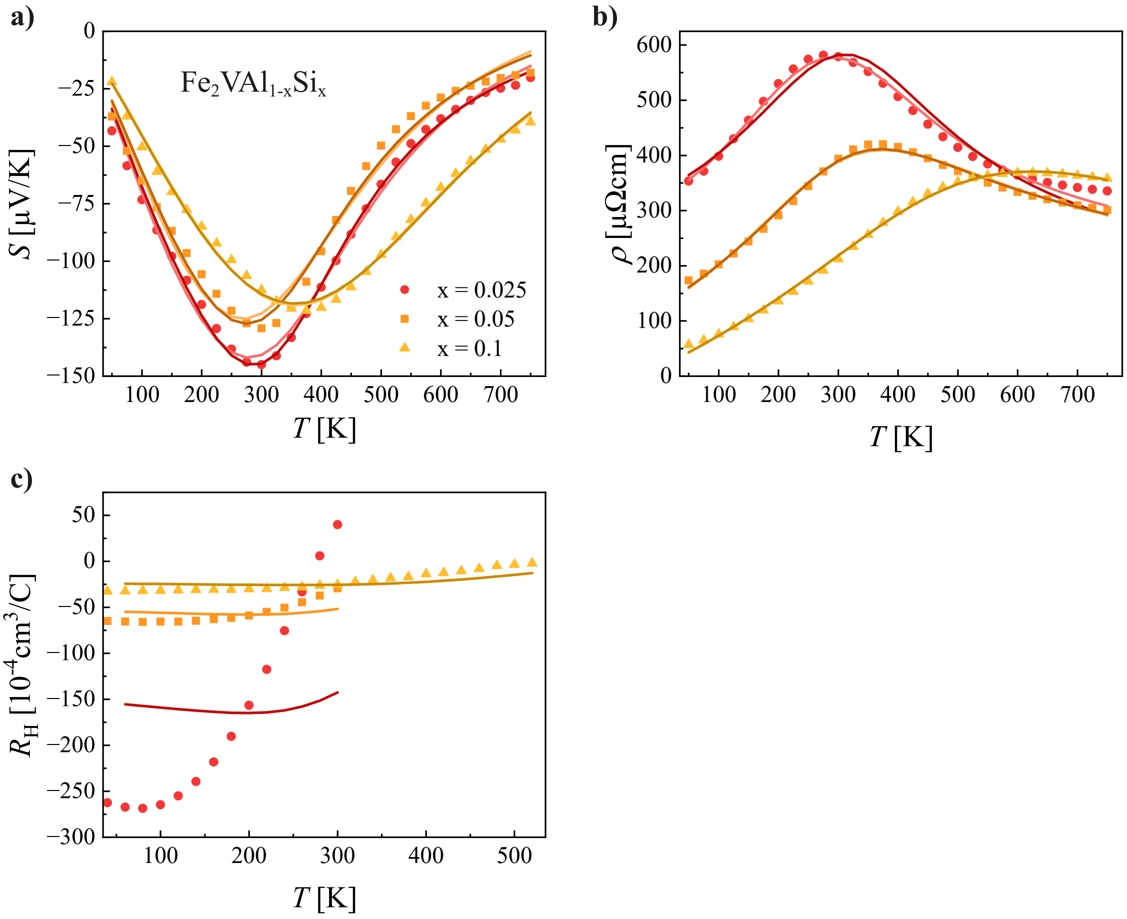

Figure 4.4: Temperature-dependent a) Seebeck coefficient S, b) electrical resistivity ρ and c) Hall coefficient R_H of different Fe$_2$VAl$_{1-x}$Si$_x$ samples. The symbols are experimental data, interpolated on an equidistant grid, while the lighter and darker line show the fit of the first and final step, respectively.

tial variation between the steps, as presented in Figure 4.5. In Fe$_2$VAl, a second, heavy conduction band is situated approximately 0.4 eV above the valence band [50]. The presence of this band is expected to impact the obtained parameters when the Fermi energy is shifted to higher energies.

The band structure parameters - ε_{21}, E_g and E_F - follow the expected behavior. Since neither aluminum nor silicon exhibits states near the Fermi energy in Fe$_2$VAl, the substitution of Al with Si does not influence the band masses. However, as E_F shifts to higher energies, the heavy conduction band's contribution increases, leading to a higher effective mass ratio. Additionally, the band gap remains unaltered

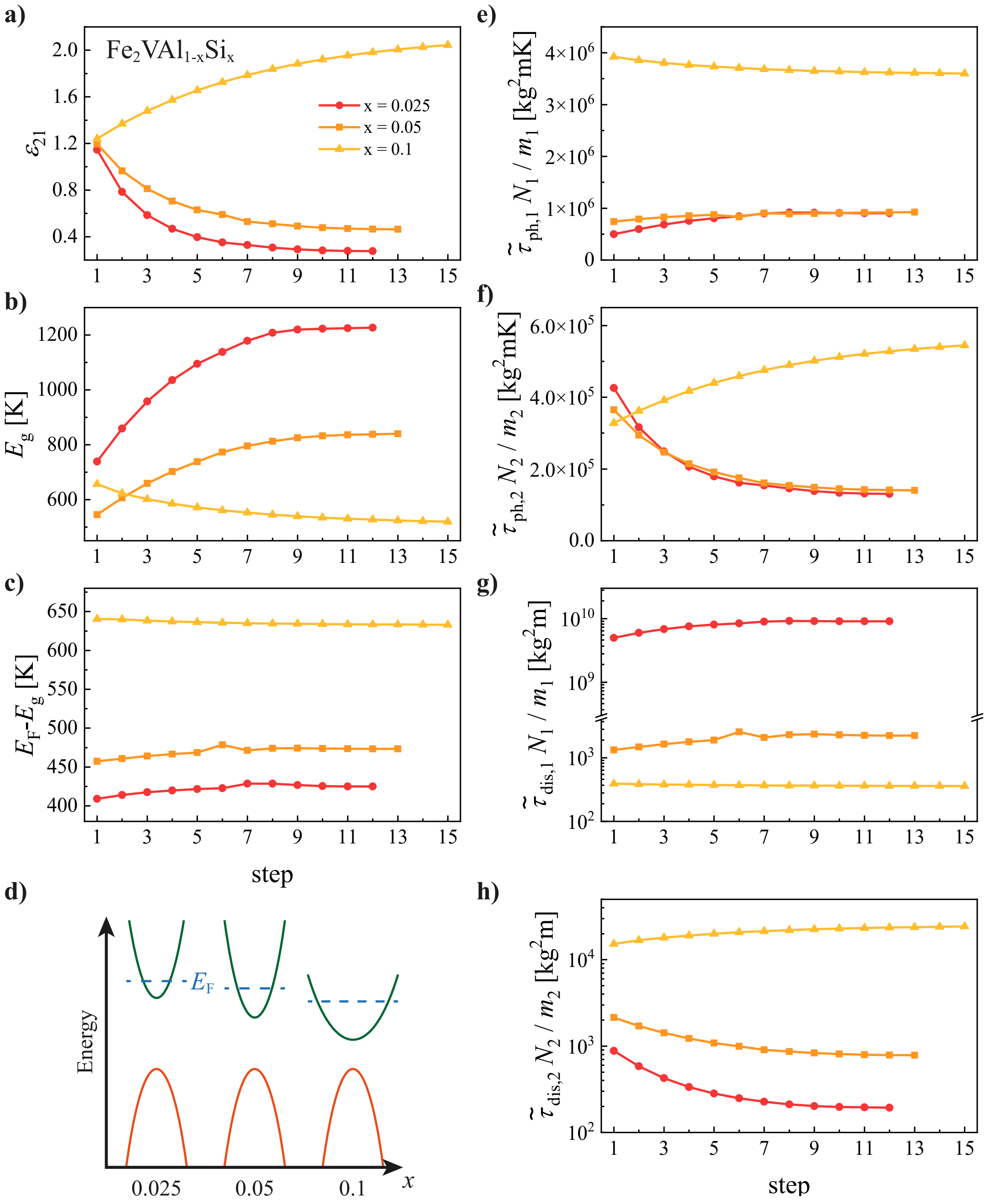

Figure 4.5: Band-structure (a, b, c) and scattering (e, f, g) parameters of different Fe$_2$VAl$_{1-x}$Si$_x$ samples as a function of the iteration step of the fitting process. d) Visualization of the band structure obtained from the fit of the Seebeck coefficient.

upon substitution with Si, indicating the independence of E_g from x. Nevertheless, as the Fermi energy shifts into the conduction band, part of the conduction band lies below E_F, resulting in a smaller average gap in the two-band description. Finally, the Fermi energy increases as anticipated. This change is visualized with respect to the band gap, as alternations in the band gap automatically shift the Fermi energy to maintain charge neutrality. The obtained band structure is obtained in Figure 4.5d.

The scattering times offer further insights into the dominant scattering processes. For $x = 0.025$ and 0.05, identical acoustic-phonon scattering times are obtained, while the values sharply increase for $x = 0.1$, indicating a shift in the dominant scattering mechanism toward alloy-disorder scattering. A closer examination of Figure 4.5g and Figure 4.5h reveals that alloy-disorder scattering becomes the dominant process in the valence band, while the opposite behavior is observed in the conduction band. Considering the increasing amount of disorder upon substitution with Si, an enhancement of alloy-disorder scattering is not unlikely.

4.5 Software

The fitting algorithm is encapsulated within a publicly available software, written in Python. As of submission date of this thesis, the software is in the final stages of completion. The figures and details presented below reflect the current status. Any variations in notation, colors or arrangement of graphs are attributed to collaborative efforts among several programmers and will be standardized before the final release.

4.5.1 Experimental data

Experimental data must be supplied in ASCII data files (e.g. „.txt“, „.dat“, etc.), organized in x-y columns. The first column should represent temperatures in Kelvin, while the second column should contain the Seebeck coefficient, electrical resistivity or Hall coefficient in SI units. The choice of units aims to prevent errors stemming from unit confusion. While it is not mandatory to provide all properties within the same temperature range or with identical temperature spacing, a sparse grid may compromise the fit’s accuracy.

Upon importing, the data are interpolated onto an equidistant grid. This not only facilitates the fitting process by using a limited number of data points but also enables the initial prediction by the neural network, which is trained on a specific temperature grid.

Supplying data for the Seebeck coefficient is mandatory to utilize the fit algorithm, as band structure information is derived from these data. The other two properties are optional and determine the obtained information (see below).

4.5.2 Different models and modes

The fit can be executed using either one, two or three parabolic bands, with the number of bands determining the fit parameters. However, careful analysis of the results is essential, as a unique solution is not guaranteed for three bands depending on the measurement data. Additionally, the required number of bands to describe the data depends on the temperature range. The single-parabolic-band model might suffice for lower temperature, while two or three bands may be necessary at elevated temperatures. Due to the significantly increased parameter space for three bands, the neural network is trained only for one and two bands. Therefore, the user needs to manually adjust the values before fitting the data.

The current software plan incorporates an automatic selection of the fitting mode based on the number of quantities imported by the user. The simplest mode involves fitting only the Seebeck coefficient and obtaining information about the band structure, including ε_{i1}, gap_i and E_F. If, additionally, data on the electrical resistivity are imported, information about the scattering parameter is obtained. The last mode encompasses a complete fit of all three properties to further yield the absolute masses of all bands.

4.5.3 User interface

The application's user interface offers several options to the user, including the choice of the number of bands and the mode (if not already limited by the quantities imported). Additionally, the user can manually adjust the fit parameters while observing the changes through a graphical visualization. Figure 4.6 illustrates the Seebeck-only mode, utilizing the two-parabolic-band model. The top toolbar shown

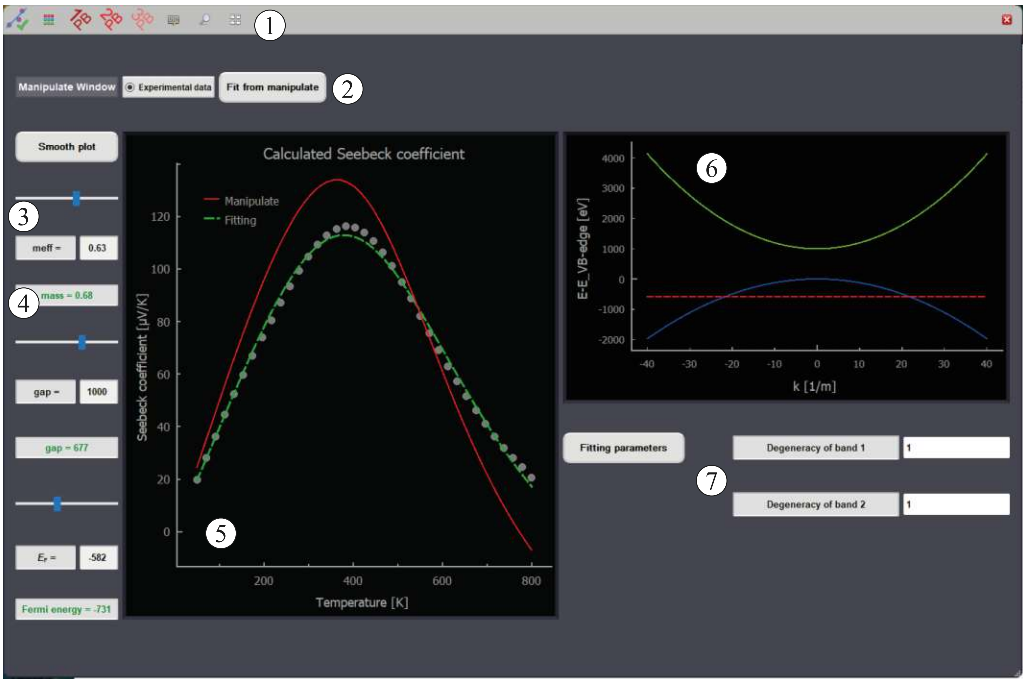

meff = 0.63
mass = 0.68
gap = 1000
gap = 677
E_F = -582
Fermi energy = -731
Degeneracy of band 1: 1
Degeneracy of band 2: 1

Figure 4.6: User interface of the fitting software, displaying the Seebeck-only mode without electrical resistivity and Hall coefficient, utilizing the two-parabolic-band model. The labeled areas include: (1) Toolbar for general settings and toggling between single-, two- and three-parabolic-band models; (2) button to initiate the fitting process; (3) manually adjustable effective mass ε_{21}, band gap E_g and Fermi energy E_F; (4) parameters derived from the fit; (5) graph depicting experimental data (gray), the Seebeck coefficient calculated from user-entered values (red) and the Seebeck coefficient obtained from the fit (green); (6) visualization of the band structure, illustrating the valence band (blue), the conduction band (green) and the Fermi energy (red); (7) manually adjustable degeneracies of both bands.

on top of the application's window provides buttons to switch between models with a different number of bands. Upon importing the Seebeck coefficient data, the interpolated data are displayed graphically, along with an initial estimation from the neural network. Users can modify fit parameters using sliders or by directly entering values into text fields, with predefined upper and lower boundaries for the parameters. Advanced settings allow users to customize these boundary values. Additionally, users can change the degeneracies of the bands, with the degeneracy ratio initially set to 1.

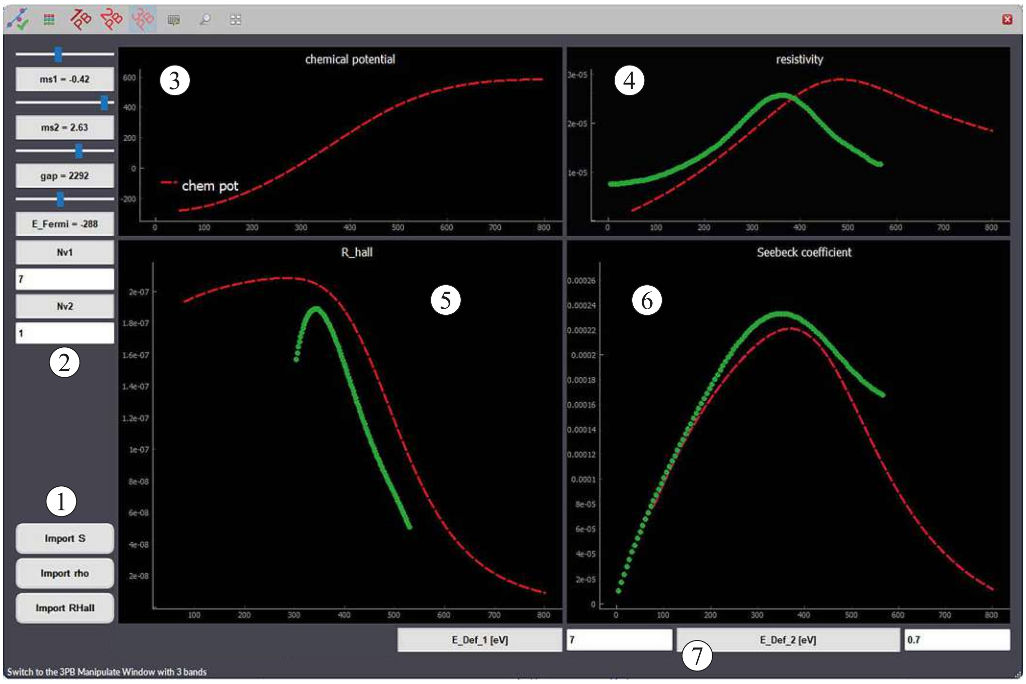

ms1 = -0.42

ms2 = 2.63

gap = 2292

E_Fermi = -288

Nv1: 7

Nv2: 1

E_Def_1 [eV]: 7

E_Def_2 [eV]: 0.7

Switch to the 3PB Manipulate Window with 3 bands

Figure 4.7: User interface of the fitting software, presenting the comprehensive fit of the Seebeck coefficient, electrical resistivity and Hall coefficient within the two-parabolic-band model. The figure excludes the fit results. the labeled areas include: (1) Buttons for importing measurement data of all three quantities; (2) manually adjustable masses of the valence and conduction band, $m_1^\star$ and $m_2^\star$, band gap E_g and Fermi energy E_F; (3) chemical potential, (4) electrical resistivity, (5) Hall coefficient and (6) Seebeck coefficient graph, illustrating the experimental data (green line) and values obtained from the set parameters; (7) manually adjustable values of the deformation potentials $\Xi_\mathsf{ph,1}$ and $\Xi_\mathsf{ph,2}$.

Once the estimation roughly aligns with the experimental data, users can execute the fit process by pressing the corresponding button. After a short processing time, dependent on the precision of the initial guess, the mode, the number of bands, and the user's computer hardware, the best fit is displayed in the graph as a green line. The obtained parameters are highlighted next to the graph, and the corresponding band structure is presented on the right-hand side. Ultimately, users can export the fit parameters along with the temperature-dependent Seebeck coefficient.

Another setting for fitting all three quantities is depicted in Figure 4.7. At the time this picture was captured, the fit was not integrated into the user interface, and hence, it is not shown. Similar to the Seebeck-only fit window illustrated in Figure 4.6, users can manually adjust the band parameters for an initial approximation of the experimental data. Since three quantities are concurrently considered, the number of parameters and the corresponding phase space are significantly larger. Depending on the material's complexity, this may require substantial *a priori* knowledge about the parameters.

5 Thermoelectric performance of multi-material systems

The properties of a single material are well defined (e.g. the resistivity is determined via the measured resistance and the geometry). However, when dealing with systems composed of multiple phases or materials, describing their properties becomes more complex. Microscopic quantities are typically defined for homogeneous materials, thus applying the mean value of the quantity across the entire volume can lead to a distorted understanding of performance, as this chapter will illustrate. Moreover, the contributions of individual constituents to the overall properties may be either overestimated or underestimated, potentially leading to errors. This issue is particularly critical in film-substrate systems, where the dimensions and thermoelectric properties of the substrate are occasionally overlooked.

In this chapter, common pitfalls in the field of thermoelectricity are discussed via two scenarios. First, the impact of the substrate on the measured performance of a film-substrate system is investigated [168]. It will be demonstrated that neglecting the substrate's contribution without justification can result in substantially overestimated results, provided the substrate meets certain criteria. Following this, the performance of a serial connection of two materials is calculated, with a particular emphasis on thermoelectric-metal composites [169]. When compared to the performance of the thermoelectric material on its own, the microscopic thermoelectric quantities exhibit extraordinary performances, although this increase is not reflected in the macroscopic quantities. The results are then extended to composites in general and it will be concluded that microscopic properties, like the power factor, are inadequate for describing the thermoelectric performance of such systems. In turn, error-resistant quantities and proper approaches to prevent misinterpretations are presented.

5.1 Thermoelectric performance of a parallel film-substrate system

Unlike bulk materials, the common preparation of films, i.e. the deposition on a mechanically much more stable substrate, does not allow to measure them independently but only together with the underlying substrate. This problem can yield substantial modifications in the measured properties due to the usually apparent mass and volume difference between film and substrate. The substrate can influence the measurement of various quantities of the film like mechanical properties [170, 171], magnetism [172], Seebeck coefficient [173, 174] as well as electrical and thermal conductivity. This has lead to the development of sophisticated measurement techniques, suitable to distinguish between the individual contributions, like nanoindentation to determine the elastic modulus and hardness of thin films [175] or the 3ω method for measuring the thermal conductivity [176]. Other properties, such as the Seebeck coefficient, can not be measured solely for the film and thus need to be interpreted with care to yield the film's properties. However, aside from deducting the contribution of the substrate, the simultaneous measurement of both properties can apparently yield enhanced performances. In recent years, several works reported an substantially improved thermoelectric performance of thin films due to an beneficial contribution of the substrate on the measured properties.

Yordanov *et al.* reported an significantly enhanced Seebeck coefficient in $Ca_3Co_4O_4$ thin films deposited on $SrTiO_3$ and $LaAlO_3$ substrates using pulsed laser deposition, compared to the bulklike values obtained on $[LaAlO_3]_{0.3}-[Sr_2AlTaO_6]_{0.7}$, $LaSrAlO_4$ and MgO substrates [174]. They attributed the enhancement of the total Seebeck coefficient S_t to contributions from the substrates and the interface layer using the well-known formula

$$S_\mathrm{t} = \frac{\sum_i S_i \sigma_i d_i}{\sum_i \sigma_i d_i} \,, \tag{5.1}$$

where σ_i is the electrical conductivity, d_i the thickness and i denotes the film, the interface layer, and the substrate, respectively. According to the authors, oxygen incorporations into the substrate above 723 K significantly decrease its resistivity, thus increasing the contribution to S_t. Under the assumption that the electric current only flows through the film, the electrical conductivity was calculated, revealing a power factor above $1.5\,\mathrm{mWm^{-1}K^{-2}}$ on $SrTiO_3$ at 993 K.

Shimizu *et al.* found an enhancement of the Seebeck coefficient from $3.8\,\mu\mathrm{VK}^{-1}$ to $-454\,\mu\mathrm{VK}^{-1}$ at 200 K in FeSe films on $\mathrm{SrTiO_3}$ by reducing the thickness to 1 nm [177]. The authors attributed the enhancement to a transition of the DOS from a three-dimensional to a two-dimensional behavior and ruled out any influence of the substrate due to the screening nature of the metallic film as well as the formation of a Schottky barrier between the layers. Together with a small resistivity, calculated using only the film's thickness, they achieved a record high power factor of $1300\,\mathrm{mWm^{-1}K^{-2}}$ at 50 K and $26\,\mathrm{mWm^{-1}K^{-2}}$ at room temperature.

Zhang *et al.* reported a power factor of $1.78\,\mathrm{mWm^{-1}K^{-2}}$ at 700 K in MoO_{2+x} on a Si substrate, being around 42 times larger than the values obtained from the same film on a quartz substrate [178]. This behavior was ascribed to an increased crystallinity on Si, as indicated by the XRD pattern, and a contribution of the substrate to the measured properties. Subsequently, a further increase of the power factor to $12.5\,\mathrm{mWm^{-1}K^{-2}}$ at 668 K was reported by reducing the thickness of the film from 700 nm to 130 nm [179].

Apart from film-substrate systems, Byeon *et al.* found extreme values of the figure of merit $zT \approx 471$ in $\mathrm{Cu_2Se}$, when a large vertical temperature gradient was applied, in addition to the horizontal one used to measure the thermovoltage [180, 181]. The vertical temperature difference inside the material ($\approx 40\,\mathrm{K}$), perpendicular to the measurement of the Seebeck coefficient,28 causes a structural phase transition at the hotter side. The authors concluded that both an extraordinary large Seebeck coefficient associated with the low-temperature phase, and the low electrical resistivity of the high-temperature phase, are measured simultaneously, leading to a very high power factor. A large value of $zT \approx 20$ was also found in $\mathrm{Ag_2S}$ by the same group under the same conditions and interpreted in a similar manner [182].

In contrast, Bergman *et al.* mathematically derived that the total power factor and figure of merit of a two-material composite are worse than those of the better material when property-changing interactions are neglected [183, 184]. Furthermore, Alvarez-Quintana obtained a reduction of the thermoelectric figure of merit for a parallel setup of a film-substrate system due to heat and current flow through the latter. The degree of reduction was found to be dependent on the ratio of the thickness of the substrate to the thickness of the film [185].

To elucidate the physics behind the seemingly beneficial contribution of the substrate reported multiple times, the thermoelectric behavior of multi-layer systems is investigated from a theoretical point of view, utilizing an equivalent electric-circuit model. It is important to note that the following derivations fully neglect effects such as diffusion, energy filtering, confinement, lattice distortion, epitaxial growth, charge transfer or others, which can additionally modify the layers' properties and may contribute to some of the cases reported above. The model presented below only considers the interplay of the single properties of each layer to the total performance.

5.1.1 Analysis of the thermoelectric properties

When a temperature gradient is applied parallel to the surface of a film, all layers, including the substrate, are effected as well. In order to allow for a proper evaluation of the measured performance, all individual quantities and potential contributions need to be considered accurately. Each layer in a multi-layer system comprises electrical and thermal resistances, and a voltage $U = -S\Delta T$ that is proportional to the material's Seebeck coefficient S. Here, an equal temperature difference is assumed for all layers. For the purpose of calculating the overall Seebeck coefficient and electrical and thermal conductivity, the parallel system can be modeled by an electric circuit with voltage sources and internal electrical resistances. A common scenario of this type is a film deposited on a substrate, as shown in Figure 5.1a. To focus on the contribution of the substrate, the model neglects a potential interface layer between film and substrate as well as effects altering the properties of either layer, most importantly diffusion, although they can be considered by modifying the individual quantities.

The interface connections in Figure 5.1a divide the circuit into smaller subcircuits. The subvoltages cause circular currents flowing through the surface and the nearest interface connection, as alternative paths have higher resistances. As a result, opposing interface currents from neighboring circuits cancel out each other, leading to the net current I_{circ} only flowing through the edge of the interface (see Appendix B for further details). To fully describe the system it is therefore sufficient to only connect the layers at both ends, as shown in Figure 5.1b.

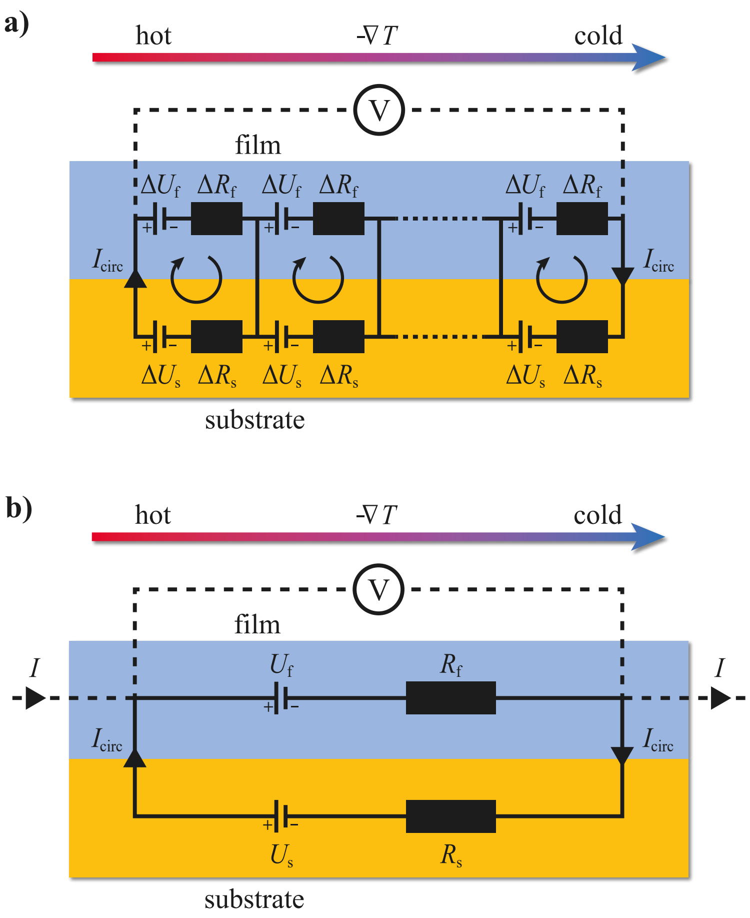

Figure 5.1: (a) Electric circuit modeling the film-substrate system without an interface layer. Each layer consists of a voltage source $U_i = \sum \Delta U_i$ and an electrical resistance $R_i = \sum \Delta R_i$, with $i = \{\mathrm{f}, \mathrm{s}\}$ denoting the film and the substrate, respectively. The voltage difference leads to circular currents I_{circ}, altering the measured Seebeck coefficient. (b) Simplified model without the inner connections between film and substrate. The resistance is measured by applying an external current I. Reproduced from Ref. [168].

Power factor

When measuring electrical resistance and thermovoltage, film and substrate form a parallel system. Without considering the chemical interaction at the interface, the total resistance R_t can thus be written as

$$R_\mathrm{t} = \frac{R_\mathrm{f} R_\mathrm{s}}{R_\mathrm{f} + R_\mathrm{s}} \ , \tag{5.2}$$

with R_f and R_s being the resistance of the film and the substrate, respectively. R_f is therefore calculated as

$$R_\mathrm{f} = (1 + \varepsilon_\sigma)\, R_\mathrm{t} \ , \quad \text{with} \quad \varepsilon_\sigma := \frac{R_\mathrm{t}}{R_\mathrm{s} - R_\mathrm{t}} = \frac{R_\mathrm{f}}{R_\mathrm{s}} \ , \tag{5.3}$$

in which ε_σ is the ratio of the resistance of the film to the resistance of the substrate and determines the influence of the substrate on the total Seebeck coefficient and electrical conductivity of the system, as shown below.

Unlike the resistance, the thermovoltage is measured in open-circuit conditions. In order to understand the effect of the combined layers on the Seebeck coefficient, a modification of the entire thermovoltage due to the short-circuiting of the two materials needs to be taken into consideration. The circular current arising in the film-substrate system when a temperature gradient is present along the surface changes the measured thermovoltage due to the potential drop at the resistor. Applying Kirchhoff's law, the value of the current is obtained:

$$I_\mathrm{circ} = \frac{U_\mathrm{s} - U_\mathrm{f}}{R_\mathrm{f} + R_\mathrm{s}} \ . \tag{5.4}$$

Thus, the measured voltage U_t and Seebeck coefficient S_t can be calculated as

$$\begin{aligned} U_\mathrm{t} &= U_\mathrm{f} + I_\mathrm{circ} R_\mathrm{f} \\ &= \frac{U_\mathrm{f} R_\mathrm{s} + U_\mathrm{s} R_\mathrm{f}}{R_\mathrm{s} + R_\mathrm{f}} \end{aligned} \tag{5.5}$$

and

$$S_\mathrm{t} = \frac{S_\mathrm{f} R_\mathrm{s} + S_\mathrm{s} R_\mathrm{f}}{R_\mathrm{s} + R_\mathrm{f}} \ , \tag{5.6}$$

where U_f, U_s and S_f, S_s are the voltage and the Seebeck coefficient of the film and the substrate, respectively. As film and substrate usually have the same surface dimensions, Equation 5.6 can be rewritten in accordance to Equation 5.1 as

$$S_\mathrm{t} = \frac{S_\mathrm{f} \sigma_\mathrm{f} d_\mathrm{f} + S_\mathrm{s} \sigma_\mathrm{s} d_\mathrm{s}}{\sigma_\mathrm{f} d_\mathrm{f} + \sigma_\mathrm{s} d_\mathrm{s}} \ , \tag{5.7}$$

with the electrical conductivity σ_f, σ_s and the thickness d_f, d_s of the film and the substrate, respectively. For a multi-layer system (e.g. a film-substrate system containing interface layers) the setup can be modified by adding additional parallel voltage sources with internal resistances. This yields the more general expression for the total Seebeck coefficient of a system with i layers,

$$S_\mathrm{t} = \frac{\sum_i S_i G_i}{\sum_i G_i} , \tag{5.8}$$

with i denoting the different layers and $G_i = 1/R_i$ being the electrical conductance. For equal surface dimensions of every layer, a common scenario in film fabrication, the equation above simplifies to Equation 5.1. This formula is frequently used to calculate the influence of the substrate and/or interface layer on the total Seebeck coefficient.

Inserting Equation 5.3 into Equation 5.6 gives the total Seebeck coefficient of a two-layer system in dependence of the weighting parameter ε_σ:

$$S_\mathrm{t}\left(\varepsilon_\sigma\right) = \frac{S_\mathrm{f} + \varepsilon_\sigma S_\mathrm{s}}{1 + \varepsilon_\sigma} . \tag{5.9}$$

Considering this formula, the contribution of the substrate only depends on the parameter ε_σ and the total Seebeck coefficient has the according limits

$$S_\mathrm{t} = \begin{cases} S_\mathrm{f} & \text{for} \quad \varepsilon_\sigma = 0 \\ S_\mathrm{s} & \text{for} \quad \varepsilon_\sigma \to \infty \end{cases} . \tag{5.10}$$

For $\varepsilon_\sigma = 0$, the resistance of the substrate is diverging, thus the Seebeck coefficient of the film is measured. This is the case of an entirely insulating substrate like glass. On the other hand, for an insulating film or metallic substrate ($\varepsilon_\sigma \to \infty$), the Seebeck coefficient of the substrate is measured. For all other values of ε_σ, the total Seebeck coefficient lies between those of the individual layers due to the arising current, which aligns the single Seebeck coefficients. When $S_\mathrm{s} > S_\mathrm{f}$, however, S_t can be larger than S_f, which can lead to misinterpretations when no careful analysis of the absolute value of ε_σ is performed beforehand. In the usual case of equal surface dimensions of film and substrate, ε_σ can be rewritten as

$$\varepsilon_\sigma = \frac{\sigma_\mathrm{s} d_\mathrm{s}}{\sigma_\mathrm{f} d_\mathrm{f}} , \tag{5.11}$$

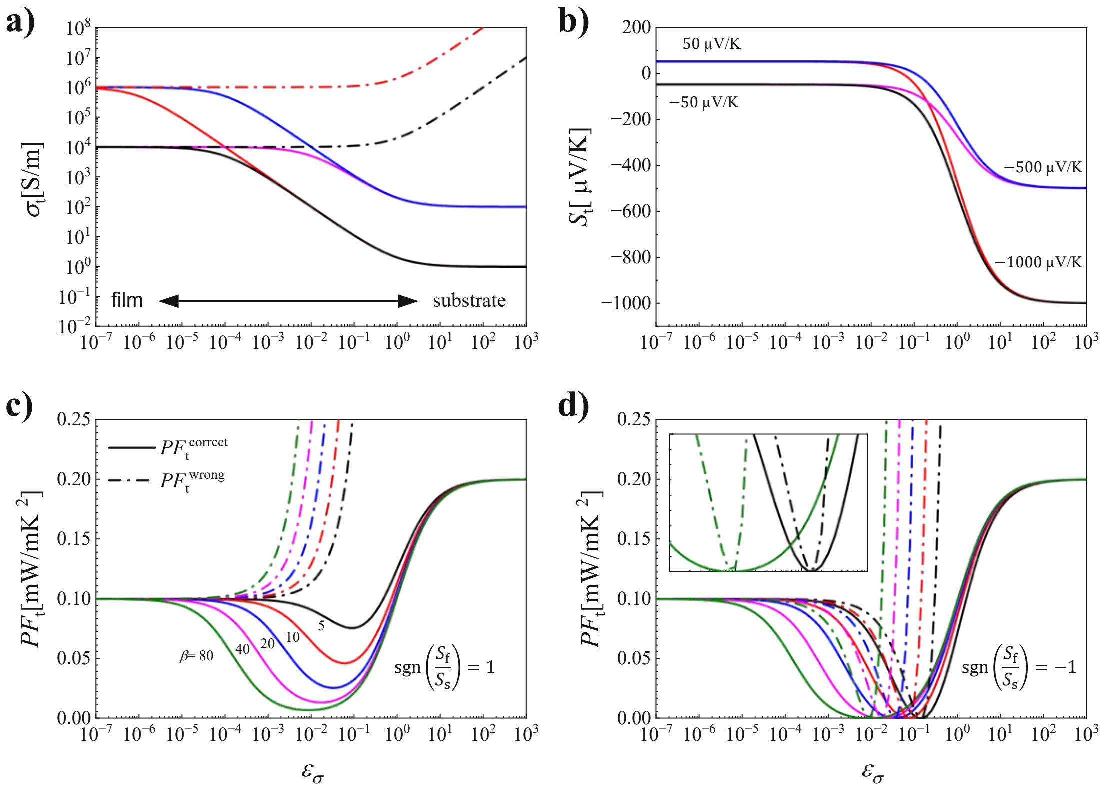

Figure 5.2: Calculated total a) Seebeck coefficient S_t, b) electrical conductivity σ_t and c, d) power factor PF_t of a film-substrate system for different values of the individual Seebeck coefficient and electrical conductivity, using the equations derived in the text. The dash-dotted lines show the wrong conductivity and the power factor obtained by using the thickness of the film to calculate the conductivity from the measured resistance. The power factor is shown for different values of $\beta = \sqrt{\sigma_f/\sigma_s}$ and equal (c) as well as opposite (d) signs of the Seebeck coefficients. The values approach those of the film and the substrate for $\varepsilon_\sigma = 0$ and $\varepsilon_\sigma \to \infty$, respectively. The inset in d) shows PF in the vicinity of the zero for $\beta = 5$ (black line) and 80 (green line). Reproduced from Ref. [168].

and only depends on the individual electrical conductivities and thicknesses.

Figure 5.2a shows S_t as a function of ε_σ for different combinations of the Seebeck coefficient of the film, $S_f = \{-50\,\mu\text{VK}^{-1}, +50\,\mu\text{VK}^{-1}\}$, and the substrate, $S_s = \{-500\,\mu\text{VK}^{-1}, -1000\,\mu\text{VK}^{-1}\}$. Here, the values and signs are arbitrarily chosen but mirror the fact that the substrate is usually a semiconductor or insulator with large Seebeck coefficient. The influence of the substrate would further be similar for positive Seebeck coefficients. Notably, S_t shows the strongest ε_σ dependency around $\varepsilon_\sigma = 1$, when the resistances of film and substrate become comparable.

Since the thermoelectric properties depend on the film as well as the substrate, both need to be considered when calculating the overall power factor $PF_\mathrm{t} = S_\mathrm{t}^2 \sigma_\mathrm{t}$ of the system. In order to be able to compare the power factor of film-substrate systems with bulk materials, the total thickness ($d_\mathrm{t} = d_\mathrm{f} + d_\mathrm{s}$) must be used to calculate the total electrical conductivity, as long as no better assumption about the penetration depth of the current into the substrate can be made. This means that the total electrical conductivity (see Figure 5.2b) is given from Equation 5.3 as

$$\begin{aligned} \sigma_\mathrm{t}\left(\varepsilon_\sigma\right) &= \left(1+\varepsilon_\sigma\right)\sigma_\mathrm{f}\frac{d_\mathrm{f}}{d_\mathrm{t}} \\ &= \frac{\left(1+\varepsilon_\sigma\right)\sigma_\mathrm{s}\sigma_\mathrm{f}}{\sigma_\mathrm{s}+\varepsilon_\sigma\sigma_\mathrm{f}} \end{aligned} \tag{5.12}$$

with the limits

$$\sigma_\mathrm{t} = \begin{cases} \sigma_\mathrm{f} & \text{for} \quad \varepsilon_\sigma = 0 \\ \sigma_\mathrm{s} & \text{for} \quad \varepsilon_\sigma \to \infty \end{cases} . \tag{5.13}$$

Similar to the the total Seebeck coefficient, the electrical conductivity of the film and substrate is measured for $\varepsilon_\sigma = 0$ and $\varepsilon_\sigma \to \infty$, respectively. On the other hand, if only the thickness of the film is used for calculating the electrical conductivity from the measured resistance ($d_\mathrm{t} = d_\mathrm{f}$), as is usually done, one obtains

$$\sigma_\mathrm{t}^\mathrm{wrong}\left(\varepsilon_\sigma\right) = \sigma_\mathrm{f}\left(1+\varepsilon_\sigma\right) . \tag{5.14}$$

It can be seen that for Equation 5.14, the total conductivity diverges ($\sigma_\mathrm{t} \to \infty$) if the thickness of the film approaches 0 ($\varepsilon_\sigma \to \infty$). Thus, Equation 5.14 is only a good approximation for small values of ε_σ, when either the film is sufficiently thick or the resistivity of the substrate is appropriately large compared to the resistivity of the film, meaning that the substrate is absolutely insignificant for electrical transport. The reason for the divergence of conductivity as the thickness of the film approaches zero is relatively straightforward. The calculated conductivity of a single material, obtained from the measured conductance, remains constant regardless of its dimensions. However, in the case of a two-layer setup, where both layers make a significant contribution to conduction, the measured conductance does not decrease at the same rate as the thickness of one of the layers. As a result, as one layer becomes thinner, the error in the calculation becomes larger, ultimately leading to seemingly infinite conductivity when the thickness of the film becomes zero, since the conductance is still finite as current is passing through the other layer.

Using Equation 5.9 and Equation 5.12, a more robust and general expression for the power factor of film-substrate systems can be derived (see Figure 5.2c):

$$PF_\mathrm{t}\left(\varepsilon_\sigma\right) = \frac{S_\mathrm{f}^2 + 2\varepsilon_\sigma S_\mathrm{f} S_\mathrm{s} + \varepsilon_\sigma^2 S_\mathrm{s}^2}{\left(\sigma_\mathrm{s} + \varepsilon_\sigma \sigma_\mathrm{f}\right)\left(1+\varepsilon_\sigma\right)} \sigma_\mathrm{s}\sigma_\mathrm{f} \, , \tag{5.15}$$

with the limits

$$PF_\mathrm{t} = \begin{cases} S_\mathrm{f}^2 \sigma_\mathrm{f} = PF_\mathrm{f} & \text{for} \quad \varepsilon_\sigma = 0 \\ S_\mathrm{s}^2 \sigma_\mathrm{s} = PF_\mathrm{s} & \text{for} \quad \varepsilon_\sigma \to \infty \end{cases} . \tag{5.16}$$

PF_f and PF_s are the power factors of the film and the substrate, respectively. Equation 5.15 can also be rewritten in terms of the individual power factors:

$$PF_\mathrm{t}\left(\varepsilon_\sigma\right) = \frac{\left(\sqrt{PF_\mathrm{f}} + \varepsilon_\sigma \beta \, \mathrm{sgn}\left(\frac{S_\mathrm{f}}{S_\mathrm{s}}\right) \sqrt{PF_\mathrm{s}}\right)^2}{\left(1+\varepsilon_\sigma \beta^2\right)\left(1+\varepsilon_\sigma\right)} \, , \tag{5.17}$$

with $\beta = \sqrt{\sigma_\mathrm{f}/\sigma_\mathrm{s}}$ being a material-dependent parameter. Notably, for $0 < \varepsilon_\sigma < \infty$ the total power factor is *always smaller* than the larger power factor of the two single materials (see Figure 5.2c and Figure 5.2d). This shows that combining the Seebeck coefficient and electrical conductivity of the film and the substrate can never improve the total thermoelectric performance, but only deteriorate it. The sign function accounts for the possibility of Seebeck coefficients of different signs of the film and the substrate. In this case, the total power factor becomes zero at a certain ε_σ when the individual thermovoltages cancel each other out. Qualitatively, the signs of the single Seebeck coefficients does not change the overall behavior.

On the other hand, wrongly neglecting the current passing through the substrate and hence using Equation 5.14 leads to a total power factor of

$$PF_\mathrm{t}^\mathrm{wrong}\left(\varepsilon_\sigma\right) = \frac{\left(\sqrt{PF_\mathrm{f}} + \varepsilon_\sigma \beta \, \mathrm{sgn}\left(\frac{S_\mathrm{f}}{S_\mathrm{s}}\right) \sqrt{PF_\mathrm{s}}\right)^2}{1+\varepsilon_\sigma} \, , \tag{5.18}$$

which *always* will result in power factors *larger* than that of the film alone for $0 < \varepsilon_\sigma < \infty$ in case of equal signs of the Seebeck coefficients. For opposing signs, the total power factor is still *always* overestimated but can adopt values below S_f (see Figure 5.2d and the inset therein).

It is worth point out that this model, as it currently stands, is only quantitatively applicable to thick films. For thinner films, though the influence of the substrate increases even further, the impact of interface layers can modify the overall behavior significantly. Thus, the derived equations can not be used to accurately calculate the total performance without taking this into consideration by either using Equation 5.8 instead of Equation 5.9 or adjusting the values of the individual properties.

Figure of merit

The thermal conductivity can be measured without a distorting influence of the substrate using e.g. the 3ω method [176] or picosecond laser flash or thermoreflectance method [186, 187]. In addition to that, the influence of the substrate on the total thermal conductance is usually handled more cautiously due to the high thermal conductivity of many commonly used substrates like Si, MgO or $SrTiO_3$. Consequently, the thermal conductivity is less prone to misinterpretations.

Because of the similarity between thermal and electrical conduction, the derivation steps of the total thermal conductivity are similar to the electrical conductivity. Based on Equation 5.12, the thermal conductivity of the simple system of non-interacting film and substrate is

$$\lambda_\mathrm{t}\left(\varepsilon_\lambda\right) = \frac{\left(1+\varepsilon_\lambda\right)\lambda_\mathrm{s}\lambda_\mathrm{f}}{\lambda_\mathrm{s}+\varepsilon_\lambda\lambda_\mathrm{f}}\ , \tag{5.19}$$

with λ_f and λ_s being the thermal conductivity of the film and the substrate, respectively, and

$$\varepsilon_\lambda = \frac{\lambda_\mathrm{s}d_\mathrm{s}}{\lambda_\mathrm{f}d_\mathrm{f}} \tag{5.20}$$

denoting the contribution of the substrate to the thermal conduction. Once more, the total thermal conductivity has the limits

$$\lambda_\mathrm{t} = \begin{cases} \lambda_\mathrm{f} & \text{for} \quad \varepsilon_\lambda = 0 \\ \lambda_\mathrm{s} & \text{for} \quad \varepsilon_\lambda \to \infty \end{cases} \tag{5.21}$$

and lies between the individual thermal conductivities for all other values.

Combining Equation 5.15 and Equation 5.19, the total figure of merit zT_t of the film-substrate system can be written as

$$zT_\mathrm{t} = \frac{PF_\mathrm{t}}{\lambda_\mathrm{t}} T = \frac{\left(\sqrt{zT_\mathrm{f}} + \sqrt{\varepsilon_\sigma \varepsilon_\lambda}\,\mathrm{sgn}\left(\frac{S_\mathrm{f}}{S_\mathrm{s}}\right)\sqrt{zT_\mathrm{s}}\right)^2}{\left(1+\varepsilon_\sigma\right)\left(1+\varepsilon_\lambda\right)} \,, \tag{5.22}$$

with the value of the film zT_f and the substrate zT_s. The total figure of merit can only have values between that of the film and the substrate, but never exceed the performance of the better layer. If, on the other hand, zT_t is calculated from the thermal conductivity of the film λ_f and the wrong power factor from Equation 5.18, a wrong value is obtained:

$$zT_\mathrm{t}^\mathrm{wrong} = \frac{PF_\mathrm{t}^\mathrm{wrong}}{\lambda_\mathrm{f}} T = \frac{\left(\sqrt{zT_\mathrm{f}} + \sqrt{\varepsilon_\sigma \varepsilon_\lambda}\,\mathrm{sgn}\left(\frac{S_\mathrm{f}}{S_\mathrm{s}}\right)\sqrt{zT_\mathrm{s}}\right)^2}{\left(1+\varepsilon_\sigma\right)\left(1+\varepsilon_\lambda\right)} \,. \tag{5.23}$$

Again, for same signs of the single Seebeck coefficients, the figure of merit always exceeds that of the film.

The results clearly show that despite an increased Seebeck coefficient or electrical conductivity due to the contribution of the substrate may look beneficial, the thermoelectric performance can never be enhanced solely by the combination of the individual properties. This of course is only apparent if the influence of the substrate is considered when calculating the electrical conductivity. Otherwise, the power factor and figure of merit can attain wrong values beyond that of the film.

While these results were derived for a film-substrate system, they are valid for any two-layer and multi-layer system in general, since no specific assumption about the layers were made. This means that a set of parallel layers will always have worse thermoelectric properties than the best-performing layer. However, it has to be emphasized that this does not exclude the possibility of an enhancement of the thermoelectric film performance with respect to the bulk material, e.g. through a substrate-induced change of the crystal structure [49].

5.1.2 Comparison with experimental data

To validate the formulas derived above, the Seebeck coefficient in Equation 5.9 is compared with experimental data from literature, where an influence of a conductive substrate on the overall properties is reported. Figure 5.3a shows the Seebeck

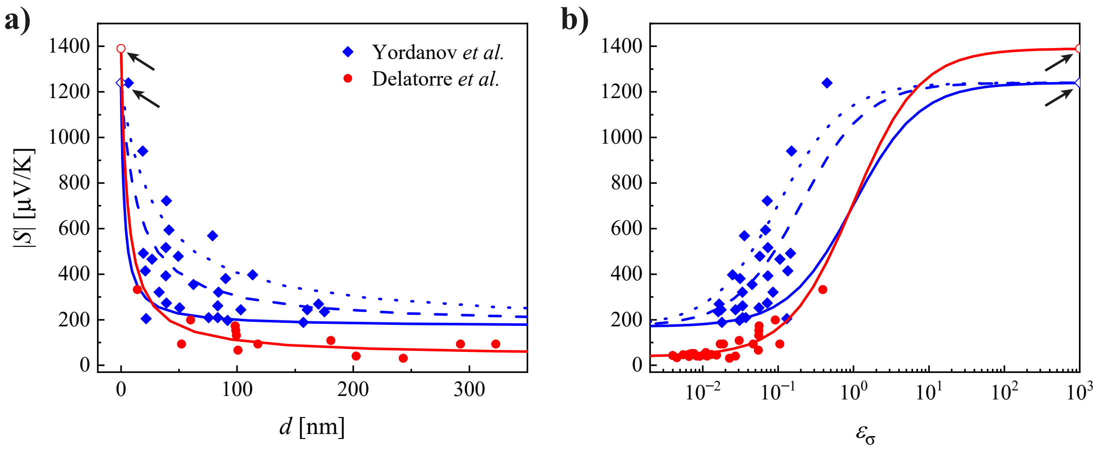

Figure 5.3: Seebeck coefficient of $Cu_{0.38}Ni_{0.62}$ films on Si [173] (red symbols) and $Ca_3Co_4O_9$ films on $SrTiO_3$ [174] (blue symbols) in dependence of the thickness of the film (a) and the value of ε_σ (b). The solid lines show the total Seebeck coefficient calculated from Equation 5.9, whereas the dashed and dotted lines are based on the assumption that $R_\mathrm{f}/R_\mathrm{s}$ is 5 times and 10 times larger, respectively. The Seebeck coefficient of the pristine substrates is shown by unfilled symbols and indicated by arrows. The values of the individual Seebeck coefficients, resistivities and thicknesses were taken from the respective literature. Reproduced from Ref. [168].

coefficient as a function of the film thickness of a $Ca_3Co_4O_9$ film on a $SrTiO_3$ substrate [174] and a metallic $Cu_{0.38}Ni_{0.62}$ film on a Si substrate [173]. The steadily increasing effect of the substrate with decreasing film thickness is clearly visible for films below 100 nm. Furthermore, plotting the data versus ε_σ, similarly to Figure 5.2b, reveals remarkable agreement of the measured data with the trend predicted by the model presented here, as shown in Figure 5.3b. The solid lines show the calculated Seebeck coefficient versus ε_σ using Equation 5.9 without any free parameters. While the experimental data of the Cu-Ni films on Si follow the model curve extremely well, the absolute Seebeck coefficient of the $Ca_3Co_4O_9$ films on $SrTiO_3$ are larger than predicted. This is most likely ascribed to two main issues, as indicated by the authors of Ref. [174] themselves: (i) the presence of a potential interface layer, which could be considered using Equation 5.8; and (ii) the very volatile incorporation of oxygen into $SrTiO_3$, having a drastic influence on the resistances. In fact, a correction of the ratio of the resistances, $R_\mathrm{f}/R_\mathrm{s}$, by a factor

		$S_\mathrm{s}/S_\mathrm{f}$		
		2	10	100
δ_S	0.1	$1.1 \cdot 10^{-1}$	$1.1 \cdot 10^{-2}$	$1.0 \cdot 10^{-3}$
	0.05	$5.3 \cdot 10^{-2}$	$5.6 \cdot 10^{-3}$	$5.1 \cdot 10^{-4}$
	0.01	$1.0 \cdot 10^{-2}$	$1.1 \cdot 10^{-3}$	$1.0 \cdot 10^{-4}$

Table 5.1: Approximated threshold values of ε_σ in dependence of the desired upper limit of the relative error $\delta_S = (S_\mathrm{t} - S_\mathrm{f})/S_\mathrm{f}$ for various ratios of the individual Seebeck coefficients of substrate and film.

5 to 10 leads to a significant improvement of the agreement between the second set of experimental data and the model prediction.

5.1.3 Criterion for the contribution of the substrate

After clarifying that the substrate can have a detrimental effect on the overall power factor and figure of merit compared to the properties of the film, the size of the measurement error when determining the thermoelectric properties of such systems is investigated. Since the thermal conductivity of the film can be measured separately and without contributions of the substrate, a potential error of the thermal conductivity is not considered here.

The deviation of the measured Seebeck coefficient from that of the film depends on both the ratio of the Seebeck coefficients of the film and the substrate and the value of ε_σ. While the former is related to the film and the substrate and can therefore only by controlled via the choice of the substrate, the latter can also be altered by varying the thickness of the film.

Using Equation 5.9, the relative error δ_S of the measured Seebeck coefficient S_t with respect to the one of the film S_f can be written as

$$\delta_S = \frac{S_\mathrm{t} - S_\mathrm{f}}{S_\mathrm{f}} = \frac{\varepsilon_\sigma}{1 + \varepsilon_\sigma} \left(\frac{S_\mathrm{s}}{S_\mathrm{f}} - 1 \right) . \tag{5.24}$$

Table 5.1 shows the threshold values of ε_σ if the relative error of the Seebeck coefficient should not exceed δ_S.

From the total Seebeck coefficient in Equation 5.9, it might look appealing to calculate the Seebeck coefficient of the film using the measured Seebeck coefficient, the substrate's Seebeck coefficient and ε_σ. This formula is in fact occasionally used to estimate the contribution of the substrate [49]. However, since the exact Seebeck coefficient of the substrate is sometimes not known, it is more precise to assure a neglectable contribution by choosing an ε_σ value based on Equation 5.24 and Table 5.1.

Regarding the electrical conductivity, the value calculated from the film's thickness will be higher than the conductivity of the film in case of a contributing substrate. This problem can be circumvented by using Equation 5.12, which accounts for the total thickness. It is, however, appropriate to use Equation 5.14 if the error

$$\delta_\sigma = \frac{\sigma_\mathrm{t}^\mathrm{wrong} - \sigma_\mathrm{f}}{\sigma_\mathrm{f}} = \varepsilon_\sigma \; . \tag{5.25}$$

is considered.

A visualization of the errors in Equation 5.24 and Equation 5.25 is presented in Figure 5.4 for different ratios $S_\mathrm{s}/S_\mathrm{f}$. For $S_\mathrm{s}/S_\mathrm{f} > 2$, a requirement usually fulfilled in systems with semiconducting or insulating substrates, the error of the Seebeck coefficient exceeds that of the conductivity in the region of interest. Thus, when evaluating the threshold of ε_σ, the use of Equation 5.24 or Table 5.1 is often sufficient.

Apart from determining the value of ε_σ, the process can be abbreviated by depositing the film on a well-known insulating material such as glass [178, 188–194], MgO [174, 195–200], ZrO_2 [201–203] or plastic [204–211], which is indeed very common to circumvent issues of a contributing substrate. On the other hand, reported results on semiconducting substrates should be interpreted with additional caution as their influence cannot be ruled out completely despite having a seemingly high resistivity [174, 178, 179, 190, 212–220].

To conclude, it is mandatory to clarify the potential contribution of various substrates on the total performance before choosing an appropriate material for thermoelectric thin-film deposition. This is arguably best done by following three crucial steps:

1. Roughly estimating the electrical conductivity and Seebeck coefficient of both the film and the substrate.

2. Calculating the threshold value of ε_σ based on the desired limit of the error $\delta_{S,\sigma}$ from Equation 5.24 and Equation 5.25.

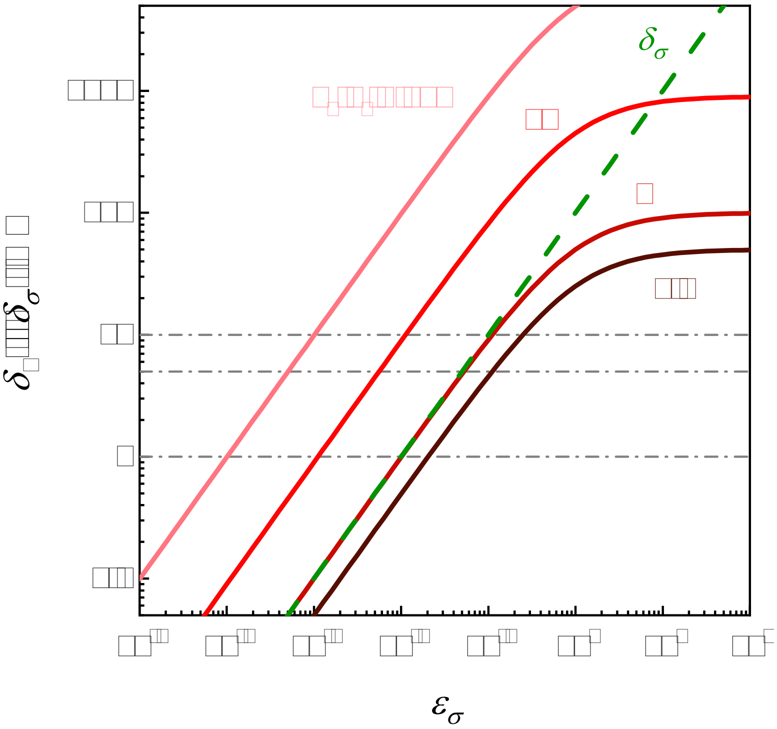

Figure 5.4: Relative error of the Seebeck coefficient for various ratios of the individual Seebeck coefficients of substrate S_s and film S_f (red solid lines) and relative error of the electrical conductivity (green dashed line) in dependence of the weighting parameter ε_σ. The gray dash-dotted lines mark relative errors of $1\,\%$, $5\,\%$ and $10\,\%$. Reproduced from Ref. [168].

3. Choosing the thickness of the film (and the substrate if possible) according to Equation 5.11 or selecting a different substrate with lower electrical conductivity and/or Seebeck coefficient.

Aside from the influence on the electrical conductivity and Seebeck coefficient, the plausibility of a low thermal conductivity of the film in the presence of a highly heat-conducting substrate needs to be questioned, as the overall figure of merit of the system is deteriorated. Furthermore, when comparing the performance of a film-substrate system to the respective bulk material, it is important to consider the total thickness of the system, including any non-contributing substrates. This will ensure an accurate calculation of the total power factor and figure of merit, taking into account the additional space acquired by the substrate.

5.2 Thermoelectric performance of a serial connection of two materials

Composites represent an interesting idea to enhance the thermoelectric properties via the incorporation of an additional material or phase into the main matrix. For composites comprising different materials or structures, effects like a reduction of the lattice thermal conductivity from increased phonon scattering at defects on various length scales [221–223] and an increase of the Seebeck coefficient due to energy filtering at boundaries [222, 224–226] can significantly increase the thermoelectric performance.

In the 1990s, Bergman *et al.* claimed in two studies that a „high-performance thermoelectric“ and a „benign metal“, *i.e.* a metal with high electrical and thermal conductivity, combined in a favorable spatial configuration, can drastically boost the power factor $PF = S^2\sigma$ [184] but not the figure of merit zT [183]. In absence of intrinsic property changes, such as interface effects, this would restrict the potential of composites to a high PF. Numerous studies have supported the occurrence of a largely enhanced power factor either theoretically or experimentally [227–235]. On the other hand, a debate about the merit of a boosted power factor due to incorporation of a simple metal is still missing.

In this section, a fundamental question will be discussed: How and to what extent do the thermoelectric properties of the individual constituents contribute towards the overall properties of a composite? To answer this, the relevant physical processes in composites and the origin of the seemingly enhanced power factor in such systems will be elucidated from a simple model of two serially connected materials. The results will qualitatively accord with the results of Bergman *et al.* and highlight the vacuity of microscopic quantities such as the power factor. Notably, the model largely disregards influences of interfaces on electrical and thermal transport, which are usually present in composites and modify the measured properties.

5.2.1 Analysis of the thermoelectric properties

Bergman and Fel calculated the overall power factor of two-material composites for different spatial configurations [184]. They reported that the power factor can be improved through either alternating serial slabs or a spherical structure where

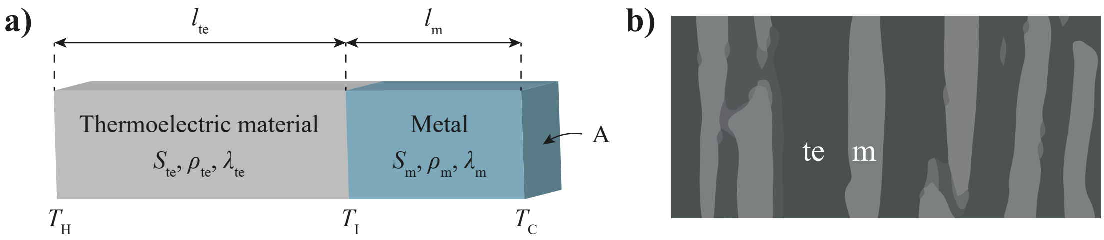

Figure 5.5: a) Schematic sketch of a serial connection of a thermoelectric material with length l_{te} and a metal with length l_m. Both materials have individual Seebeck coefficients S, electrical resistivities ρ and thermal conductivities λ. The hot temperature at the end of the thermoelectric material, the temperature at the interface and the cold temperature at the end of the metal are denoted as T_H, T_I and T_C, respectively. b) Sketch of the microstructure for a fictious thermoelectric composite material with a serial slab configuration. Reproduced from Ref. [169].

the metal is coated by the thermoelectric material. The latter scenario is often a good approximation to more realistic structures, as stated by the authors. Here, the focus is put on calculating the slab configuration since it is easier to model and provides a better understanding about the origin of the apparent performance changes. Nonetheless, the qualitative similarity between the two configurations [184] allows to generalize the conclusions to all composites.

Figure 5.5a shows the model with the respective quantities of the thermoelectric and the metal used to calculate the overall properties. It is similar to the model of Bergman and Fel, but with only one interface instead of alternating slabs. When ignoring interface effects, as done in both studies, these two models are equivalent. Figure 5.5b provides a realistic example for the application of the model in a two-phase composite material.

Power factor

First, the ideal scenario of a composite comprising a thermoelectric material (te) and an ideal metal (m), i.e. $\rho_m \to 0$, therefore $\lambda_m \to \infty$ due to the Wiedemann-Franz law, is calculated. In the following, the total thermoelectric properties of the composite are written without index. From $\lambda_m \to \infty$ of the metal follows that the temperature drop at the interface $T_I = T_C$ and the whole temperature drop occurs in the thermoelectric material, yielding the thermovoltage

$$U = S_{\mathrm{te}}\left(T_{\mathrm{H}} - T_{\mathrm{C}}\right) = S_{\mathrm{te}}\Delta T \ . \tag{5.26}$$

The total Seebeck coefficient S is calculated as $S = U/\Delta T$, thus

$$S = S_{\mathrm{te}} \ . \tag{5.27}$$

The total resistance is only composed of ρ_{te} due to $\rho_{\mathrm{m}} = 0$ in the ideal metal, which gives

$$\rho = R_{\mathrm{te}}\frac{A}{l_{\mathrm{te}} + l_{\mathrm{m}}} = \rho_{\mathrm{te}}\frac{l_{\mathrm{te}}}{l_{\mathrm{te}} + l_{\mathrm{m}}} = \rho_{\mathrm{te}}\delta_{\mathrm{te}} \ , \tag{5.28}$$

with the volume fraction of the thermoelectric material δ_{te}. While the Seebeck coefficient is not affected by the metal, the resistivity - obtained by averaging the total resistance over the volume of the entire composite - seemingly decreases due to $\delta_{\mathrm{te}} < 1$, resulting in an increase of the total power factor:

$$PF = \frac{S^2}{\rho} = \frac{S_{\mathrm{te}}^2}{\rho_{\mathrm{te}}\delta_{\mathrm{te}}} = PF_{\mathrm{te}}\frac{1}{\delta_{\mathrm{te}}} \ . \tag{5.29}$$

A real metal with finite resistivities and Seebeck coefficient ($S_{\mathrm{m}} \ll S_{\mathrm{te}}$) partially contributes to the thermoelectric transport and modifies the overall properties. The temperature drops in the thermoelectric and the metal, $\Delta_{\mathrm{te}} = T_{\mathrm{H}} - T_{\mathrm{I}}$ and $\Delta_{\mathrm{m}} = T_{\mathrm{I}} - T_{\mathrm{C}}$, can be calculated from the thermal conductance $C_i = \lambda_{\mathrm{i}}A/l_i$ of both materials:

$$\Delta T_{\mathrm{te}} = \frac{C_{\mathrm{m}}}{C_{\mathrm{te}} + C_{\mathrm{m}}}\Delta T = \frac{l_{\mathrm{te}}\lambda_{\mathrm{m}}}{l_{\mathrm{m}}\lambda_{\mathrm{te}} + l_{\mathrm{te}}\lambda_{\mathrm{m}}}\Delta T \ , \tag{5.30}$$

$$\Delta T_{\mathrm{m}} = \frac{C_{\mathrm{te}}}{C_{\mathrm{te}} + C_{\mathrm{m}}}\Delta T = \frac{l_{\mathrm{m}}\lambda_{\mathrm{te}}}{l_{\mathrm{m}}\lambda_{\mathrm{te}} + l_{\mathrm{te}}\lambda_{\mathrm{m}}}\Delta T \ . \tag{5.31}$$

Unlike the previous case, the measured thermovoltage now has contributions from both the thermoelectric and the metal and is

$$U = S_{\mathrm{m}}\Delta T_{\mathrm{m}} + S_{\mathrm{te}}\Delta T_{\mathrm{te}} \tag{5.32}$$

$$= \frac{S_{\mathrm{m}}l_{\mathrm{m}}\lambda_{\mathrm{te}} + S_{\mathrm{te}}l_{\mathrm{te}}\lambda_{\mathrm{m}}}{l_{\mathrm{m}}\lambda_{\mathrm{te}} + l_{\mathrm{te}}\lambda_{\mathrm{m}}}\Delta T. \tag{5.33}$$

This leads to

$$S = \frac{S_\mathrm{m} l_\mathrm{m} \lambda_\mathrm{te} + S_\mathrm{te} l_\mathrm{te} \lambda_\mathrm{m}}{l_\mathrm{m} \lambda_\mathrm{te} + l_\mathrm{te} \lambda_\mathrm{m}} \, . \tag{5.34}$$

The total Seebeck coefficient can be written using a material-related quantity ε_λ, following the notation of section 5.1 about the thermoelectric properties of a film-substrate [168]:

$$S = \frac{S_\mathrm{te} + \varepsilon_\lambda S_\mathrm{m}}{1 + \varepsilon_\lambda} \qquad \text{with} \qquad \varepsilon_\lambda = \frac{C_\mathrm{te}}{C_\mathrm{m}} = \frac{l_\mathrm{m} \lambda_\mathrm{te}}{l_\mathrm{te} \lambda_\mathrm{m}} \, . \tag{5.35}$$

Depending on the ratio between the individual thermal conductances, the total Seebeck coefficient lies between those of the thermoelectric material and the metal.

The finite resistivity further leads to a contribution of the metal to the total electrical resistance

$$R = R_\mathrm{te} + R_\mathrm{m} = \rho_\mathrm{te} \frac{l_\mathrm{te}}{A} + \rho_\mathrm{m} \frac{l_\mathrm{m}}{A} \, , \tag{5.36}$$

and thus the electrical resistivity becomes

$$\rho = R \frac{A}{l} = \rho_\mathrm{te} \left(\delta_\mathrm{te} + \frac{\rho_\mathrm{m}}{\rho_\mathrm{te}} \left(1 - \delta_\mathrm{te} \right) \right) \, , \tag{5.37}$$

which is a linear function depending on the volume fraction of the thermoelectric material. By introducing another quantity,

$$\varepsilon_\sigma = \frac{R_\mathrm{m}}{R_\mathrm{te}} = \frac{l_\mathrm{te} \rho_\mathrm{m}}{l_\mathrm{m} \rho_\mathrm{te}} \, , \tag{5.38}$$

Equation 5.37 can be written as

$$\rho = \rho_\mathrm{te} \delta_\mathrm{te} \left(1 + \varepsilon_\sigma \right) \, . \tag{5.39}$$

Combining Equation 5.35 and Equation 5.39 leads to the total power factor of the system:

$$\begin{aligned} PF &= \frac{S^2}{\rho} \\ &= \left(\frac{S_\mathrm{te} + \varepsilon_\lambda S_\mathrm{m}}{1 + \varepsilon_\lambda} \right)^2 \frac{1}{\rho_\mathrm{te} \delta_\mathrm{te} \left(1 + \varepsilon_\sigma \right)} \, . \end{aligned} \tag{5.40}$$

The difference in the δ_te dependence of the Seebeck coefficient and the resistivity allows for extreme values of the power factor if a well-conducting metal is used.

The net power factor can also be written in terms of the single power factors and the volume fraction of the thermoelectric:

$$PF\left(\delta_{\mathrm{te}}\right) = \frac{\left(\sqrt{PF_{\mathrm{te}}} + \varepsilon_\lambda\left(\delta_{\mathrm{te}}\right)\sqrt{\frac{\rho_{\mathrm{m}}}{\rho_{\mathrm{te}}}}\,\mathrm{sgn}\left(\frac{S_{\mathrm{m}}}{S_{\mathrm{te}}}\right)\sqrt{PF_{\mathrm{m}}}\right)^2}{\delta_{\mathrm{te}}\left(1+\varepsilon_\lambda\left(\delta_{\mathrm{te}}\right)\right)^2\left(1+\varepsilon_\sigma\left(\delta_{\mathrm{te}}\right)\right)}\,, \tag{5.41}$$

with the δ_{te}-dependent notation of the material-related quantities

$$\varepsilon_\varphi(\delta_{\mathrm{te}}) = \frac{\varphi_{\mathrm{te}}}{\varphi_{\mathrm{m}}}\left(\frac{1}{\delta_{\mathrm{te}}} - 1\right)\Bigg|_{\varphi=\lambda,\sigma}\,. \tag{5.42}$$

A comparison between Equation 5.41 and the results of Bergman and Fel is presented in Figure 5.6a for three selected systems calculated by the authors. The models show excellent agreement despite the different mathematical approaches. The power factor exhibits a local maximum if the incorporation of a metal into the main phase decreases the resistivity faster than the square of the Seebeck coefficient. Here, this is only the case in $(Bi_2Te_3)_{0.2}(Sb_2Te_3)_{0.8}$-Al, where a sufficient ratio of the electrical and thermal conductivities ($\sigma_{\mathrm{m}}/\sigma_{\mathrm{te}} = 270$) and thermal conductivities ($\lambda_{\mathrm{m}}/\lambda_{\mathrm{te}} = 67.2$) is given. In $CoSb_3$-Ni, the thermal conductivities are too similar ($\lambda_{\mathrm{m}}/\lambda_{\mathrm{te}} = 1.8$), which causes a significant temperature drop inside the Ni phase and makes an enhancement impossible. The Bi_2Te_3-PbTe composite instructively shows that a combination of two thermoelectrics only worsens the overall performance if additional scattering, diffusion or other interrelated effects are not of importance. The extremely low power factor in $CoSb_3$-Ni for $\delta_{\mathrm{te}} \approx 0.08$ is due to the opposite signs of the Seebeck coefficients of $CoSb_3$ and Ni, which leads to a cancellation of the opposing thermovoltages.

In Figure 5.6b, the model's prediction is compared with the experimental power factor of a serial $Fe_2VAl_{1.5}$-Cu composite, measured for various volume fractions. The power factor reaches $4.5\,\mathrm{mWm^{-1}K^{-2}}$ at 350 K for a volume fraction of $Fe_2VAl_{1.5}$ of $\delta_{\mathrm{te}} = 0.25 \pm 0.1$, a value being more than 4 times larger than that of the pristine thermoelectric [51]. The composite was made using Spark plasma sintering with a pressure of 50 MPa and a temperature of 1100 °C.

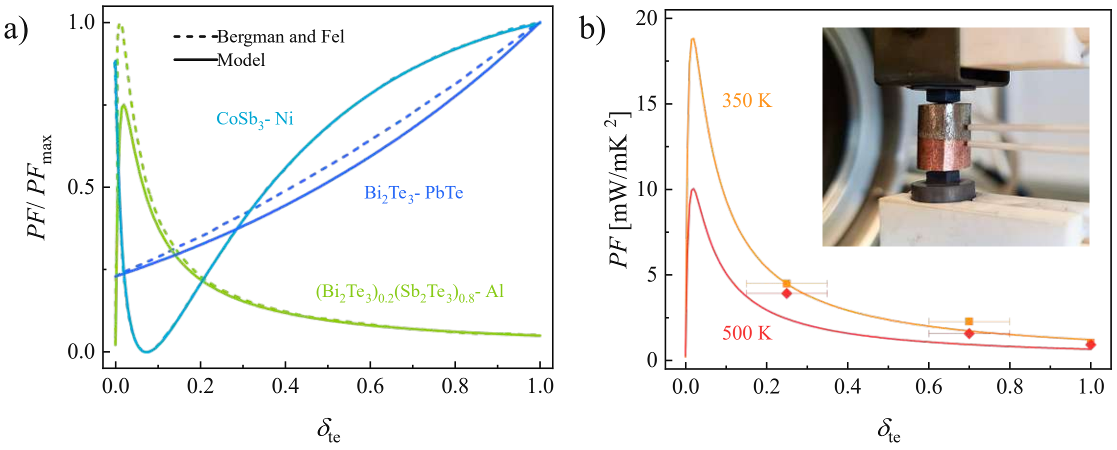

Figure 5.6: a) Comparison of the total power factor PF between the model of Bergman and Fel [184] and the model described in the text, applied on three different systems. The reference line of the CoSb$_3$-Ni system is not visible due to its excellent alignment with the model. The values of the individual thermoelectric properties were taken from Ref. [184]. b) Comparison of the power factor of a Fe$_2$VAl$_{1.5}$-Cu composite and the values predicted by Equation 5.41. The composite was measured for $25\,\%$, $70\,\%$ and $100\,\%$ volume fraction of the thermoelectric material. Because of the irregular interface and uncertainty in the determination of the volume fraction due to the finite thickness of the thermocouple, an error of $10\pm\,\%$ was assumed for the volume fraction. The inset shows the experimental setup for the measurement of the system with $\delta_{\mathrm{te}} = 0.7$. The thermoelectric properties of Fe$_2$VAl$_{1.5}$ and Cu were taken from Ref. [51] and Ref. [236–238], respectively. Reproduced from Ref. [169].

Figure of merit

In the next step, the figure of merit zT will be calculated for a serial composite, starting from an ideal metal with infinite conductivities. The total thermal conductance Λ can be calculated, in accordance to the electrical conductance, as

$$\frac{1}{\Lambda} = \frac{1}{\Lambda_{\mathrm{te}}} = \frac{l_{\mathrm{te}}}{\lambda_{\mathrm{te}} A} := \frac{l_{\mathrm{te}} + l_{\mathrm{m}}}{\lambda A} \,, \tag{5.43}$$

leading to

$$\lambda = \lambda_{\mathrm{te}} \frac{l_{\mathrm{te}} + l_{\mathrm{m}}}{l_{\mathrm{te}}} = \lambda_{\mathrm{te}} \frac{1}{\delta_{\mathrm{te}}} \,. \tag{5.44}$$

The thermal conductivity increases with decreasing volume fraction of the thermoelectric material, opposite to the electrical resistivity (see Equation 5.28). Combining Equation 5.44 with the power factor in Equation 5.29 yields the net figure of merit of the ideal system:

$$zT = \frac{PF}{\lambda} T = \frac{PF_{\mathrm{te}}\,\delta_{\mathrm{te}}}{\lambda_{\mathrm{te}}\,\delta_{\mathrm{te}}} T = zT_{\mathrm{te}}\ . \tag{5.45}$$

Apparently, the increase in the thermal conductivity counterbalances the increase in the power factor and leads to the same zT.

The total thermal conductivity is modified when the thermal conductivity of the metal is no longer infinite. It then becomes

$$\frac{1}{\Lambda} = \frac{1}{\Lambda_{\mathrm{te}}} + \frac{1}{\Lambda_{\mathrm{m}}} = \frac{l_{\mathrm{te}}}{\lambda_{\mathrm{te}} A} + \frac{l_{\mathrm{m}}}{\lambda_{\mathrm{m}} A} := \frac{l_{\mathrm{te}} + l_{\mathrm{m}}}{\lambda A}\ , \tag{5.46}$$

$$\lambda = \frac{\lambda_{\mathrm{te}}}{\delta_{\mathrm{te}}\,(1+\varepsilon_\lambda)}\ . \tag{5.47}$$

From that a convenient relation of the total figure of merit can be derived:

$$\begin{aligned} zT &= \frac{PF}{\lambda} T \\ &= \frac{\left(\sqrt{zT_{\mathrm{te}}} + \sqrt{\varepsilon_\lambda \varepsilon_\sigma}\,\mathrm{sgn}\left(\frac{S_{\mathrm{m}}}{S_{\mathrm{te}}}\right)\sqrt{zT_{\mathrm{m}}}\right)^2}{(1+\varepsilon_\lambda)\,(1+\varepsilon_\sigma)}\ . \end{aligned} \tag{5.48}$$

As an example, the thermoelectric power factor PF and figure of merit zT of a composite consisting of Na-doped polycrystalline SnSe [239] as a high-performance thermoelectric materials mixed with elemental Ag as well as another thermoelectric material, Se-doped PbTe [240], is calculated. The result is shown in Figure 5.7. While PF reaches $\approx 250\,PF_{\mathrm{te}}$ in Ag with 0.1 % SnSe, the figure of merit in composites differs from the power factor in that a local maximum is absent. Hence, the zT of the composite always ranges between the values obtained for the pristine material, i.e. it is always smaller than the zT of the thermoelectric. A striking feature in Figure 5.7 is that in case of a thermoelectric-metal composite the figure of merit remains nearly constant even at very low volume fractions of the thermoelectric material due to the exceptionally large difference in the electrical and thermal conductivity of both materials. This can be explained by the fact that in

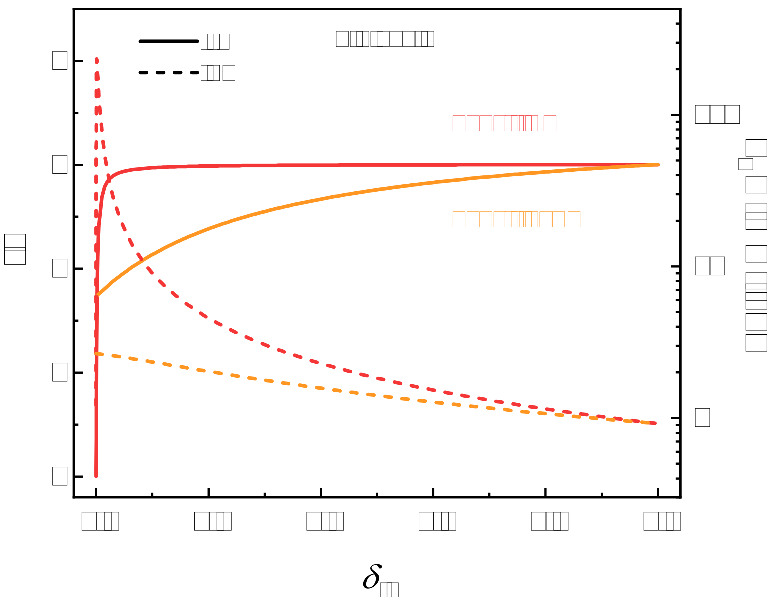

Figure 5.7: Total figure of merit zT (solid lines) and power factor (dashed lines) of a serial connection of Na-doped polycrystalline SnSe and Ag (red line) and Se-doped PbTe (orange line) at $780\,\mathrm{K}$ in dependence of the volume fraction δ_{te} of SnSe, calculated from Equation 5.41 and Equation 5.48. The values of the material properties were taken from literature [236–240]. Reproduced from Ref. [169].

a serial configuration most of the temperature drop occurs across the thermoelectric material, preserving the thermovoltage, while the balance between increased electrical and thermal conductivity maintains zT. Deviation from ideal conduction in the metal is the only factor that decreases the overall zT (see Equation 5.45). In contrast to that, both PF and zT of a thermoelectric-thermoelectric composite show a more linear behavior as a function of the volume fraction, revealing the limitation of such systems and necessity of additional effects that truly change the microscopic properties, such as interface scattering or diffusion.

The derivations of the thermoelectric properties presented here neglect interfaces between the constituents of the composite. Interfaces can lead to scattering of charge carriers and phonons and cause a modification of all thermoelectric quantities. Their influence is proportional to the electrical and thermal resistance as well as the number of interfaces. In Appendix C, a qualitative description of the effect of interfaces is provided. Nevertheless, the statements concluded from the ideal system are still valid if interface scattering is not the dominant mechanism determining the composite's performance.

5.2.2 Clearing up the delusion - microscopic vs. macroscopic performance

Electrical conductivity σ, thermal conductivity λ and similar quantities are material-specific intrinsic properties. In an electrical circuit consisting of several components with different properties - like the composites discussed here - the microscopic definition of the resistivity becomes ill-defined due to spatial homogeneity. Likewise, the PF becomes meaningless, as it does not reflect the total power output any more. Instead, the proper quantities to compare the performance of such networks are total power output P, heat conductance Λ and resistance R. Such macroscopic quantities are generally more robust and less prone to mistakes and misinterpretations since they a measured directly and do not require considerations of the dimensions and microstructure of the system. Notably, $zT = S^2\sigma/\lambda T$ is a macroscopic quantity as well, as σ and λ depend on the dimensions in the same way. Thus, the figure of merit can be written as

$$zT = \frac{S^2\sigma}{\lambda}T = \frac{S^2\sigma A/l}{\lambda A/l}T = \frac{S^2}{R\,\Lambda}T\,. \tag{5.49}$$

To further elucidate the meaning of the power factor of composites, PF, zT and the power output are compared for three different systems comprising the state-of-the-art material SnSe and elemental Ag, as shown in Figure 5.8a. These include a pure thermoelectric (I), a thermoelectric-metal composite (II) as well as the pure thermoelectric with reduced length (III). Again, interfaces will be neglected, which will yield different results than would be obtained experimentally. However, the informative values of the distinct difference between the setups is still assured. It is well known that the maximum power transfer to a load connected to a thermoelectric generator occurs for equal resistances [241], thus

$$P_{\max} = \frac{U^2}{4R}\,, \tag{5.50}$$

with U and R being the total generated thermovoltage and resistance of the composite, respectively. Utilizing the definitions $U = S\Delta T$, $PF = S^2\sigma$ and $R = l/(\sigma A)$,

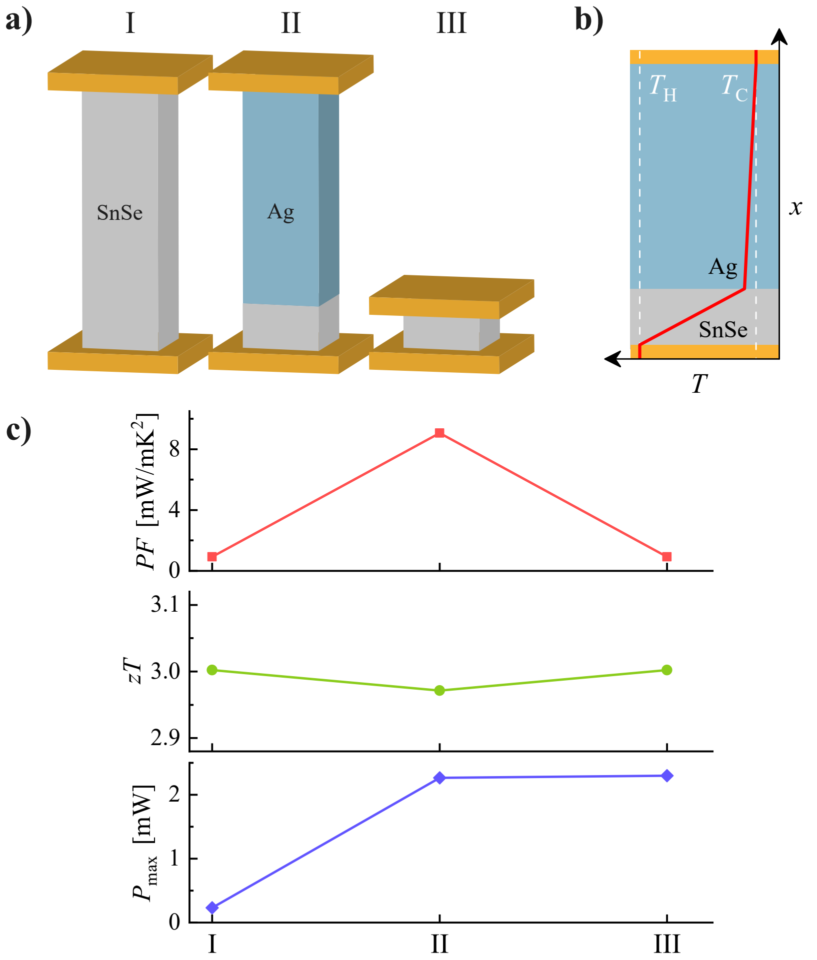

Figure 5.8: a) Sketch of the three systems compared in the text with respect to their thermoelectric performance. I: (Na-doped polycrystalline) SnSe, II: SnSe-Ag composite with $\delta_{\text{te}} = 0.1$, III: SnSe with reduced length similar to system II. b) Temperature profile of system II. c) Power factor, figure of merit and maximum power output for all three systems. The power output was calculated using $l = 1\,\text{cm}$, $A = 1\,\text{mm}^2$, $T = 300\,\text{K}$ and $\Delta T = 100\,\text{K}$. For the sake of simplicity, all thermoelectric properties were taken at $780\,\text{K}$ [236–239]. Reproduced from Ref. [169].

which equals a transformation of the composite into a single „average“ material, Equation 5.50 can be rewritten as

$$P_{\text{max}} = \frac{A}{4l} PF^2 \Delta T \; . \tag{5.51}$$

In Figure 5.8b, the temperature profile of system II is sketched. Unlike in system I and III, where the temperature decreases linearly between the electrodes, the temperature drops mainly along the thermoelectric component (compare Equation 5.30 and Equation 5.31). The total power factor, figure of merit and power output are shown in Figure 5.8c.

On first glance, the SnSe-Ag composite (II) seems to perform better than pure SnSe (I) in terms of power factor and power output, while reducing the figure of merit only moderately. Substituting part of the thermoelectric material by a metal improves the power generated by reducing the total resistivity while the Seebeck coefficient S remains almost unaffected, thereby seemingly decoupling S and σ, two transport properties which are usually difficult to enhance simultaneously [11]. However, it is not the metal per se that improves the performance but rather the length reduction of the thermoelectric, while the temperature drop across the thermoelectric remains the same - an approximation that cannot always be realized in applications. Indeed, a comparison between systems II and III shows that for the same volume of the active thermoelectric component, the power output is marginally higher without the metal despite the fact that the metal composite has a ten times higher power factor. Thus, the enhancement of the power factor found by several studies and also in Ref. [169] merely results from a nonsensical comparison of two materials with different volume fractions of the active thermoelectric component. Therefore, the power factor is no longer a valid indicator for thermoelectric performance in composite materials. Since a large PF neither indicates a higher zT nor a higher power output in such composites, the power factor becomes a meaningless parameter for evaluating composite materials or devices. Only in fixed-length setups, if power output is more critical than efficiency, the use of composites can significantly increase power output by reducing the volume fraction of the thermoelectric material and lowering the resistance - given that the same temperature drop can be realized across the thermoelectric material with reduced length, i.e. a significantly enhanced temperature gradient $\mathrm{d}T/\mathrm{d}l$.

The showcase presented above nicely illustrates the necessity to consider the dimensions of the material if inhomogeneities are present, as is the case in composites. Accordingly, the use of macroscopic, measurable quantities is inevitable.

Another potential application for thermoelectric materials with high power fac-

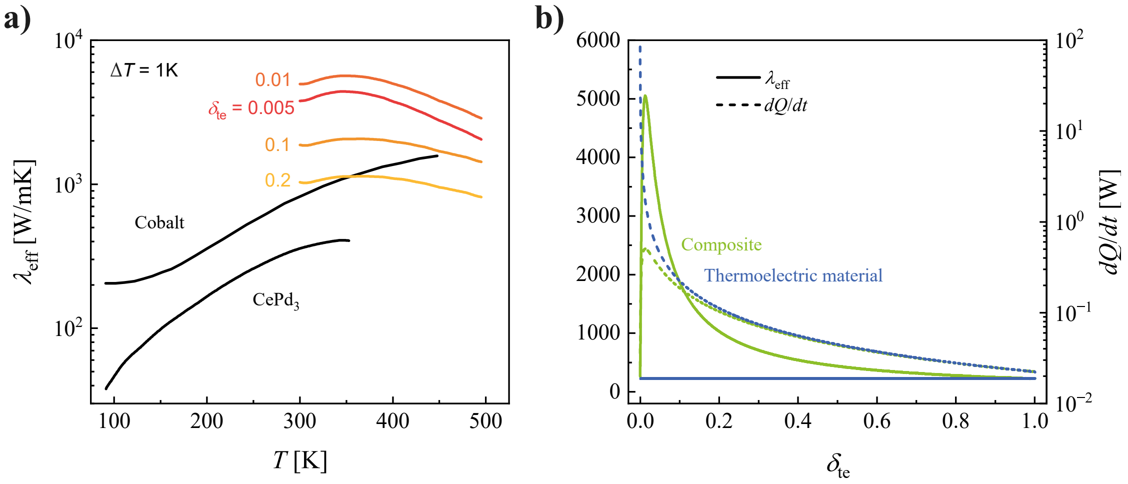

Figure 5.9: a) Effective thermal conductivity vs temperature for Bi_2Te_3-Al composites with different volume fractions δ_{te}, calculated from Equation 5.52. The black solid lines show reference materials [242]. b) δ_{te}-dependent effective thermal conductivity (solid lines) and cooling power (dashed lines) of a composite and a single thermoelectric material with a length equal to the share in the composite. The cooling power was calculated from Equation 5.53 using $l = 1\,\mathrm{cm}$, $A = 1\,\mathrm{mm}^2$ and $\Delta T = 1\,\mathrm{K}$. The properties of Bi_2Te_3 and Al were taken from literature [75, 236, 237, 243]. Reproduced from Ref. [169].

tors is the so-called active cooling, which combines traditional heat conduction with the Peltier effect to enhance cooling capabilities [242]. In this context, a large thermal conductivity and power factor are desired to maximize the effective thermal conductivity λ_{eff}:

$$\lambda_{\mathrm{eff}} = \lambda + \frac{PFT_{\mathrm{H}}^2}{2\Delta T}\ , \tag{5.52}$$

with the temperature of the hot side T_{H}. Active cooling does indeed look like a promising application when composites are compared to conventional materials. Figure 5.9a shows the effective thermal conductivity λ_{eff} of a Bi_2Te_3-Al composite for different volume fractions of the thermoelectric and compares it with pure Cobalt and $CePd_3$ [242]. λ_{eff} is significantly enhanced in metal-dominated composites. However, it is important to examine the macroscopic quantity - the actual cooling power - as the high power factor can be misleading and give a false impression of the performance. A closer look at the cooling power,

$$\frac{\mathrm{d}Q}{\mathrm{d}t} = \lambda_{\mathrm{eff}}\frac{A}{l}\Delta T = \left(\Lambda + \frac{S^2 T_{\mathrm{H}}^2}{2R\Delta T}\right)\Delta T \tag{5.53}$$

expressed with the macroscopic quantities $\Lambda = \lambda\frac{A}{l}$ and $\frac{S^2}{R} = PF\frac{A}{l}$, reveals the inferiority of composites to pure thermoelectrics (see Figure 5.9b). For all volume fractions, the composite has a lower cooling efficiency despite the higher effective thermal conductivity. While the resistance can be decreased by substituting part of the thermoelectric material with a metal, thus enhancing the cooling power, the performance is always worse compared to the pure thermoelectric with reduced length. Similar to Equation 5.51, the metal-incorporated material appears better due to a comparison of a different amount of thermoelectric material.

5.2.3 The best composite

Before exploring the potential applications of composites, it is important to acknowledge that the formulas used to predict the thermoelectric performance are subject to ideal conditions and may not accurately reflect real-world scenarios. This is because they do not account for the impact of external factors such as contact resistances and inter-phase scattering. As a result, the actual performance may differ from predicted values. That being said, realistic composites with arbitrarily arranged microstructures can often be approximated by a model where one component adopts a spherical shape enclosed by the other, which shows the same thermoelectric tendency as the parallel slab model [184]. Thus, the following statements should be valid in most cases.

As was shown above, an enhancement of the thermoelectric properties due to a combination of a high-performance thermoelectric and a simple metal in a serial configuration is not possible without intrinsic property changes of the individual constituents of the composite or the occurrence of interface effects. When considering the significant impact of these secondary effects on the properties of real composite materials, and the frequent use of composites to improve the figure of merit, it prompts the question of which materials are best suited for making composites.

As was shown above, the total figure of merit zT stays almost constant down to a few percent of the volume fraction of the thermoelectric material when a well-

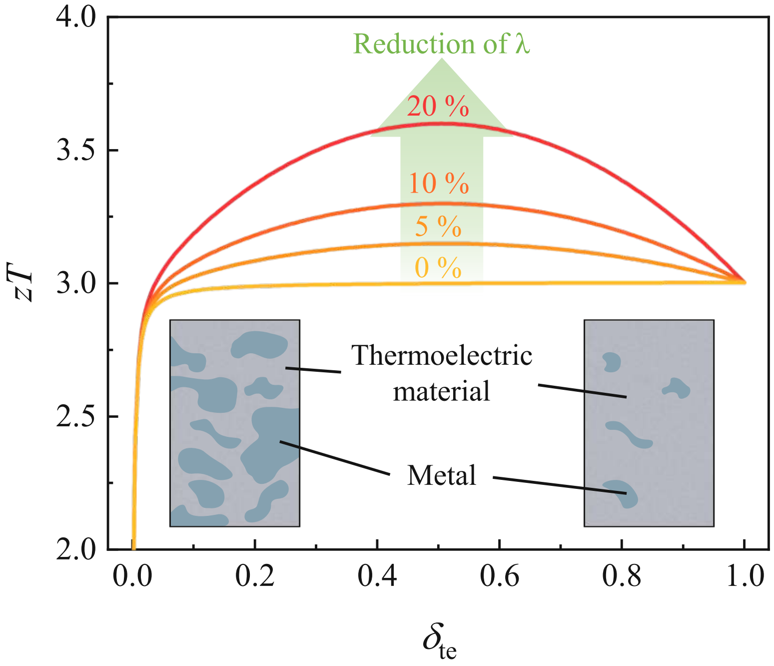

Figure 5.10: Figure of merit zT of a SnSe-Ag composite for different reductions of λ due to increased scattering on the metallic structures. The reduction was calculated from a simple δ_{te}-dependent relation, as explained in the text, such that the reduction equals $5\,\%$, $10\,\%$ and $20\,\%$ for $\delta_{\mathrm{te}} = 0.5$. Reproduced from Ref. [169].

conducting metal is used as the second material (see Figure 5.7). This opens a gigantic playground to reduce the lattice thermal conductivity of the thermoelectric material via increased boundary scattering, as sketched in Figure 5.10. For the reduction of the thermal conductivity due to boundary scattering, the simple relation

$$\lambda_{\mathrm{red}}\left(\delta_{\mathrm{te}}\right) = \frac{\lambda}{1 + a\delta_{\mathrm{te}}\left(1 - \delta_{\mathrm{te}}\right)} \tag{5.54}$$

was assumed. The parameter a is chosen such that the reduction equals $5\,\%$, $10\,\%$ and $20\,\%$ for $\delta_{\mathrm{te}} = 0.5$.

Despite this oversimplified δ_{te} dependency of the reduction of the thermal conductivity, it is clearly visible that scattering of phonons with long mean free paths on mesoscale-sized metallic structures will have a positive effect on the performance [244]. Hence, adding a non-soluble and highly conducting metal is a cheap and profitable strategy to achieve a larger figure of merit or reduce the amount of the thermoelectric material.

In summary, the results obtained above elucidate the origin of the extreme power factor values derived for composites, which are caused by a drastic reduction of the resistance while the thermovoltage only changes moderately due to the uniform temperature gradient. Furthermore, the misleading value of the power factor was shown by a comparison with measurable macroscopic quantities such as the power output and figure of merit. Nevertheless, in theory, incorporating a simple metal with maximal thermal and electrical conductivity into a thermoelectric can have a positive effect on the overall performance, stemming from phonon scattering on interfaces.

Part II

Material Research and Experimental Results

6 Devices and sample preparation

This chapter provides an overview of the devices used for sample preparation and conducting experiments. It includes both a brief discussion on the underlying physics as well as the description of the various effects influencing the real or measured properties of the samples.

6.1 Sample preparation

Sample preparation encompasses both bulk materials and thin films. Bulk materials were prepared by weighing in high-purity (99.9 % or 99.99 %) elements and subsequently melting them together using high-frequency inducting melting. The films, on the other hand, were synthesized from targets using direct-current (DC) magnetron sputtering.

6.1.1 High-frequency induction melting

The home-made setup utilized for melting elements into bulk samples is shown in Figure 6.1. The process involves placing the elements into cavities of the water-cooled copper piece, which determines the ultimate shape of the material. The system, surrounded by a quartz tube, is then evacuated using a turbomolecular pump and a subsequent rotary vane pump, followed by flushing with inert argon gas. This process is repeated multiple times to ensure a clean atmosphere. Finally, the sealed chamber is filled with argon to prevent material evaporation.

By supplying the surrounding copper coils with a high-frequency current, an alternating magnetic field arises, leading to an alternating electric field. This field penetrates the material, inducing electron motion and causing Joule heating, eventually resulting in the melting of the elements. The necessity for electric conduction

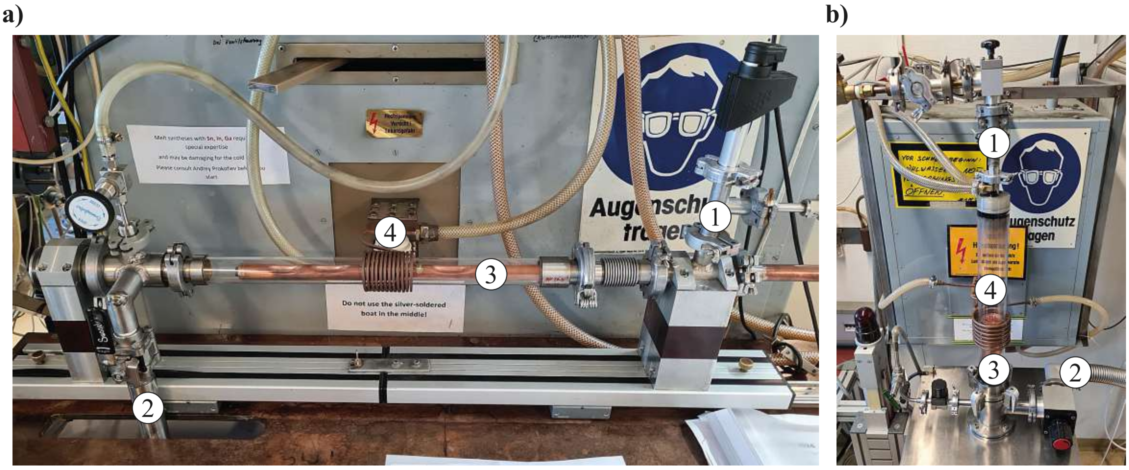

Figure 6.1: Image of the home-made systems used for melting elements utilizing high-frequency induction to obtain small samples for measuring bulk properties (a) and ellipsoidal samples with a diameter of $\approx 26\,\text{mm}$ appropriate for target preparation (b). The marked areas are: (1) gas inlet, (2) connection to pumping station, comprising a turbomolecular and a rotary vane pump, (3) water-cooled copper piece with distinctly shaped cavities, (4) copper coil connected to a high-frequency generator.

of the constituting elements limits this setup to metallic elements. However, thermal contact between the materials enables the simultaneous melting of conducting and non-conducting elements. To ensure a homogeneous distribution of elements within the alloy or compound and thus the formation of the desired crystal structure, the melting process is repeated several times.

The obtained ingots from both setups are presented in Figure 6.2. The resulting small ingot allows for the extraction of multiple rectangular pieces to measure various transport properties. The remaining material is used for determining the crystal structure by grinding it into a fine powder. In contrast, the larger ingot contains enough material to cut out two sputter targets with a diameter of 25.4 mm and a thickness ranging from 2 to 3 mm. Additionally, sufficient material remains for the measurement of the target's thermoelectric properties and crystal structure. This comprehensive approach allows for a direct comparison of the thermoelectric properties of films and their respective bulk analog.

Figure 6.2: 5 g (top left) and 35 g (top right) ingots prepared by induction melting. The smaller ingot is proper for cutting out rectangular samples for bulk-property measurements (bottom left), while a target with 25.4 mm diameter can be extracted from the larger ingot (bottom right).

6.1.2 Magnetron sputtering

Over time, various different coating techniques have been developed, encompassing solid, liquid and vapor deposition processes [245]. Vapor deposition proves to be a powerful resource to produce films on substrates with a high degree of hardness, density, smoothness and oxidation resistance [246]. Among the techniques within vapor deposition, sputtering is a notable example of physical vapor deposition (PVD). In this work, DC magnetron sputtering, employing a single target, was used for film fabrication. An image of the home-made device and a schematic depicting the working principle are presented in Figure 6.3. The central component of the system is a cubic chamber, connected to both a gas inflow and a pumping station. Similar to the induction-melting system, the pumping station consists of a turbomolecular pump followed by a rotary vane pump. Inside the chamber, the target is mounted and electrically linked to an external power supply, while the substrate typically faces and opposes the target. Prior to the sputtering process,

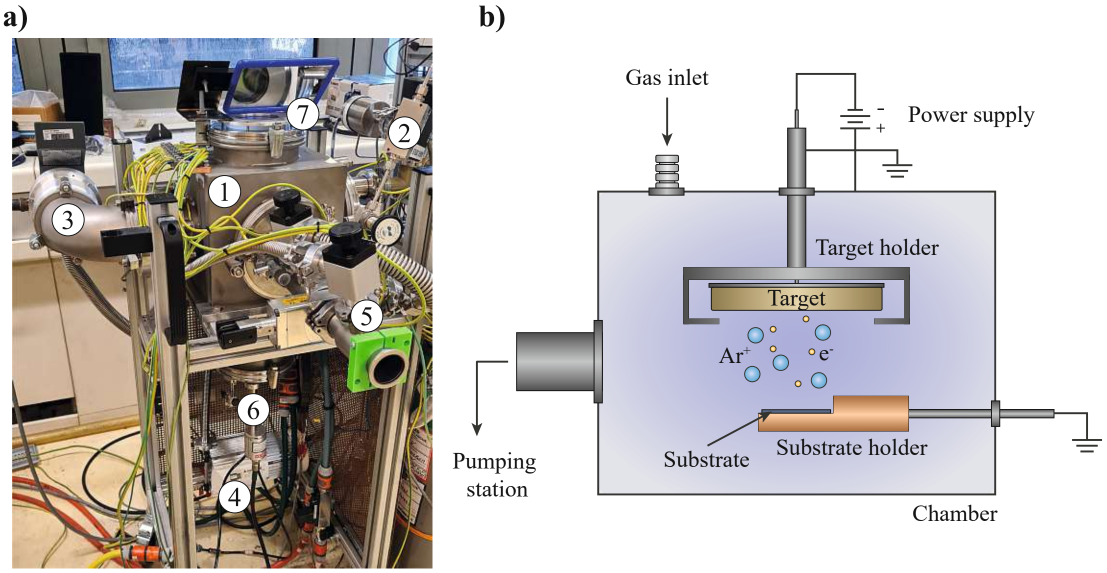

Figure 6.3: a) Image of the home-made sputtering setup. The marked areas are: (1) sputter chamber, (2) gas inlet with a mass flow controller, (3) turbomolecular pump, (4) rotary vane pump, (5) vacuum lock to insert the substrate holder, (6) target holder, (7) mirror. b) Visualization of the sputter process with the target situated above the substrate.

the chamber is evacuated and filled with a gas, commonly argon. Subsequently, a negative voltage is applied to the target. Within a gas, a small number of ions and free electrons are present, accelerated towards or away from the target. Once the electrons reach a certain energy level, interactions with other gas particles lead to additional ionizations. The ionized atoms, upon colliding with the target, result in the ejection of particles that move toward to substrate. Upon reaching the substrate, these particles adhere and form a layer.

The amount of material removed from the target depends on multiple parameters, the most important one being the sputter yield of the constituents. In a target comprising multiple elements, not all atoms are ejected at the same rate. The number of dislodged atoms per impinging ion is given by the so-called sputter yield Y:

$$Y = \frac{\text{number of ejected atoms}}{\text{number of incident ions}} \,. \tag{6.1}$$

The sputter yield depends on the sublimation energy, the scattering cross section,

Target	Energy [eV]					
	50	100	200	300	500	1000
Al	0.025	0.156	0.426	0.647	0.986	1.527
Ti	0.012	0.074	0.201	0.307	0.469	0.731
V	0.014	0.098	0.276	0.426	0.658	1.034
Fe	0.048	0.21	0.511	0.752	1.117	1.704
Ni	0.046	0.204	0.500	0.737	1.098	1.682
Ta	0.006	0.054	0.167	0.265	0.423	0.691
Au	0.124	0.374	0.788	1.113	1.608	2.428

Table 6.1: Sputter yield of Al, Ti, V, Fe and Ta for different energies of Ar ions impinging perpendicular to the surface. The values were calculated from [249].

the energy and incident angle of the impinging ion and the crystal structure of the target [247, 248]. Table 6.1 provides the sputter yield values for different single-element targets at various energies of Ar ions under normal incidence. The sputter yield naturally increases with impinging energy, but can substantially differ between different elements. The mathematical description of the sputter yield from collision cascades is [250]

$$Y = \frac{3}{4\pi^2}\alpha\frac{4M_1M_2}{(M_1+M_2)^2}\frac{E_t}{E_b} \qquad (E_t < 1\,\mathrm{keV})\ , \tag{6.2}$$

$$Y = 3.56\,\alpha\frac{Z_1Z_2}{Z_1^{2/3}+Z_2^{2/3}}\frac{M_1}{M_1+M_2}\frac{S_n(E)}{E_b} \qquad (E_t > 1\,\mathrm{keV})\ . \tag{6.3}$$

Here, Z_1, Z_2, M_1 and M_2 are the atomic numbers and masses of the impinging ion and target atom, respectively. E_t denotes the threshold energy required to eject the particle from the surface and E_b represents its surface binding energy. The parameter α is a measure of the efficiency of momentum transfer during the collision, while $S_n(E)$ is the energy loss per unit length due to nuclear collisions. This parameter is a function of the energy as well as masses and atomic numbers of the atoms involved [250].

The sputter yields of the constituent elements within an alloy or compound may differ from that of a single-element target. However, they are often related to each other. A significant advantage of sputtering, in contrast to various other vapor-deposition processes like thermal evaporation, is that after an initial depletion phase, the particle ratio of the ejected atoms aligns with the composition of the target. In case of thermal evaporation, the stoichiometry of the ejected atoms is influenced by the individual partial pressures as well as the surface composition, yielding an inaccurate stoichiometry for the film.

In the context of sputtering, the initial flux ψ is directly proportional to the sputter yield Y and the surface concentration C. For a binary alloy composed of atoms A and B, the flux ratio is given by [251]

$$\frac{\psi_A}{\psi_B} = \frac{Y_A C_A}{Y_B C_B} \,, \tag{6.4}$$

with $C_A = n_A/n$ and $C_B = n_B/n$. n_A and n_B are the number of atoms A and B and $n = n_A + n_B$ is the total number of atoms. After a short period during which n_i impinging atoms hit the target, $n_i Y_A C_A$ atoms A are dislodged from the surface. This alters the concentration to

$$C'_A = \frac{n_A - n_i Y_A C_A}{n} = C_A \left(1 - \frac{n_i Y_A}{n}\right) \,. \tag{6.5}$$

This change in concentration subsequently modifies the flux ratio to

$$\frac{\psi'_A}{\psi'_B} = \frac{Y_A C'_A}{Y_B C'_B} = \frac{Y_A C_A}{Y_B C_B} \frac{1 - \frac{n_i Y_A}{n}}{1 - \frac{n_i Y_B}{n}} \,. \tag{6.6}$$

If the sputter yield of atom A is higher than that of B, more particles of atom A are ejected relative to their stoichiometry. This in turn reduces the number of atoms remaining on the surface and thus lowers the amount of subsequently dislodged atoms A. Ultimately, the flux ratio becomes [250]

$$\frac{\psi_A}{\psi_B} = \frac{C_A}{C_B} \,, \tag{6.7}$$

corresponding to the stoichiometry of the alloy. Therefore, after an initial phase, the system acquires equilibrium.

It is important to emphasize that while the dislodgement of constituents from the target aligns with the stoichiometry, obtaining the desired stoichiometry in the resulting film is not guaranteed. This is attributed to two factors: i) the angular distribution of the atoms is not the same [252–255] and ii) the ejected atoms experience scattering with gas atoms while moving to the substrate, causing deviations from their intended paths [253, 256, 257].

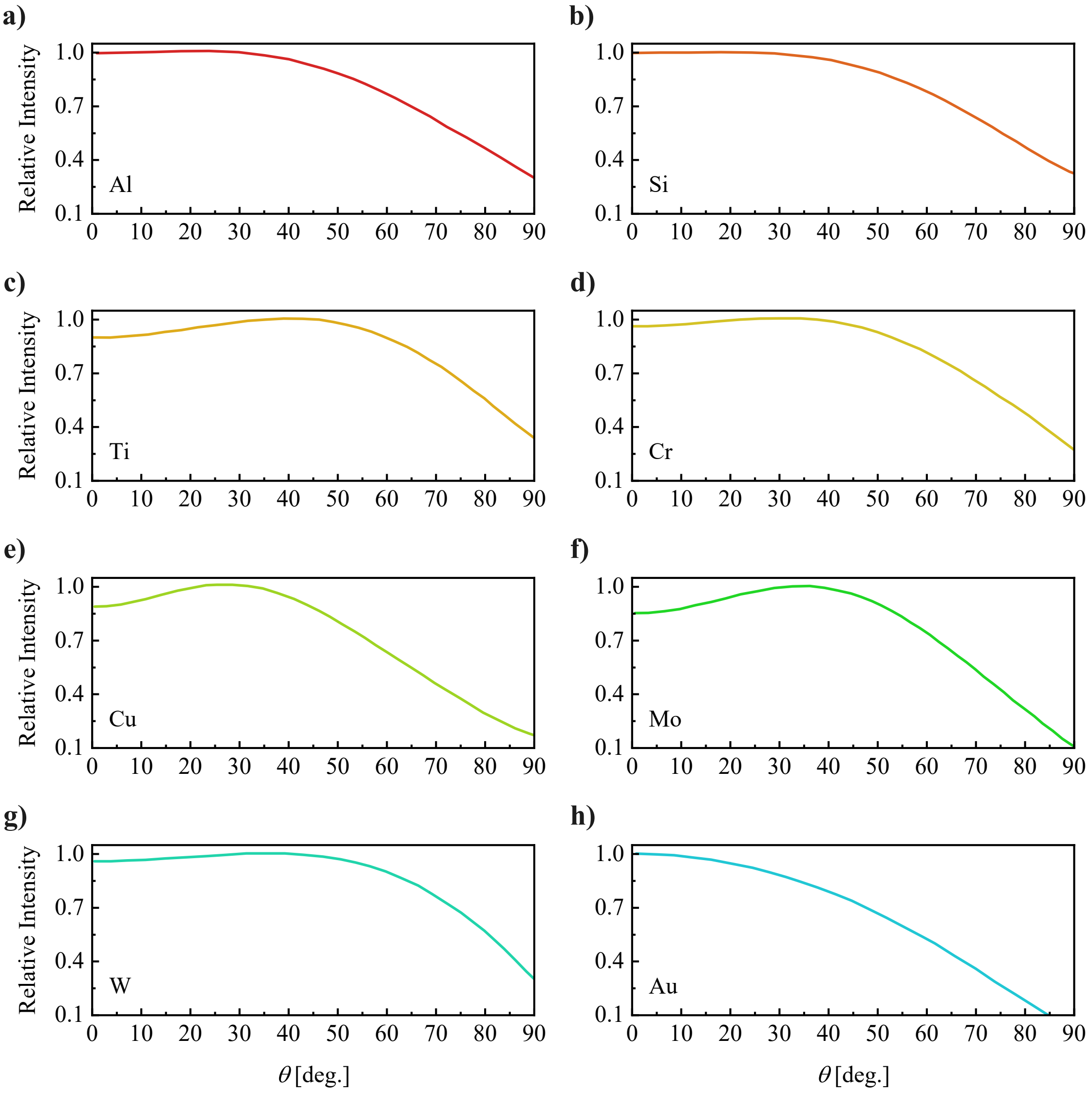

Figure 6.4: Angular distribution of various elements ejected from single-element targets in a magnetron-sputtering system. The values were taken from Ref. [255].

Figure 6.4 shows the angular distribution of elements dislodged from the target in a magnetron-sputtering system with Ar ions, arranged according to their atomic number. The elements can be divided into two groups. While some have the maximum at 0° (Si, Au), others tend to be dislodged at higher angles (Al, Ti, Cr, Cu, Mo, W). Depending on the distance, offset and size of the substrate, this can lead to a film stoichiometry different to that of the target. This is illustrated in

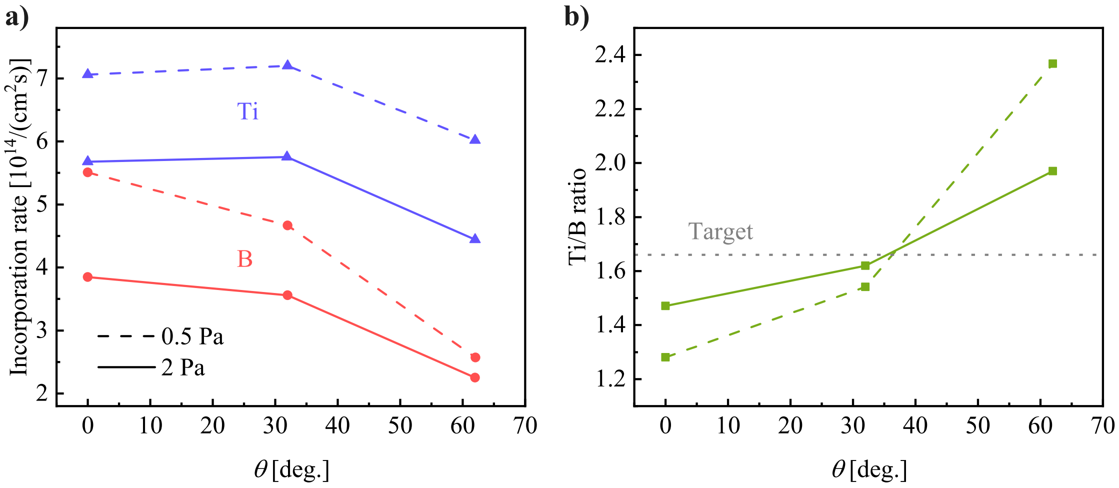

Figure 6.5: a) Angular distribution of the incorporation rate of Ti and B and b) ratio Ti/B of the film composition at 0.5 and 2 Pa. The composition of the target ($Ti_{1.66}B$) is shown as dotted line. The values were taken from Ref [253].

Figure 6.5, depicting the stoichiometry ratio of Ti and B from a $Ti_{1.66}B$ target under various pressures. This highlights the significant impact of particle distraction on the composition. The angular distribution depends on the atomic number of the target element as well as its sputter yield and surface binding energy [254].

The films presented in the next chapter were synthesized using a magnetron-sputtering setup. The magnetic field facilitates the process by confining secondary electrons, ejected from the target due to ion impingement, on cycloidal drift orbits [258]. This confinement enhances their residence time in the vicinity of the target and leads to a denser plasma and higher deposition rates. Figure 6.6 shows the magnet system of the target holder together with the substrate holder, which is inserted into the sputter chamber.

In a first approximation, the angular distribution follows a cosine law [258], resulting in a reduced deposition rate at larger angles. Given the finite size of the substrate and the correlation between the maximum angle and the distance between substrate and target, selecting an appropriate distance is important to ensure a uniformly distributed film thickness. To achieve this, the distribution was approximated and calculated. The details can be found in Appendix E. For a target with a diameter of 25.4 mm and a rectangular substrate with a longer side of 10 mm, a distance of 30 mm between the target and substrate was chosen. This choice

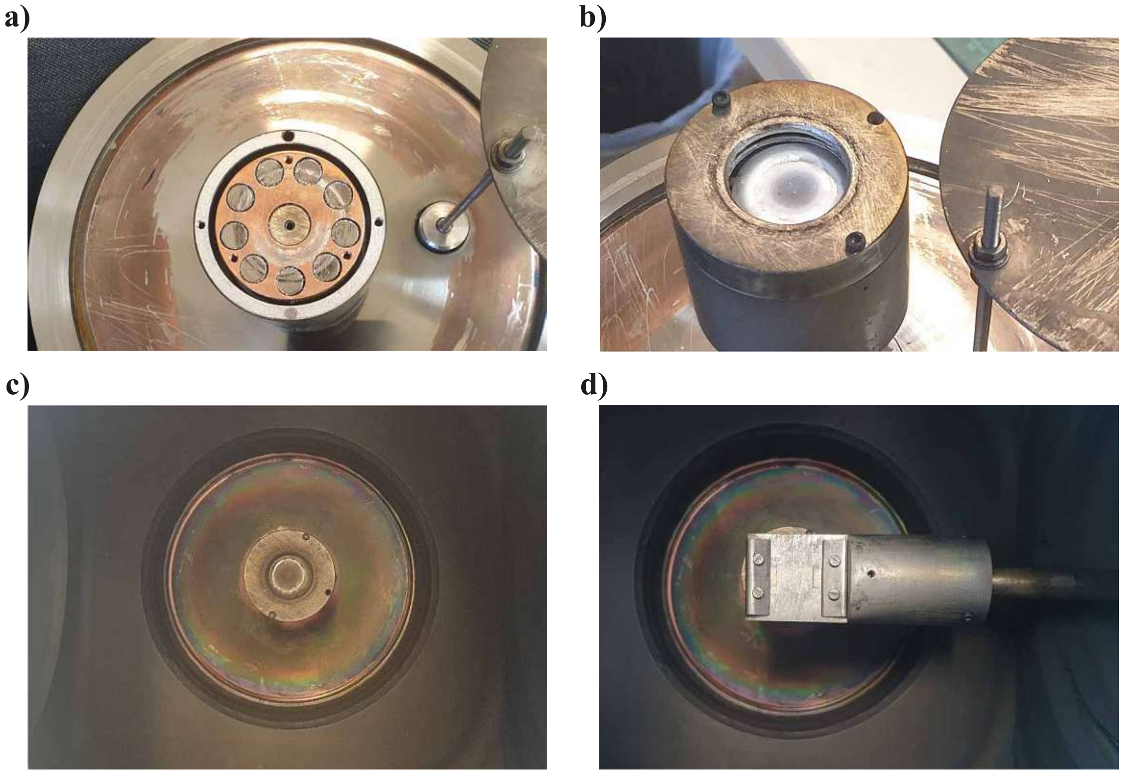

Figure 6.6: Images of the target and substrate holder of the magnetron-sputtering setup. a) Magnet system situated beneath the target, comprising 9 outer magnets and one inner magnet with inverse magnetization, causing a rotationally symmetrical magnetic field. b) Target holder with mounted target and open shutter. c) Top view of the target holder mounted inside the sputter chamber. d) Substrate holder inserted into the chamber and rotated away from the opposing target. The substrate (not shown) is clamped down by two clips, also ensuring electrical connection to the ground.

ensured a maximum thickness deviation of 16 % while simultaneously keeping the deposition rate as high as possible.

The deposition rate was determined by measuring the film thickness after a distinct deposition duration, utilizing the Tylor Hobson Surftronic S-128 surface roughness tester (see Figure 6.7). Prior to deposition, half of the substrate is covered to prevent any deposition on that portion. The shielding results in a well-defined edge of the film, enabling the measurement of the thickness. Given that the determination of the thickness has an inaccuracy of several percent, the measurement was conducted on multiple different positions, providing a robust average

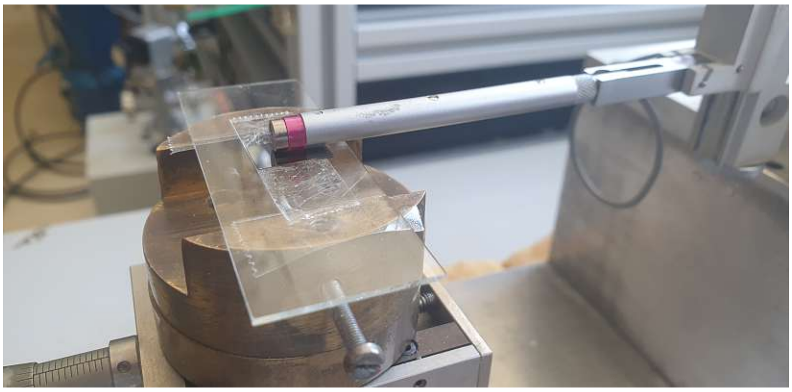

Figure 6.7: Image of the surface roughness tester utilized for measuring the film thickness. The substrate is fixed on a glass plate with a tape.

thickness.

6.2 Determination of composition and crystal structure

As emphasized in the previous section, the composition of films can deviate significantly from that of the target. Given that composition is a critical parameter influencing the structure as well as the thermoelectric and mechanical properties, its determination is of importance.

The bulk composition is measured using the Zetium X-Ray fluorescence (XRF) spectrometer from Panalytical, equipped with a Rh X-ray tube anode. XRF employs photons to probe the sample, exciting inner-shell electrons. Upon the void being filled by another electron, a photon with a wavelength characteristic of the element is emitted and measured by a detector. Comparing the measured signal with a reference material provides the composition of the sample.

For thin films, the application of XRF spectrometry is more complex due to the interdependence of intensity, composition and thickness [259]. Consequently, the films' composition is determined using the secondary-electron microscope (SEM) FEI Quanta 250 FEG with an energy-dispersive X-Ray (EDX) detector. To enhance accuracy, the respective target sample is utilized as reference material.

The crystal structure of both bulk and thin-film samples is determined using

X-ray diffraction (XRD) on an X'Pert MPDII diffractometer from Panalytical with a Cu anode in the Bragg-Brentao geometry. To minimize reflection peaks from the single-crystalline substrates, an offset of 3 ° to 4 ° is applied.

6.3 Measurement of thermoelectric properties

Measurements of bulk materials and film-substrate systems follow the same principles. However, while bulk samples can be measured independently and directly, films are always measured in presence of the underlying substrate, potentially influencing the measured properties (refer to chapter 5 for more details). Furthermore, the finite size and distinct structure of film-substrate samples necessitate a special sample holder for certain measurements.

6.3.1 Seebeck coefficient

The Seebeck coefficient S of the samples is measured above room temperature using the ZEM-3 from ULVAC in the high-temperature setup. S is determined from the resulting thermovoltage U due to a temperature difference ΔT. To increase the accuracy, the measurement is typically conducted at N different temperature differences and the Seebeck coefficient calculated as [260]

$$S(T) = -\frac{\left(\sum_{i=1}^{N} \Delta T_i\right)\left(\sum_{i=1}^{N} U_i\right) - N\left(\sum_{i=1}^{N} \Delta T_i U_i\right)}{\left(\sum_{i=1}^{N} \Delta T_i\right)^2 - N\left(\sum_{i=1}^{N} \Delta T_i^2\right)} + S_{\mathrm{wire}}(T)\,. \tag{6.8}$$

S_{wire} is the Seebeck coefficient of the thermocouple, which needs to be subtracted from the measured value.

For film samples, the substrate is mounted onto a Macor-based holder and secured with platinum clamps to ensure a high mechanical stability. To further facilitate electric conduction, graphite paper is put between the Pt clamps and the film. The film holder as well as the setup of the Seebeck measurement can be seen in Figure 6.8. Prior to deposition, the chamber is evacuated and flushed with He several times to ensure an oxygen-free environment. Then, the sample is heated to different base temperatures, at which the thermovoltage is measured at three temperature differences.

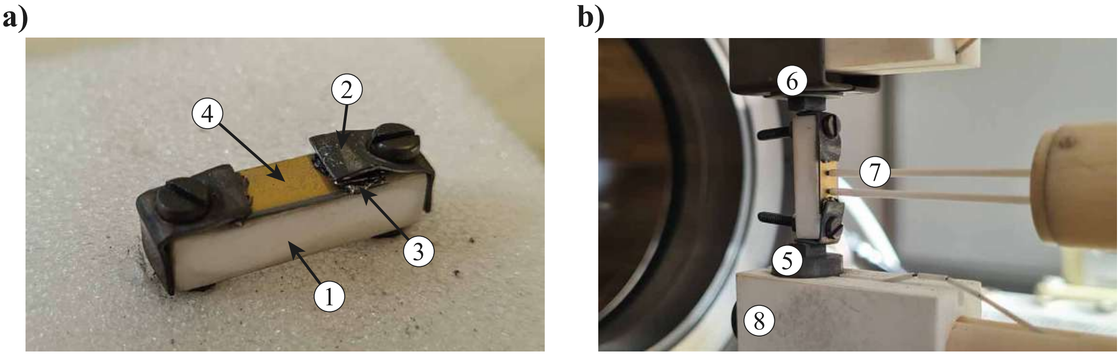

Figure 6.8: a) Film sample holder for measuring the Seebeck coefficient and electrical resistivity, showing the Macor base (1), the platinum clamps (2) with the graphite paper (3) and the sample (4). b) Mounted sample holder, connected to the lower (5) and upper (6) electrode as well as the probe thermocouples (7). The heater (8) is placed below the sample.

6.3.2 Electrical resistivity

In addition to the Seebeck coefficient, the ZEM-3 is employed to simultaneously measure the electrical resistivity of both bulk and film samples, using the same holder for the films. Unlike the Seebeck coefficient, the electrical resistivity is measured two times per temperature in opposing directions to eliminate any spurious non-zero voltage. If U_0 is the offset voltage, the resistance R of the sample is obtained by measuring the voltage U resulting from applying the current I in both directions:

$$\begin{aligned} U_1 &= RI + U_0 \ , \\ U_2 &= -RI + U_0 \ , \\ R &= \frac{1}{2I}\left(U_1 - U_2\right) \ . \end{aligned} \tag{6.9}$$

In addition to that, the voltage is measured using the four-probe method by passing the current through the outer contacts and probing the voltage with the connected thermocouples. This way, any influence of contact resistances is avoided.

6.3.3 Thermal conductivity

To determine the thermal conductivity of bulk samples, the Linseis Laser Flash LFA 500 is utilized. Prior to measurement, both sides of the sample are coated with a graphite spray, ensuring a high thermal absorption and equal surface conditions.The sample is then placed in a chamber, surrounded by a furnace and positioned between a pulsed xenon lamp and an infrared detector (see Figure 6.9a). Similar to the ZEM-3, the system is evacuated and flushed with helium several times to purify the atmosphere. A small amount of helium is then inserted to facilitate effective heat exchange between the sample and the furnace.

During the measurement, the sample is heated to several temperatures. Subsequently, a pulsed light flash from the xenon lamp hits and heats the bottom of the sample. A detector traces the temperature rise on the top of the sample over time. The speed of temperature transport is reflected in the thermal diffusivity α, which is calculated as [261]

$$\alpha = 0.13879\frac{L^2}{t_{1/2}} \ , \tag{6.10}$$

where L is the thickness of the sample and $t_{1/2}$ denotes the time it takes for the top of the sample to heat up to half of the maximum (see Figure 6.9b). From the thermal diffusivity, the thermal conductivity λ is obtained as [262]

$$\lambda(T) = \rho(T)c_\mathrm{p}(T)\alpha(T) \ , \tag{6.11}$$

with the density ρ and the specific heat capacity c_p. While the density theoretically varies with temperature, it is often approximated using the value at room temperature. ρ can either be estimated from the lattice parameter obtained by XRD or determined from measuring the mass and volume of a sample. The specific heat capacity requires an additional measurement, as it substantially influences the temperature dependence of the thermal conductivity. c_p is frequently approximated by the Dulong-Petit law, which states that the heat capacity C of many elements converges at high temperatures to

$$C = 3Nk_\mathrm{B} \ , \tag{6.12}$$

where N is the number of atoms in the sample. This yields for the specific heat capacity

$$c = \frac{3R}{M} \ , \tag{6.13}$$

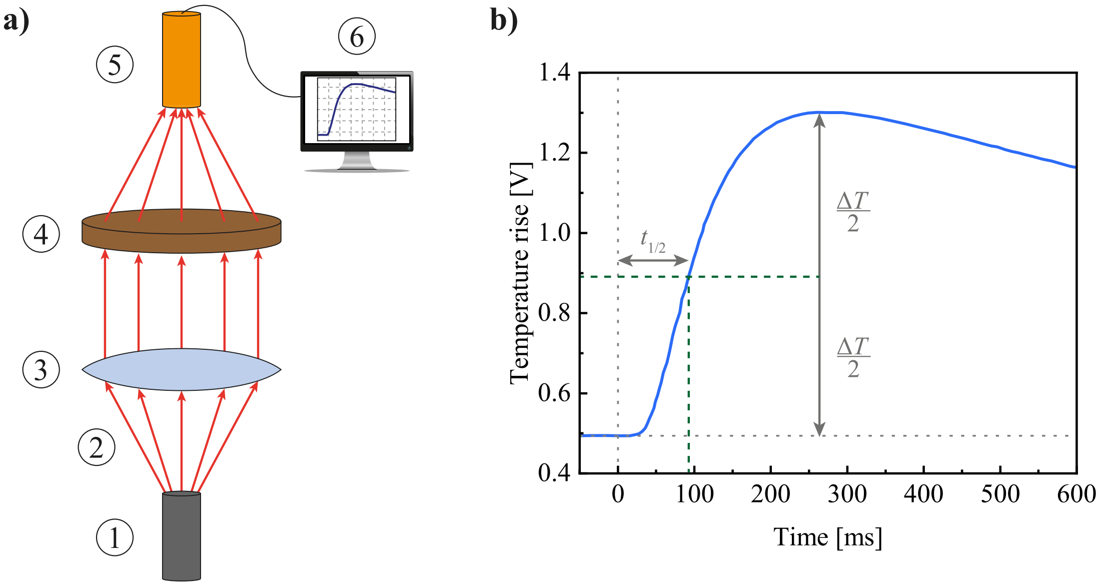

Figure 6.9: a) Illustration of the working concept of a flash system. The graphic shows the pulsed xenon source (1) generating a concentrated phonon package (2). A system of lenses (3) directs the light toward the bottom of the sample (4), inducing surface heating. Subsequently, infrared phonons from the upper surface are captured by a detector (5), which generates a signal that is processed by a software (6). b) Example of a measured signal. The phonons hitting the detector generate a voltage proportional to the sample surface temperature. Based on the time of the light pulse, the time $t_{1/2}$, indicating when the surface attains half of its total heating ΔT, is evaluated.

with the universal gas constant R and the molar mass M. In many cases, this approximation tends to overestimate the specific heat capacity. However, since the thermal conductivity enters the figure of merit with an indirect proportionality, the performance is typically underestimated rather than overestimated.

The Linseis LFA 500 is not capable for measuring thin films, as the substrate holds the majority of the mass and volume. Instead, more sophisticated techniques, such as the 3ω [176] or the transient thermoreflectance technique [263], need to be employed.

7 Thermoelectric properties of metallic NiAu films

As discussed in chapter 2, semiconductors are generally considered superior to metals in terms of the thermoelectric performance [264].

This superiority arises from their low carrier concentration, resulting in large Seebeck coefficients S [11]. However, the trade-off is a low electrical conductivity σ, creating an intrinsic entanglement between these two electronic properties. Despite numerous proposed strategies to enhance the power factor [240, 265–267], achieving a simultaneous improvement in both S and σ remains a challenging task.

This chapter introduces an interesting approach to decouple S and σ through *s*-*d* scattering. Ultra-high power factors were reported in bulk Ni−Au alloys [33], though with the drawback of their high cost. It is worth noting that the resistivity of metallic alloys is significantly lower than that of state-of-the-art thermoelectric material like Bi_2Te_3 [63]. Since the resistance of a thermoelectric module must match the load resistance [268, 269], this can potentially limit the practical applicability. To address this, an attempt was made to synthesize Ni−Au alloys as thin films on substrates, aiming to maintain their electronic properties while reducing dimensionality and the amount of material required, thus making the synthesis more cost-effective [270].

7.1 Motivation

In good metals, characterized by $\lambda_{\mathrm{el}} \gg \lambda_{\mathrm{ph}}$, where λ_{el} and λ_{ph} denote the contributions to the thermal conductivity from electrons and phonons, respectively, and the figure of merit can be approximated as [11]

$$zT = \frac{S^2}{L} - \mathcal{O}\left(\frac{\lambda_{\mathrm{ph}}}{\lambda_{\mathrm{el}}}\right) \,. \tag{7.1}$$

Here, the Wiedemann-Franz law $\lambda_{\mathrm{el}} = \sigma L T$, with $L = 2.44 \cdot 10^{-8}\,\mathrm{W\Omega K^{-2}}$ being the Lorenz number, is employed. In the metallic limit, the thermoelectric performance thus relies solely on the Seebeck coefficient of the material. Research on semiconductors is based on the assumption that a finite band gap is essential to achieve an asymmetry in the electronic density of states $D(E)$ with respect to the Fermi energy. At low temperatures, this is elucidated by the well-known Mott formula [271, 272]:

$$S(T) = -\frac{\pi^2 k_{\mathrm{B}}^2 T}{3e}\left[\frac{1}{D(E)}\frac{\mathrm{d}D(E)}{\mathrm{d}E} + \frac{1}{\tau(E)}\frac{\mathrm{d}\tau(E)}{\mathrm{d}E}\right]_{E=E_{\mathrm{F}}} \,, \tag{7.2}$$

Here, $\tau(E)$ is the temperature-dependent scattering time. While it is not uncommon to disregard the temperature dependence of the scattering time in a first approximation and describe the low-temperature Seebeck coefficient based on the shape of the DOS near the Fermi energy E_{F} [273], it is essential to note that τ can exhibit strong energy dependence, significantly modifying the overall $S(T)$ [274]. Recent theoretical calculations on $\mathrm{Ni}_x\mathrm{Au}_{1-x}$, combined with experimental data, have demonstrated a significant increase in the Seebeck coefficient in transition metals when the Fermi energy closely aligns with the edge of the d states [33]. While both elements belong to the transition element group, the d states of Au are completely filled, with the Fermi energy situated in s states, whereas in Ni, they are not fully occupied. Figure 7.1 shows the DOSs of pure Au and Ni as well as that of the solid solution.

In general, the Seebeck coefficient, comprising contributions from s and d bands, is determined by the expression [275]

$$S = \frac{S_s\sigma_s + S_d\sigma_d}{\sigma_s + \sigma_d} \,. \tag{7.3}$$

Arguably, the electrical conductivity of d states is significantly lower than that of s states ($\sigma_d \ll \sigma_s$), diminishing their contribution despite the considerably higher derivative $\mathrm{d}D(E)/\mathrm{d}E$. This leads to the simplification

$$S \approx S_s \,. \tag{7.4}$$

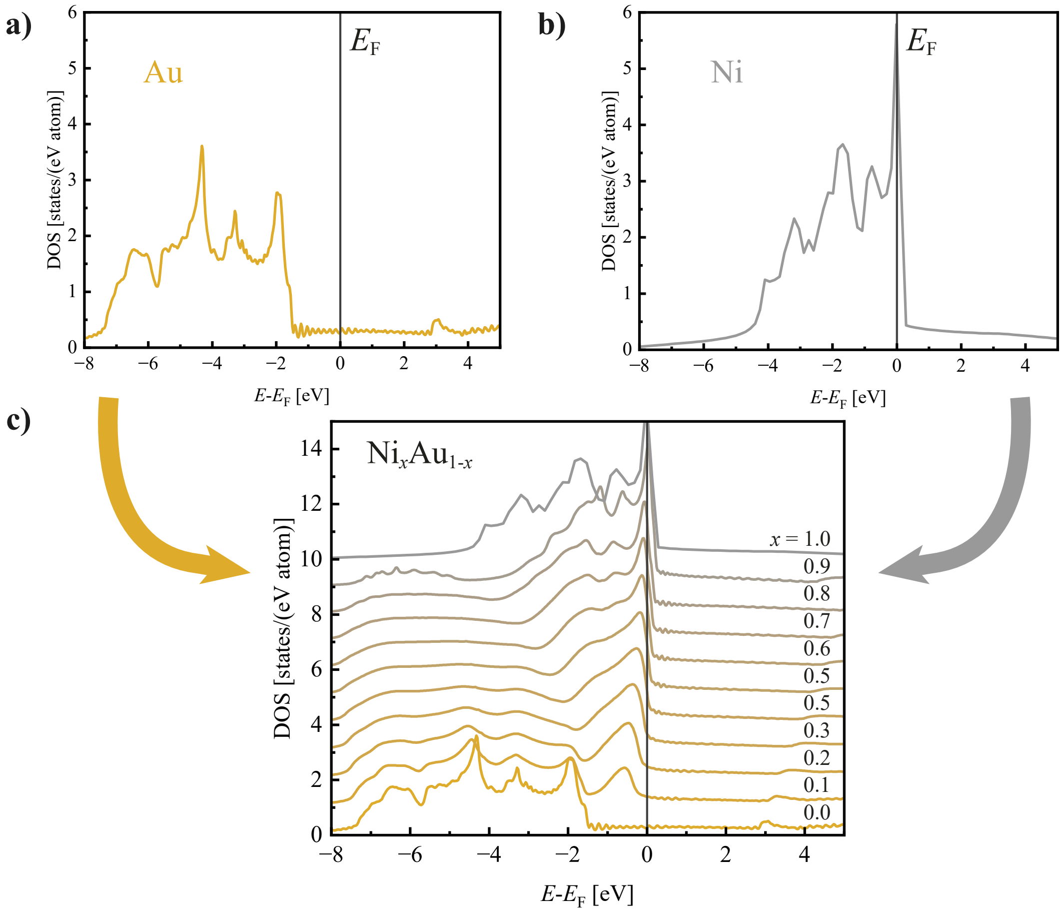

Figure 7.1: Density of states DOS of a) Au, b) Ni and c) Ni_xAu_{1-x} with respect to the Fermi energy E_F. The data were taken from Ref. [33].

In the context of the Mott formula Equation 7.2, the first term is negligible in s states due to their broad bandwidth. Conversely, in the case of Au s states scattering into Ni d states, there is a significant increase in the scattering rate τ^{-1} within the energy range of Ni d states. This results in a substantial enhancement of the second term in Equation 7.2, namely $\mathrm{d}\ln(\tau^{-1})/\mathrm{d}E$, and therefore $S \propto \mathrm{d}\ln(D_d(E))/\mathrm{d}E$, as the scattering rate depends on the phase space of the final state [276].

By partially substituting Ni with Au, effectively shifting the Fermi energy closer to the edge of the d band (see Figure 7.1), a remarkable increase in the power factor was achieved, reaching $34\,\mathrm{mWm^{-1}K^{-2}}$ in $Ni_{0.1}Au_{0.9}$ at 560 K [33]. This extraordinary large value was additionally facilitated by the fact that incorporating much larger Au atoms into the Ni matrix increases the distance between the Ni atoms. This negative chemical pressure leads to a smaller overlap of the d states, causing an even stronger localization and increase of $\mathrm{d}\ln(D_d(E))/\mathrm{d}E$.

7.2 Experimental details

The sputter target was prepared using a Ni disk with a diameter of 25.4 mm, onto which either two or three flattened Au pieces were affixed through spot-welding. Once in place, the target was compressed with a pressure of 200 bar. This not only facilitated electrical and thermal contact but also ensured a robust mechanical connection. Each Au piece weighed approximately 0.5 g, enabling the sputtering of films with a total thickness of 10 to 15 µm per target in the current setup. This showcases the cost-efficiency of this approach.

It is worth noting that the overall thickness is limited to < 1.5 mm due to the ferromagnetism of Ni. Beyond this limit, the target disrupts the magnetic field within the sputter chamber, causing a short-circuiting of the field. Consequently, the thickness significantly impacts the required gas pressure to initiate the gas discharge and thus the film's composition, as discussed in chapter 6.

The sputtering process was conducted at a temperature of 500 °C with a power of 5 W or 10 W, a target-substrate distance of 30 mm and a working gas pressure of 5 Pa. Prior to deposition, the substrates were cleaned with both acetone and ethanol. The substrates comprised unpolished Si and yttria-stabilized zirconia (YSZ) as well as polished quartz glass.

7.3 Results

7.3.1 Composition and crystal structure

The composition details of all samples are presented in Figure 7.2a. The x-axis depicts the sample number in chronological order, effectively representing the progression of the target ablation. It is apparent that the amount of Ni increases as more material is removed from the target. This phenomenon is likely attributed

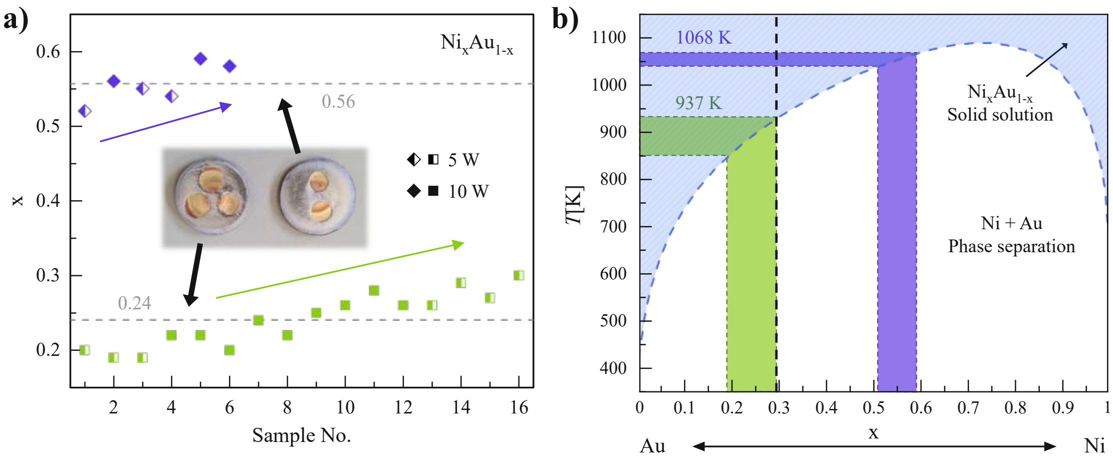

Figure 7.2: a) Composition of all Ni_xAu_{1-x} films identified by the sample number. The purple and green points belong to films sputtered from the target with two and three Au pieces shown in the inset, respectively. Half-filled symbols indicate films made at a power of 5 W, while filled symbols represent films made at 10 W. The gray dashed lines highlight the mean amount of Ni in the films. b) Phase diagram of binary Ni–Au [277]. The blue area marks the region of solubility. The purple and green areas highlight the necessary annealing temperature to obtain a single phase. For $x < 0.3$, illustrated by the black dashed line, perfect solubility was found for bulk alloys even without quenching [33]. Reproduced from Ref. [270].

to the finite volume of the Au pieces, in contrast to the quasi infinite Ni layer underneath. Films originating from the target with less Au exhibit an average Ni content of $x = 0.56$, roughly twice the amount found in films deposited from the Au-rich target ($x = 0.24$ on average) [270]. It is essential to highlight that achieving precise control over the composition through the strategic placement of Au is challenging due to several uncertainties, such as the precise positioning relative to the magnetron-sputtering ablation ring and the size, shape and even thickness of the Au pieces. This factor can influence the distribution of the ion current onto the target. Instead, attaining the desired composition necessitates adjustments of parameters such as the working gas pressure, target-substrate distance and offset and the DC power, all of which are known to impact the film's composition [247, 253, 255, 257]. For example, an examination of the Ni-rich data in Figure 7.2a reveals that the amount of Ni is slightly higher at 10 W compared to 5 W. It is important to note that the conventional theory, which states that the ratio of ejected atoms equals the target's composition due to surface adjustments (see chapter 6) does not apply in this context. This is because the two elements are spatially separated and not intermixed, resembling multi-target sputtering. This makes the individual energy-dependent sputter yield a critical factor to consider [247].

The phase diagram of binary Ni−Au alloys is depicted in Figure 7.2b [277]. In the blue-shaded area, the elements are completely soluble, hence forming a solid solution. Below a threshold temperature, depending on the composition [277], they tend to segregate, leading to the formation of Ni-rich and Au-rich phases. To achieve single-phase films, it is necessary to sputter or anneal at 937 K and 1068 K for films produced from targets with 3 and 2 Au components, respectively. Stabilization of the solid solution was achieved in bulk Ni−Au at room temperature by rapidly quenching the samples in water, effectively preserving the metastable crystal structure [33]. However, it is worth noting that for $x < 0.3$ the authors observed that a single phase could also be obtained through gradual furnace cooling, as indicated by the black dashed line in Figure 7.2b.

To investigate the structural behavior below the solid-solution regime, the films were annealed at 873 K for three days. The resulting diffraction pattern of films on quartz glass, Si and YSZ is presented in Figure 7.3. Before annealing, the films deposited on glass, with a composition of $Ni_{0.58}Au_{0.42}$, exhibit a phase resembling $Ni_{0.6}Au_{0.4}$ with minor traces of pure Au (see Figure 7.3a). Upon annealing, the structure undergoes a transition, shifting towards an Au-rich $Ni_{0.12}Au_{0.88}$ phase along with pure Ni. This transformation aligns with findings from bulk alloy measurements [33].

On Si substrates (Figure 7.3b), the same $Ni_{0.6}Au_{0.4}$ phase is formed within the $Ni_{0.52}Au_{0.48}$ sample, while the Au-rich film predominantly consists of $Ni_{0.2}Au_{0.8}$, despite a subtle presence of Ni-rich peaks. This agrees with the alloy's stability predicted for $x < 0.3$. Subsequent to the annealing process, an almost pure Au phase ($Ni_{0.03}Au_{0.97}$) forms regardless of the initial composition. Any remaining Ni disperses from the primary phase, manifesting as cubic $NiSi_2$. Notably, the crystal structure exhibits only slight variations between the samples with $x = 0.22$ and $x = 0.52$, primarily reflecting differences in the $NiSi_2$ content. The Au-rich samples additionally contain tiny amounts of a Cu−Au phase, which could originate from

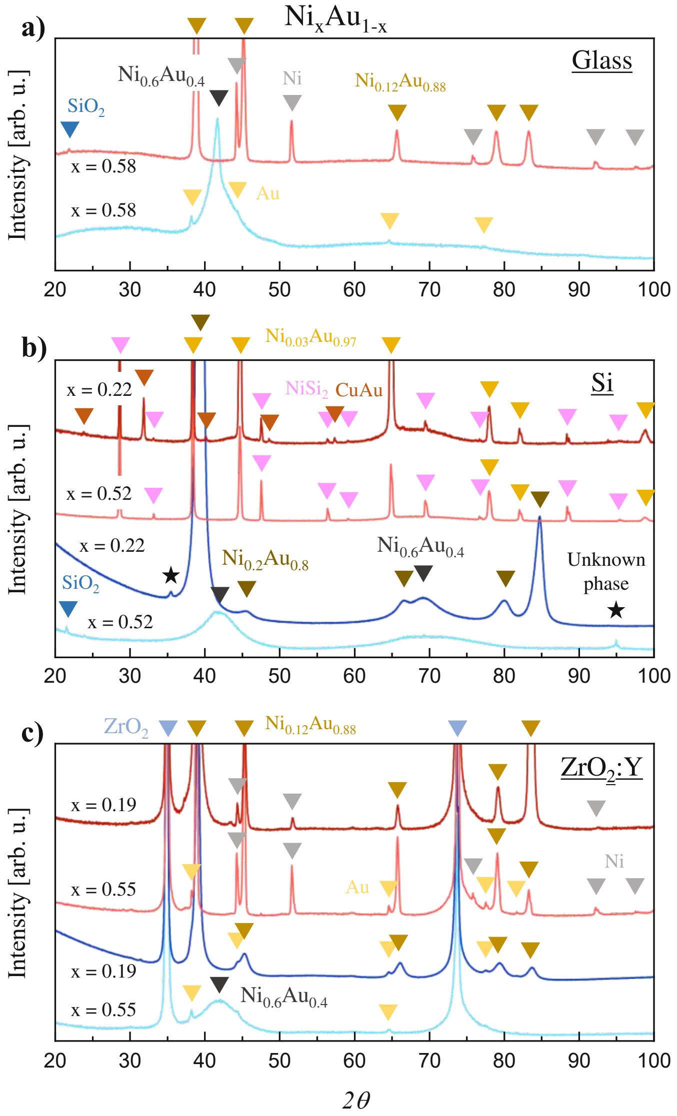

Figure 7.3: X-ray diffraction pattern of NiAu films on a) polished quartz glass, b) unpolished Si and c) unpolished YSZ. In each case, the blue and red lines represent samples before and after annealing at 873 K for three days, respectively. The Ni content, denoted as x is displayed on the left side of each line for reference. Reproduced from Ref. [270].

the copper plate of the sputter chamber.

The films deposited on YSZ with a composition of $Ni_{0.55}Au_{0.45}$ exhibit a tendency similar to that observed in the samples on quartz glass, as depicted in Figure 7.3c.

Without annealing, these films adopt a $Ni_{0.6}Au_{0.4}$ phase together with pure Au. Upon annealing, this phase disperses into $Ni_{0.12}Au_{0.88}$ along with the emergence of pure Ni. Much like the films on Si, the same crystal structure is observed on YSZ after annealing, irrespective of the composition. However, in the case of Au-rich films, the reduced Ni content leads to a decrease of pure Ni.

In summary, no significant differences are observed among the three substrates regarding the Ni_xAu_{1-x} phase. On Si, however, $NiSi_2$ forms, while in the oxide substrates, pure Ni persists. Prior to annealing, most samples contain minor traces of pure Au, hinting at a potential lack of thermal energy to stabilize into the favorable crystal structure. This is likely attributed to the fact that the temperature on the film is moderately smaller than 500 °C. The substrate heater is positioned within a copper plate beneath the substrate. The weak thermal contact between the copper and the substrate causes a decrease of the temperature which is exacerbated by the low thermal conductivity of glass ($\lambda \approx 1\,\mathrm{Wm^{-1}K^{-1}}$) and YSZ ($\lambda \approx 2\,\mathrm{Wm^{-1}K^{-1}}$) [278, 279]. Conversely, on Si, the temperature is closer to the set temperature due to the significantly larger thermal conductivity ($\lambda \approx 150\,\mathrm{Wm^{-1}K^{-1}}$) [69] and the thinner substrate (280 µm compared to 560 µm of YSZ and 1 mm of glass). These circumstance facilitates the formation of the desired crystal structure on Si.

7.3.2 Thermoelectric properties

Considering that pure Ni and Au exhibit Seebeck coefficients of only $\approx -18\,\mathrm{\mu VK^{-1}}$ and $\approx 2\,\mathrm{\mu VK^{-1}}$ at room temperature, respectively [238, 280], it is reasonable to expect that films exhibiting multiple phases would yield a lower performance compared to the bulk material comprising the same Ni_xAu_{1-x} stoichiometry. This expectation is based on the fact that multiple, non-interacting phases tend to have a detrimental effect on the overall thermoelectric performance, resulting from an averaging of thermoelectric properties across the constituents, as elucidated in chapter 5 [169].

The measured thermoelectric properties, along with the estimated figure of merit zT derived from Equation 7.1, are illustrated in Figure 7.4. For comparative purposes, the data of bulk $Ni_{0.2}Au_{0.8}$ and $Ni_{0.6}Au_{0.4}$ alloys are included [33], representing compositions that closely resemble those of the films.

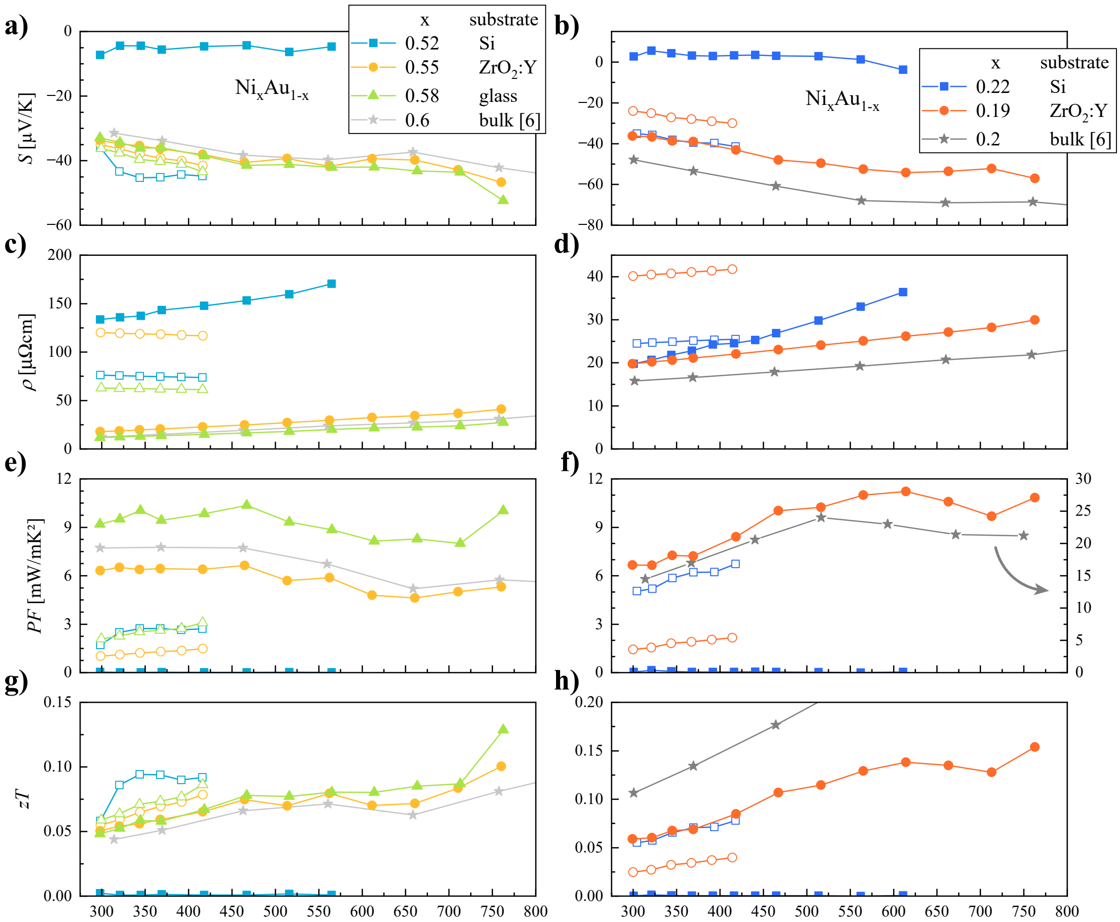

Figure 7.4: a, b) Seebeck coefficient S, c, d) electrical resistivity ρ, e, f) power factor PF and g, h) figure of merit zT of films deposited on Si, YSZ and glass substrates. Unfilled and filled data points correspond to samples before and after annealing at 873 K. The gray lines show bulk properties of annealed and slowly cooled $Ni_{0.6}Au_{0.4}$ and $Ni_{0.2}Au_{0.8}$ for comparison, taken from Ref. [33]. Reproduced from Ref. [270].

Due to the exceedingly low electrical resistivity of Ni–Au alloys, a contribution of any of the substrates can be ruled out at room temperature [168]. However, at elevated temperatures, the substantial decrease in electrical resistivity in Si results in a modification of the measured Seebeck coefficient and electrical resistivity of the film-substrate system, leading to non-physical values above 550 K (refer to chapter 5 for details).

The Seebeck coefficient does not exhibit a significant dependence on the substrate, as corroborated by the X-ray diffraction pattern. An exception to this trend is observed in annealed films on Si substrate, where a considerable reduction in the Seebeck coefficient is evident. This decline is presumable a consequence of Si diffusion and the substantial formation of a $NiSi_2$ phase. Thus, Si proves to be an unsuitable substrates for thermoelectric films containing Ni.

Given that bulk $Ni_{0.6}Au_{0.4}$ undergoes a phase segregation into an Au-rich and a Ni-rich phase [33], similar to the films with less Au, both exhibit a parallel trend in the thermoelectric properties. This is especially present in the Seebeck coefficient, as illustrated in Figure 7.4a. However, it is worth noting that the resistivity initially exhibits higher values before annealing, attributed to limited ordering within the crystal, but aligns significantly well following heat treatment, as shown in Figure 7.4c. Consequently, both the power factor and figure of merit of the films show impressive concordance with the bulk counterpart, ultimately yielding values of $10\,\mathrm{mWm^{-1}K^{-2}}$ and 0.13 at 760 K, respectively (see Figure 7.4e,g) [270].

Conversely, the phase stability observed in Au-rich bulk and films yields comparable results on YSZ. Although the Seebeck coefficient is slightly higher in the bulk material, as evident in Figure 7.4b, due to the presence of pure Ni in the film, the electrical resistivity in Au-rich films is initially elevated before annealing. While annealing reduces this value by enhancing ordering, the resistivity remains slightly higher than that of the respective bulk. Ultimately, these deviations result in a less favorable performance compared to the bulk materials, with $PF = 11.2\,\mathrm{mWm^{-1}K^{-2}}$ at 615 K and $zT = 0.15\,\mathrm{K}$ (refer to Figure 7.4f,h) [270].

Adopting the method suggested to obtain single-phase samples with $x > 0.3$ [33], films were annealed in an Ar-filled quartz glass tube at 937 K and 1068 K, followed by rapid quenching in water. Unfortunately, this approach proved challenging as the thermal shock caused by the substrate to fracture. Further experiments involving rapid cooling of the quartz ampule also proved unsuccessful and had a detrimental effect on the thermoelectric properties of the material.

7.4 Conclusion

Concluding, it can be stated that Ni_xAu_{1-x} films have been successfully prepared via DC magnetron sputtering, employing a single Ni target to which Au pieces were affixed. The Au components had a combined weight ranging from 1 to 2 g, allowing for the production of films with a cumulative thickness of 10 to 15 µm per target, demonstrating the cost-effectiveness of this single-target approach.

Achieving precise control of the composition proved challenging due to various uncertainties. To manipulate the composition effectively, sputtering-related parameters, such as the working-gas pressure, power and substrate-target distance and offset, have to be tuned.

After deposition, the films exhibited phases close to the initial stoichiometry, though the limited degree of ordering and traces of secondary phases hampered the overall performance. Upon annealing at 873 K, the phases transformed, shifting towards Au-rich phases and pure Ni. The thermoelectric properties depend on the amount of pure Ni or related phases, such as $NiSi_2$. Ultimately, a power factor of $11.2\,mWm^{-1}K^{-2}$ and figure of merit of 0.15 was achieved in $Ni_{0.19}Au_{0.81}$ deposited on YSZ.

To optimize the performance of NiAu films, rapid quenching in water appears to be necessary. However, the challenge lies in finding a suitable setup or substrate to prevent film failure during this process. Thus, future work should focus on using different substrates with better mechanical properties to withstand the thermal shock during water quenching.

8 Film composition tuning by off-stoichiometric target sputtering

In this chapter, the strategy for optimizing the composition of films produced through DC magnetron sputtering by adjusting the target's stoichiometry is elucidated, using Fe_2VAl-based films as a case study. As emphasized in chapter 6, achieving the desired stoichiometry in films can be a challenging task, primarily due to different scattering interactions of the ejected particles with the working gas. Despite the target's composition adapting to the different sputter yields of the constituents, a big benefit of sputtering compared to other deposition techniques, this can result in a film composition deviating from the intended stoichiometry.

This significant challenge can be addressed through various methods. The simplest approach involves multi-target sputtering [281–284], which employs multiple targets with distinct discharge power to control the composition. These targets may consist of single elements, alloys or compounds. However, this approach requires a proper sputter chamber equipped with multiple target holders.

Another strategy is the use of chips placed on the target to compensate for deficiencies in one or more elements [106, 285, 286]. These chips can be composed of one or multiple elements and may vary in size. While this allows for a simple adaptation of the composition, the accuracy is not very high compared to other methods.

Furthermore, adjustments of the composition can be achieved by modifying sputter parameters such as the sputter angle [285, 287, 288], power [289] or gas pressure [253, 290, 291], among others. This approach works well for two-element alloys, but may yield insufficient results in case of more constituents.

All of these strategies provide the ability to tailor the composition of sputtered films to meet the required stoichiometry, each with its own set of advantages and disadvantages. The approach presented here, adapting the target composition, tackles this issue in a different way. By varying the composition of the target, films with the desired ratio of constituents are obtained. While it requires the ability to synthesize targets, it avoids the necessity of an appropriately equipped sputter chamber, as is the case in multi-target sputtering, and does not exhibit the same accuracy and reproducibility challenges faced when placing a chip on a target.

8.1 Methodology

The stoichiometry of the target is changed according to the deviation of the film's composition. This process is conducted iteratively, starting with the synthesis of a film from a target, followed by a composition measurement. If the composition deviates from the desired stoichiometry, an error calculation is performed, leading to the synthesis of another target with an adapted composition. The procedural steps are visually represented in the flow chart shown in Figure 8.1. The initial target may be comprise either the stoichiometric composition or, when information about deficiencies in one or more constituents is pre-known, an off-stoichiometry. Despite the minimal mass loss during the induction melting of the target, resulting in a composition closely aligned with the initially weighed-in stoichiometry, the precise composition is determined through XRF measurements.

As highlighted in chapter 6, the determination of the film's composition relied on SEM-EDX measurements rather than XRF. To increase accuracy, relatively thick films of 2 µm were synthesized, effectively eliminating any signals from the substrate. Additionally, measurements were conducted at three distinct positions on the 10 mm x 5 mm large samples to ensure a sufficient average. To avoid mistakes arising from calibration inaccuracies, simultaneous measurements of the target were executed, thereby determining the error of the EDX system. Figure 8.2 provides an exemplary visualization of the composition determination process.

From the figure it becomes evident that the EDX measurements yields slightly inaccurate results. By assuming that the XRF results depict the correct stoichiometry, the EDX error ε for each element can be computed. These values are subsequently used to derive the actual composition of the film from the measured values. Furthermore, a comparison of the EDX outcomes enables the determination of the

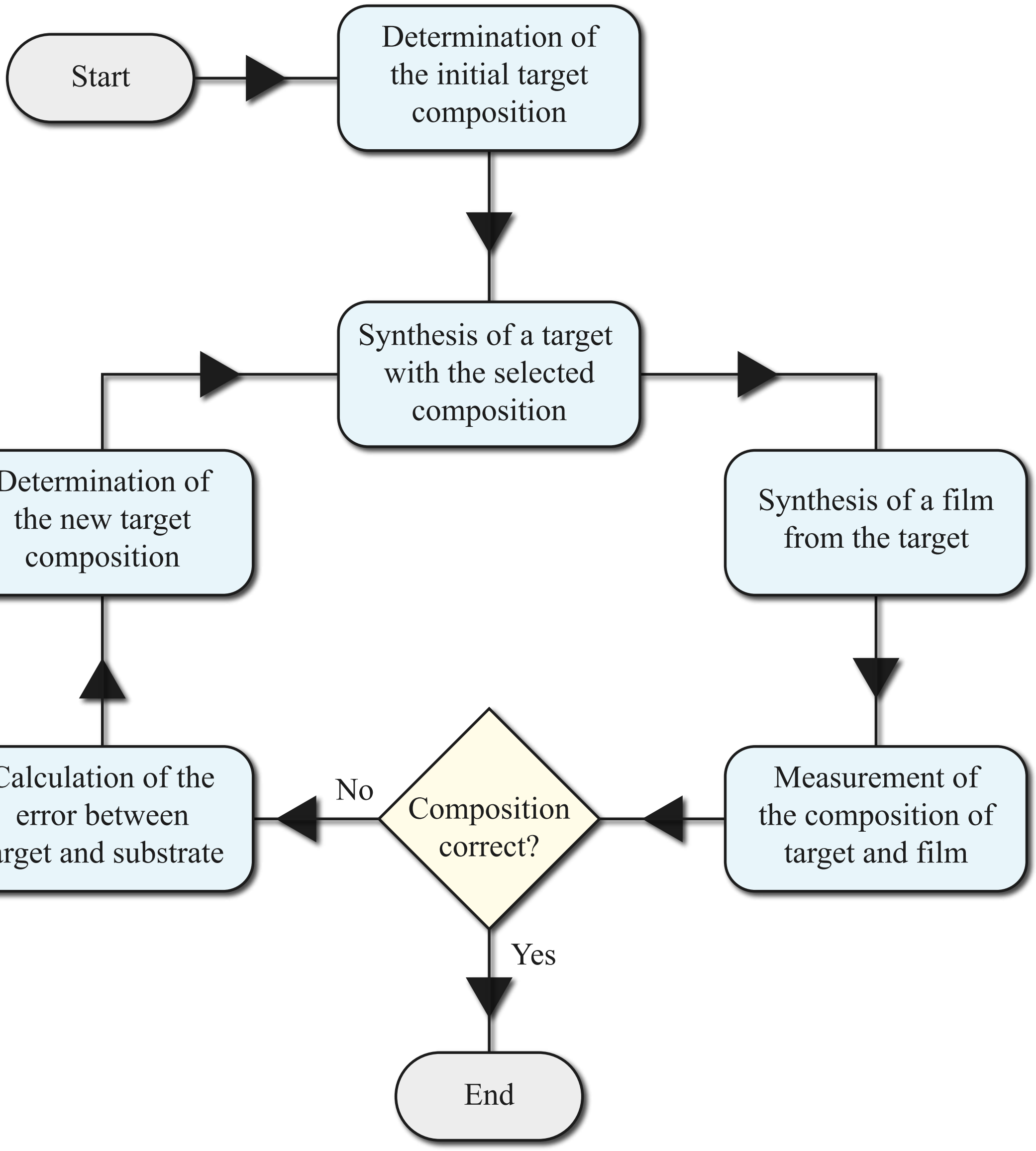

Figure 8.1: Flow chart illustrating the iterative optimization process for refining the film composition through adjustments to the stoichiometry of the target.

deviation δ between the target and film stoichiometry due to different behavior of the constituents during sputtering. Ultimately, δ is employed to evaluate the required target composition for achieving the correct film stoichiometry.

Despite the impression that the correct film composition is obtained after the first adoption of the target, a subsequent alteration in the target's composition induces

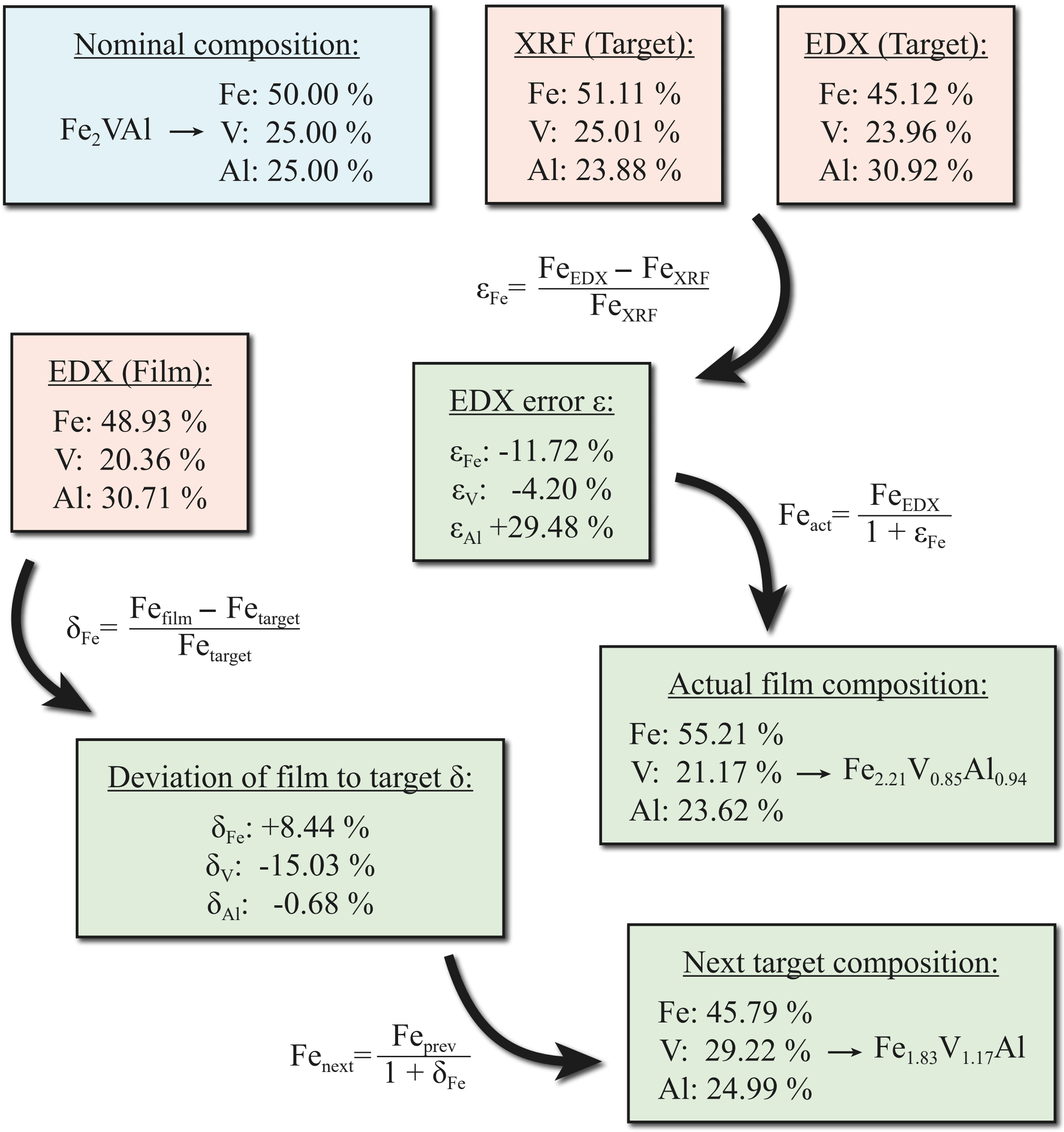

Figure 8.2: Visualization of the sequential process of determining both the film and subsequent target compositions. The blue area shows the initially weighed-in, nominal composition of Fe_2VAl. Measurement data is depicted in orange, while green areas represent calculated values. Equations present next to the arrows highlight the utilized formalism, using Fe as an illustrative example.

a change in the sputter behavior. This arises e.g. from inhomogeneities within the target, resulting from finite solubility of its constituents and the emergence of impurity phases [292]. These impurities may also possess magnetic moments, influencing the magnetic field in the vicinity of the target.

Nevertheless, through an iterative process, the deviation of the film's composition from the nominal value is gradually reduced. Each adjustment in the target composition refines the sputtering dynamics, ultimately yielding the desired stoichiometry.

8.2 Results

To further elaborate on the practicality and applicability of this approach, films with three distinct stoichiometries based on the full-Heusler compound Fe_2VAl - specifically Fe_2VAl, $Fe_2V_{0.9}Ti_{0.1}Al$ and Fe_2TaAl - were synthesized and measured with respect to their structural and thermoelectric properties. All films were sputtered on unpolished yttria-stabilized zirconia (YSZ) substrates.

For the first two compounds, Fe_2VAl and $Fe_2V_{0.9}Ti_{0.1}Al$, notable success was achieved, obtaining the desired composition within a few iteration steps. However, the synthesis of Fe_2TaAl encountered significant challenges related to the stability of the target material, ultimately leading to its abandonment, as discussed below.

8.2.1 Composition and structure

The composition of films with the desired composition of Fe_2VAl and $Fe_2V_{0.9}Ti_{0.1}Al$ in shown in Figure 8.3a and Figure 8.3b, respectively, for various synthesized targets. Films sputtered from stoichiometric targets exhibit severe off-stoichiometric compositions, $Fe_{2.21}V_{0.85}Al_{0.94}$ and $Fe_{2.10}V_{0.79}Ti_{0.08}Al_{1.04}$, which underscores the importance to investigate the composition rather than relying on the assumption that it reflects the target's composition. Notably, an excess of Fe is evident in both systems, while deficiencies in V and Ti are observed, similar to previously reported results on Fe_2VAl-based films [106, 188]. It is important to emphasize that the off-stoichiometry can not be attributed to a single element but rather represents a collective behavior of the compound.

A total of four iterations were necessary to achieve a convenient stoichiometry in the films for both systems. Ultimately, a composition of $Fe_{2.02}V_{0.99}Al$ and

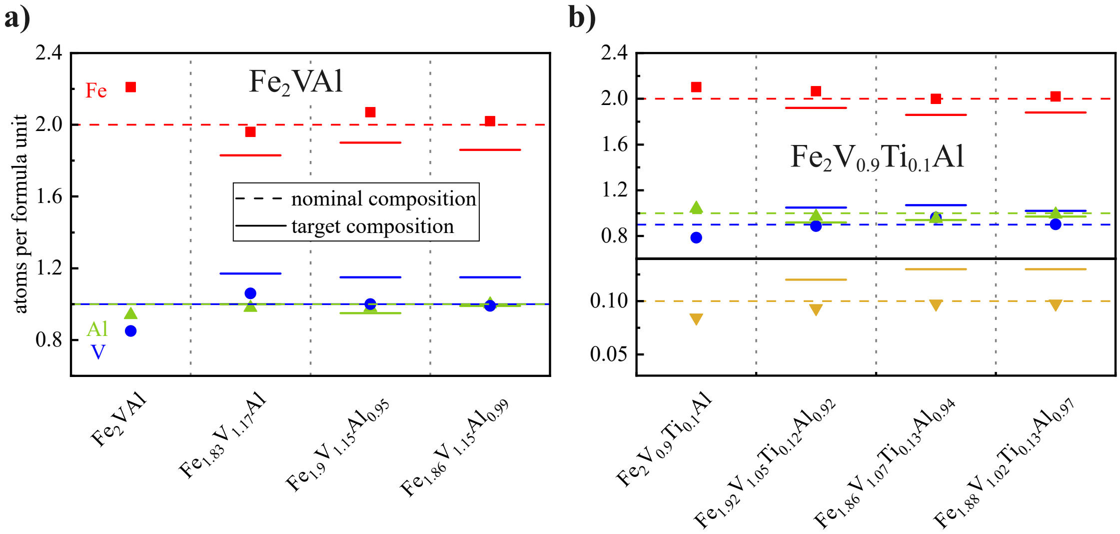

Figure 8.3: Atoms per formula unit of films made from different a) Fe_2VAl-based and b) $Fe_2V_{0.9}Ti_{0.1}Al$-based targets. Nominal stoichiometry is denoted by dashed lines, while solid lines represent the target's composition. The films' composition resulted from the final target is $Fe_{2.02}V_{0.99}Al$ and $Fe_{2.02}V_{0.9}Ti_{0.1}Al_{0.99}$.

$Fe_{2.02}V_{0.9}Ti_{0.1}Al_{0.99}$ was obtained from $Fe_{1.86}V_{1.15}Al_{0.99}$ and $Fe_{1.88}V_{1.02}Ti_{0.13}Al_{0.97}$ targets, respectively, closely resembling the desired stoichiometry.

While Fe_2TaAl is predicted to exhibit superior thermoelectric properties owing to its advantageous electronic structure [50, 293–295], the synthesis of this material in bulk form has proven challenging due to the formation of different phases. However, as long as the multiple phases are homogeneously distributed within the target, there is no need for a single-phase target. The films sputtered from the nominal target exhibit a composition of $Fe_{2.14}Ta_{1.12}Al_{0.74}$. Attempts to modify the target's stoichiometry to $Fe_{1.82}Ta_{0.87}Al_{1.31}$ failed due to a lack of mechanical stability, causing the bulk material to fracture upon cooling down after induction melting. This issue persisted even after slight changes in the composition, hence the composition was eventually abandoned.

To further elucidate the structural characteristics, the X-ray diffraction pattern of stoichiometric Fe_2VAl and $Fe_2V_{0.9}Ti_{0.1}Al$, as well as that of the films with the closest composition, is presented in Figure 8.4. The structural analysis of the targets reveals the presence of all dominant peaks characteristic of the full-Heusler structure. Of particular significance are the (111) and (200) lines, appearing at ≈

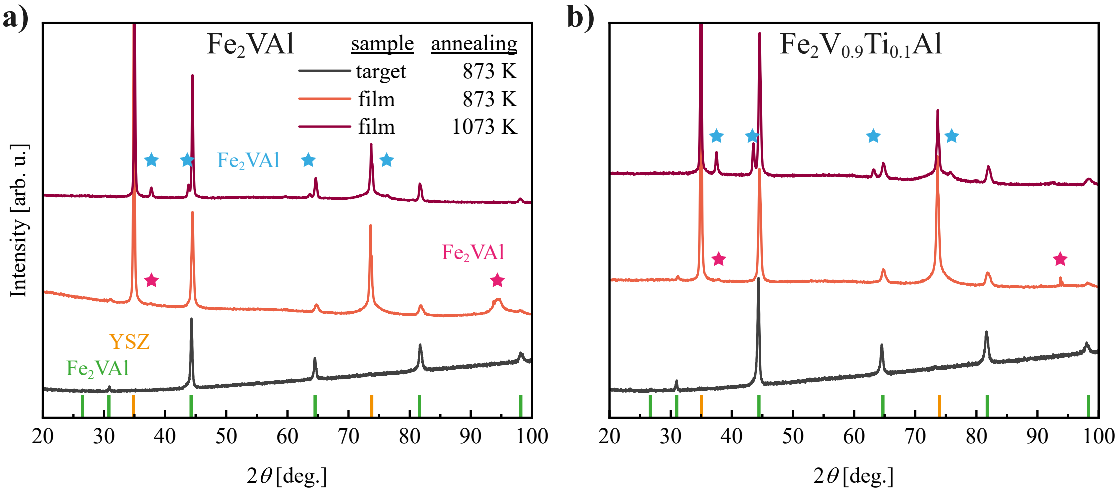

Figure 8.4: X-ray diffraction pattern of a) Fe_2VAl and b) $Fe_2V_{0.9}Ti_{0.1}Al$, featuring the stoichiometric targets (gray line) alongside the films with the closest composition annealed at 873 K and 1073 K for 3 days. Peaks from the full-Heusler structure and YSZ substrate are highlighted with green and orange marks, respectively. Different impurity phases present in the films are depicted with pink and blue symbols.

27 ° and ≈ 31 °, respectively. These lines serve as indicators of the degree of disorder within the material. In the event of *B*2 disorder, where a complete disordering of the V and Al sites occurs, the (111) peak vanishes, while the fully disordered *A*2 structure lacks both lines [123]. Although not clearly visible in Figure 8.4, both peaks are present in the targets, suggesting nearly complete ordering.

On the contrary, the films do not exhibit a fully-ordered structure. Aside from peaks originating from the substrate and disorder-independent peaks from the full-Heusler structure, films annealed at 873 K reveal only the (200) peak. Furthermore, upon annealing at 1073 K, both the (111) and (200) lines are absent. Simultaneously, additional impurity phases, presumable oxides, form during the annealing process.

8.2.2 Thermoelectric properties

The thermoelectric properties of both the stoichiometric and final target were measured, alongside those of films with the closest composition. The results for Fe_2VAl are presented in Figure 8.5. Bulk Fe_2VAl has a Seebeck coefficient and electrical

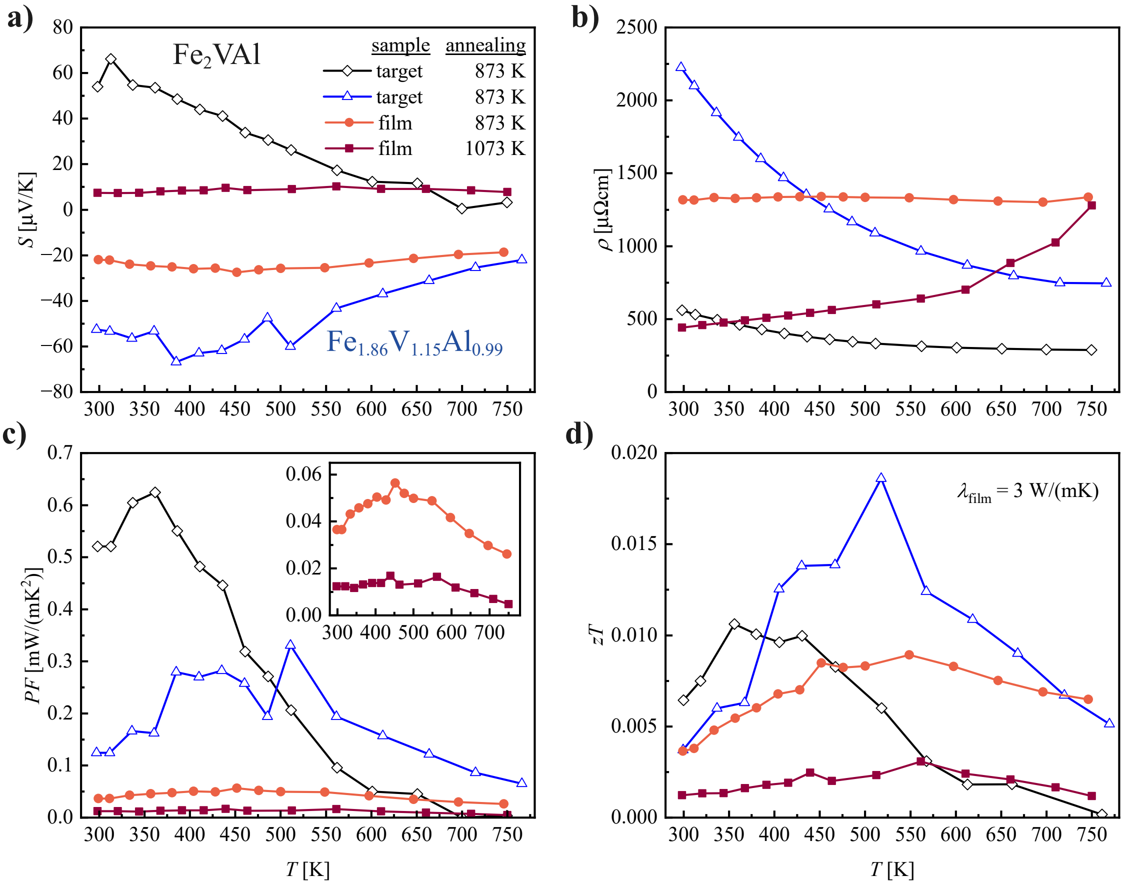

Figure 8.5: a) Seebeck coefficient S, b) electrical resistivity ρ, c) power factor PF and d) figure of merit zT of the Fe$_2$VAl target (black symbols) and the films with the closest stoichiometry after annealing at 873 K (light red symbols) and 1073 K (dark red symbols) as a function of temperature. In addition, the thermoelectric properties of the final target are included (blue symbols). zT of the films was calculated assuming a temperature-independent thermal conductivity of 3 Wm^{-1}K^{-1}, consistent with prior findings [296].

resistivity exhibiting a semiconductorlike behavior, consistent with prior finding for this material [50, 51, 103, 297]. Moreover, the properties of the final off-stoichiometric target align with those measured for Fe$_{2-x}$V$_{1+x}$Al [298]. Notably, despite a decrease in the valence electron concentration compared to the stoichiometric material, a negative Seebeck coefficient is observed.

The peculiar electronic structure of Fe$_2$VAl, representing a small-gap semiconductor or semimetal [165–167], results in significant variations of all thermoelectric quantities due to disorder or changes in the charge carrier concentration from off-stoichiometry [299]. Consistent with this, a large negative Seebeck coefficient was previously reported in $B2$-disordered Fe_2VAl [300], aligning with the measured Seebeck coefficient of the $B2$-disordered film annealed at 873 K. The electrical resistivity exhibits an almost constant behavior, suggesting imperfect crystallization of the Heusler structure within the film due to limited thermal energy during sputtering and annealing. Annealing at 1073 K, inducing a metallic structure, deteriorates the Seebeck coefficient to $< 10\,\mu VK^{-1}$. Furthermore, the electrical resistivity is changed into a linearly increasing behavior dominated by electron-phonon interaction, typical for metals.

Ultimately, a maximum power factor of $5.6 \cdot 10^{-2}\,mWm^{-1}K^{-2}$ at 450 K was achieved. Assuming a constant thermal conductivity of $3\,Wm^{-1}K^{-1}$ [296], a figure of merit of $8.2 \cdot 10^{-3}$ at 550 K was obtained. Despite these values not reaching reported performances of other Fe_2VAl films, this is attributed to finite crystallization and limited degree of order in the structure rather than off-stoichiometry.

The thermoelectric properties of both bulk and film $Fe_2V_{0.9}Ti_{0.1}Al$ are depicted in Figure 8.6. The bulk sample displays a Seebeck coefficient of $65\,\mu VK^{-1}$ alongside a small, linearly increasing resistivity, consistent with previously reported results [301]. Moreover, a power factor exceeding $2\,mWm^{-1}K^{-2}$ and a figure of merit of 0.05 are achieved. The final off-stoichiometric target exhibits a semiconductorlike resistivity with a negative slope, indicating that the Fermi energy is positioned close to the valence band's edge. This assumption is supported by the slightly increased Seebeck coefficient.

Similar to the Fe_2VAl discussed above, films with a composition resembling $Fe_2V_{0.9}Ti_{0.1}Al$ exhibit a disorder-induced negative Seebeck coefficient, characteristic of this material class [300]. After annealing at 873 K, the Seebeck coefficient reaches approximately $-40\,\mu VK^{-1}$. This is associated with an increased resistivity displaying a small negative temperature dependence, indicative of disorder-dominated transport. Eventually, a broad maximum power factor of $0.12\,mWm^{-1}K^{-2}$ is achieved between 330 and 490 K (see inset of Figure 8.6c). Once again, this value falls below previously reported performances of fully-ordered $Fe_2V_{0.9}Ti_{0.1}Al$ films [201], attributed to the formation of impurity phases upon annealing at 1073 K and a

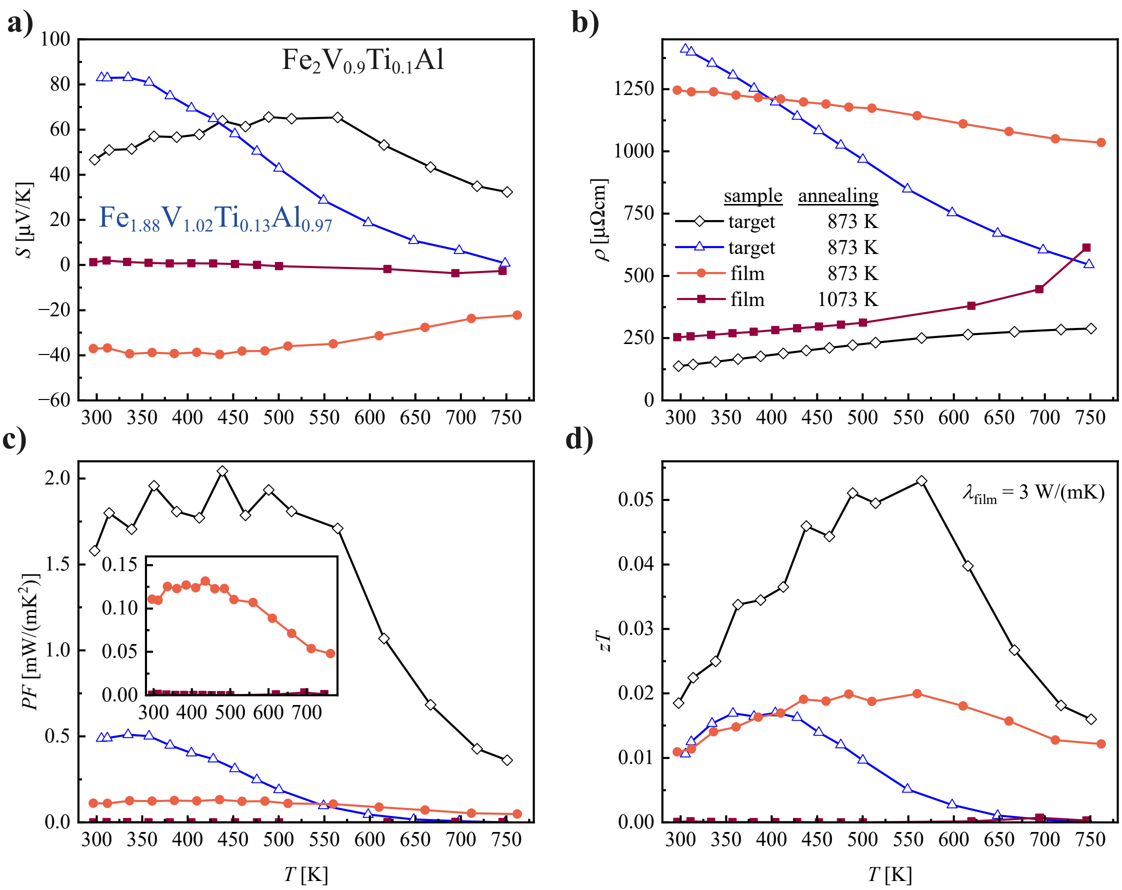

Figure 8.6: a) Seebeck coefficient S, b) electrical resistivity ρ, c) power factor PF and d) figure of merit zT of the $Fe_2V_{0.9}Ti_{0.1}Al$ target (black symbols) and the films with the closest stoichiometry after annealing at 873 K (light red symbols) and 1073 K (dark red symbols) as a function of temperature. In addition, the thermoelectric properties of the final target are included (blue symbols). zT of the films was calculated assuming a temperature-independent thermal conductivity of $3\,\mathrm{Wm^{-1}K^{-1}}$, consistent with prior findings [296].

reduction in the degree of ordering, thereby diminishing the thermoelectric performance.

On the other hand, recent findings from film sputtered from a stoichiometric $Fe_2V_{0.9}Ti_{0.1}Al$ align with the presented films in terms of composition, resembling $Fe_{2.19}V_{0.83}T_{0.07}Al_{0.91}$. The severe off-stoichiometry lead to an overall performance of only $PF \approx 0.06\,\mathrm{mWm^{-1}K^{-2}}$. Thus, by the approach presented here, controlling the stoichiometry of the films through variations in the target's composition, a substantial enhancement in performance could be achieved.

In summary, it can be stated that the films' composition could be successfully tuned by adapting the stoichiometry of the target through an iterative process. Despite the moderate thermoelectric performance of the obtained films, attributed to a non-perfect formation of the full-Heusler structure, this provides a promising route towards synthesizing films from a single-target sputtering device.

9 Conclusion

The scope of this thesis encompassed different aspects of thermoelectricity. The first part focused on investigating the thermoelectric quantities in the regime of a parabolic-band approximation of the band structure. A comprehensive exploration of the Seebeck coefficient, electrical resistivity and Hall coefficient culminated in the development of a collaborative software tool. This tool, written in Python and encapsulated in a publicly available application, fits temperature-dependent properties to obtain information about the band structure - namely the position of the Fermi energy, the band gaps and the mass ratios weighted with the degeneracies - and dominant scattering processes. The flexibility to toggle between a single-, two- and three-parabolic-band model ensures a broad applicability. The integration of a neural network, providing an initial fit guess, coupled with an intuitive user interface, facilitates a straightforward analysis of studied materials.

Additionally, the thesis delved into a theoretical exploration of the thermoelectric properties of multi-material configurations, unraveling the contributions of the individual constituents. Investigations on film-substrate systems elucidated the substrate's potential impact on measured properties, especially when its resistance approaches that of the film. This situation could lead to misinterpretations of the film's performance. The effect is proportional to the material-related quantity $\varepsilon = \sigma_\mathrm{s} d_\mathrm{s}/(\sigma_\mathrm{f} d_\mathrm{f})$, where σ is the electrical conductivity, d the thickness and f and s denote the film and substrate, respectively.

A similar study on composites comprising a thermoelectric material and a highly conducting material revealed the misleading nature of distinct thermoelectric quantities. The conductive properties of the metal decouple the Seebeck coefficient and electrical conductivity, potentially resulting in extreme power factor values. However, a minute examination of the efficiency of composites with varying metal-to-thermoelectric ratios revealed their inferior performance compared to the thermoelectric alone. This conclusion was corroborated by measurements on serial Cu-$Fe_2VAl_{1.5}$ composites with different metal amounts. Ultimately, the actual power output and figure of merit were proposed as error-resistant quantities to prevent misinterpretations of future composite studies.

Finally, NiAu films were synthesized through magnetron sputtering from a Ni target with affixed Au pieces, showcasing a significant cost reduction compared to the bulk material. Despite challenges in crystallizing the desired structure, a large power factor of $11.2\,\mathrm{mWm^{-1}K^{-2}}$ at 614 K was obtained in $Ni_{0.27}Au_{0.73}$. Neglecting the phonon contribution to thermal conduction, justified by the dominance of electrons in metallic systems, yielded a figure of merit of $zT = 0.15$ at 763 K, in alignment with the respective bulk performance. Nevertheless, issues concerning the stability of film and substrate arose when attempting to reproduce the quenching procedure necessary to obtain a single-phase compound for $\mathrm{Ni} > 0.3$.

Acknowledgments

First of all, I would like to express my sincere gratitude to Prof. Ernst Bauer, my supervisor, for his enduring support and invaluable guidance throughout my doctoral studies. His vast expertise in the field of solid-state physics has been helpful in overcoming numerous challenges and I am grateful for his readiness to assist whenever needed.

Special thanks to Prof. Christoph Eisenmenger-Sittner for generously providing access to the magnetron-sputtering chamber and related equipment, significantly contribution to the success of my research.

I extend my appreciation to Prof. Oscar Juan Dura from the University of Castilla-La Mancha and Prof. Bo Brummerstedt Iversen from the Aarhus University for offering a stay at their institute. Their guidance and insights into experimental procedures have been crucial to my academic growth.

I am thankful to Prof. Takao Mori from the University of Tsukuba for heading and managing the MIRAI project (JPMJMI19A1) and providing financial support for the projects described in this thesis.

My sincere thanks to Bernhard Hinterleitner for introducing me to the field of thermoelectricity and guiding my initial steps in the laboratory.

I am grateful to my colleagues, Michael Parzer and Fabian Garmroudi, for engaging discussions on physics, constructive criticism on written papers and valuable input during challenging times in my doctoral studies.

Prof. Johannes de Boor deserves appreciation for his useful contribution on the fitting software setup and its underlying physics.

I extend my thanks to the students I had the privilege to supervise, whose dedication accelerated experimental work and enabled me to to focus on multiple projects concurrently.

A special appreciation goes to Gerda Rogl and Andrej Pustogow for insightful discussions on various relevant topics.

Thanks to Werner Artner from the X-ray Center of TU Wien and the staff at USTEM and the university's workshop for their continuous support in addressing various experimental challenges.

I am profoundly thankful to my mother, sister and family-in-law for their endless support, which has been a source of strength throughout my doctoral journey.

Last but certainly not least, I express my deepest gratitude to my wife, Cornelia Riss, for her unwavering support. Her encouragement, understanding and motivation have been an anchor in overcoming challenges and completing my thesis.

Part III

Appendix

A Properties of the Seebeck coefficient of a parabolic band

While the Seebeck coefficient may exhibit a complex shape in real materials, the use of parabolic bands for the band structure yields excellent agreement in many cases. Then, the Seebeck coefficient is easily calculated. particularly interesting is the low- and high-temperature limit of a single parabolic band, as it provides fundamental understanding.

A.1 Low-temperature limit of the Seebeck coefficient

The derivation presented assumes a single parabolic band. However, as the derived results are only valid at low temperatures ($k_\mathrm{B}T \ll E_\mathrm{F}$), it is also limit for multiple bands if only one band is present in the vicinity of the Fermi energy.

To obtain the low-temperature behavior of the Seebeck coefficient, the Sommerfeld expansion for small temperatures is of essence [158]:

$$\int_{-\infty}^{\infty} \frac{H(E)}{e^{\beta(E-\mu)}+1}\,\mathrm{d}E = \int_{-\infty}^{\mu} H(E)\,\mathrm{d}E + \frac{\pi^2}{6}\left(\frac{1}{\beta}\right)^2 H'(\mu) + \mathcal{O}\left(\frac{1}{\beta\mu}\right)^4 . \tag{A.1}$$

Here, $H(E)$ is an arbitrary function of E, $\beta = 1/(k_\mathrm{B}T)$ is the inverse temperature and μ is the chemical potential. Equation A.1 yields for the Fermi-Dirac integral of 0^th and 1^st order

$$F_0(\eta) = \int_0^{\infty} \frac{1}{e^{\xi-\eta}+1}\mathrm{d}\xi \approx \eta \tag{A.2}$$

and

$$F_1(\eta) = \int_0^{\infty} \frac{\xi}{e^{\xi-\eta}+1}\mathrm{d}\xi \approx \frac{\eta^2}{2} + \frac{\pi^2}{6} . \tag{A.3}$$

Inserting Equation A.2 and Equation A.3 into the general formula of the Seebeck coefficient of a single parabolic conduction band with $\lambda = 0$,

$$S\left(T\right) = \frac{k_\mathrm{B}}{e}\left[\eta - 2\frac{F_1\left(\eta, T\right)}{F_0\left(\eta, T\right)}\right] , \tag{A.4}$$

yields

$$\begin{aligned} S(T) &\approx \frac{k_\mathrm{B}}{e}\left[\eta - \frac{2}{\eta}\left(\frac{\eta^2}{2} + \frac{\pi^2}{6}\right)\right] \\ &= -\frac{\pi^2 k_\mathrm{B}}{3e}\eta = -\frac{\pi^2 k_\mathrm{B}}{3e}\frac{k_\mathrm{B}T}{\mu} . \end{aligned} \tag{A.5}$$

Finally, approximating the chemical potential as E_F at low temperatures results in

$$S(T) \approx -\frac{\pi^2 k_\mathrm{B}}{3e}\frac{k_\mathrm{B}T}{E_\mathrm{F}} . \tag{A.6}$$

As a side note, it should be mentioned that the well-known Mott formula [271, 272],

$$S(T) = -\frac{\pi^2 k_\mathrm{B}^2 T}{3e}\left[\frac{1}{\sigma(E)}\frac{\mathrm{d}\sigma(E)}{\mathrm{d}E}\right]_{E=E_\mathrm{F}} , \tag{A.7}$$

which approximates the Seebeck coefficient of metals and semimetals, is also obtained by a Sommerfeld expansion of the energy-dependent electrical conductivity $\sigma(E) = D(E)v^2(E)\tau(E)$. Different to the derivation above, this approximation is not limited to parabolic bands. Under the assumption of a temperature-independent velocity, the equation simplifies to

$$S(T) = -\frac{\pi^2 k_\mathrm{B}^2 T}{3e}\left[\frac{1}{D(E)}\frac{\mathrm{d}D(E)}{\mathrm{d}E} + \frac{1}{\tau(E)}\frac{\mathrm{d}\tau(E)}{\mathrm{d}E}\right]_{E=E_\mathrm{F}} . \tag{A.8}$$

A.2 High-temperature limit of the Seebeck coefficient

The Fermi-Dirac integral of j^th order, $F_j\left(\eta(T)\right)$, can be expressed with the Dirichlet eta function $\tilde{\eta}$ for $T \to \infty$:

$$F_j\left(\eta \to 0\right) = \tilde{\eta}(j+1) = \sum_{n=1}^{\infty}\frac{(-1)^{n-1}}{n^{j+1}} . \tag{A.9}$$

The Dirichlet eta function can be explicitly written for $j = 0$ and $j = 1$:

$$F_0\left(\eta \to 0\right) = \tilde{\eta}(1) = \ln(2)\ , \tag{A.10}$$

$$F_1\left(\eta \to 0\right) = \tilde{\eta}(2) = \frac{\pi^2}{12}\ . \tag{A.11}$$

By inserting Equation A.10 and Equation A.11 into the general notation of the Seebeck coefficient (Equation 3.32),

$$S\left(T\right) = \frac{k_\mathrm{B}}{e}\left[\eta(T) - \frac{\lambda+2}{\lambda+1}\frac{F_{\lambda+1}\left(\eta(T)\right)}{F_\lambda\left(\eta(T)\right)}\right]\ , \tag{A.12}$$

reveals the high-temperature limit of the Seebeck coefficient of a single parabolic band for acoustic-phonon and alloy-disorder scattering ($\lambda = 0$):

$$S\left(T \to \infty\right) = \frac{k_\mathrm{B}}{e}\left[\eta(T \to \infty) - 2\frac{F_1\left(\eta(T \to \infty)\right)}{F_0\left(\eta(T \to \infty)\right)}\right] \tag{A.13}$$

$$= -\frac{2k_\mathrm{B}\pi^2}{12e\ln(2)} \tag{A.14}$$

B Calculation of the current distribution in film-substrate systems

The current arising in a parallel two-layer system flows through the interface only at the edge of the sample. This can be shown by assuming an additional interface connection between the film and the substrate with resistance R_i in addition to the junctions at both ends (see Figure B.1). All arising voltages and currents (depicted in Figure B.1b) can be written as:

$$\begin{aligned}
U_1 &= (1-x)\,R_\mathrm{f} I_1 + (1-x)\,U_\mathrm{f}\ ,\\
U_2 &= R_\mathrm{i} I_2\ ,\\
U_3 &= x R_\mathrm{f} I_3 + x U_\mathrm{f}\ ,\\
U_4 &= x R_\mathrm{s} I_4 - x U_\mathrm{s}\ ,\\
U_5 &= (1-x)\,R_\mathrm{s} I_5 - (1-x)\,U_\mathrm{s}\ ,
\end{aligned} \tag{B.1}$$

with the indices f, s and i denoting the film, substrate and interface, respectively. x is the relative position of the additional connection. These equations can be written in a more compact way:

$$\mathbf{U} = \tilde{\mathbf{Z}}\mathbf{I} + \mathbf{U}_\mathrm{q}\ . \tag{B.2}$$

Here, $\mathbf{U}_\mathrm{q}$ is given by

$$\mathbf{U}_\mathrm{q} = \begin{pmatrix} (1-x)\,U_\mathrm{f} \\ 0 \\ xU_\mathrm{f} \\ -xU_\mathrm{s} \\ -(1-x)\,U_\mathrm{s} \end{pmatrix} \tag{B.3}$$

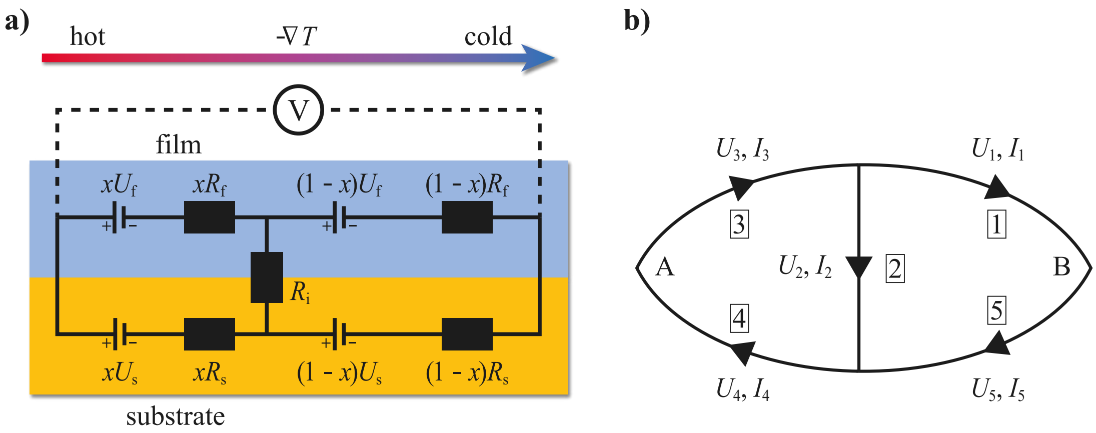

Figure B.1: a) Electrical circuit describing the parallel film-substrate model discussed in chapter 5, with an additional connection between film and substrate at the relative position $0 < x < 1$ with resistance R_i. The total thermovoltage and resistance of the film and the substrate are denoted as U_f, R_f and U_s, R_s, respectively. b) Simplified picture used for solving the circuit by applying network analysis. U_i and I_i, with $i = [1, 5]$, specify the potential drop and the current along the branches, respectively. Reproduced from Ref. [168].

and $\tilde{\mathbf{Z}}$ is

$$\tilde{\mathbf{Z}} = \begin{pmatrix} (1-x)\,R_\mathrm{f} & 0 & 0 & 0 & 0 \\ 0 & R_\mathrm{i} & 0 & 0 & 0 \\ 0 & 0 & xR_\mathrm{f} & 0 & 0 \\ 0 & 0 & 0 & xR_\mathrm{s} & 0 \\ 0 & 0 & 0 & 0 & (1-x)\,R_\mathrm{s} \end{pmatrix}. \tag{B.4}$$

This equation can be solved and yields

$$\mathbf{I} = \frac{U_\mathrm{s} - U_\mathrm{f}}{R_\mathrm{f} + R_\mathrm{s}} \begin{pmatrix} 1 \\ 0 \\ 1 \\ 1 \\ 1 \end{pmatrix} \tag{B.5}$$

for the currents of the different branches and

$$\mathbf{U} = \frac{R_\mathrm{s}U_\mathrm{f} + R_\mathrm{f}U_\mathrm{s}}{R_\mathrm{f} + R_\mathrm{s}} \begin{pmatrix} 1-x \\ 0 \\ x \\ -x \\ -(1-x) \end{pmatrix} \tag{B.6}$$

for the branch voltages. As expected, the current through the interface becomes zero ($I_2 = 0$) and the current passes through the interface only at the edge of the system, yielding equal currents for all branches: $I_1 = I_3 = I_4 = I_5$. Furthermore, $U_2 = 0$ and the measured voltage becomes

$$U_\mathrm{meas} = U_1 + U_3 = -(U_4 + U_5) = \frac{R_\mathrm{s}U_\mathrm{f} + R_\mathrm{f}U_\mathrm{s}}{R_\mathrm{f} + R_\mathrm{s}} \,, \tag{B.7}$$

therefore independent of the interface resistance R_i and its relative position x. The same holds true for a larger number of interface connections at arbitrary positions.

When additionally adding interface resistances R_i' on both ends of the circuit, the (indisputable more realistic) situation becomes a bit different. The current I_2 through the interface inside the sample is then proportional to

$$I_2 \propto (1-2x)R_\mathrm{i}' \tag{B.8}$$

and only vanishes for either $R_\mathrm{i}' = 0$, which was discussed above, or $x = 0.5$, *i.e.* the interface connection is positioned exactly in the middle of the sample. For an asymmetric arrangement $x \neq 0.5$, a current will flow through the interface connection, altering the measured voltage. However, assuming an infinite number of interface connections with equal resistances, representing real systems, eventually leads to a symmetric distribution of resistances. This results in opposing currents of neighboring sub-circuits cancel each other out, similar to what is depicted in Figure 5.1. Ultimately, this again leads to vanishing currents through inner interface connections.

Over all, the simple model derived in the main text describes the underlying processes fairly well and conveniently describes the potential contribution of the substrate to the total thermoelectric properties.

C Consideration of small interface resistances

In a composite, the interactions at the interfaces between different constituents can alter its thermoelectric performance. These interfaces can cause scattering of charge carriers, resulting in locally reduced electrical and thermal conductivity. More importantly, phonon scattering on interface structures hampers heat conduction, lowering the overall thermal conductivity but also causing a discontinuity of the temperature at the interface. Such a scenario is illustrated in Figure C.1. Similar to the derivation of Equation 5.30 and Equation 5.31, the temperature drop across both the thermoelectric material and the metal can be derived:

$$\Delta T_{\mathrm{te}} = \frac{\Lambda_{\mathrm{i}}\Lambda_{\mathrm{m}}}{\Lambda_{\mathrm{i}}\Lambda_{\mathrm{te}} + \Lambda_{\mathrm{i}}\Lambda_{\mathrm{m}} + \Lambda_{\mathrm{te}}\Lambda_{\mathrm{m}}}\Delta T\ , \tag{C.1}$$

$$\Delta T_{\mathrm{m}} = \frac{\Lambda_{\mathrm{i}}\Lambda_{\mathrm{te}}}{\Lambda_{\mathrm{i}}\Lambda_{\mathrm{te}} + \Lambda_{\mathrm{i}}\Lambda_{\mathrm{m}} + \Lambda_{\mathrm{te}}\Lambda_{\mathrm{m}}}\Delta T\ , \tag{C.2}$$

with the thermal conductances $\Lambda_j = \lambda_j A / l_j$ and $j = \{\mathrm{te, m, i}\}$ denoting the thermoelectric, metal and interface, respectively.

Using the thermal resistance $\theta_j = 1/\Lambda_j$, these equations can be written more conveniently as

$$\begin{aligned} \Delta T_{\mathrm{te}} &= \frac{\theta_{\mathrm{te}}}{\theta_{\mathrm{te}} + \theta_{\mathrm{m}} + \theta_{\mathrm{i}}}\Delta T \\ &= \left(1 + \frac{\theta_{\mathrm{i}}}{\theta_{\mathrm{te}} + \theta_{\mathrm{m}}}\right)^{-1} \Delta T_{\mathrm{te}}^{id} \end{aligned} \tag{C.3}$$

and

$$\Delta T_{\mathrm{m}} = \left(1 + \frac{\theta_{\mathrm{i}}}{\theta_{\mathrm{te}} + \theta_{\mathrm{m}}}\right)^{-1} \Delta T_{\mathrm{m}}^{id}\ . \tag{C.4}$$

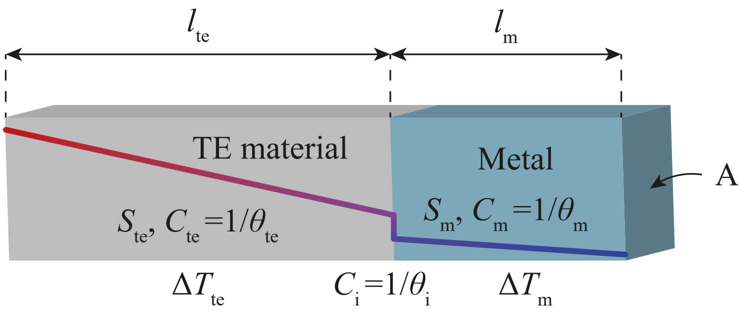

Figure C.1: Schematic sketch of a serial connection of a thermoelectric material (length l_{te}) and a metal (length l_{m}), incorporating an interface thermal resistance. Both material possess individual Seebeck coefficients S and thermal conductances $\Lambda = 1/\theta$, while the interface is characterized by an additional thermal conductance. The temperature difference across the thermoelectric material and the metal are denoted as ΔT_{te} and ΔT_{m}, respectively. The solid line sketches the temperature profile. Reproduced from Ref. [169].

Here, $\Delta T_{\mathrm{te}}^{id}$ and $\Delta T_{\mathrm{m}}^{id}$ represent the temperature differences in the ideal system without interface resistances.

The measured thermopower is given by

$$\begin{aligned} U &= S_{\mathrm{te}}\Delta T_{\mathrm{te}} + S_{\mathrm{m}}\Delta T_{\mathrm{m}} \\ &= \left(1 + \frac{\theta_{\mathrm{i}}}{\theta_{\mathrm{te}} + \theta_{\mathrm{m}}}\right)^{-1} U^{\mathrm{id}} \; . \end{aligned} \tag{C.5}$$

As expected, the measured voltage is smaller than that of the ideal system without interface U^{id}. For a larger number N of interfaces, the Seebeck coefficient can be written as

$$S = \left(1 + \frac{N\theta_{\mathrm{i}}}{\theta_{\mathrm{te}} + \theta_{\mathrm{m}}}\right)^{-1} S^{\mathrm{id}} \; , \tag{C.6}$$

Furthermore, an equivalent trend can be observed for the overall thermal conductivity of the system. Taking into account the influence of the interface, the thermal resistance becomes

$$\theta = \theta_{\mathrm{te}} + \theta_{\mathrm{m}} + N\theta_{\mathrm{i}} = \theta_{\mathrm{te}}\left(1 + \varepsilon_{\lambda} + \frac{N\theta_{\mathrm{i}}}{\theta_{\mathrm{te}}}\right) \; . \tag{C.7}$$

This leads to the following expression for the thermal conductivity:

$$\begin{aligned}\lambda &= \frac{\lambda_{\mathrm{te}}}{\delta_{\mathrm{te}}\left(1+\varepsilon_{\lambda}+\frac{N\theta_{\mathrm{i}}}{\theta_{\mathrm{te}}}\right)} \\ &= \left(1+\frac{N\theta_{\mathrm{i}}}{\theta_{\mathrm{te}}+\theta_{\mathrm{m}}}\right)^{-1}\lambda^{\mathrm{id}}\,.\end{aligned} \tag{C.8}$$

A similar impact of the interface can be derived for the electrical resistivity:

$$\rho = \left(1+\frac{NR_{\mathrm{i}}}{R_{\mathrm{te}}+R_{\mathrm{m}}}\right)\rho^{\mathrm{id}}\,, \tag{C.9}$$

with R_{i} being the electrical resistance of the interface.

In summary, the interfaces between the constituents of a composite can influence all thermoelectric properties, namely causing a reduction of the Seebeck coefficient as well as the electrical and thermal conductivity. The extent of this influence depends on the electrical and thermal resistance of the interface compared to the values of the constituents, as well as the number of interfaces, reflecting the structure of the composite.

D Training of neural network for accelerated fitting

In chapter 4, a fitting algorithm based on a parabolic-band model was introduced and discussed, providing a convenient description of the band structure. This model allows to fit the measured Seebeck coefficient, electrical resistivity and Hall coefficient data to obtain band structure features. For a system comprising n bands, the fit estimates $3n$ and $4n$ parameters for a single and two dominant scattering processes, respectively. These parameters include the Fermi energy E_F, the band gap E_g between the first band and all additional bands, the ratio of the masses weighted by the degeneracies ε, the absolute band masses as well as the scattering times. If only the Seebeck coefficient or Seebeck coefficient and electrical resistivity are fitted, the number of fit parameters decreases accordingly (refer to chapter 3 for details).

Before initiating the fitting process, which starts with a fit of the Seebeck coefficient data, a rough estimation of the relevant band parameters is mandatory. The scattering times and absolute band masses, on the other hand, are initially set to 1. The success of fitting the Seebeck coefficient data and extracting the band structure features, as well as the time required for the fit, depend on the initial values chosen as the starting point. While the software allows for manual parameter adjustments beforehand, a neural network was trained to calculate and predict these parameters based on the temperature-dependent Seebeck coefficient. Depending on the model's accuracy, this approach is expected to significantly reduce the fitting time and, ideally, make the user's manual adjustments unnecessary.

In practice, fitting with multiple bands often yields almost degenerate results, particularly when considering the ratio of degeneracies. Different sets of band parameters may produce nearly equivalent Seebeck coefficients, introducing subtle nuances that are not effectively resolved by the neural network or the least-squares fit. Consequently, the setup has been adjusted to necessitate users to provide values for the degeneracies of the bands, ensuring accurate predictions of the band structure. Furthermore, due to the expanded phase space of the three-parabolic-band model, the network's training was confined to single and two parabolic bands. The subsequent sections delve into the training specifics for two bands.

The neuronal networks presented below were constructed using the Keras library for Python [302], which is based on the TensorFlow library developed by Google [303].

D.1 Data generation

The effectiveness of neural network training relies on the structure of the training data. In many cases, the set of band parameters for a given $S(T)$ can be ambiguous. For example, in a two-band system where the Fermi energy is situated deeply inside the valence band, the size of the band gap plays no rule at lower temperatures. Only at elevated temperatures does the influence of the second band becomes apparent, causing a deviation in the Seebeck coefficient from linear behavior. This inherent ambiguity limits the network's ability to identify the correct features, thereby hindering the training process. Consequently, careful data preparation becomes crucial. A dataset comprising a total of 20,000 training and 2,000 test data was created. This dataset encompasses both input and output data, providing the network with information about the Seebeck coefficient and its corresponding band structure.

D.1.1 Input data

The input data contain the Seebeck coefficient calculated at equidistant temperatures. The temperature interval was set from 300 K to 600 K with intervals of 25 K, resulting in a total of

$$M = \frac{600\,\mathrm{K} - 300\,\mathrm{K}}{25\,\mathrm{K}} + 1 = 13 \tag{D.1}$$

data points for the input layer. This temperature range has been selected to encompass a significant portion of data available in the literature, ensuring the model's broad applicability. The degeneracy ratio is initially set to 1. Given the extremely large possibilities of ratios $\delta N = N_2/N_1$, training the network for all values of δN is impractical. For most materials, the network's prediction for $\delta N = 1$ is expected to yield a converging fit, even if the user later decides to adjust the value.

D.1.2 Output data

For the neural network trained with the two-band system, one band was predefined as a valence band and the other as a conduction band. This configuration exhibits more distinct features than a two-band system comprising bands of equal sign, making it more relevant in the field of thermoelectricity. To ensure applicability across a broad spectrum of materials, the three band-structure parameters need to be carefully selected. The values were generated using the following procedure:

Weighted ratio of effective masses ε: The effective mass ratio is randomly assigned values between 0.2 and 5, ensuring that the second band can be no more than five times lighter or heavier than the first band, including the ratio of degeneracies. The parameter is generated according to a logarithmic distribution to balance the probabilities of lighter and heavier bands:

$$\varepsilon = 10^{\alpha} \,, \tag{D.2}$$

with α being randomly set to a value between $\log(0.2)$ and $\log(5)$.

Band gap $E_\mathbf{g}$: The band gap follows a random normal distribution with a mean value of 2000 K and a standard deviation of 1000 K. As a result, approximately 95 % of the values fall within the range of 0 K to 4000 K. This parameter determines the distance between the maximum or minimum of the two parabolas. This distribution is weighted towards positive band gaps, emphasizing semiconductors, which are the predominant class of materials in the field of thermoelectricity.

Fermi energy $E_\mathbf{F}$: Similarly to the band gap, the Fermi energy follows a normal distribution, with a standard deviation of 1000 K. The mean value is randomly assigned to the band minimum of either band. This choice reflects the typical characteristics of thermoelectric materials, where the Fermi energy tends to be close to

	Weighted mass ratio ε	Band gap E_g	Fermi energy E_F
a	0	2000	900
c	1	1000	1500

Table D.1: Parameters a and c used to normalize the three fitting parameters ε, E_g and E_F to values between -1 and 1 (0 to 1 in case of the effective mass ratio).

the band gap. Furthermore, if the Fermi energy resides within the band gap, it is positioned equidistantly between the two bands.

Figure D.1 presents the probability distribution of the training data for all three parameters. To accommodate the large variations in parameter values, normalization was applied, transforming the values to a standardized range between -1 and 1 (or 0 to 1 in the case of the effective mass ratio). This normalization not only facilitates the learning process and enhances the prediction accuracy of the model, but also enables the use of appropriate activation functions between the layers. These activation functions effectively rescale the outcomes after each layer, maintaining values within the range of -1 to 1.

Normalization is accomplished using the function

$$f(x) = \frac{x-a}{|x-a|+c}\,, \tag{D.3}$$

where a and c are adjustable parameters. Multiple values were tested to ensure a balanced distribution of parameters across the entire interval. The optimal parameters, providing the most effective normalization, are detailed in Table D.1. The normalized band parameters are depicted in Figure D.1b, d and f.

D.2 Architecture of the neural network

The size and structure of the neural networks' architecture has to be adjusted based on the complexity of the data. In Figure D.2, a general overview of the architecture of the trained neural networks is presented. Determining the optimal architecture involved considerations of various parameters, including the number l of hidden layers, the number n_l of nodes per hidden layer, the dropout rate [304],

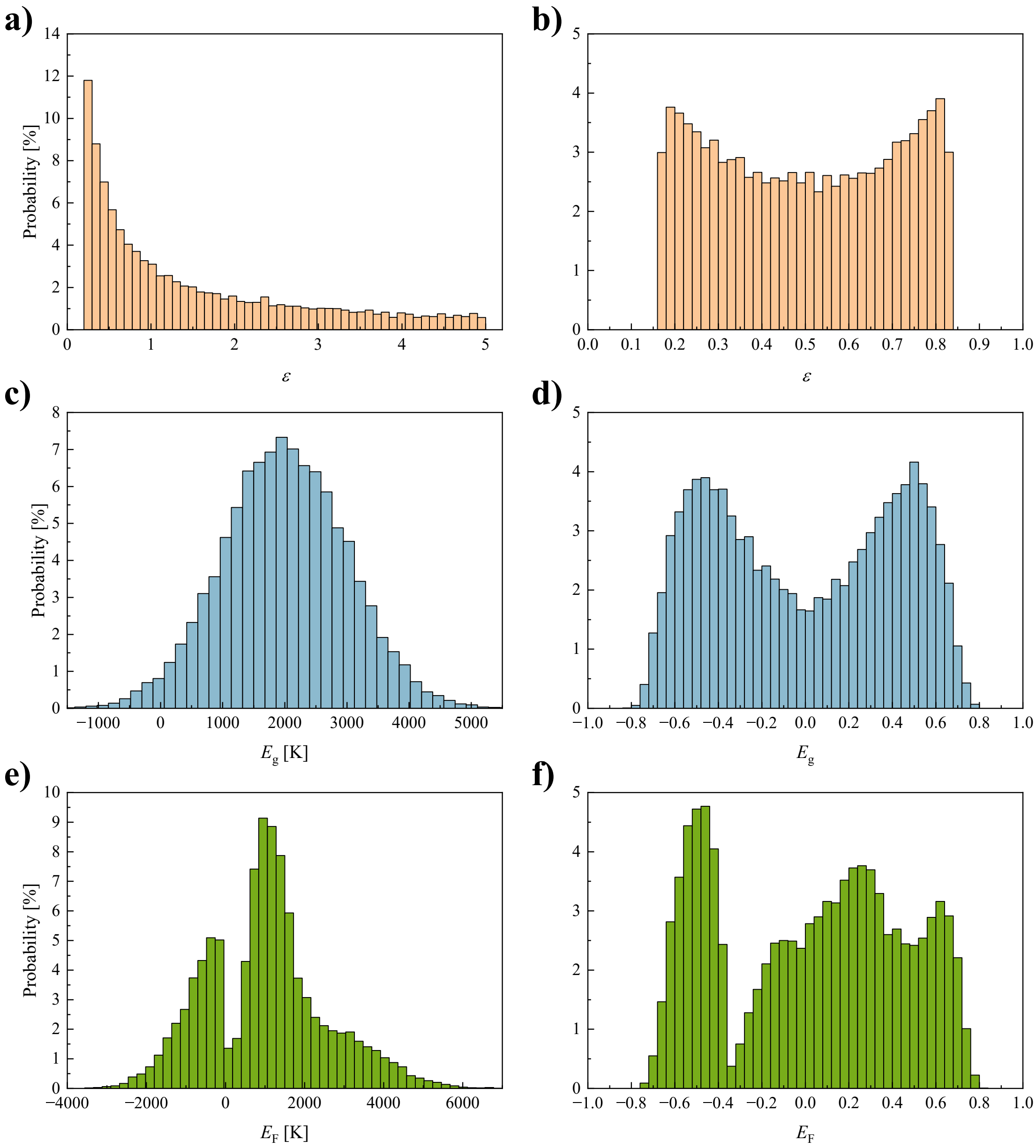

Figure D.1: Probability distribution of randomly generated (a, b) weighted mass ratio ε, (c, d) band gap E_g and (e, f) Fermi energy E_F. The left and right figures show the values before and after normalization onto the interval $(-1, 1)$ according to the formalism introduced in the main text, respectively.

the activation function and the optimizer. The loss was evaluated by calculating the mean squared error.

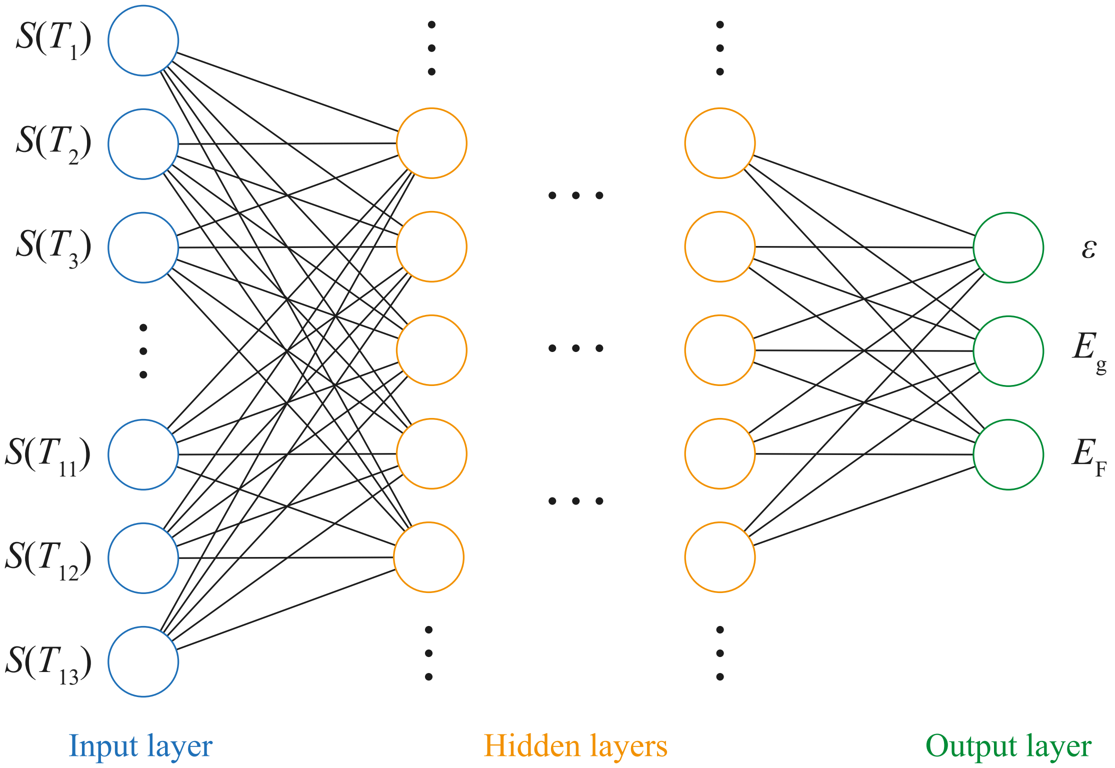

Figure D.2: Schematic drawing of the general architecture of sequential neural networks. The input layer (blue) consists of 13 nodes, each one representing a value of the Seebeck coefficient on an equally spaced temperature grid. Then, a variable number l of so-called hidden layers (orange) follows, each one with n_l nodes. Finally, an output layer (green) is connected to the last hidden layer, comprising three nodes, which represent the three band-structure parameters. The open circles depict single nodes, which add together the incoming values, weighted with individual weights.

Given the impracticality of testing all potential architecture, approximately 1000 neural networks with randomized parameters were generated, trained and tested. The ultimate performance of each model was evaluated based on the root mean squared error of the Seebeck coefficient, calculated using the predicted set of band-structure parameters. The exploration of this parameter space was subsequently refined, as specific configurations demonstrated significantly better or worse performance than others. Ultimately, the most effective neural network architecture consisted of four hidden layers ($l = 4$) with node counts of $n_1 = 143$, $n_2 = 67$, $n_3 = 62$ and $n_4 = 76$. Furthermore, the use of a dropout rate was found to have a

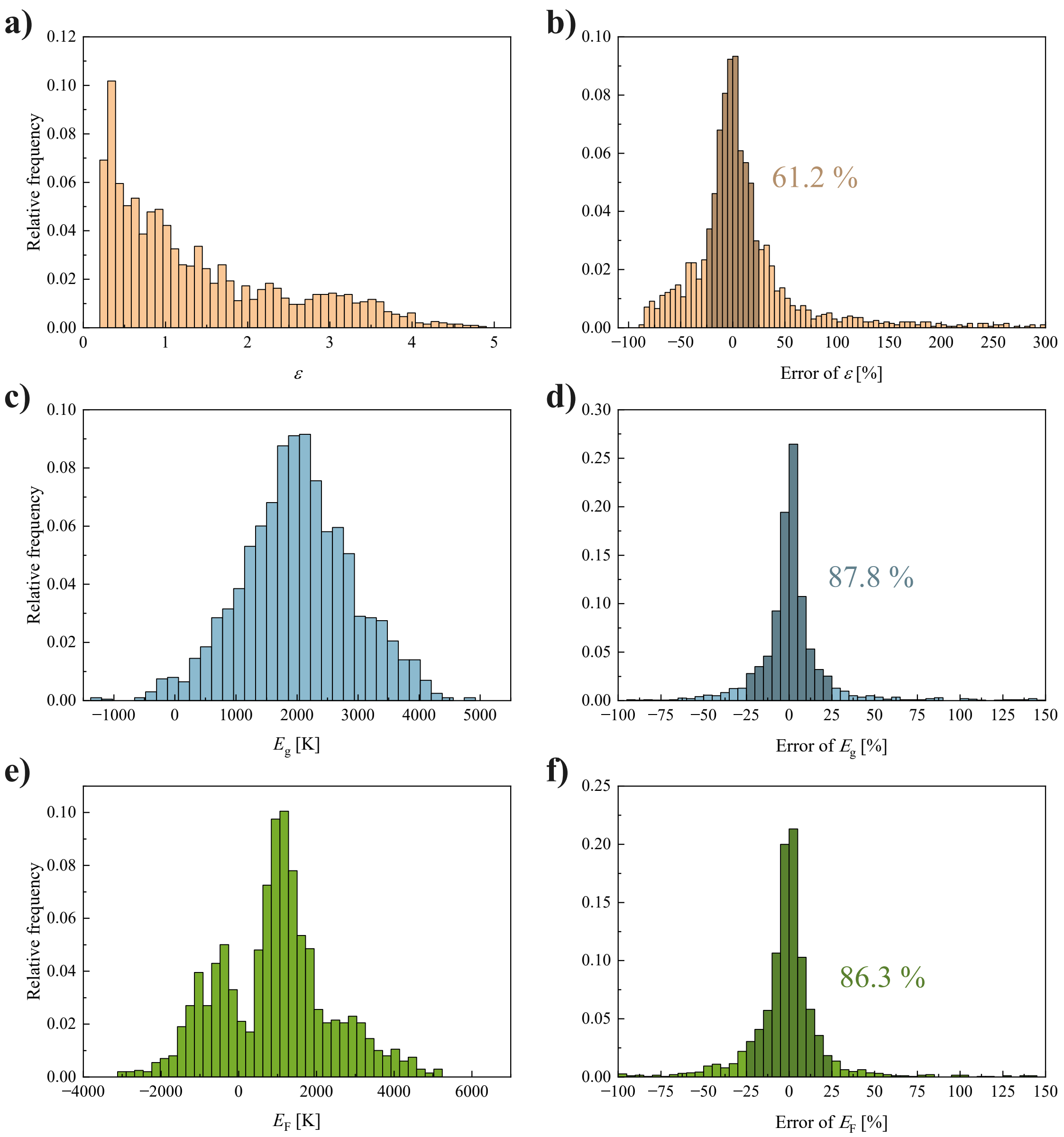

Figure D.3: Distribution of the neural network's predicted values of a) ε, b) E_g and c) E_F, together with the respective errors (b, d, f). The numbers shown in the figures on the right denote the cumulative fraction of predictions within $\pm 25\,\%$ of the actual values. The parameters were calculated from 2000 test data.

detrimental effect and was therefore omitted. An activation function in the form of a hyperbolic tangent was applied, and the optimization process utilized the *adam* optimizer [305].

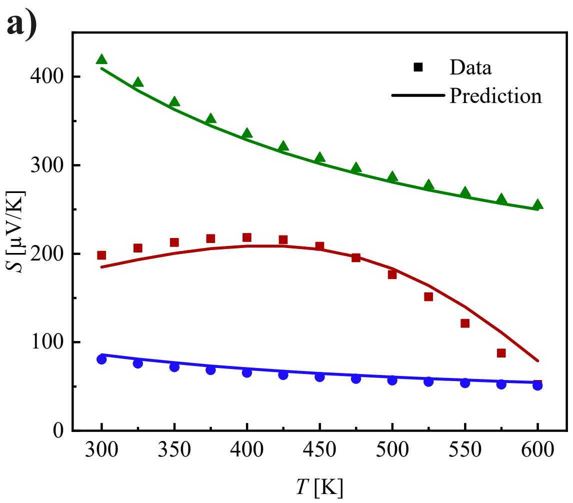

b)

	ε_{21}	E_g [K]	E_F [K]
Data	0.32	2643	1321
Prediction	0.35	2636	1317
Data	0.31	2578	-318
Prediction	0.27	2634	-358
Data	1.15	2398	1199
Prediction	1.16	2424	1235

Figure D.4: a) Seebeck coefficient curves derived from test data parameters (symbols) alongside with those calculated from the predicted parameter sets (lines). b) Table presenting both the predicted and actual band-structure parameters.

The parameters predicted by the neural network from the provided test data are visualized in Figure D.3. While the test data itself are not displayed, it is important to note that they were generated with the same parameter distribution as the training data. Hence, a comparison between Figure D.3 and Figure D.1 reveals the strong alignment of the predictions with the expected parameter distribution.

Furthermore, when analyzing the errors between the predicted and actual values (as depicted in Figure D.3b, d and f), it becomes evident that the majority of predictions fall within a 25 % margin of the actual values for E_g and E_F. In the case of ε, the error is larger, primarily attributed to the smaller values of ε, which can result in relatively large relative errors even for relatively small absolute deviations.

Examples of the network's prediction are presented in Figure D.4a. The excellent alignment between the predicted curve and the test data underscores the model's high accuracy. This is further emphasized in Figure D.4b, where the values are depicted. While these examples represent optimal scenarios, the network's prediction proves sufficient in the majority of cases, providing a solid starting point for the subsequent fitting procedure. This remarkable results enable the user to obtain fit results directly after importing the experimental data. Only in cases where the neural network's estimation is too imprecise for the fit to converge, further adjustments of the band parameters may be required. Overall, the neural network significantly accelerates the entire fitting process.

E Thickness distribution of magnetron sputtering

The dislodged mass M from a target with surface A_t within the time interval Δt is described by [250]

$$M_t = \int_0^{\Delta t} \int_{A_t} \Gamma \, \mathrm{d}A\mathrm{d}t \;, \tag{E.1}$$

where Γ signifies the mass loss rate, depending on the average sputter yield Y, the average mass of ejected particles m and the particle current density of impinging ions j:

$$\Gamma = Yjm \;. \tag{E.2}$$

In the case of a planar target, material is ejected into a hemisphere, following a cosine distribution. The quantity of material reaching an infinitesimally small surface $\mathrm{d}A$ along the hemisphere at an angle θ and distance r is expressed by

$$\mathrm{d}M_t = M_t \cos\theta \frac{\mathrm{d}A}{\pi r^2} \;. \tag{E.3}$$

The material reaching an opposing substrate further depends on the inclination angle with respect to the target, denoted as α. For a sufficiently small substrate surface A_s, the projection onto the hemisphere is given by $A_s \cos\alpha$. Substituting the substrate's surface into Equation E.3 yields

$$\mathrm{d}M_s = M_t \frac{\cos\theta \cos\alpha}{\pi r^2} \mathrm{d}A_s \;. \tag{E.4}$$

A visualization incorporating relevant quantities is shown in Figure E.1a. For parallel substrate and target, $\theta = \alpha$. Then, by using the relation $\cos\theta = d/r$, the equation simplifies to

$$\frac{\mathrm{d}M_s}{\mathrm{d}A_s} = M_\mathrm{t} \frac{\cos\theta^4}{\pi d^2} \;, \tag{E.5}$$

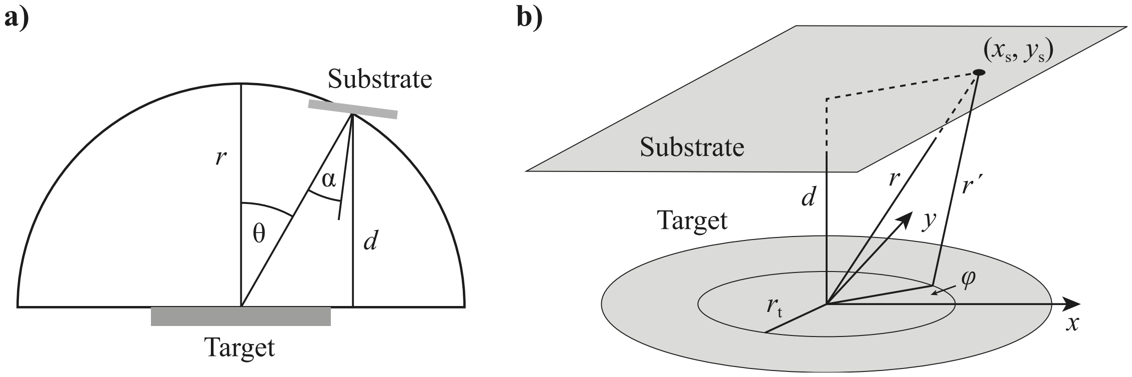

Figure E.1: a) Two-dimensional and b) three-dimensional sketch of the relevant quantities and their relation for deriving the film-thickness distribution on a substrate.

where d denotes the orthogonal distance between substrate and target.

In a magnetron sputtering setup, particles are not uniformly dislodged from the target but rather along a small ring with a radius r_t due to the cycloidal movement of secondary electrons. The amount of material reaching the position $(x_\mathrm{s},\, y_\mathrm{s})$ on the substrate from a ring position characterized by the angle φ is (see Figure E.1b)

$$\begin{aligned} G(\varphi, x_\mathrm{s}, y_\mathrm{s}) &= \frac{\mathrm{d}M_\mathrm{s}}{\mathrm{d}A_\mathrm{s}} = \frac{M_\mathrm{t}}{\pi}\frac{d^2}{r'^4}\,, && \text{(E.6)} \\ &= \frac{M_\mathrm{t}}{\pi}\frac{d^2}{\left[d^2 + (x_\mathrm{s} - x_\mathrm{t} - r_\mathrm{t}\cos\varphi)^2 + (y_\mathrm{s} - y_\mathrm{t} - r_\mathrm{t}\sin\varphi)^2\right]^2}\,. && \text{(E.7)} \end{aligned}$$

Here, x_t and y_t represent the origin coordinates of the target, allowing for a potential offset between target and substrate.

The cumulative mass ejected from the target is obtained by integrating across the entire ring:

$$I(x_\mathrm{s}, y_\mathrm{s}) = \int_0^{2\pi} G(\varphi, x_\mathrm{s}, y_\mathrm{s})\mathrm{d}\varphi\,. \tag{E.8}$$

Figure E.2 shows the thickness profile $I(x, y)$ on a substrate from an 1-inch (25.4 mm) target with a 14 mm diameter sputter ring. For small distances d between target and substrate, the ring-shaped expulsion of particles from the target manifests in the substrate's thickness distribution. With increasing distance, the distribution levels out and adopts a more uniform shape. As depicted in Figure E.2b, the relative difference between the maximum and minimum thickness experiences a pronounced

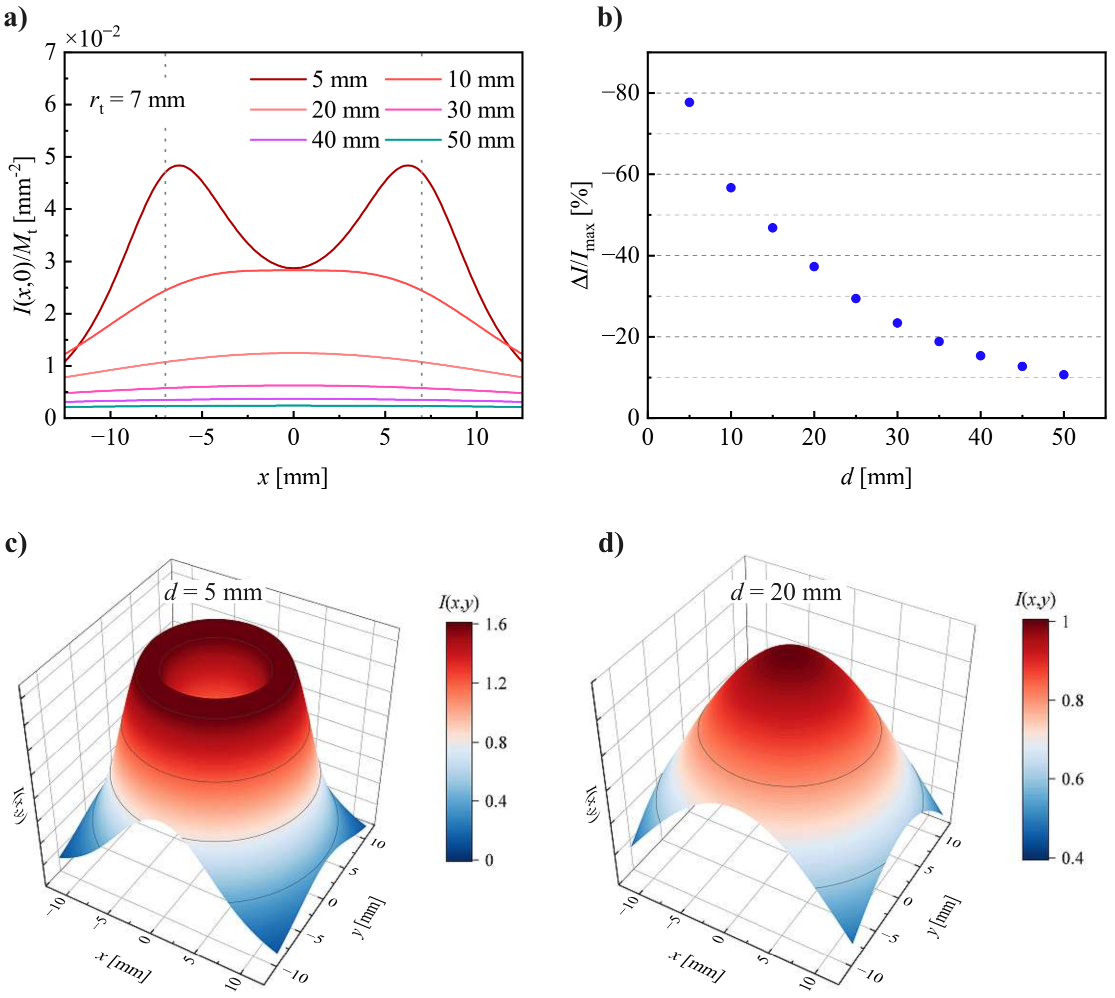

Figure E.2: Calculation of the thickness distribution on a 20 x 25 mm substrate opposing a 1-inch (25.4 mm) target with 14 mm diameter sputter ring. a) Thickness distribution and b) maximum difference in film thickness across one direction for different distances between target and substrate. c,d) Three-dimensional visualizations of the thickness profile for a distance of 5 mm (c) and 20 mm (d).

decline with increasing distance. Consequently, the distance is a pivotal factor influencing the accuracy when deducing properties from measured quantities, such as electrical resistivity. Figure E.2c,d present three-dimensional thickness profiles at distances of $d = 5$ mm and 20 mm, respectively, elucidating the evolving spatial characteristics of the film deposition. The *Mathematica* code employed for the computation of the thickness profile is available in [306].

List of Figures

List of Tables

Bibliography

[1] D. T. Price, R. Alfaro, K. Brown, M. Flannigan, R. A. Fleming, E. Hogg, M. Girardin, T. Lakusta, M. Johnston, D. McKenney *et al.* *Anticipating the consequences of climate change for Canada's boreal forest ecosystems.* Environmental Reviews **21**, 322 (2013).

[2] W. Thuiller, S. Lavergne, C. Roquet, I. Boulangeat, B. Lafourcade, and M. B. Araujo. *Consequences of climate change on the tree of life in Europe.* Nature **470**, 531 (2011).

[3] J.-C. Ciscar, A. Iglesias, L. Feyen, L. Szabó, D. Van Regemorter, B. Amelung, R. Nicholls, P. Watkiss, O. B. Christensen, R. Dankers *et al.* *Physical and economic consequences of climate change in Europe.* Proceedings of the National Academy of Sciences **108**, 2678 (2011).

[4] T. Wheeler and J. Von Braun. *Climate change impacts on global food security.* Science **341**, 508 (2013).

[5] H. Lee, K. Calvin, D. Dasgupta, G. Krinner, A. Mukherji, P. Thorne, C. Trisos, J. Romero, P. Aldunce, K. Barret *et al.* *IPCC, 2023: Climate Change 2023: Synthesis Report, Summary for Policymakers. Contribution of Working Groups I, II and III to the Sixth Assessment Report of the Intergovernmental Panel on Climate Change [Core Writing Team, H. Lee and J. Romero (eds.)]. IPCC, Geneva, Switzerland.* (2023).

[6] *Population.* `https://www.un.org/en/global-issues/population`. Accessed: 2023-02-15.

[7] *World Energy Balances: Overview.* `https://www.iea.org/reports/world-energy-balances-overview`. Accessed: 2023-08-22.

[8] C. Forman, I. K. Muritala, R. Pardemann, and B. Meyer. *Estimating the global waste heat potential.* Renewable and Sustainable Energy Reviews **57**, 1568 (2016).

[9] C. Herring and M. Nichols. *Thermionic emission.* Reviews of modern physics **21**, 185 (1949).

[10] D. B. Go, J. R. Haase, J. George, J. Mannhart, R. Wanke, A. Nojeh, and R. Nemanich. *Thermionic energy conversion in the twenty-first century: advances and opportunities for space and terrestrial applications.* Frontiers in Mechanical Engineering **3**, 13 (2017).

[11] G. J. Snyder and E. S. Toberer. *Complex thermoelectric materials.* Nature materials **7**, 105 (2008).

[12] L. Boltzmann. *Lectures on gas theory.* Univ of California Press (2022).

[13] R. Landauer. *Spatial variation of currents and fields due to localized scatterers in metallic conduction.* IBM Journal of research and development **1**, 223 (1957).

[14] A. Zevalkink, D. M. Smiadak, J. L. Blackburn, A. J. Ferguson, M. L. Chabinyc, O. Delaire, J. Wang, K. Kovnir, J. Martin, L. T. Schelhas *et al. A practical field guide to thermoelectrics: Fundamentals, synthesis, and characterization.* Applied Physics Reviews **5** (2018).

[15] C. Jeong, R. Kim, M. Luisier, S. Datta, and M. Lundstrom. *On Landauer versus Boltzmann and full band versus effective mass evaluation of thermoelectric transport coefficients.* Journal of Applied Physics **107**, 023707 (2010).

[16] G. Mahan and J. Sofo. *The best thermoelectric.* Proceedings of the National Academy of Sciences **93**, 7436 (1996).

[17] A. Jain, S. P. Ong, G. Hautier, W. Chen, W. D. Richards, S. Dacek, S. Cholia, D. Gunter, D. Skinner, G. Ceder *et al. Commentary: The Materials Project: A materials genome approach to accelerating materials innovation.* APL materials **1** (2013).

[18] D. M. Rowe. *Materials, preparation, and characterization in thermoelectrics.* CRC press (2017).

[19] J. Harrison and J. Hauser. *Alloy scattering in ternary III-V compounds.* Physical Review B **13**, 5347 (1976).

[20] M. Glicksman. *Mobility of electrons in germanium-silicon alloys.* Physical Review **111**, 125 (1958).

[21] J. Mao, J. Shuai, S. Song, Y. Wu, R. Dally, J. Zhou, Z. Liu, J. Sun, Q. Zhang, C. dela Cruz *et al.* *Manipulation of ionized impurity scattering for achieving high thermoelectric performance in n-type* Mg_3Sb_2*-based materials.* Proceedings of the National Academy of Sciences **114**, 10548 (2017).

[22] D. Chattopadhyay and H. Queisser. *Electron scattering by ionized impurities in semiconductors.* Reviews of Modern Physics **53**, 745 (1981).

[23] W. Baber. *The contribution to the electrical resistance of metals from collisions between electrons.* Proceedings of the Royal Society of London. Series A-Mathematical and Physical Sciences **158**, 383 (1937).

[24] T. J. Seebeck. *Ueber den Magnetismus der galvanischen Kette* (1822).

[25] V. Johnson and K. Lark-Horovitz. *Theory of thermoelectric power in semiconductors with applications to germanium.* Physical Review **92**, 226 (1953).

[26] H. Goldsmid and R. Douglas. *The use of semiconductors in thermoelectric refrigeration.* British Journal of Applied Physics **5**, 386 (1954).

[27] C. Herring. *Theory of the thermoelectric power of semiconductors.* Physical Review **96**, 1163 (1954).

[28] H. Goldsmid. *XXVII. Thermoelectric applications of semiconductors.* International Journal Of Electronics **1**, 218 (1955).

[29] P. Price. *Theory of transport effects in semiconductors: thermoelectricity.* Physical Review **104**, 1223 (1956).

[30] J. Mao, Y. Wang, H. S. Kim, Z. Liu, U. Saparamadu, F. Tian, K. Dahal, J. Sun, S. Chen, W. Liu *et al.* *High thermoelectric power factor in Cu–Ni alloy originate from potential barrier scattering of twin boundaries.* Nano Energy **17**, 279 (2015).

[31] H. Kang, Z. Yang, X. Yang, J. Li, W. He, Z. Chen, E. Guo, L.-D. Zhao, and T. Wang. *Preparing bulk Cu–Ni–Mn based thermoelectric alloys and synergistically improving their thermoelectric and mechanical properties using nanotwins and nanoprecipitates.* Materials Today Physics **17**, 100332 (2021).

[32] C. V. Manzano, O. Caballero-Calero, M. Tranchant, E. Bertero, P. Cervino-Solana, M. Martin-Gonzalez, and L. Philippe. *Thermal conductivity reduction by nanostructuration in electrodeposited CuNi alloys.* Journal of Materials Chemistry C **9**, 3447 (2021).

[33] F. Garmroudi, M. Parzer, A. Riss, C. Bourgès, S. Khmelevskyi, T. Mori, E. Bauer, and A. Pustogow. *High thermoelectric performance in metallic NiAu alloys via interband scattering.* Science Advances **9**, eadj1611 (2023).

[34] G. Rogl, A. Grytsiv, P. Heinrich, E. Bauer, P. Kumar, N. Peranio, O. Eibl, J. Horky, M. Zehetbauer, and P. Rogl. *New bulk p-type skutterudites* $DD_{0.7}Fe_{2.7}Co_{1.3}Sb_{12-x}X_x$ *(X=Ge, Sn) reaching* $ZT > 1.3$. Acta Materialia **91**, 227 (2015).

[35] G. Rogl, A. Grytsiv, K. Yubuta, S. Puchegger, E. Bauer, C. Raju, R. Mallik, and P. Rogl. *In-doped multifilled n-type skutterudites with* $ZT = 1.8$. Acta Materialia **95**, 201 (2015).

[36] M. Rull-Bravo, A. Moure, J. Fernández, and M. Martín-González. *Skutterudites as thermoelectric materials: revisited.* Rsc Advances **5**, 41653 (2015).

[37] G. Nolas, D. Morelli, and T. M. Tritt. *Skutterudites: A phonon-glass-electron crystal approach to advanced thermoelectric energy conversion applications.* Annual Review of Materials Science **29**, 89 (1999).

[38] C. Han, Q. Sun, Z. Li, and S. X. Dou. *Thermoelectric enhancement of different kinds of metal chalcogenides.* Advanced Energy Materials **6**, 1600498 (2016).

[39] Y. Shi, C. Sturm, and H. Kleinke. *Chalcogenides as thermoelectric materials.* Journal of Solid State Chemistry **270**, 273 (2019).

[40] A. Maignan, E. Guilmeau, F. Gascoin, Y. Bréard, and V. Hardy. *Revisiting some chalcogenides for thermoelectricity.* Science and technology of advanced materials (2012).

[41] J.-A. Dolyniuk, B. Owens-Baird, J. Wang, J. V. Zaikina, and K. Kovnir. *Clathrate thermoelectrics.* Materials Science and Engineering: R: Reports **108**, 1 (2016).

[42] T. Takabatake, K. Suekuni, T. Nakayama, and E. Kaneshita. *Phonon-glass electron-crystal thermoelectric clathrates: Experiments and theory.* Rev. Mod. Phys. **86**, 669 (2014).

[43] M. Christensen, S. Johnsen, and B. B. Iversen. *Thermoelectric clathrates of type I.* Dalton Trans. **39**, 978 (2010).

[44] H. Kleinke. *New bulk materials for thermoelectric power generation: clathrates and complex antimonides.* Chemistry of materials **22**, 604 (2010).

[45] L. Huang, Q. Zhang, B. Yuan, X. Lai, X. Yan, and Z. Ren. *Recent progress in half-Heusler thermoelectric materials.* Materials Research Bulletin **76**, 107 (2016).

[46] T. Zhu, C. Fu, H. Xie, Y. Liu, and X. Zhao. *High efficiency half-Heusler thermoelectric materials for energy harvesting.* Advanced Energy Materials **5**, 1500588 (2015).

[47] W. G. Zeier, J. Schmitt, G. Hautier, U. Aydemir, Z. M. Gibbs, C. Felser, and G. J. Snyder. *Engineering half-Heusler thermoelectric materials using Zintl chemistry.* Nature Reviews Materials **1**, 1 (2016).

[48] J.-W. G. Bos and R. A. Downie. *Half-Heusler thermoelectrics: a complex class of materials.* Journal of Physics: Condensed Matter **26**, 433201 (2014).

[49] B. Hinterleitner, I. Knapp, M. Poneder, Y. Shi, H. Müller, G. Eguchi, C. Eisenmenger-Sittner, M. Stöger-Pollach, Y. Kakefuda, N. Kawamoto *et al.*

Thermoelectric performance of a metastable thin-film Heusler alloy. Nature **576**, 85 (2019).

[50] F. Garmroudi, A. Riss, M. Parzer, N. Reumann, H. Müller, E. Bauer, S. Khmelevskyi, R. Podloucky, T. Mori, K. Tobita *et al.* *Boosting the thermoelectric performance of* Fe_2VAl*-type Heusler compounds by band engineering.* Physical Review B **103**, 085202 (2021).

[51] M. Parzer, F. Garmroudi, A. Riss, S. Khmelevskyi, T. Mori, and E. Bauer. *High solubility of Al and enhanced thermoelectric performance due to resonant states in* Fe_2VAl_x. Applied Physics Letters **120** (2022).

[52] G. Joshi, H. Lee, Y. Lan, X. Wang, G. Zhu, D. Wang, R. W. Gould, D. C. Cuff, M. Y. Tang, M. S. Dresselhaus *et al.* *Enhanced thermoelectric figure-of-merit in nanostructured p-type silicon germanium bulk alloys.* Nano letters **8**, 4670 (2008).

[53] X. Wang, H. Lee, Y. Lan, G. Zhu, G. Joshi, D. Wang, J. Yang, A. Muto, M. Tang, J. Klatsky *et al.* *Enhanced thermoelectric figure of merit in nanostructured n-type silicon germanium bulk alloy.* Applied Physics Letters **93** (2008).

[54] R. Basu and A. Singh. *High temperature* $Si-Ge$ *alloy towards thermoelectric applications: A comprehensive review.* Materials Today Physics **21**, 100468 (2021).

[55] H. Lee, D. Vashaee, D. Wang, M. S. Dresselhaus, Z. Ren, and G. Chen. *Effects of nanoscale porosity on thermoelectric properties of SiGe.* Journal of Applied Physics **107** (2010).

[56] A. Minnich, H. Lee, X. Wang, G. Joshi, M. Dresselhaus, Z. Ren, G. Chen, and D. Vashaee. *Modeling study of thermoelectric SiGe nanocomposites.* Physical Review B **80**, 155327 (2009).

[57] B. Russ, A. Glaudell, J. J. Urban, M. L. Chabinyc, and R. A. Segalman. *Organic thermoelectric materials for energy harvesting and temperature control.* Nature Reviews Materials **1**, 1 (2016).

[58] Q. Zhang, Y. Sun, W. Xu, and D. Zhu. *Organic thermoelectric materials: emerging green energy materials converting heat to electricity directly and efficiently.* Advanced Materials **26**, 6829 (2014).

[59] Y. Chen, Y. Zhao, and Z. Liang. *Solution processed organic thermoelectrics: towards flexible thermoelectric modules.* Energy & Environmental Science **8**, 401 (2015).

[60] Q. Yan and M. G. Kanatzidis. *High-performance thermoelectrics and challenges for practical devices.* Nature materials **21**, 503 (2022).

[61] C. Fu, S. Bai, Y. Liu, Y. Tang, L. Chen, X. Zhao, and T. Zhu. *Realizing high figure of merit in heavy-band p-type half-Heusler thermoelectric materials.* Nature communications **6**, 8144 (2015).

[62] S. Sakurada and N. Shutoh. *Effect of Ti substitution on the thermoelectric properties of (Zr,Hf)NiSn half-Heusler compounds.* Applied Physics Letters **86** (2005).

[63] B. Zhu, X. Liu, Q. Wang, Y. Qiu, Z. Shu, Z. Guo, Y. Tong, J. Cui, M. Gu, and J. He. *Realizing record high performance in n-type Bi_2Te_3-based thermoelectric materials.* Energy & Environmental Science **13**, 2106 (2020).

[64] L.-D. Zhao, S.-H. Lo, Y. Zhang, H. Sun, G. Tan, C. Uher, C. Wolverton, V. P. Dravid, and M. G. Kanatzidis. *Ultralow thermal conductivity and high thermoelectric figure of merit in SnSe crystals.* nature **508**, 373 (2014).

[65] Y. Pei, A. LaLonde, S. Iwanaga, and G. J. Snyder. *High thermoelectric figure of merit in heavy hole dominated PbTe.* Energy & Environmental Science **4**, 2085 (2011).

[66] M. S. El-Genk. *Deployment history and design considerations for space reactor power systems.* Acta Astronautica **64**, 833 (2009).

[67] A. Yaroshevsky. *Abundances of chemical elements in the Earth's crust.* Geochemistry International **44**, 48 (2006).

[68] R. He, W. Heyn, F. Thiel, N. Pérez, C. Damm, D. Pohl, B. Rellinghaus, C. Reimann, M. Beier, J. Friedrich *et al.* *Thermoelectric properties of silicon and recycled silicon sawing waste.* Journal of Materiomics **5**, 15 (2019).

[69] H. Shanks, P. Maycock, P. Sidles, and G. Danielson. *Thermal conductivity of silicon from 300 to 1400 K.* Physical Review **130**, 1743 (1963).

[70] J. Dismukes, L. Ekstrom, and R. Paff. *Lattice parameter and density in germanium-silicon alloys.* The Journal of Physical Chemistry **68**, 3021 (1964).

[71] N. Mori. *Electronic band structures of silicon-germanium (SiGe) alloys.* In *Silicon–Germanium (SiGe) Nanostructures*, pp. 26–42. Elsevier (2011).

[72] E. M. Fadaly, A. Dijkstra, J. R. Suckert, D. Ziss, M. A. Van Tilburg, C. Mao, Y. Ren, V. T. van Lange, K. Korzun, S. Kölling *et al.* *Direct-bandgap emission from hexagonal Ge and SiGe alloys.* Nature **580**, 205 (2020).

[73] V. Pecunia, S. R. P. Silva, J. D. Phillips, E. Artegiani, A. Romeo, H. Shim, J. Park, J.-H. Kim, J. S. Yun, and G. C. Welch. *Roadmap on Energy Harvesting Materials.* Journal of Physics: Materials (2023).

[74] G. Zhu, H. Lee, Y. Lan, X. Wang, G. Joshi, D. Wang, J. Yang, D. Vashaee, H. Guilbert, A. Pillitteri *et al.* *Increased phonon scattering by nanograins and point defects in nanostructured silicon with a low concentration of germanium.* Physical review letters **102**, 196803 (2009).

[75] I. T. Witting, T. C. Chasapis, F. Ricci, M. Peters, N. A. Heinz, G. Hautier, and G. J. Snyder. *The thermoelectric properties of bismuth telluride.* Advanced Electronic Materials **5**, 1800904 (2019).

[76] Q. Zhang, J. Liao, Y. Tang, M. Gu, C. Ming, P. Qiu, S. Bai, X. Shi, C. Uher, and L. Chen. *Realizing a thermoelectric conversion efficiency of 12% in bismuth telluride/skutterudite segmented modules through full-parameter optimization and energy-loss minimized integration.* Energy & Environmental Science **10**, 956 (2017).

[77] Y. Hosokawa, K. Tomita, and M. Takashiri. *Growth of single-crystalline* Bi_2Te_3 *hexagonal nanoplates with and without single nanopores during*

temperature-controlled solvothermal synthesis. Scientific Reports **9**, 10790 (2019).

[78] O. Ben-Yehuda, R. Shuker, Y. Gelbstein, Z. Dashevsky, and M. Dariel. *Highly textured Bi_2Te_3-based materials for thermoelectric energy conversion.* Journal of applied physics **101** (2007).

[79] S. Lee, K. Esfarjani, T. Luo, J. Zhou, Z. Tian, and G. Chen. *Resonant bonding leads to low lattice thermal conductivity.* Nature communications **5**, 3525 (2014).

[80] W. G. Zeier, A. Zevalkink, Z. M. Gibbs, G. Hautier, M. G. Kanatzidis, and G. J. Snyder. *Thinking like a chemist: intuition in thermoelectric materials.* Angewandte Chemie International Edition **55**, 6826 (2016).

[81] G. Li, U. Aydemir, S. I. Morozov, M. Wood, Q. An, P. Zhai, Q. Zhang, W. A. Goddard III, and G. J. Snyder. *Superstrengthening Bi_2Te_3 through Nanotwinning.* Physical review letters **119**, 085501 (2017).

[82] I. Austin. *The optical properties of bismuth telluride.* Proceedings of the Physical Society **72**, 545 (1958).

[83] H. Zhang, C.-X. Liu, X.-L. Qi, X. Dai, Z. Fang, and S.-C. Zhang. *Topological insulators in Bi_2Se_3, Bi_2Te_3 and Sb_2Te_3 with a single Dirac cone on the surface.* Nature physics **5**, 438 (2009).

[84] Y. Chen, J. G. Analytis, J.-H. Chu, Z. Liu, S.-K. Mo, X.-L. Qi, H. Zhang, D. Lu, X. Dai, Z. Fang *et al. Experimental realization of a three-dimensional topological insulator, Bi_2Te_3.* science **325**, 178 (2009).

[85] M. Hong, Z.-G. Chen, and J. Zou. *Fundamental and progress of Bi_2Te_3-based thermoelectric materials.* Chinese Physics B **27**, 048403 (2018).

[86] W. Xie, S. Wang, S. Zhu, J. He, X. Tang, Q. Zhang, and T. M. Tritt. *High performance Bi_2Te_3 nanocomposites prepared by single-element-melt-spinning spark-plasma sintering.* Journal of Materials Science **48**, 2745 (2013).

[87] H. Li, H. Jing, Y. Han, Y. Xu, G.-Q. Lu, and L. Xu. *Microstructure and transport properties of copper-doped p-type BiSbTe alloy prepared by mechanical alloying and subsequent spark plasma sintering.* Journal of alloys and compounds **576**, 369 (2013).

[88] L. Bulat, I. Drabkin, V. Karatayev, V. Osvenskii, Y. N. Parkhomenko, M. Lavrentev, A. Sorokin, D. Pshenai-Severin, V. Blank, G. Pivovarov *et al.* *Structure and transport properties of bulk nanothermoelectrics based on* $Bi_xSb_{2-x}Te_3$ *fabricated by SPS method.* Journal of electronic materials **42**, 2110 (2013).

[89] P. Nguyen, K. Lee, J. Moon, S. I. Kim, K. Ahn, L. Chen, S. Lee, R. Chen, S. Jin, and A. Berkowitz. *Spark erosion: a high production rate method for producing* $Bi_{0.5}Sb_{1.5}Te_3$ *nanoparticles with enhanced thermoelectric performance.* Nanotechnology **23**, 415604 (2012).

[90] J. Son, M. Oh, B. Kim, S. Park, B. Min, M. Kim, and H. Lee. *Effect of ball milling time on the thermoelectric properties of p-type* $(Bi,Sb)_2Te_3$*.* Journal of alloys and compounds **566**, 168 (2013).

[91] M. Imamuddin and A. Dupre. *Thermoelectric properties of p-type* Bi_2Te_3*-*Sb_2Te_3*-*Sb_2Se_3 *alloys and n-type* Bi_2Te_3*-*Bi_2Se_3 *alloys in the temperature range 300 to 600 K.* physica status solidi (a) **10**, 415 (1972).

[92] F. Wu, H. Song, F. Gao, W. Shi, J. Jia, and X. Hu. *Effects of different morphologies of* Bi_2Te_3 *nanopowders on thermoelectric properties.* Journal of electronic materials **42**, 1140 (2013).

[93] H. Kim, M.-K. Han, C.-H. Yo, W. Lee, and S.-J. Kim. *Effects of* Bi_2Se_3 *nanoparticle inclusions on the microstructure and thermoelectric properties of* Bi_2Te_3*-based nanocomposites.* Journal of electronic materials **41**, 3411 (2012).

[94] C. Yu, X. Zhang, M. Leng, A. Shaga, D. Liu, F. Chen, and C. Wang. *Preparation and thermoelectric properties of inhomogeneous bismuth telluride alloyed nanorods.* Journal of alloys and compounds **570**, 86 (2013).

[95] L. Hu, Y. Zhang, H. Wu, Y. Liu, J. Li, J. He, W. Ao, F. Liu, S. J. Pennycook, and X. Zeng. *Synergistic compositional–mechanical–thermal effects leading to a record high zT in n-type* V_2VI_3 *alloys through progressive hot deformation.* Advanced Functional Materials **28**, 1803617 (2018).

[96] J. Pei, B. Cai, H.-L. Zhuang, and J.-F. Li. Bi_2Te_3*-based applied thermoelectric materials: research advances and new challenges.* National science review **7**, 1856 (2020).

[97] F. Heusler. *Über magnetische manganlegierungen.* Verhandlungen der Deutschen Physikalischen Gesellschaft **5**, 219 (1903).

[98] M. Gilleßen and R. Dronskowski. *A combinatorial study of inverse Heusler alloys by first-principles computational methods.* Journal of computational chemistry **31**, 612 (2010).

[99] T. Graf, C. Felser, and S. S. Parkin. *Simple rules for the understanding of Heusler compounds.* Progress in solid state chemistry **39**, 1 (2011).

[100] F. Casper, T. Graf, S. Chadov, B. Balke, and C. Felser. *Half-Heusler compounds: novel materials for energy and spintronic applications.* Semiconductor Science and Technology **27**, 063001 (2012).

[101] L. Bainsla and K. Suresh. *Equiatomic quaternary Heusler alloys: A material perspective for spintronic applications.* Applied Physics Reviews **3**, 031101 (2016).

[102] J. K. Kawasaki, S. Chatterjee, P. C. Canfield, and G. Editors. *Full and half-Heusler compounds.* MRS Bulletin **47**, 555 (2022).

[103] B. Hinterleitner, P. Fuchs, J. Rehak, F. Garmroudi, M. Parzer, M. Waas, R. Svagera, S. Steiner, M. Kishimoto, R. Moser *et al. Stoichiometric and off-stoichiometric full Heusler* $Fe_2V_{1-x}W_xAl$ *thermoelectric systems.* Physical Review B **102**, 075117 (2020).

[104] E. Alleno. *Review of the thermoelectric properties in nanostructured* Fe_2VAl*.* Metals **8**, 864 (2018).

[105] S. Anand, R. Gurunathan, T. Soldi, L. Borgsmiller, R. Orenstein, and G. J. Snyder. *Thermoelectric transport of semiconductor full-Heusler VFe_2Al.* Journal of Materials Chemistry C **8**, 10174 (2020).

[106] S. Hiroi, M. Mikami, and T. Takeuchi. *Thermoelectric Properties of Fe_2VAl-Based Thin-Films Deposited at High Temperature.* Materials transactions **57**, 1628 (2016).

[107] S. Masuda, K. Tsuchiya, J. Qiang, H. Miyazaki, and Y. Nishino. *Effect of high-pressure torsion on the microstructure and thermoelectric properties of Fe_2VAl-based compounds.* Journal of Applied Physics **124**, 035106 (2018).

[108] C. Felser, L. Wollmann, S. Chadov, G. H. Fecher, and S. Parkin. *Basics and prospectives of magnetic Heusler compounds.* Heusler Alloys: Properties, Growth, Applications pp. 37–48 (2016).

[109] Y. Feng, J. Rhee, T. Wiener, D. W. Lynch, B. Hubbard, A. Sievers, D. Schlagel, T. Lograsso, and L. Miller. *Physical properties of Heusler-like Fe_2VAl.* Physical Review B **63**, 165109 (2001).

[110] I. Galanakis, P. Dederichs, and N. Papanikolaou. *Slater-Pauling behavior and origin of the half-metallicity of the full-Heusler alloys.* Physical Review B **66**, 174429 (2002).

[111] C. S. Lue, C. Chen, J. Lin, Y. Yu, and Y. Kuo. *Thermoelectric properties of quaternary Heusler alloys $Fe_2VAl_{1-x}Si_x$.* Physical Review B **75**, 064204 (2007).

[112] M. Mikami, Y. Kinemuchi, K. Ozaki, Y. Terazawa, and T. Takeuchi. *Thermoelectric properties of tungsten-substituted Heusler Fe_2VAl alloy.* Journal of Applied Physics **111**, 093710 (2012).

[113] M. Mikami, S. Tanaka, and K. Kobayashi. *Thermoelectric properties of Sb-doped Heusler Fe_2VAl alloy.* Journal of Alloys and Compounds **484**, 444 (2009).

[114] Y. Nishino, S. Deguchi, and U. Mizutani. *Thermal and transport properties of the Heusler-type $Fe_2VAl_{1-x}Ge_x$ ($0 \leqslant x \leqslant 0.20$) alloys: Effect of doping*

on lattice thermal conductivity, electrical resistivity, and Seebeck coefficient. Physical Review B **74**, 115115 (2006).

[115] M. Vasundhara, V. Srinivas, and V. Rao. *Low-temperature electrical transport in Heusler-type* $Fe_2V(AlSi)$ *alloys.* Journal of Physics: Condensed Matter **17**, 6025 (2005).

[116] M. Vasundhara, V. Srinivas, and V. Rao. *Electronic transport in Heusler-type* $Fe_2VAl_{1-x}M_x$ *alloys (M=B,In,Si).* Physical Review B **77**, 224415 (2008).

[117] F. Garmroudi, M. Parzer, A. Riss, N. Reumann, B. Hinterleitner, K. Tobita, Y. Katsura, K. Kimura, T. Mori, and E. Bauer. *Solubility limit and annealing effects on the microstructure & thermoelectric properties of* $Fe_2V_{1-x}Ta_xAl_{1-y}Si_y$ *Heusler compounds.* Acta Materialia **212**, 116867 (2021).

[118] Y. Terazawa, M. Mikami, T. Itoh, and T. Takeuchi. *Effects of heavy element substitution on electronic structure and lattice thermal conductivity of* Fe_2VAl *thermoelectric material.* Journal of electronic materials **41**, 1348 (2012).

[119] T. Takeuchi, Y. Terazawa, Y. Furuta, A. Yamamoto, and M. Mikami. *Effect of heavy element substitution and off-stoichiometric composition on thermoelectric properties of* Fe_2VAl*-based Heusler phase.* Journal of electronic materials **42**, 2084 (2013).

[120] S. Choi, S. Hiroi, M. Inukai, S. Nishino, R. Sobota, D. Byeon, M. Mikami, M. Matsunami, and T. Takeuchi. *Effects of partial substitution by 5d heavy elements on the thermal transport in* Fe_2VAl *thin films.* Physical Review B **101**, 104312 (2020).

[121] S. Hiroi, S. Nishino, S. Choi, O. Seo, J. Kim, Y. Chen, C. Song, A. Tayal, O. Sakata, and T. Takeuchi. *Phonon scattering at the interfaces of epitaxially grown* Fe_2VAl/W *and* Fe_2VAl/Mo *superlattices.* Journal of Applied Physics **125**, 225101 (2019).

[122] K. Kudo, S. Yamada, J. Chikada, Y. Shimanuki, T. Ishibe, S. Abo, H. Miyazaki, Y. Nishino, Y. Nakamura, and K. Hamaya. *Significant reduc-*

tion in the thermal conductivity of Si-substituted Fe_2VAl epilayers. Physical Review B **99**, 054201 (2019).

[123] S. Maier, S. Denis, S. Adam, J.-C. Crivello, J.-M. Joubert, and E. Alleno. *Order-disorder transitions in the Fe_2VAl Heusler alloy.* Acta Materialia **121**, 126 (2016).

[124] H. Matsuura, M. Ogata, T. Mori, and E. Bauer. *Theory of huge thermoelectric effect based on a magnon drag mechanism: Application to thin-film Heusler alloy.* Physical Review B **104**, 214421 (2021).

[125] Q. Ma, H. Fang, and M. Zhang. *Theoretical analysis and design optimization of thermoelectric generator.* Applied Thermal Engineering **127**, 758 (2017).

[126] M. H. Elsheikh, D. A. Shnawah, M. F. M. Sabri, S. B. M. Said, M. H. Hassan, M. B. A. Bashir, and M. Mohamad. *A review on thermoelectric renewable energy: Principle parameters that affect their performance.* Renewable and sustainable energy reviews **30**, 337 (2014).

[127] T. Zoller, C. Nagel, R. Ehrenpfordt, and A. Zimmermann. *Packaging of small-scale thermoelectric generators for autonomous sensor nodes.* IEEE Transactions on Components, Packaging and Manufacturing Technology **7**, 1043 (2017).

[128] R. Bonin, D. Boero, M. Chiaberge, and A. Tonoli. *Design and characterization of small thermoelectric generators for environmental monitoring devices.* Energy Conversion and Management **73**, 340 (2013).

[129] V. Leonov, T. Torfs, P. Fiorini, and C. Van Hoof. *Thermoelectric converters of human warmth for self-powered wireless sensor nodes.* IEEE Sensors Journal **7**, 650 (2007).

[130] C. Wang, S. Tang, X. Liu, G. Su, W. Tian, and S. Qiu. *Experimental study on heat pipe thermoelectric generator for industrial high temperature waste heat recovery.* Applied Thermal Engineering **175**, 115299 (2020).

[131] H. Kaibe, T. Kajihara, S. Fujimoto, K. Makino, and H. Hachiuma. *Recovery of plant waste heat by a thermoelectric generating system*. Komatsu Technical Report **57**, 26 (2011).

[132] N. Kristiansen, G. Snyder, H. Nielsen, and L. Rosendahl. *Waste heat recovery from a marine waste incinerator using a thermoelectric generator*. Journal of electronic materials **41**, 1024 (2012).

[133] M. Jiang. *An overview of radioisotope thermoelectric generators*. Introduction to Nuclear Energy PH241-Stanford University-Winter (2013).

[134] B. Blanke, J. Birden, K. Jordan, and E. Murphy. *Nuclear battery-thermocouple type summary report*. Tech. rep., Mound Lab., Miamisburg, Ohio (1960).

[135] G. R. Schmidt, T. J. Sutliff, and L. Dudzinksi. *Radioisotope power: A key technology for deep space exploration*. Radioisotopes–Applications in Physical Sciences pp. 419–456 (2011).

[136] J. Werner, K. Lively, and D. Kirkham. *A multi-mission radioisotope thermoelectric generator (MMRTG) for Mars 2020*. In *2017 IEEE Aerospace Conference*, pp. 1–6. IEEE (2017).

[137] C. E. Whiting, C. D. Barklay, and B. A. Tolson. *Understanding Degradation and Heat Losses in the MMRTG and an Improved Analysis of F1 on Curiosity*. In *2022 IEEE Aerospace Conference (AERO)*, pp. 1–9. IEEE (2022).

[138] T. C. Holgate, R. Bennett, L. Renomeron, S. Keyser, I. Chi, J. Ni, K. Yu, T. Caillat, and S. Pinkowski. *Analysis of raw materials sourcing and the implications for the performance of skutterudite couples in multi-mission radioisotope thermoelectric generators*. Journal of Electronic Materials **48**, 7526 (2019).

[139] T. C. Holgate, Y. Song, D. Shi, R. Utz, T. Chung, R. Bennett, S. Keyser, T. E. Hammel, R. Sievers, T. Caillat *et al.* *Enhancement of the Multi-Mission Radioisotope Thermoelectric Generator with Efficient Skutterudite Thermoelectric Couples: Current Status of the Skutterudite Technology Maturation*

Program. In *14th International Energy Conversion Engineering Conference*, p. 4817 (2016).

[140] D. Champier. *Thermoelectric generators: A review of applications.* Energy Conversion and Management **140**, 167 (2017).

[141] Z. Wang, V. Leonov, P. Fiorini, and C. Van Hoof. *Realization of a wearable miniaturized thermoelectric generator for human body applications.* Sensors and Actuators A: Physical **156**, 95 (2009).

[142] M. N. Hasan, M. Nafea, N. Nayan, and M. S. Mohamed Ali. *Thermoelectric generator: materials and applications in wearable health monitoring sensors and internet of things devices.* Advanced Materials Technologies **7**, 2101203 (2022).

[143] Y. Yang, Z.-H. Lin, T. Hou, F. Zhang, and Z. L. Wang. *Nanowire-composite based flexible thermoelectric nanogenerators and self-powered temperature sensors.* Nano Research **5**, 888 (2012).

[144] R. Feng, F. Tang, N. Zhang, and X. Wang. *Flexible, high-power density, wearable thermoelectric nanogenerator and self-powered temperature sensor.* ACS applied materials & interfaces **11**, 38616 (2019).

[145] H. Cheng, Y. Du, B. Wang, Z. Mao, H. Xu, L. Zhang, Y. Zhong, W. Jiang, L. Wang, and X. Sui. *Flexible cellulose-based thermoelectric sponge towards wearable pressure sensor and energy harvesting.* Chemical Engineering Journal **338**, 1 (2018).

[146] Y. Wang, W. Zhu, Y. Deng, B. Fu, P. Zhu, Y. Yu, J. Li, and J. Guo. *Self-powered wearable pressure sensing system for continuous healthcare monitoring enabled by flexible thin-film thermoelectric generator.* Nano Energy **73**, 104773 (2020).

[147] Y. Zhang, M. Cleary, X. Wang, N. Kempf, L. Schoensee, J. Yang, G. Joshi, and L. Meda. *High-temperature and high-power-density nanostructured thermoelectric generator for automotive waste heat recovery.* Energy Conversion and Management **105**, 946 (2015).

[148] *Reduced energy consumption by massive thermoeelctric waste heat recovery in light duty trucks.* https://cordis.europa.eu/project/id/218541/reporting. Accessed: 2022-10-27.

[149] M. Josijević, D. Živković, D. Gordić, D. Končalović, and V. Vukašinović. *The analysis of commercially available electric cars.* Mobil Veh Mech **48**, 19 (2022).

[150] T. Kousksou, J.-P. Bédécarrats, D. Champier, P. Pignolet, and C. Brillet. *Numerical study of thermoelectric power generation for an helicopter conical nozzle.* Journal of Power Sources **196**, 4026 (2011).

[151] P. Aranguren, D. Astrain, A. Rodríguez, and A. Martínez. *Experimental investigation of the applicability of a thermoelectric generator to recover waste heat from a combustion chamber.* Applied Energy **152**, 121 (2015).

[152] T. Kuroki, K. Kabeya, K. Makino, T. Kajihara, H. Kaibe, H. Hachiuma, H. Matsuno, and A. Fujibayashi. *Thermoelectric generation using waste heat in steel works.* Journal of electronic materials **43**, 2405 (2014).

[153] A. F. May, E. S. Toberer, A. Saramat, and G. J. Snyder. *Characterization and analysis of thermoelectric transport in n-type* $Ba_8Ga_{16-x}Ge_{30+x}$. Physical Review B **80**, 125205 (2009).

[154] A. F. May, E. Flage-Larsen, and G. J. Snyder. *Electron and phonon scattering in the high-temperature thermoelectric* $La_3Te_{4-z}M_z$ *(M = Sb, Bi).* Physical Review B **81**, 125205 (2010).

[155] S. K. Bux, M. T. Yeung, E. S. Toberer, G. J. Snyder, R. B. Kaner, and J.-P. Fleurial. *Mechanochemical synthesis and thermoelectric properties of high quality magnesium silicide.* Journal of Materials Chemistry **21**, 12259 (2011).

[156] J. De Boor, T. Dasgupta, H. Kolb, C. Compere, K. Kelm, and E. Mueller. *Microstructural effects on thermoelectric efficiency: A case study on magnesium silicide.* Acta materialia **77**, 68 (2014).

[157] J. de Boor. *On the applicability of the single parabolic band model to advanced thermoelectric materials with complex band structures.* Journal of Materiomics **7**, 603 (2021).

[158] N. W. Ashcroft and N. D. Mermin. *Solid state physics.* Cengage Learning (2022).

[159] O. L. Anderson. *A simplified method for calculating the Debye temperature from elastic constants.* Journal of Physics and Chemistry of Solids **24**, 909 (1963).

[160] S.-F. Wang, Y.-F. Hsu, J.-C. Pu, J. C. Sung, and L. Hwa. *Determination of acoustic wave velocities and elastic properties for diamond and other hard materials.* Materials Chemistry and Physics **85**, 432 (2004).

[161] K. A. Gschneidner Jr. *Physical properties and interrelationships of metallic and semimetallic elements.* In *Solid state physics*, vol. 16, pp. 275–426. Elsevier (1964).

[162] R. Gross and A. Marx. *Festkörperphysik.* Oldenbourg Wissenschaftsverlag Verlag (2012).

[163] Y. Nishino. *Development of thermoelectric materials based on Fe_2VAl Heusler compound for energy harvesting applications.* In *IOP Conference Series: Materials Science and Engineering*, vol. 18, p. 142001. IOP Publishing (2011).

[164] S. Bandaru and P. Jund. *Electronic structure of the Heusler compound Fe_2VAl and its point defects by ab initio calculations.* physica status solidi (b) **254**, 1600441 (2017).

[165] B. Hinterleitner, F. Garmroudi, N. Reumann, T. Mori, E. Bauer, and R. Podloucky. *The electronic pseudo band gap states and electronic transport of the full-Heusler compound Fe_2VAl.* Journal of Materials Chemistry C **9**, 2073 (2021).

[166] A. Berche, M. T. Noutack, M.-L. Doublet, and P. Jund. *Unexpected band gap increase in the Fe_2VAl Heusler compound.* Materials Today Physics **13**, 100203 (2020).

[167] D. Singh and I. Mazin. *Electronic structure, local moments, and transport in* Fe_2VAl. Physical Review B **57**, 14352 (1998).

[168] A. Riss, M. Stöger, M. Parzer, F. Garmroudi, N. Reumann, B. Hinterleitner, T. Mori, and E. Bauer. *Criteria for Erroneous Substrate Contribution to the Thermoelectric Performance of Thin Films.* Physical Review Applied **19**, 054024 (2023).

[169] A. Riss, F. Garmroudi, M. Parzer, A. Pustogow, T. Mori, and E. Bauer. *Thermoelectric power factor of composites.* Physical Review Applied **21**, 014002 (2024).

[170] R. Saha and W. D. Nix. *Effects of the substrate on the determination of thin film mechanical properties by nanoindentation.* Acta materialia **50**, 23 (2002).

[171] T. Tsui and G. Pharr. *Substrate effects on nanoindentation mechanical property measurement of soft films on hard substrates.* Journal of Materials research **14**, 292 (1999).

[172] A. Ney, T. Kammermeier, V. Ney, K. Ollefs, and S. Ye. *Limitations of measuring small magnetic signals of samples deposited on a diamagnetic substrate.* Journal of Magnetism and Magnetic Materials **320**, 3341 (2008).

[173] R. Delatorre, M. Sartorelli, A. Schervenski, A. Pasa, and S. Güths. *Thermoelectric properties of electrodeposited CuNi alloys on Si.* Journal of applied physics **93**, 6154 (2003).

[174] P. Yordanov, P. Wochner, S. Ibrahimkutty, C. Dietl, F. Wrobel, R. Felici, G. Gregori, J. Maier, B. Keimer, and H.-U. Habermeier. *Perovskite substrates boost the thermopower of cobaltate thin films at high temperatures.* Applied Physics Letters **110**, 253101 (2017).

[175] G. Pharr and W. Oliver. *Measurement of thin film mechanical properties using nanoindentation.* Mrs Bulletin **17**, 28 (1992).

[176] C. Dames. *Measuring the thermal conductivity of thin films: 3 omega and related electrothermal methods.* Annual Review of Heat Transfer **16** (2013).

[177] S. Shimizu, J. Shiogai, N. Takemori, S. Sakai, H. Ikeda, R. Arita, T. Nojima, A. Tsukazaki, and Y. Iwasa. *Giant thermoelectric power factor in ultrathin FeSe superconductor.* Nature communications **10**, 1 (2019).

[178] J. Zhang, W. Song, X. Ge, Z. Luo, and S. Yue. *Boosted thermoelectric properties of molybdenum oxide thin films deposited on Si substrates.* Modern Physics Letters B **33**, 1950016 (2019).

[179] X. Ge, H. Zhu, and S. Yue. *Optimization of large power factor in molybdenum oxide thin films deposited on Si substrate.* Modern Physics Letters B **34**, 2050200 (2020).

[180] D. Byeon, R. Sobota, K. Delime-Codrin, S. Choi, K. Hirata, M. Adachi, M. Kiyama, T. Matsuura, Y. Yamamoto, M. Matsunami *et al.* *Discovery of colossal Seebeck effect in metallic* Cu_2Se. Nature communications **10**, 1 (2019).

[181] D. Byeon, R. Sobota, S. Singh, S. Ghodke, S. Choi, N. Kubo, M. Adachi, Y. Yamamoto, M. Matsunami, and T. Takeuchi. *Long-Term Stability of the Colossal Seebeck Effect in Metallic* Cu_2Se. Journal of Electronic Materials pp. 1–7 (2020).

[182] G. Kim, D. Byeon, S. Singh, K. Hirata, S. Choi, M. Matsunami, and T. Takeuchi. *Mixed-phase effect of a high Seebeck coefficient and low electrical resistivity in* Ag_2S. Journal of Physics D: Applied Physics **54**, 115503 (2021).

[183] D. J. Bergman and O. Levy. *Thermoelectric properties of a composite medium.* Journal of Applied Physics **70**, 6821 (1991).

[184] D. J. Bergman and L. G. Fel. *Enhancement of thermoelectric power factor in composite thermoelectrics.* Journal of Applied physics **85**, 8205 (1999).

[185] J. Alvarez-Quintana. *Impact of the substrate on the efficiency of thin film thermoelectric technology.* Applied Thermal Engineering **84**, 206 (2015).

[186] T. Baba. *Analysis of one-dimensional heat diffusion after light pulse heating by the response function method.* Japanese Journal of Applied Physics **48**, 05EB04 (2009).

[187] T. Baba, N. Taketoshi, and T. Yagi. *Development of ultrafast laser flash methods for measuring thermophysical properties of thin films and boundary thermal resistances.* Japanese Journal of Applied Physics **50**, 11RA01 (2011).

[188] W. Gao, Z. Liu, T. Baba, Q. Guo, D.-M. Tang, N. Kawamoto, E. Bauer, N. Tsujii, and T. Mori. *Significant off-stoichiometry effect leading to the N-type conduction and ferromagnetic properties in titanium doped* Fe_2VAl *thin films.* Acta Materialia **200**, 848 (2020).

[189] F. Qiu, W. Shin, M. Matsumiya, N. Izu, I. Matsubara, and N. Murayama. *Miniaturization of thermoelectric hydrogen sensor prepared on glass substrate with low-temperature crystallized SiGe film.* Sensors and Actuators B: Chemical **103**, 252 (2004).

[190] Y. Hu, E. Sutter, W. Si, and Q. Li. *Thermoelectric properties and microstructure of c-axis-oriented* $Ca_3Co_4O_9$ *thin films on glass substrates.* Applied Physics Letters **87** (2005).

[191] X. Zhang, Z. Pei, J. Gong, and C. Sun. *Investigation on the electrical properties and inhomogeneous distribution of ZnO:Al thin films prepared by dc magnetron sputtering at low deposition temperature.* Journal of applied physics **101** (2007).

[192] Z. Yu, X. Wang, Y. Du, S. Aminorroaya-Yamni, C. Zhang, K. Chuang, and S. Li. *Fabrication and characterization of textured* Bi_2Te_3 *thermoelectric thin films prepared on glass substrates at room temperature using pulsed laser deposition.* Journal of crystal growth **362**, 247 (2013).

[193] S. Mortazavinatanzi, M. Mirhosseini, L. Song, B. B. Iversen, L. Rosendahl, and A. Rezania. *Zinc antimonide thin film based flexible thermoelectric module.* Materials Letters **280**, 128582 (2020).

[194] N. A. Khan, M. A. Alnuwaiser, M. R. Javed, S. Ikram, A. Ali, M. Y. Ali, M. Amami, M. A. Nawaz, K. Javaid, M. S. Hussain *et al.* *Effect of Sn*

concentration on the structural, morphological and thermoelectric transport properties of zinc Stannates thin films. Ceramics International **48**, 35237 (2022).

[195] M. Matsumiya, F. Qiu, W. Shin, N. Izu, N. Murayama, and S. Kanzaki. *Thin-film Li-doped NiO for thermoelectric hydrogen gas sensor.* Thin Solid Films **419**, 213 (2002).

[196] T. Jaeger, C. Mix, M. Schwall, X. Kozina, J. Barth, B. Balke, M. Finsterbusch, Y. U. Idzerda, C. Felser, and G. Jakob. *Epitaxial growth and thermoelectric properties of TiNiSn and* $Zr_{0.5}Hf_{0.5}NiSn$ *thin films.* Thin Solid Films **520**, 1010 (2011).

[197] P. V. Burmistrova, J. Maassen, T. Favaloro, B. Saha, S. Salamat, Y. Rui Koh, M. S. Lundstrom, A. Shakouri, and T. D. Sands. *Thermoelectric properties of epitaxial ScN films deposited by reactive magnetron sputtering onto MgO (001) substrates.* Journal of Applied Physics **113** (2013).

[198] A. T. Duong, S. Rhim, Y. Shin, V. Q. Nguyen, and S. Cho. *Magneto-transport and thermoelectric properties of epitaxial* $FeSb_2$ *thin film on MgO substrate.* Applied Physics Letters **106** (2015).

[199] P. V. Burmistrova, D. N. Zakharov, T. Favaloro, A. Mohammed, E. A. Stach, A. Shakouri, and T. D. Sands. *Effect of deposition pressure on the microstructure and thermoelectric properties of epitaxial ScN (001) thin films sputtered onto MgO (001) substrates.* Journal of Materials Research **30**, 626 (2015).

[200] Y. Kurosaki, S. Yabuuchi, A. Nishide, N. Fukatani, and J. Hayakawa. *Thermoelectric properties of composition-controlled* Fe_2TiSi*-based full-Heusler thin films.* Applied Physics Express **15**, 085502 (2022).

[201] M. Mikami, T. Kamiya, and K. Kobayashi. *Microstructure and thermoelectric properties of Heusler* Fe_2VAl *thin-films.* Thin Solid Films **518**, 2796 (2010).

[202] J. Buršík, M. Soroka, K. Knížek, J. Hirschner, P. Levinskỳ, and J. Hejtmánek. *Oriented thin films of* $Na_{0.6}CoO_2$ *and* $Ca_3Co_4O_9$ *deposited by spin-coating method on polycrystalline substrate.* Thin Solid Films **603**, 400 (2016).

[203] A. Pérez-Rivero, M. Cabero, M. Varela, R. Ramírez-Jiménez, F. Mompean, J. Santamaría, J. Martínez, and C. Prieto. *Thermoelectric functionality of* $Ca_3Co_4O_9$ *epitaxial thin films on yttria-stabilized zirconia crystalline substrate*. Journal of Alloys and Compounds **710**, 151 (2017).

[204] L. Goncalves, C. Couto, P. Alpuim, A. G. Rolo, F. Völklein, and J. Correia. *Optimization of thermoelectric properties on* Bi_2Te_3 *thin films deposited by thermal co-evaporation*. Thin Solid Films **518**, 2816 (2010).

[205] M. Hokazono, H. Anno, and N. Toshima. *Thermoelectric properties and thermal stability of PEDOT: PSS films on a polyimide substrate and application in flexible energy conversion devices*. Journal of Electronic Materials **43**, 2196 (2014).

[206] C. T. Hong, Y. H. Kang, J. Ryu, S. Y. Cho, and K.-S. Jang. *Spray-printed CNT/P3HT organic thermoelectric films and power generators*. Journal of materials Chemistry A **3**, 21428 (2015).

[207] T. Varghese, C. Hollar, J. Richardson, N. Kempf, C. Han, P. Gamarachchi, D. Estrada, R. J. Mehta, and Y. Zhang. *High-performance and flexible thermoelectric films by screen printing solution-processed nanoplate crystals*. Scientific reports **6**, 33135 (2016).

[208] Z. Lin, C. Hollar, J. S. Kang, A. Yin, Y. Wang, H.-Y. Shiu, Y. Huang, Y. Hu, Y. Zhang, and X. Duan. *A solution processable high-performance thermoelectric copper selenide thin film*. Advanced Materials **29**, 1606662 (2017).

[209] S. Yang, K. Cho, J. Yun, J. Choi, and S. Kim. *Thermoelectric characteristics of* γ*-*Ag_2Te *nanoparticle thin films on flexible substrates*. Thin Solid Films **641**, 65 (2017).

[210] K. Kusano, A. Yamamoto, M. Nakata, T. Suemasu, and K. Toko. *Thermoelectric inorganic SiGe film synthesized on flexible plastic substrate*. ACS Applied Energy Materials **1**, 5280 (2018).

[211] W. Ren, Y. Sun, D. Zhao, A. Aili, S. Zhang, C. Shi, J. Zhang, H. Geng, J. Zhang, L. Zhang *et al. High-performance wearable thermoelectric generator*

with self-healing, recycling, and Lego-like reconfiguring capabilities. Science advances **7**, eabe0586 (2021).

[212] M. Takashiri, T. Borca-Tasciuc, A. Jacquot, K. Miyazaki, and G. Chen. *Structure and thermoelectric properties of boron doped nanocrystalline* $Si_{0.8}Ge_{0.2}$ *thin film.* Journal of Applied Physics **100** (2006).

[213] M. Aguirre, S. Canulescu, R. Robert, N. Homazava, D. Logvinovich, L. Bocher, T. Lippert, M. Döbeli, and A. Weidenkaff. *Structure, microstructure, and high-temperature transport properties of* $La_{1-x}Ca_xMnO_{3-\delta}$ *thin films and polycrystalline bulk materials.* Journal of Applied Physics **103** (2008).

[214] H. B. Lee, J. H. We, H. J. Yang, K. Kim, K. C. Choi, and B. J. Cho. *Thermoelectric properties of screen-printed ZnSb film.* Thin Solid Films **519**, 5441 (2011).

[215] P. Mele, S. Saini, H. Honda, K. Matsumoto, K. Miyazaki, H. Hagino, and A. Ichinose. *Effect of substrate on thermoelectric properties of Al-doped ZnO thin films.* Applied Physics Letters **102** (2013).

[216] A. Nozariasbmarz, A. T. Rad, Z. Zamanipour, J. S. Krasinski, L. Tayebi, and D. Vashaee. *Enhancement of thermoelectric power factor of silicon germanium films grown by electrophoresis deposition.* Scripta Materialia **69**, 549 (2013).

[217] J. Jacob, R. Wahid, A. Ali, R. Zahra, S. Ikram, N. Amin, A. Ashfa, U. Rehman, S. Hussain, D. S. Al-Othmany *et al.* *Growth of* Cu_2InO_4 *thin films on Si substrate by thermal evaporation technique and enhancement of thermoelectric properties by post-growth annealing.* Physica B: Condensed Matter **562**, 59 (2019).

[218] U. Rehman, J. Jacob, K. Mahmood, A. Ali, A. Ashfaq, N. Amin, S. Ikram, W. Ahmad, and S. Hussain. *Direct growth of ZnSnO nano-wires by thermal evaporation technique for thermoelectric applications.* Physica B: Condensed Matter **570**, 232 (2019).

[219] U. Rehman, K. Mahmood, A. Ali, A. Ashfaq, A. Rehman, M. A. un Nabi, M. I. Arshad, N. Amin, S. Ikram, and S. Hussain. *Optimizing the electrical*

transport properties of ZnSnO thin films by post growth annealing in air. Optik **204**, 164148 (2020).

[220] A. Grießer, T. Kraus, O. Klein, and H. Karl. *Low-resistance electrical contact between epitaxially grown thermoelectric oxide material* $(Ca_2CoO_3)_{0.62}CoO_2$ *and iridium*. Thin Solid Films **717**, 138420 (2021).

[221] J. Zhang, H. Ming, D. Li, X. Qin, J. Zhang, L. Huang, C. Song, and L. Wang. *Ultralow thermal conductivity and high thermoelectric performance of n-type* $Bi_2Te_{2.7}Se_{0.3}$*-based composites incorporated with GaAs nanoinclusions*. ACS Applied Materials & Interfaces **12**, 37155 (2020).

[222] N. Neophytou, X. Zianni, H. Kosina, S. Frabboni, B. Lorenzi, and D. Narducci. *Simultaneous increase in electrical conductivity and Seebeck coefficient in highly boron-doped nanocrystalline Si*. Nanotechnology **24**, 205402 (2013).

[223] B. Nan, X. Song, C. Chang, K. Xiao, Y. Zhang, L. Yang, S. Horta, J. Li, K. H. Lim, M. Ibáñez *et al. Bottom-Up Synthesis of SnTe-Based Thermoelectric Composites*. ACS Applied Materials & Interfaces **15**, 23380 (2023).

[224] X. Yang, X. Qin, J. Zhang, D. Li, H. Xin, and M. Liu. *Enhanced thermopower and energy filtering effect from synergetic scattering at heterojunction potentials in the thermoelectric composites with semiconducting nanoinclusions*. Journal of alloys and compounds **558**, 203 (2013).

[225] B. Madavali, H.-S. Kim, K.-H. Lee, and S.-J. Hong. *Enhanced Seebeck coefficient by energy filtering in Bi-Sb-Te based composites with dispersed* Y_2O_3 *nanoparticles*. Intermetallics **82**, 68 (2017).

[226] N. Neophytou, S. Foster, V. Vargiamidis, G. Pennelli, and D. Narducci. *Nanostructured potential well/barrier engineering for realizing unprecedentedly large thermoelectric power factors*. Materials Today Physics **11**, 100159 (2019).

[227] H. Odahara, O. Yamashita, K. Satou, S. Tomiyoshi, J.-i. Tani, and H. Kido. *Increase of the thermoelectric power factor in Cu/Bi/Cu, Ni/Bi/Ni, and Cu/Bi/Ni composite materials*. Journal of applied physics **97**, 103722 (2005).

[228] O. Yamashita, H. Odahara, and K. Satou. *Enhancement in thermoelectric power factor of M/T/N and M/Bi/M/Bi/M (M and N=Cu or Ni) composite devices welded with T=Bi or* $Bi_{0.88}Sb_{0.12}$ *alloy*. Journal of materials science **40**, 1071 (2005).

[229] M. Mikami, N. Ando, and R. Funahashi. *The effect of Ag addition on electrical properties of the thermoelectric compound* $Ca_3Co_4O_9$. Journal of Solid State Chemistry **178**, 2186 (2005).

[230] O. Yamashita, H. Odahara, K. Satou, and S. Tomiyoshi. *Enhancement of the thermoelectric power factor in Ag/Bi-Te/Ag composite devices*. Journal of materials science **41**, 3089 (2006).

[231] J. Heremans and C. Jaworski. *Experimental study of the thermoelectric power factor enhancement in composites*. Applied Physics Letters **93**, 122107 (2008).

[232] A. Sotelo, M. Torres, G. Constantinescu, S. Rasekh, J. Diez, and M. Madre. *Effect of Ag addition on the mechanical and thermoelectric performances of annealed* $Bi_2Sr_2Co_{1.8}O_x$ *textured ceramics*. Journal of the European Ceramic Society **32**, 3745 (2012).

[233] F. Kahraman, M. Madre, S. Rasekh, C. Salvador, P. Bosque, M. Torres, J. Diez, and A. Sotelo. *Enhancement of mechanical and thermoelectric properties of* $Ca_3Co_4O_9$ *by Ag addition*. Journal of the European Ceramic Society **35**, 3835 (2015).

[234] B. Zhan, Y. Liu, J. Lan, C. Zeng, Y.-H. Lin, and C.-W. Nan. *Enhanced thermoelectric performance of* Bi_2O_2Se *with Ag addition*. Materials **8**, 1568 (2015).

[235] S. D. Sharma, B. Khasimsaheb, Y. Chen, and S. Neeleshwar. *Enhanced thermoelectric performance of* Cu_2ZnSnS_4 *(CZTS) by incorporating Ag nanoparticles*. Ceramics International **45**, 2060 (2019).

[236] C. Ho, M. Ackerman, K. Wu, S. Oh, and T. Havill. *Thermal conductivity of ten selected binary alloy systems*. Journal of Physical and Chemical Reference Data **7**, 959 (1978).

[237] C. Y. Ho, M. Ackerman, K. Wu, T. Havill, R. Bogaard, R. Matula, S. Oh, and H. James. *Electrical resistivity of ten selected binary alloy systems*. Journal of physical and chemical reference data **12**, 183 (1983).

[238] C. Ho, R. Bogaard, T. Chi, T. Havill, and H. James. *Thermoelectric power of selected metals and binary alloy systems*. Thermochimica acta **218**, 29 (1993).

[239] C. Zhou, Y. K. Lee, Y. Yu, S. Byun, Z.-Z. Luo, H. Lee, B. Ge, Y.-L. Lee, X. Chen, J. Y. Lee *et al.* *Polycrystalline SnSe with a thermoelectric figure of merit greater than the single crystal*. Nature materials **20**, 1378 (2021).

[240] Y. Pei, X. Shi, A. LaLonde, H. Wang, L. Chen, and G. J. Snyder. *Convergence of electronic bands for high performance bulk thermoelectrics*. Nature **473**, 66 (2011).

[241] J. Chen, Z. Yan, and L. Wu. *The influence of Thomson effect on the maximum power output and maximum efficiency of a thermoelectric generator*. Journal of applied physics **79**, 8823 (1996).

[242] M. Adams, M. Verosky, M. Zebarjadi, and J. Heremans. *Active peltier coolers based on correlated and magnon-drag metals*. Physical Review Applied **11**, 054008 (2019).

[243] R. J. Gripshover, J. B. VanZytveld, and J. Bass. *Thermopower of pure aluminum*. Physical Review **163**, 598 (1967).

[244] K. Biswas, J. He, I. D. Blum, C.-I. Wu, T. P. Hogan, D. N. Seidman, V. P. Dravid, and M. G. Kanatzidis. *High-performance bulk thermoelectrics with all-scale hierarchical architectures*. Nature **489**, 414 (2012).

[245] A. Makhlouf. *Current and advanced coating technologies for industrial applications*. In *Nanocoatings and ultra-thin films*, pp. 3–23. Elsevier (2011).

[246] *The Difference Between Physical Vapor Deposition (PVD) & Chemical Vapor Deposition (CVD)*. `https://www.azom.com/article.aspx?ArticleID=17130`. Accessed: 2022-10-24.

[247] N. Matsunami, Y. Yamamura, Y. Itikawa, N. Itoh, Y. Kazumata, S. Miyagawa, K. Morita, R. Shimizu, and H. Tawara. *Energy dependence of the yields of ion-induced sputtering of monatomic solids.* Unknown (1983).

[248] K. Wasa. *2 - Sputtering Phenomena.* In K. Wasa, I. Kanno, and H. Kotera (editors), *Handbook of Sputtering Technology (Second Edition)*, pp. 41–75. William Andrew Publishing, Oxford, second edition edn. (2012).

[249] *A Simple Sputter Yield Calculator.* https://www.iap.tuwien.ac.at/www/surface/sputteryield. Accessed: 2022-10-27.

[250] M. Ohring. *Materials Science of Thin Films: Depositon and Structure.* Elsevier (2001).

[251] R. A. Levy. *Microelectronic materials and processes*, vol. 164. Springer Science & Business Media (2012).

[252] S. Mahieu, G. Buyle, D. Depla, S. Heirwegh, P. Ghekiere, and R. De Gryse. *Monte Carlo simulation of the transport of atoms in DC magnetron sputtering.* Nuclear Instruments and Methods in Physics Research Section B: Beam Interactions with Materials and Atoms **243**, 313 (2006).

[253] J. Neidhardt, S. Mráz, J. M. Schneider, E. Strub, W. Bohne, B. Liedke, W. Möller, and C. Mitterer. *Experiment and simulation of the compositional evolution of Ti–B thin films deposited by sputtering of a compound target.* Journal of applied physics **104** (2008).

[254] Y. V. Martynenko, A. Rogov, and V. Shul'Ga. *Angular distribution of atoms during the magnetron sputtering of polycrystalline targets.* Technical physics **57**, 439 (2012).

[255] A. Rogov and Y. V. Kapustin. *Angular Distributions during Magnetron Sputtering of Polycrystalline Mg, Al, Si, Ti, Cr, Cu, Zn, Ge, Zr, Nb, Mo, Ag, In, Sn, W, Pt, Au, and Bi Targets.* Instruments and Experimental Techniques **63**, 776 (2020).

[256] J. Shi, C. Chen, H. Yu, and S. Zhang. *The effect of process conditions on the properties of bioactive films prepared by magnetron sputtering.* Vacuum **83**, 249 (2008).

[257] E. Särhammar, E. Strandberg, J. Sundberg, H. Nyberg, T. Kubart, S. Jacobson, U. Jansson, and T. Nyberg. *Mechanisms for compositional variations of coatings sputtered from a* WS_2 *target.* Surface and Coatings Technology **252**, 186 (2014).

[258] K. Seshan and D. Schepis. *Handbook of thin film deposition.* William Andrew (2018).

[259] T. Huang. *Thin-film characterization by X-ray fluorescence.* X-Ray Spectrometry **20**, 29 (1991).

[260] J. Mackey, A. Sehirlioglu, and F. Dynys. *Detailed Uncertainty Analysis of the ZEM-3 Measurement System.* In *International Conference on Thermoelectrics*, GRC-E-DAA-TN16200 (2014).

[261] K.-e. Shinzato and T. Baba. *A laser flash apparatus for thermal diffusivity and specific heat capacity measurements.* Journal of thermal analysis and calorimetry **64**, 413 (2001).

[262] S. Min, J. Blumm, and A. Lindemann. *A new laser flash system for measurement of the thermophysical properties.* Thermochimica Acta **455**, 46 (2007).

[263] D. Zhao, X. Qian, X. Gu, S. A. Jajja, and R. Yang. *Measurement techniques for thermal conductivity and interfacial thermal conductance of bulk and thin film materials.* Journal of Electronic Packaging **138**, 040802 (2016).

[264] A. Ioffe. *The problem of new energy sources.* The socialist reconstruction and science **1**, 23 (1932).

[265] J. P. Heremans, V. Jovovic, E. S. Toberer, A. Saramat, K. Kurosaki, A. Charoenphakdee, S. Yamanaka, and G. J. Snyder. *Enhancement of thermoelectric efficiency in PbTe by distortion of the electronic density of states.* Science **321**, 554 (2008).

[266] F. Ahmed, N. Tsujii, and T. Mori. *Thermoelectric properties of* $CuGa_{1-x}Mn_xTe_2$*: power factor enhancement by incorporation of magnetic ions.* Journal of Materials Chemistry A **5**, 7545 (2017).

[267] N. Tsujii, A. Nishide, J. Hayakawa, and T. Mori. *Observation of enhanced thermopower due to spin fluctuation in weak itinerant ferromagnet.* Science advances **5**, eaat5935 (2019).

[268] D. M. Rowe. *CRC handbook of thermoelectrics.* CRC press (2018).

[269] A. Rodríguez, J. Vián, D. Astrain, and A. Martínez. *Study of thermoelectric systems applied to electric power generation.* Energy Conversion and Management **50**, 1236 (2009).

[270] A. Riss, F. Garmroudi, M. Parzer, C. Eisenmenger-Sittner, A. Pustogow, T. Mori, and E. Bauer. *Material-efficient preparation and thermoelectric properties of metallic NiAu films with ultra-high power factor* (2024).

[271] N. F. Mott and E. A. Davis. *Electronic processes in non-crystalline materials.* Oxford university press (2012).

[272] M. Jonson and G. Mahan. *Mott's formula for the thermopower and the Wiedemann-Franz law.* Physical Review B **21**, 4223 (1980).

[273] S. Watanabe, M. Ohno, Y. Yamashita, T. Terashige, H. Okamoto, and J. Takeya. *Validity of the Mott formula and the origin of thermopower in* π*-conjugated semicrystalline polymers.* Physical Review B **100**, 241201 (2019).

[274] N. Mott. *A discussion of the transition metals on the basis of quantum mechanics.* Proceedings of the Physical Society **47**, 571 (1935).

[275] R. Liu, Y. Ge, D. Wang, and Z. Shuai. *Understanding the Temperature Dependence of the Seebeck Coefficient from First-Principles Band Structure Calculations for Organic Thermoelectric Materials.* CCS Chemistry **3**, 1477 (2021).

[276] P. A. M. Dirac. *The quantum theory of the emission and absorption of radiation.* Proceedings of the Royal Society of London. Series A, Containing Papers of a Mathematical and Physical Character **114**, 243 (1927).

[277] J. Wang, X.-G. Lu, B. Sundman, and X. Su. *Thermodynamic assessment of the Au – Ni system.* Calphad **29**, 263 (2005).

[278] C. Kittel. *Interpretation of the thermal conductivity of glasses.* Physical Review **75**, 972 (1949).

[279] J.-F. Bisson, D. Fournier, M. Poulain, O. Lavigne, and R. Mévrel. *Thermal conductivity of yttria-zirconia single crystals, determined with spatially resolved infrared thermography.* Journal of the American Ceramic Society **83**, 1993 (2000).

[280] H. Ahmad and D. Greig. *The electrical resistivity and thermopower of nickel-copper alloys.* Le Journal de Physique Colloques **35**, C4 (1974).

[281] A. Boyd, C. O'Kane, and B. Meenan. *Control of calcium phosphate thin film stoichiometry using multi-target sputter deposition.* Surface and Coatings Technology **233**, 131 (2013).

[282] P. Fan, Z.-h. Zheng, Y.-z. Li, Q.-y. Lin, J.-t. Luo, G.-x. Liang, X.-m. Cai, D.-p. Zhang, and F. Ye. *Low-cost flexible thin film thermoelectric generator on zinc based thermoelectric materials.* Applied Physics Letters **106** (2015).

[283] Z.-k. Cai, P. Fan, Z.-h. Zheng, P.-j. Liu, T.-b. Chen, X.-m. Cai, J.-t. Luo, G.-x. Liang, and D.-p. Zhang. *Thermoelectric properties and micro-structure characteristics of annealed N-type bismuth telluride thin film.* Applied surface science **280**, 225 (2013).

[284] R. Lan, S. L. Otoo, P. Yuan, P. Wang, Y. Yuan, and X. Jiang. *Thermoelectric properties of Sn doped GeTe thin films.* Applied Surface Science **507**, 145025 (2020).

[285] N. Fukatani, Y. Kurosaki, S. Yabuuchi, A. Nishide, and J. Hayakawa. *Improved power factor in low thermal conductive Fe_2VAl-based full-Heusler thin films by composition-control with off-axis sputtering method.* Applied Physics Letters **112** (2018).

[286] F. Machda, S. Singh, K. Kuga, A. K. Ang, M. Matsunami, and T. Takeuchi. *Thermoelectric performance of* $Fe_2V_{0.9}W_{0.1}Al$ *thin films deposited on n-type Si substrates.* Japanese Journal of Applied Physics **62**, 055502 (2023).

[287] C. Wu, C. Tseng, Y. Fanchiang, C. Cheng, K. Lin, S. Yeh, S. Yang, C. Wu, T. Liu, M. Wu *et al. High-quality thulium iron garnet films with tunable perpendicular magnetic anisotropy by off-axis sputtering–correlation between magnetic properties and film strain.* Scientific Reports **8**, 11087 (2018).

[288] S. Hou, J. Kwo, R. Watts, J.-Y. Cheng, and D. Fork. *Structure and properties of epitaxial* $Ba_{0.5}Sr_{0.5}TiO_3/SrRuO_3/ZrO_2$ *heterostructure on Si grown by off-axis sputtering.* Applied physics letters **67**, 1387 (1995).

[289] S. Kim, Y.-S. Lee, and N.-H. Kim. *Homogeneity-and Stoichiometry-Induced Electrical and Optical Properties of Cu−Se Thin Films by RF Sputtering Power.* Materials **16**, 6087 (2023).

[290] Y. Hakuraku, S. Miyata, T. Inoue, and S. Nozoe. *thin films deposited by stoichiometric target sputtering.* Superconductor Science and Technology **11**, 179 (1998).

[291] T. Selinder, G. Larsson, U. Helmersson, and S. Rudner. *Resputtering effects on the stoichiometry of* $YBa_2Cu_3O_x$ *thin films.* Journal of applied physics **69**, 390 (1991).

[292] H. Miyazaki, S. Tanaka, N. Ide, K. Soda, and Y. Nishino. *Thermoelectric properties of Heusler-type off-stoichiometric* $Fe_2V_{1+x}Al_{1-x}$ *alloys.* Materials Research Express **1**, 015901 (2013).

[293] S. A. Khandy, I. Islam, D. C. Gupta, M. A. Bhat, S. Ahmad, T. A. Dar, S. Rubab, S. Dhiman, and A. Laref. *A case study of* Fe_2TaZ*(Z=Al, Ga, In) Heusler alloys: hunt for half-metallic behavior and thermoelectricity.* RSC advances **8**, 40996 (2018).

[294] S. A. Khandy, I. Islam, D. C. Gupta, R. Khenata, and A. Laref. *Lattice dynamics, mechanical stability and electronic structure of Fe-based Heusler semiconductors.* Scientific reports **9**, 1475 (2019).

[295] D. I. Bilc, G. Hautier, D. Waroquiers, G.-M. Rignanese, and P. Ghosez. *Low-dimensional transport and large thermoelectric power factors in bulk semiconductors by band engineering of highly directional electronic states.* Physical review letters **114**, 136601 (2015).

[296] Y. Furuta, K. Kato, T. Miyawaki, H. Asano, and T. Takeuchi. *Fe_2VAl-based thermoelectric thin films prepared by a sputtering technique.* Journal of electronic materials **43**, 2157 (2014).

[297] Y. Nishino, M. Kato, S. Asano, K. Soda, M. Hayasaki, and U. Mizutani. *Semiconductorlike behavior of electrical resistivity in Heusler-type Fe_2VAl compound.* Physical review letters **79**, 1909 (1997).

[298] Y. Nishino and Y. Tamada. *Doping effects on thermoelectric properties of the off-stoichiometric Heusler compounds $Fe_{2-x}V_{1+x}Al$.* Journal of Applied Physics **115**, 123707 (2014).

[299] E. Alleno, A. Diack-Rasselio, M. T. Noutack, and P. Jund. *Optimization of the thermoelectric properties in self-substituted Fe_2VAl.* Physical Review Materials **7**, 075403 (2023).

[300] F. Garmroudi, M. Parzer, A. Riss, A. V. Ruban, S. Khmelevskyi, M. Reticcioli, M. Knopf, H. Michor, A. Pustogow, T. Mori *et al.* *Anderson transition in stoichiometric Fe_2VAl: high thermoelectric performance from impurity bands.* Nature Communications **13**, 3599 (2022).

[301] M. Mikami, K. Ozaki, H. Takazawa, A. Yamamoto, Y. Terazawa, and T. Takeuchi. *Effect of Ti substitution on thermoelectric properties of W-doped Heusler Fe_2VAl alloy.* Journal of electronic materials **42**, 1801 (2013).

[302] F. Chollet *et al.* *Keras.* `https://github.com/fchollet/keras` (2015).

[303] M. Abadi, A. Agarwal, P. Barham, E. Brevdo, Z. Chen, C. Citro, G. S. Corrado, A. Davis, J. Dean, M. Devin, S. Ghemawat, I. Goodfellow, A. Harp, G. Irving, M. Isard, Y. Jia, R. Jozefowicz, L. Kaiser, M. Kudlur, J. Levenberg *et al.* *TensorFlow: Large-Scale Machine Learning on Heterogeneous Systems* (2015). Software available from tensorflow.org.

[304] N. Srivastava, G. Hinton, A. Krizhevsky, I. Sutskever, and R. Salakhutdinov. *Dropout: a simple way to prevent neural networks from overfitting*. The journal of machine learning research **15**, 1929 (2014).

[305] D. P. Kingma and J. Ba. *Adam: A method for stochastic optimization*. arXiv preprint arXiv:1412.6980 (2014).

[306] M. Stöger. *Investigation of the relationship between Fe_2VAl-based thin films sputtered of silicon and their bulk analogon with respect to the thermoelectric properties* (2021).

List of publications

1. **Riss, A.**, Lasisch, E., Podbelsek, S., Parzer, M., Garmroudi, F., Eisenmenger-Sittner, C., Pustogow, A., Mori, T., & Bauer, E. Composition-tuned enhancement of thermoelectric properties in Fe_2VAl-based thin films. To be published.

2. **Riss, A.**, Garmroudi, F., Parzer, M., Eisenmenger-Sittner, C., Pustogow, A., Mori, T., & Bauer, E. Material-efficient preparation and thermoelectric properties of metallic NiAu films. To be published.

3. **Riss, A.**, Garmroudi, F., Parzer, M., Pustogow, A., Mori, T., & Bauer, E. (2024). Thermoelectric power factor of composites. Physical Review Applied, 21(1), 014002. `https://doi.org/10.1103/PhysRevApplied.21.014002`

4. Pecunia, V., Silva, S. R. P., Phillips, J. D., Artegiani, E., Romeo, A., Shim, H., ... **Riss, A.**, ... & Welch, G. C. (2023). Roadmap on Energy Harvesting Materials. Journal of Physics: Materials. `https://doi.org/10.1088/2515-7639/acc550`

5. Garmroudi, F., Parzer, M., Knopf, M., **Riss, A.**, Michor, H., Ruban, A. V., ... & Bauer, E. (2023). Unveiling the structure-property relationship in metastable Heusler compounds by systematic disorder tuning. Physical Review B, 107(1), 014108. `https://doi.org/10.1103/PhysRevB.107.014108`

6. Garmroudi, F., Parzer, M., **Riss, A.**, Pustogow, A., Mori, T., & Bauer, E. (2023). Pivotal role of carrier scattering for semiconductorlike transport in Fe_2VAl. Physical Review B, 107(8), L081108. `https://doi.org/10.1103/PhysRevB.107.L081108`

7. **Riss, A.**, Stöger, M., Parzer, M., Garmroudi, F., Reumann, N., Hinterleitner, B., ... & Bauer, E. (2023). Criteria for Erroneous Substrate Contribution to

the Thermoelectric Performance of Thin Films. Physical Review Applied, 19(5), 054024. https://doi.org/10.1103/PhysRevApplied.19.054024

8. Chatterjee, D., Puphal, P., Barthélemy, Q., Willwater, J., Süllow, S., Baines, C., ... **Riss, A.**, ... & Bert, F. (2023). From spin liquid to magnetic ordering in the anisotropic kagome Y-kapellasite $Y_3Cu_9(OH)_{19}Cl_8$: A single-crystal study. Physical Review B, 107(12), 125156. https://doi.org/10.1103/PhysRevB.107.125156

9. Garmroudi, F., Parzer, M., **Riss, A.**, Bourgès, C., Khmelevskyi, S., Mori, T., ... & Pustogow, A. (2023). High thermoelectric performance in metallic NiAu alloys via interband scattering. Science Advances, 9(37), eadj1611. https://doi.org/10.1126/sciadv.adj1611

10. Rogl, G., Garmroudi, F., **Riss, A.**, Yan, X., Sereni, J. G., Bauer, E., & Rogl, P. (2022). Understanding thermal and electronic transport in high-performance thermoelectric skutterudites. Intermetallics, 146, 107567. https://doi.org/10.1016/j.intermet.2022.107567

11. Garmroudi, F., Parzer, M., **Riss, A.**, Beyer, S., Khmelevskyi, S., Mori, T., ... & Bauer, E. (2022). Large thermoelectric power factors by opening the band gap in semimetallic Heusler alloys. Materials Today Physics, 27, 100742. https://doi.org/10.1016/j.mtphys.2022.100742

12. Parzer, M., Garmroudi, F., **Riss, A.**, Khmelevskyi, S., Mori, T., & Bauer, E. (2022). High solubility of Al and enhanced thermoelectric performance due to resonant states in Fe_2VAl_x. Applied Physics Letters, 120(7). https://doi.org/10.1063/5.0077159

13. Garmroudi, F., Parzer, M., **Riss, A.**, Ruban, A. V., Khmelevskyi, S., Reticcioli, M., ... & Bauer, E. (2022). Anderson transition in stoichiometric Fe_2VAl: high thermoelectric performance from impurity bands. Nature Communications, 13(1), 3599. https://doi.org/10.1038/s41467-022-31159-w

14. Salamakha, L., Sologub, O., **Riss, A.**, Michor, H., Müller, H., Stöger, B., ... & Bauer, E. (2022). Complex transport and magnetism of the ternary boride

$YbPt_5B_2$. Physical Review B, 105(20), 205112. https://doi.org/10.1103/PhysRevB.105.205112

15. Reumann, N., **Riss, A.**, Garmroudi, F., Parzer, M., Kovacevic, J., Mori, T., & Bauer, E. (2022). Thermoelectric properties and low-temperature transport anomalies in the p-type full-Heusler compounds $Fe_{2-x}Cr_xVAl$. Physical Review B, 106(23), 235138. https://doi.org/10.1103/PhysRevB.106.235138

16. Garmroudi, F., **Riss, A.**, Parzer, M., Reumann, N., Müller, H., Bauer, E., ... & Kimura, K. (2021). Boosting the thermoelectric performance of Fe_2VAl-type Heusler compounds by band engineering. Physical Review B, 103(8), 085202. https://doi.org/10.1103/PhysRevB.103.085202

17. Mukherjee, S., Aramanda, S. K., Legese, S. S., **Riss, A.**, Rogl, G., Femi, O. E., ... & Chattopadhyay, K. (2021). Anisotropy of microstructure and its influence on thermoelectricity: the case of $Cu_2Te-Sb_2Te_3$ eutectic. ACS Applied Energy Materials, 4(10), 11867-11877. https://doi.org/10.1021/acsaem.1c02664

18. Garmroudi, F., Parzer, M., **Riss, A.**, Reumann, N., Hinterleitner, B., Tobita, K., ... & Bauer, E. (2021). Solubility limit and annealing effects on the microstructure & thermoelectric properties of $Fe_2V_{1-x}Ta_xAl_{1-y}Si_y$ Heusler compounds. Acta Materialia, 212, 116867. https://doi.org/10.1016/j.actamat.2021.116867

19. **Riss, A.** (2019). Herstellung und Untersuchung von dünnen Schichten, basierend auf der Heusler-Verbindung Fe_2VAl, im Hinblick auf thermoelektrische Anwendungen (Master's thesis, Wien). https://doi.org/10.34726/hss.2019.62408

Lebenslauf
Alexander Riss

Ausbildung

04/2019 - 03/2024:	**Doktorat an der TU Wien** Thema: „Study of thermoelectric properties of multi-material composites and thin films versus the single-material performances“
10/2022:	**Forschungsaufenthalt an der Castilla-La Mancha University (Spanien)**
01/2021 - 02/2021:	**Forschungsaufenthalt an der Aarhus University (Dänemark)**
04/2019 - 12/2019:	**Zivildienst**
04/2017 - 03/2019:	**Masterstudium an der TU Wien** Thema der Diplomarbeit: „Herstellung und Untersuchung von dünnen Schichten, basierend auf der Heusler-Verbindung Fe_2VAl, im Hinblick auf thermoelektrische Anwendungen“ **Mit Auszeichnung bestanden (Notendurchschnitt: 1,05)**
10/2013 - 03/2017:	**Bachelorstudium an der TU Wien** Thema der Bachelorarbeit: „Electron dynamics in attosecond transient absorption spectroscopy“ **Mit Auszeichnung bestanden (Notendurchschnitt: 1,19)**
09/2009 - 06/2013:	**Oberstufenrealgymnasium De La Salle Schule Strebersdorf**

Beruflicher Werdegang

04/2019 - 03/2024:	**Projektmitarbeiter an der TU Wien im Zuge des Doktorates** - Betreung zahlreicher Studenten in unterschiedlichen Projekten - Veröffentlichung mehrerer wissenschaftlicher Publikationen - Teilnahme an internationalen Konferenzen in Europa und Amerika - Mehrwöchige Forschungsaufenthalte in Spanien und Dänemark
08/2020:	**Gründung der Living Room Escape OG**
03/2018 - 11/2018:	**Projektmitarbeiter an der TU Wien im Zuge der Diplomarbeit**

04/2016 - 02/2017:	**Tutor an der TU Wien bei geringfügiger Anstellung**
09/2016:	**Ferialpraktikum bei Gerstenmayer GmbH**
08/2015:	**Ferialpraktikum an der TU Wien**

Persönliche Fähigkeiten und Kompetenzen

Fremdsprachen:	Deutsch (Muttersprache) Englisch (fließend)
IT-Kenntnisse:	Sehr gute Kenntnisse: MS Office, LaTeX, Adobe Illustrator Gute Kenntnisse: Adobe Photoshop, Visual Studio Code, GitHub
Programmiersprachen:	Sehr gute Kenntnisse: Python Grundkenntnisse: Java, HTML/CSS, C, C++
Sonstige Interessen:	Data Science/Big Data Künstliche Intelligenz

[redacted]

Wien, am 04.02.2024

Unterschrift